

**Development of Non-contact Ultrasonic Guided Wave-based Methodology for Inspection of Steam Generator Tubes of PFBR**

*By*

**M.M. Narayanan  
(PHYS 02 2012 04 012)**

**Indira Gandhi Center for Atomic Research, Kalpakkam**

*A thesis submitted to the  
Board of Studies in Physical Sciences  
In partial fulfillment of requirements  
for the Degree of  
**DOCTOR OF PHILOSOPHY**  
of  
**HOMI BHABHA NATIONAL INSTITUTE***

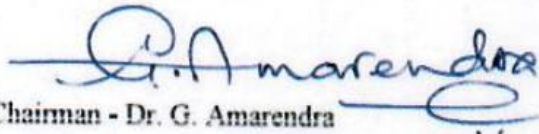


**August, 2019**

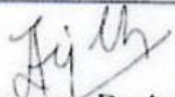
# Homi Bhabha National Institute

## Recommendations of the Viva Voce Committee

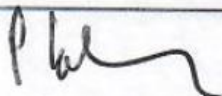
As members of the Viva Voce Committee, we certify that we have read the dissertation prepared by M.M. Narayanan entitled "Development of Non-contact Ultrasonic Guided Wave-based Methodology for Inspection of Steam Generator Tubes of PFBR" and recommend that it may be accepted as fulfilling the thesis requirement for the award of Degree of Doctor of Philosophy.

  
Chairman - Dr. G. Amarendra

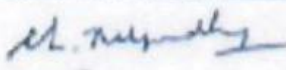
Date: April 28, 2021

  
Guide / Convener - Dr. Anish Kumar

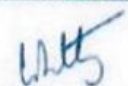
Date: April 28, 2021

  
Examiner - Prof. Peter Cawley, Imperial College, London

Date: 1 May 2021

  
Member 1 - Dr. C.K. Mukhopadhyay

Date: April 28, 2021

  
Member 2 - Dr. C.V. Krishnamurthy, IITM, Chennai

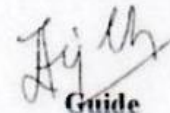
Date: April 28, 2021

Final approval and acceptance of this thesis is contingent upon the candidate's submission of the final copies of the thesis to HBNI.

I hereby certify that I have read this thesis prepared under my direction and recommend that it may be accepted as fulfilling the thesis requirement.

Date: April 28, 2021

Place: Kalpakkam

  
Guide

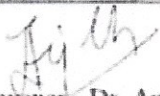
# Homi Bhabha National Institute

## Recommendations of the Viva Voce Committee

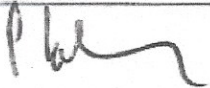
As members of the Viva Voce Committee, we certify that we have read the dissertation prepared by M.M. Narayanan entitled "Development of Non-contact Ultrasonic Guided Wave-based Methodology for Inspection of Steam Generator Tubes of PFBR" and recommend that it may be accepted as fulfilling the thesis requirement for the award of Degree of Doctor of Philosophy.

  
Chairman - Dr. G. Amarendra

Date: April 28, 2021

  
Guide / Convener - Dr. Anish Kumar

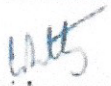
Date: April 28, 2021

  
Examiner - Prof. Peter Cawley, Imperial College, London

Date: 1 May 2021

  
Member 1 - Dr. C.K. Mukhopadhyay

Date: April 28, 2021

  
Member 2 - Dr. C.V. Krishnamurthy, IITM, Chennai

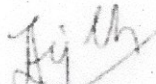
Date: April 28, 2021

Final approval and acceptance of this thesis is contingent upon the candidate's submission of the final copies of the thesis to HBNI.

I hereby certify that I have read this thesis prepared under my direction and recommend that it may be accepted as fulfilling the thesis requirement.

Date: April 28, 2021

Place: Kalpakkam

  
Guide

## STATEMENT BY AUTHOR

This dissertation has been submitted in partial fulfillment of requirements for an advanced degree at Homi Bhabha National Institute (HBNI) and is deposited in the Library to be made available to borrowers under rules of the HBNI.

Brief quotations from this dissertation are allowable without special permission, provided that accurate acknowledgement of source is made. Requests for permission for extended quotation from or reproduction of this manuscript in whole or in part may be granted by the Competent Authority of HBNI when in his or her judgment the proposed use of the material is in the interests of scholarship. In all other instances, however, permission must be obtained from the author.

M.M.Narayanan (M.M. NARAYANAN)

Name & Signature

of the student

## DECLARATION

I, hereby declare that the investigation presented in the thesis has been carried out by me. The work is original and has not been submitted earlier as a whole or in part for a degree / diploma at this or any other Institution / University.

M.H. Nanyan. (M.M. NARAYANAN)

Name & Signature

of the student

## List of publications arising from the thesis

### Journals

1. **M.M. Narayanan**, Anish Kumar, S. Thirunavukkarasu, C.K. Mukhopadhyay, Development of Ultrasonic Guided Wave Inspection Methodology for Steam Generator Tubes of Prototype Fast Breeder Reactor, Ultrasonics, Volume 93, 2019, 112-121. <https://doi.org/10.1016/j.ultras.2018.11.003>. (Impact factor: 3.065).
2. **M.M. Narayanan**, V. Arjun, Anish Kumar, C.K. Mukhopadhyay, Development of In-bore Magnetostrictive Transducer for Ultrasonic Guided-Wave Based-inspection of Steam Generator Tubes of PFBR, Ultrasonics 106 (2020) 106148. <https://doi.org/10.1016/j.ultras.2020.106148>. (Impact factor: 3.065).
3. **M.M. Narayanan**, V. Arjun, Anish Kumar, Influence of Thermal Expansion Bend and Tubesheet Geometry on Guided Wave Inspection of Steam Generator Tubes of a Fast Breeder Reactor, Structural Health Monitoring, 2021 (Impact factor: 4.87). <https://doi.org/10.1177/1475921720983520>
4. V. Arjun, **M.M. Narayanan**, S. Thirunavukkarasu, Anish Kumar, An Approach for Optimization of Geometrical Parameters of a Magnetostrictive Ultrasonic Guided Wave Probe, IEEE Sensors Journal, 2021 (Impact factor: 3.073). Doi: 10.1109/JSEN.2021.3053604

## Conference proceedings/Book Chapter

1. **M.M. Narayanan**, Anish Kumar, C.K. Mukhopadhyay, Detection of Multiple Flaws in Steam Generator Tubes of PFBR Using Ultrasonic Guided Waves, Structural Integrity Assessment: Proceedings of ICONS 2018, pp. 737-747, 2019, Lecture Notes in Mechanical Engineering book series (LNME), Springer, Singapore, [https://doi.org/10.1007/978-981-13-8767-8\\_63](https://doi.org/10.1007/978-981-13-8767-8_63). (**Best Paper and 2<sup>nd</sup> best Oral Presentation Award**).
2. **M.M. Narayanan**, Anish Kumar, S. Thirunavukkarasu, C.K. Mukhopadhyay, Detection of Service-Induced Damage in Steam Generator Tubes of PFBR using Ultrasonic Guided Waves, Proceedings of NDE 2018 Conference & Exhibition on Non-Destructive Evaluation, December 19-21, 2018, Mumbai. <http://www.ndt.net/?id=24365>. (**Paper and Oral Presentation**).

*M.M. Narayanan*

[M.M. Narayanan]

## **DEDICATIONS**

Solely dedicated to my parents and the almighty

## ACKNOWLEDGEMENTS

Undertaking this Ph.D. has been a true research experience for me and it would not have been possible to do without the support and guidance that I received from many people.

I would like to first thank my supervisor **Dr. Anish Kumar** for all the support and encouragement he gave me, during the course of my Ph.D. Without his support, guidance, ideas and time-to-time discussions this Ph.D. would not have been achievable.

I sincerely thank my doctoral committee chairman, **Dr. G. Amarendra** and the doctoral committee members, **Dr. C.K. Mukhopadhyay** and **Dr. C.V. Krishnamurthy**, IITM, **Chennai** for many useful suggestions and yearly evaluation of the progress of the work.

I am really grateful to my co-worker **Shri V. Arjun** for his support in many forms during my work. I would like to express my thanks to **Dr. Thirunavukkarsu** for many useful discussions and for sharing his specimens with me for my work. I owe my thanks to **Dr. Govind Kumar Sharma** for his advice during difficult times and introducing time-frequency analysis to me. I also thank **Dr. Mahadevan** for spending his valuable time with me in debugging my FE programs and for his support. I would like to express my thanks and gratitude to my friend **Shri Vishweshwaran** for helping me in designing complex geometries and in meshing issues. Further, I sincerely thank **Shri Arunmuthu** for sharing his workstation for FE analyses. I would like to extend my thanks to **Dr. Dhayalan** for many useful discussions. I also thank **Shri S. Arun Kumar** for taking good quality photographs of my specimens and the experimental set-up. Finally, I also thank **Dr. T. Saravanan** for his encouragement and support during the course of my work.

Many thanks are due to **Smt. Nivedha** for coil winding and **Shri Sukumar** for fabrication of magnetostrictive transducers. I also acknowledge the timely support of **Shri Saxena** for machining my specimens. I also express my gratitude to my friend **Shri Manoj Kumar Raja** for his unsolicited advice in making the thesis.

I express my thanks to **Dr. T. Jayakumar, Rtd. Group Director, MMG, IGCAR** for his encouragement to take up FE modelling and for his support. I am grateful to **Dr. S.V.M. Satyanarayana, Professor, Central University, Pondicherry** who has taught me and changed my approach towards physics.

I am very indebted to my father **Shri V.C. Muralidharan** and my sister **Smt. M. Indumathi** for their moral support during the challenging times of the work.

# Table of Contents

<i>Synopsis</i> .....	<i>xiv</i>
<i>List of Figures</i> .....	<i>xvii</i>
<i>List of Tables</i> .....	<i>xxx</i>
<i>List of Abbreviations and Symbols</i> .....	<i>xxxi</i>
<b><i>Chapter 1. Introduction</i></b> .....	<b><i>1</i></b>
1.1 Background context .....	1
1.2 Outline of the thesis .....	4
<b><i>Chapter 2. Review of Literature, Theory and Motivation</i></b> .....	<b><i>8</i></b>
2.1 Chapter overview .....	8
2.2 Introduction.....	8
2.2.1 Prototype Fast Breeder Reactor.....	8
2.2.2 Steam generators of PFBR and scope for ultrasonic guided wave NDE .....	10
2.2.3 International experience on NDE of nuclear steam generator tubes and selection of a rapid NDE technique for PFBR SG tubes .....	13

2.2.4	Ultrasonic guided waves in tubes .....	15
2.2.5	Signal processing techniques .....	33
2.3	Theory .....	42
2.3.1	Theory of guided waves in hollow cylinders.....	42
2.3.2	Magnetostriction .....	46
2.3.3	Finite element analysis.....	56
2.4	Motivation and Objectives .....	60
<b><i>Chapter 3. General Methods: Experiments and Simulation .....</i></b>		<b>65</b>
3.1	Chapter overview .....	65
3.2	Experimental set-up.....	65
3.3	Specimen details.....	69
3.4	Generation of Dispersion curves .....	74
3.4.1	Disperse Software .....	74
3.5	Finite element (FE) simulation details .....	75
3.5.1	3D-FE models developed in FE simulation software ABAQUS.....	75
3.5.2	FE models developed in FE simulation software COMSOL.....	80

***Chapter 4. Optimization of Guided Wave Mode for Long-range Propagation and Study of Feasibility for Detection of Common Defects in SG Tubes of PFBR.....91***

4.1	Chapter overview .....	91
4.2	Mode selection through Disperse software and FE simulation.....	91
4.2.1	Guided mode properties and mode selection using Disperse software .....	91
4.2.2	Mode excitability using FE simulation.....	94
4.3	Results and discussion .....	98
4.3.1	Experimental results for a 1.0 m long SG tube .....	98
4.3.2	Long range propagation of L(0,2) mode at 250 kHz in a 3.8 m long SG tube segment .....	100
4.3.3	Finite element simulation for tubes with defects and experimental validation .....	102
4.3.4	Experimental results for circumferential defects in the thermal expansion bent section of the steam generator tube.....	121
4.4	Summary .....	122

***Chapter 5. Development of In-bore Magnetostrictive Transducer for Generating Optimized Ultrasonic Longitudinal Guided Wave Mode in SG Tubes .....125***

5.1 Chapter overview ..... 125

5.2 Need for in-bore magnetostrictive transducer ..... 125

5.3 Results and discussion..... 128

5.3.1 FE simulation in COMSOL ..... 128

5.3.2 Experimental validation ..... 144

5.4 Conclusions ..... 154

***Chapter 6. Studies on SG Tubes of Mockup SG Test Facility using the Developed In-bore Magnetostrictive Transducer and Influence of Thermal Expansion Bend and Tubesheet on L(0,2) Mode.....157***

6.1 Chapter overview ..... 157

6.2 Results and Discussion ..... 157

6.2.1 Response of axi-symmetric full circumferential grooves in SG tubes of mockup SG set-up ..... 158

6.2.2	Response of non-axi-symmetric defects in SG tubes of mockup SG set-up .....	165
6.2.3	Influence of tubesheet thickness and spigot weld on guided wave signal .....	177
6.3	Conclusions.....	183
<b><i>Chapter 7. Summary and Future work.....</i></b>		<b>186</b>
7.1	Summary .....	186
7.2	Significant Contributions .....	191
7.3	Future works .....	192

## List of Figures

Fig. 2.1. Schematic of steam generator of the Prototype Fast Breeder Reactor [6]. .....	11
Fig. 2.2 (a) Phase velocity and (b) group velocity dispersion curves of a ferritic steel tube of outer diameter 17.2 mm and wall thickness 2.3 mm. ....	17
Fig. 2.3 (a) A signal obtained in a plain pipe and (b) a signal obtained in a long pipe with two welds which are 15 m apart by using transducers attached to a pipe for a full circumference [53]. .....	22
Fig. 2.4. Spectrogram superimposed on dispersion curves of 2 mm thick steel plate [105]. ....	36
Fig. 2.5. Flowchart of Discrete Wavelet Transform. ....	40
Fig. 2.6. Implementation of Discrete Wavelet Transform using filter bank. ....	42
Fig. 2.7. Schematic of (a) Joule effect and (b) Villari effect [135]. .....	49
Fig. 2.8. Generation and sensing of a longitudinal wave in a ferromagnetic pipe using magnetostrictive phenomena [135]. .....	49
Fig. 2.9. Schematic of magnetostrictive strain versus applied magnetic field. ....	49
Fig. 2.10. Amplitude of the generated wave in a ferromagnetic specimen due to Lorentz force and magnetostrictive force [140]. ....	50

## *List of Figures*

- Fig. 3.1 (a) Photograph of experimental set-up with an ultrasonic transducer coupled to the end of an SG tube and (b) schematic of the experimental set-up. .... 67
- Fig. 3.2 (a) Photograph of in-house developed in-bore magnetostrictive transducer, (b) photograph of the experimental set-up with the magnetostrictive transducer inserted into an steam generator tube segment, (c) photograph showing the in-bore magnetostrictive transducer inserted in a tubesheet hole of the mockup SG setup and (d) the schematic of the experimental set-up. .... 68
- Fig. 3.3. Photograph of the experimental set-up for magnetostrictive strain measurement. ....  
..... 69
- Fig. 3.4 (a) A set of specimens used: (i) six partial circumferential defects, (ii) six partial axial defects, (iii) six partial pinholes, (iv) four tapered defects, (v) four sodium impingement defects, (vi) a combination of circumferential, axial and pinhole defects, (vii) thermal expansion bend and (viii) photograph of a thermal expansion bend and (b) photographs of circumferential, axial and pinhole defects. The dimensions and locations of the defects are given in Table 3.1. .... 71
- Fig. 3.5 (a) Photograph of mockup steam generator (SG) test facility, (b) photograph of tube-to-tubesheet joints with spigot welds, (c) side view of tubesheet with SG tubes and (d) schematic of a mockup SG tube in the mockup SG test facility. TS: Tubesheet, TC and RC: transmitter and receiver coils of length 10 mm each. X1-X5 stand for half and full circumferential grooves, as given in Table 3.2. .... 72
- Fig. 3.6. ABAQUS finite element model: (a) Excitation along z-axis of a steam generator tube and (b) excitation signal used in finite element simulation. .... 78

*List of Figures*

Fig. 3.7. ABAQUS finite element models with defects in steam generator tubes: (a) defects considered in the same line, (b) partial circumferential defect, (c) axial defect, (d) partial pinhole, (e) tapered defect, (f) sodium impingement damage and (g) thermal expansion bend. ....78

Fig. 3.8. Mesh details: (a) defect-free tube with hexahedral mesh, (b) tube end mesh, (c) circumferential defect with tetrahedral mesh, (d) axial defect with hexahedral mesh, (e) pinhole with triangular prism mesh, (f) tapered defect with triangular prism mesh, (g) sodium impingement damage with hexahedral mesh, (h) thermal expansion bend with hexahedral mesh and (i) thermal expansion bend with a pinhole with hexahedral mesh. ....79

Fig. 3.9. 2D-axisymmetric finite element models: (a) tubesheet of thickness 25 mm, as in tubesheet of the mockup steam generator, (b) tubesheet of thickness 150 mm, as in the actual tubesheet of the Prototype Fast Breeder Reactor and (c) excitation signal of 300 kHz center frequency. The only difference in Figs. 3.9a and b is the tubesheet thickness, which is 25 mm in Fig. 3.9a and 150 mm (not shown to the scale) in Fig. 3.9b. R1, R2, and R3 are receivers located at 200 mm, 960 mm and 930 mm, respectively from the excitation end. In Figs. 3.9a and b, all the dimensions are in mm. ....81

Fig. 3.10 (a) Schematic of the finite element axi-symmetric model for optimizing diameter and length of the magnet and (b) 2D-finite element axisymmetric model of an in-bore magnetostrictive transducer with optimized magnet dimensions and coil parameters. ....83

Fig. 3.11. Excitation with center frequency at 300 kHz .....85

Fig. 3.12. B-H curve for Mod. 9Cr-1Mo ferritic steel.....88

## *List of Figures*

- Fig. 3.13. Flowchart for steps followed in a finite element model for designing an in-bore magnetostrictive guided wave transducer. .... 90
- Fig. 4.1. (a) Phase velocity dispersion curves and (b) group velocity dispersion curves for SG tubes of the Prototype Fast Breeder Reactor, made of mod. 9Cr-1Mo ferritic steel with the inner diameter of 12.6 mm and the wall thickness of 2.3 mm and (c) mode shape of L(0,2) at 250 kHz. (Disperse software) ..... 92
- Fig. 4.2. (a) Axial displacement signal ( $U_z$ ) obtained at the excitation end and (b) a snapshot of L(0,2) mode at 65  $\mu$ s and (c) magnitude plot of axial displacement in the cross-section (Finite element simulation). .... 96
- Fig. 4.3 (a) A five cycle Hanning window toneburst at the center frequency of 250 kHz, (b) frequency spectrum of (a), (c) axial displacement obtained in a 1.0 m long tube (same as Fig. 4.2a) with ringing shown in the inset, (d) frequency spectrum of the ringing shown in (c), (e) group velocity dispersion curves of SG tubes showing the zero group velocity of L(0,2) mode and (f) amplitudes of the ringing for various cycles of excitation (Finite element simulation).  
..... 97
- Fig. 4.4. Experimental signal obtained from the end of the SG tube segment of 1.0 m length.  
..... 99
- Fig. 4.5. Dispersion curves overlaid on spectrograms: (a) experimental signal (Fig. 4.4) and (b) the axial displacement signal (Fig. 4.2a (FE simulation))..... 99

Fig. 4.6. (a) Experimental signal obtained in a 3.8 m long tube, (b) frequency versus time of propagation and (c) maximum amplitudes of end reflections obtained with transducers of frequencies 180 kHz, 250 kHz and 500 kHz. .... 100

Fig. 4.7. Comparison of circumferential defect signals obtained using (a) finite element (FE) simulation and (b) experiment. **A-F** are defect labels, as in Table 3.1. **G**, the tube end reflection. .... 106

Fig. 4.8. Comparison of axial defect signals obtained using (a) finite element simulation (FE) and (b) experiment. **A-F** are defect labels, as in Table 3.1. **G**, the tube end reflection. .... 106

Fig. 4.9. Comparison of pinhole defect signals obtained using finite element (FE) simulation and experiment. **B-F** are defect labels, as in Table 3.1. **G**, the tube end reflection. .... 106

Fig. 4.10. Comparison of sodium impingement damage signals obtained using finite element (FE) simulation and experiment. **A-D** are defect labels, as in Table 3.1. **G**, the tube end reflection. .... 106

Fig. 4.11. Axial displacement signals obtained for excitation at (a) left and (b) right ends of a tube with tapered defects (TD). **A-D** are defect labels, as in Table 3.1. **G**, the tube end reflection. (Finite element (FE) simulation) .... 108

Fig. 4.12. Experimental signals obtained in a tube with the combination of circumferential defects (CDs), axial defects (AD) and pinholes (PHs). Labels **A-G** represent defects whose dimensions are given in Table 3.1 and **H** represents end reflection. **A**: Full circumferential defect, **B and C**: Axial defects, **D and E**: Part-circumferential defects and **F and G**: Pinholes, as shown in Fig. 3.4a(vi). .... 108

Fig. 4.13. A comparison of amplitudes and times of flight for finite element (FE) simulation and experimental time signals: (a and b) circumferential defects, (c and d) axial defects and (e and f) partial pinholes. A-F represent defect labels, as given in Table 3.1..... 109

Fig. 4.14. Reflected amplitudes from tapered defects (TD): right and left excitation. (Finite element simulation)..... 110

Fig. 4.15. (a) A comparison of amplitudes for a tapered defect (TD), circumferential defects (CD), axial defects (AD) and pinholes (PH) of the same 0.46 mm depth and (b) error between FE estimated locations of the defects and the original locations of the defects Vs. defects. All the amplitudes are normalized with respect to the amplitude of the tapered defect. CE: circumferential extent, AL: axial length and W: Width. (Finite element simulation)..... 110

Fig. 4.16. Reflectivity of L(0,2) mode from axial defects of different lengths vs. ratio of length of the defect to the wavelength. (Finite element simulation)..... 113

Fig. 4.17. Reflectivity of L(0,2) mode for defects with different depths and widths for the same radius of curvature  $R=3.175$  mm. **A-E** stand for different defects. (Finite element simulation) ..... 114

Fig. 4.18. Axial displacement signals obtained for 50%WT deep defects with the radii of curvature: (a)  $R=3.175$  mm, (b)  $R= 5$  mm and (c)  $R= 7$  mm, respectively. ER stands for the end reflection. (Finite element simulation) ..... 115

Fig. 4.19. Axial ( $U_z$ ), radial ( $U_r$ ) and angular displacement ( $U_\theta$ ) signals obtained for 50%WT deep sodium impingement defects with the radius of curvature,  $R=3.175$  mm (Finite element simulation) ..... 116

Fig. 4.20. (a) Finite element model with a full circumferential defect (CD) and (b) finite element model with CD1 fixed at 250 mm and CD2 at different locations. .... 118

Fig. 4.21. Axial displacement signals: (a) for the case of circumferential defect (CD) at 250 mm and (b) for circumferential defect (CD1) at 250 mm and CD2 at 600 mm in a 1 m long tube. **R** denotes the tube end reflection. (Finite element simulation)..... 119

Fig. 4.22. Maximum reflected amplitudes obtained for the case of a single circumferential defect (CD) at various distances and the maximum amplitudes obtained for the case with a circumferential defect (CD1) fixed at 250 mm and with the second circumferential defect (CD2) moved for different distances in 1 m long tubes. The dimensions of the CDs are 0.92 mm depth, 1 mm width and full circumference. (Finite element simulation)..... 119

Fig. 4.23. A comparison of (a) inner diameter (ID) and (b) outer diameter (OD) pinhole signals. **A** refers to the defect signal and **B**, the tube end reflection. The diameter and the depth of the pinhole are 1 mm and 1.38 mm, respectively. (Finite element simulation) ..... 120

Fig. 4.24. Plot of inner diameter (ID) and outer diameter (OD) axial defects' response for various axial lengths. Axial defects have depths 0.46 mm and 1.38 mm. (Finite element simulation)..... 121

Fig. 4.25. Experimental signal obtained in a bent tube. **A-E** are circumferential defect labels, as in Fig. 3.4a(Vii) (and the dimensions and the locations of which are given in Table 3.1), representing corresponding defect signals. **F** stands for the tube end reflection..... 122

*List of Figures*

Fig. 5.1. (a) Photograph showing an ultrasonic transducer placed on the tubesheet of the mockup steam generator (SG) facility and (b) a signal obtained using the ultrasonic transducer placed on the tubesheet. .... 127

Fig. 5.2. 2D section of SG tube and tubesheet: (a) an ultrasonic transducer coupled to the free end of a tube, (b) an ultrasonic transducer coupled to the tubesheet and (c) a conceived model of a magnetostrictive transducer placed beyond the spigot of the tube sheet in the tube region. .... 127

Fig. 5.3. Arrow plot showing magnetic field lines. (Finite element simulation)..... 130

Fig. 5.4 (a)  $B_r$  component along the central line of the tube wall for the magnet of diameter 10 mm and length 50 mm, (b)  $B_z$  component along the central line of the tube wall for magnets of various diameters and fixed length of 50 mm and (c) magnetic induction in the tube for the diameters in Fig. 5.4b superimposed onto the experimental B-H curve for Mod. 9Cr-1Mo steel. (Finite element simulation)..... 130

Fig. 5.5 (a) Axial magnetic induction along the central line of the tube for magnets of various lengths and for a fixed diameter of 10 mm and (b) their gradients. (Finite element simulation) ..... 132

Fig. 5.6. The magnitude of magnetic field at 8.33  $\mu$ s, shown as contour plot (Finite element simulation). .... 134

Fig. 5.7 (a)  $B_r$  and (b)  $B_z$  components at the ID of the tube at the center point below the transmitter coil (TC) and (c) the variation in the maximum of  $B_z$  at the ID of the tube with distance at 8.33  $\mu$ s. (Finite element simulation) ..... 134

Fig. 5.8. Displacement signals at 300 kHz: (a) radial component ( $U_r$ ) and (b) axial component ( $U_z$ ) picked-up at 164.5 mm (center location of the receiver coil) in the tube of 650 mm length. Labels I: initial pick-up of L(0,2) mode and A: reflections from the left low-reflection boundary. (Finite element simulation) ..... 136

Fig. 5.9. Induced voltage in the receiver caused by L(0,2) mode at 300 kHz (Villari effect). Labels I: initial pick-up of L(0,2) mode and A: reflections from the left low-reflection boundary. (Finite element simulation) ..... 137

Fig. 5.10. Induced voltages caused by L(0,2) mode in the frequency range: 250 kHz – 350 kHz. (Finite element simulation)..... 137

Fig. 5.11. Maximum induced voltage in the receiver coil for different transmitter and receiver coil lengths. TC: transmitter coil. (Finite element simulation) ..... 139

Fig. 5.12. Thevenin equivalent circuits of (a) transmitter coil and (b) receiver coil..... 140

Fig. 5.13. Variation of optimum number of turns (N) with excitation frequency..... 142

Fig. 5.14 (a) Finite element (FE) simulation and (b) experimental signals obtained in a tube of 1 m length, respectively, for frequencies: 280 kHz, 300 kHz, 320 kHz and 340 kHz. Labels a, b & c indicate wave packets resulting from bi-directional propagation of L(0,2) mode and R1 & R2 represent the first and second end reflections (Gain used: 60.8 dB). I: initial pick up and NR: near end reflection..... 146

Fig. 5.15. Schematic of reflection pattern obtained in a tube with free ends due to bi-directional propagation (formation of three-echo pattern). ..... 147

*List of Figures*

Fig. 5.16 (a) A comparison of Finite Element (FE) simulation and experimental amplitudes of the first end reflections obtained in a tube of 1 m length for different frequencies, (b) the difference in the amplitudes of the first end reflections between FE and experiment vs. frequency and (c) the difference in the times of flight of the first end reflections between FE and experiment vs. frequency. Amplitude values in (a) are normalized with the corresponding amplitudes at 250 kHz for both experimental and FE simulation. .... 148

Fig. 5.17. Experimentally obtained group velocity superimposed on the group velocity dispersion curves..... 149

Fig. 5.18. Experimental signal, showing multiple end reflections, obtained in a 1.5 m long tube for the frequency of 300 kHz (Gain: 62.8 dB)..... 150

Fig. 5.19 (a) Axial displacement signal obtained in Finite element (FE) simulation and (b) experimental signals obtained in a 1.5 m long tube with a circumferential defect located at 840 mm, for frequency of 300 kHz. Gain used: 65.0 dB. I: initial pick up and NR is near end reflection. .... 152

Fig. 5.20. Experimental signals obtained at the frequency of 300 kHz in a 1.5 m long tube with 20% WT and 40% WT deep axial defects. AD1 & AD2: axial defects. Gain used: 64.8 dB ..... 152

Fig. 5.21. Experimental signals obtained in a 1060 mm long tube with a 1.5 mm dia. pinhole for the frequency of 300 kHz: (a) Magnetostrictive transducer (Gain used:85.0 dB) and (b) a piezo based ultrasonic transducer (Gain used: 32.0 dB). ER stands for end reflection. .... 153

## *List of Figures*

Fig. 6.1. Experimental signals obtained in steam generator (SG) tubes of mockup SG test facility: (a) raw and (b) processed signals corresponding to 0.69 mm deep and 2 mm wide full circumferential grooves (T#A) and (c) raw and (d) processed signals corresponding to 0.46 mm deep and 1 mm wide full circumferential grooves (T#B). The labels An-Bn stand for defects and T#(A-B) for tubes, as given in Table 3.2. Where, n=1,2,3,4 and 5. ER; End reflection. Gain used: 85 dB ..... 159

Fig. 6.2. Experimental signals obtained in steam generator (SG) tubes of mockup SG test facility: (a) raw and (b) processed signals corresponding to 0.23 mm deep and 1 mm wide full circumferential grooves (T#C). The labels Cn stand for defects and T#C for tube, as given in Table 3.2. Where, n=1,2,3,4 and 5. ER: End reflection. Gain used: 85 dB ..... 160

Fig. 6.3. Experimental signals obtained in steam generator (SG) tubes of mockup SG test facility: (a) raw and (b) processed signals for the case of defect-free tube (T#R). Gain used: 85 dB and ER: End reflection..... 160

Fig. 6.4. Symmlet 12 wavelet..... 163

Fig. 6.5. Experimental signals obtained in the steam generator (SG) tubes of the mockup SG test facility: (a) raw and (b) Discrete Wavelet Transform (DWT) processed signals corresponding to 0.69 mm deep and 2 mm wide full circumferential grooves (T#A) and (c) cross-correlated signal normalized with respect to the maximum response. The labels A1-A5 stand for defects and T#A for tube, as given in Table 3.2. ER: end reflection. .... 165

Fig. 6.6. Experimental signals obtained in steam generator (SG) tubes of mockup SG test facility: (a) raw and (b) processed signals corresponding to 0.69 mm deep and 2 mm wide half circumferential grooves (T#D) and (c) raw and (d) processed signals corresponding to

## *List of Figures*

0.46 mm deep and 2 mm wide full circumferential grooves (T#E). The labels Dn-En stand for defects and T#(D-E) for tubes, as given in Table 3.2. Where, n=1,2,3,4 and 5. ER: End reflection. Gain used: 85 dB. ....	167
Fig. 6.7. Reflected amplitudes versus defect locations in steam generator (SG) tubes of the mockup SG test facility with 0.69 mm depth full and half circumferential grooves. A and D correspond to full and half circumferential defects, respectively. ....	168
Fig. 6.8. Axial displacement signals obtained at the frequency of 300 kHz: (a) a 3 m long straight SG tube and (b) 3 m long SG tube with a thermal expansion bend. (Finite element simulation) .....	171
Fig. 6.9. Spectrograms for the cases of the finite element signals obtained in (a) a 3 m long straight SG tube and (b) a 3 m long SG tube with a thermal expansion bend. (Finite element simulation) .....	171
Fig. 6.10. Snapshots of L(0,2) mode propagation in the bend at different time instants. L(0,2) wave mode propagates from left to right. (Finite element simulation).....	172
Fig. 6.11 (a) Schematic of thermal expansion bend. Axial displacement signals obtained from pinholes at 1.5 m at the frequency of 300 kHz in a thermal expansion bend for (b) a 1.5 mm dia. pinhole at extrados and (c) a 1.5 mm dia. pinhole at intrados. (Finite element simulation) .....	173
Fig. 6.12. (a) Amplitudes of time signals (axial displacement) at different locations of a 3.0 m long defect-free thermal expansion bend, (b) reflected amplitudes received at the excitation	

end from 1.5 mm dia. pinholes at locations A, C, E, G and I and (c) variation of axial stress amplitudes across the bends. (Finite element simulation result)..... 174

Fig. 6.13. Snapshots of L(0,2) mode and mode converted waves in SG tube and tubesheet (TS): (a) incident L(0,2) mode at R1 at 43  $\mu$ s in the tube, (b) incident L(0,2) mode approaching spigot-tubesheet transition at 154  $\mu$ s, (c) mode conversion of L(0,2) mode in the tubesheet of 150 mm thickness at 183  $\mu$ s, (d) mode converted longitudinal wave (L), shear wave (S), head wave (H) and Rayleigh wave (R) in the 150 mm thick tubesheet at 196  $\mu$ s, (e) arrow plot of displacement vector superimposed on plot (d), and (f) waves in 25 mm thick tubesheet at 196  $\mu$ s. LRB stands for low reflecting boundary and it is imposed at the right edge of the tubesheet. The coordinates of the receiver points R1, R2 and R3 are (8.6 mm, 200 mm), (6.36 mm, 960 mm) and (75 mm, 930 mm), respectively with the origin (0,0) at the center of the tube at the excitation end. (Finite element simulation) ..... 179

Fig. 6.14. Magnitude of displacement vector in a tube with 150 mm thick tubesheet: (a) at R2= (6.36 mm, 960 mm) and (b) at R3= (75 mm, 930 mm). (Finite element simulation) ..... 181

Fig. 6.15. Axial displacement signals picked up at receiver point R1 located at 200 mm from the excitation end and 680 mm from spigot-tubesheet transition for (a) tubesheet (TS) thickness of 150 mm (actual SG of PFBR SG) with low-reflection boundary (LRB) at the right edge of tubesheet, (b) TS thickness of 25 mm (Mockup SG) with LRB at the right edge of the TS and (c) with LRB at the top and right edges of the 25 mm thick TS. LRB stands for low reflecting boundary. (Finite element simulation) ..... 181

## **List of Tables**

<b>Table 2.1. Operating temperatures and pressures of SGs of PFBR.....</b>	<b>11</b>
<b>Table 3.1. Types of defects, locations and their dimensions in SG tube segments.....</b>	<b>73</b>
<b>Table 3.2. Circumferential defects, locations and their dimensions in mockup SG test facility.....</b>	<b>74</b>
<b>Table 3.3. Parameters used in COMSOL FE models.....</b>	<b>86</b>
<b>Table 5.1. Optimized parameters of an in-bore transducer to generate L(0,2) mode at 300 kHz.....</b>	<b>144</b>
<b>Table 6.1. SNRs for different decomposition levels of the signal corresponding to 0.69 mm deep and 2 mm wide full circumferential grooves.....</b>	<b>163</b>

## **List of Abbreviations and Symbols**

<b>CFL</b>	Courant-Friedrichs-Lewy number
<b>DC</b>	Direct Current
<b>DWT</b>	Discrete Wavelet Transform
<b>EDM</b>	Electrical Discharge Machining
<b>EMAT</b>	Electromagnetic Acoustic Transducer
<b>EMD</b>	Empirical Mode Decomposition
<b>EMI</b>	Electromagnetic Interference
<b>FEA</b>	Finite Element Analysis
<b>GWT</b>	Guided Wave Testing
<b>ID and OD</b>	Inner and Outer Diameter
<b>IRIS</b>	Internal Rotary Inspection System
<b>ISI</b>	In-service Inspection
<b>LRUT</b>	Long Range Ultrasonic Testing
<b>MPT</b>	Magnetostrictive Patch Transducer
<b>RFECT</b>	Remote Field Eddy Current Testing
<b>SG</b>	Steam Generator
<b>SNR</b>	Signal to Noise Ratio
<b>STFT</b>	Short Time Fourier Transform
<b>SWG</b>	Standard Wire Gauge
<b>TF</b>	Time-Frequency
<b>TOF</b>	Time of Flight
<b>TS</b>	Tubesheet

$\bar{A}$	Magnetic vector potential
$A_\varphi$	Azimuthal component of $\bar{A}$
[ <b>B</b> ]	Magnetic induction matrix
$B_r, B_\varphi$ and $B_z$	Radial, circumferential and axial components of $\bar{B}$
[ <b>C</b> ]	Elastic stiffness matrix
$C_p$ and $C_s$	Longitudinal and shear wave velocity
$\{\ddot{D}\}, \{\dot{D}\}$ and $\{D\}$	Acceleration, velocity and displacement
<b>E</b>	Young's modulus
$\bar{E}$	Electric field
$\{\mathbf{F}^{\text{ext}}\}$	External force
$F_s$	Sampling frequency
[ <b>H</b> ]	Applied magnetic field matrix
$\bar{H}$	Vector potential
$H_r, H_\varphi$ and $H_z$	Radial, circumferential and axial components of magnetic field [ <b>H</b> ]
$H_r, H_\theta$ and $H_z$	Radial, circumferential and axial components of vector potential $\bar{H}$
$J^e$	Source current density
$J^{\text{induced}}$	Induced current density
[ <b>K</b> ]	Stiffness matrix
$L_T$ and $L_R$	Transmitter and receiver inductance
[ <b>M</b> ]	Mass matrix

## *List of abbreviations and symbols*

<b>MHz</b>	Mega Hertz
$N_T$ and $N_R$	Number of turns of transmitter and receiver
$R_L$	Load resistance
$R_S$	Source resistance
<b>S</b>	Piezomagnetic coefficient along axial direction
$[S^H]$	Compliance matrix
$T$	Wavelet threshold
$\bar{U}$	Displacement vector
$V$	Electrostatic potential
$V_m$	Scalar magnetic potential
$V_{ph}$	Phase velocity
$V_{gr}$	Group velocity
<b>Z</b>	Bessel functions
<b>f</b>	Frequency
<b>d</b>	Thickness of plate
$[d]$	Piezomagnetic coefficient matrix
<b>dB</b>	Decibel
<b>kHz</b>	Kilo Hertz
$l$	Coil length
$r$	Coil mean radius
$\Delta t$	Uncertainty in time
$\Delta\omega$	Uncertainty in angular frequency

**List of abbreviations and symbols**

$\Omega$	Ohm
$\beta$ and $\gamma$	Numerical damping coefficients
$[\epsilon]$	Strain matrix
$\epsilon_{rr}$ , $\epsilon_{r\theta}$ and $\epsilon_{rz}$	Normal strain in r plane and shear strains in $\theta$ and z planes
$\lambda$	Wavelength
$\lambda$ and $\mu$	Lame' constant
$\mu$	Magnetic permeability
$[\mu^\sigma]$	Magnetic permeability at constant stress
$\mu_{rr}$ and $\mu_{zz}$	Radial and axial components of permeability
$\nu$	Poisson's ratio
$\sigma$	Conductivity
$[\sigma]$	Stress matrix
$\sigma_{rr}$ , $\sigma_{r\theta}$ and $\sigma_{rz}$	Normal stress in r plane and shear stresses in $\theta$ and z planes
$\sigma_{std}$	Standard deviation
$\tau$	Time parameter
$\phi$	Scalar potential
$\omega$	Angular Frequency
$\omega_{max}$	Highest angular frequency

## ***Chapter 7. Summary and Future work***

### **7.1 Summary**

In the present study, ultrasonic longitudinal guided wave mode L(0,2) was selected using dispersion curves for the examination of steam generator tubes of PFBR. Then, the frequency range of L(0,2) mode was optimized using dispersion characteristics, attenuation, long range propagation and detection of multiple defects such as circumferential, axial, pinhole, tapered and sodium impingement defects lying along the same line. Finite element simulations were performed to understand the underlying phenomena and the results were experimentally validated. The generation of L(0,2) mode and the subsequent examination of SG tube segments were achieved by coupling ultrasonic transducers to the ends of the tubes. However, there will not be any free ends available in the actual testing, as the tubes are welded to tubesheets. Owing to this constraint, the optimized L(0,2) mode needs to be generated from the ID side of the SG tube. To this end, a novel in-bore magnetostrictive transducer for the generation of L(0,2) mode from ID side has been designed and developed with the aid of FE simulation results obtained in COMSOL. Then, the performance of the developed transducer was evaluated in terms of long-range propagation and defect detection in short SG tube segments. The results obtained were satisfactory. Finally, the usefulness of the developed transducer has been demonstrated in the SG tubes of the mockup SG facility in the detection of multiple defects. The salient results obtained in the thesis are presented below:

- ❖ An axisymmetric longitudinal mode L(0,2) was optimized in the frequency range of 170 kHz- 330 kHz using finite element simulation and experiments. The group velocity of the mode is found to be 5387 m/s and the apparent attenuation exhibited by the mode is 0.72 dB/m.

- ❖ The mode L(0,2) was examined for its long range propagation in a 3.8 m long tube and the maximum distance of propagation achieved was 45.6 m based on multiple reflections.
  
- ❖ The detection of multiple defects namely circumferential, axial, pinhole and sodium impingement defects lying in the same line of sight was examined using FE simulation and experiments. The experimental and simulation results agree well. L(0,2) mode is seen to undergo mode conversion when it interacts with non-axi-symmetric defects. Also, full multiple circumferential defects considered in a thermal expansion bend are seen to be detected with good sensitivity. All the multiple defects lying in the same line could be located fairly accurately with the required sensitivity. Further, it was observed that ID and OD axial and pinhole defects show similar responses.
  
- ❖ Following are the smallest defects detected:
  - Circumferential defect: 0.23 mm (10%WT) depth, 7 mm circumferential extent and 1 mm width.
  - Axial defect: 0.23 mm (10%WT) depth, 7 mm axial length and 1 mm width.
  - Pinhole defect: 1.38 mm (60%WT) depth and 1 mm diameter.
  - Sodium impingement defect: 0.23 mm (10%WT) deep defect of 8.6 mm length and 3.9 mm width
  - Tapered defect: 0.23 mm maximum depth (10%WT), 15 mm length and 27 mm circumferential extent.
  
- ❖ FE simulations for the reflectivity show that the reflectivity is dependent on the effective area presented by the defect. Reflectivity of axial defects is found to be

strongly dependent on the axial length with maximum at quarter and three-quarters of the wavelength and minimum at half and full wavelength.

- ❖ A 2D-axisymmetric FE model of an in-bore magnetostrictive transducer for the generation of L(0,2) mode was designed in the frequency range of 250 kHz to 350 kHz. Towards this, the diameter and the length of the magnet were optimized to be 10 mm and 100 mm, respectively. The operating point (bias) corresponding to the magnetic field (~0.82 T) generated by the magnet of diameter 10 mm was chosen. The coil parameter such as length was optimized using FE studies. The optimized length at 300 kHz turned out to be half the wavelength (=10 mm). Then, the number of turns of the transmitter and receiver coils was optimized to 80 turns using the Thevenin circuit model approach. Further, the width of the transmitter and receiver coils was calculated by considering 75% fill-factor and the width turned out to be 0.4674 mm, which corresponds to 2 layers of 34 SWG copper wire. With all the above parameters, L(0,2) mode was seen to be successfully generated, propagated and received in the model.
- ❖ With the aid of the results, a transducer has been developed for the generation of L(0,2) mode in the frequency range of 250 kHz to 350 kHz from the ID side of an SG tube.
- ❖ FE results obtained for frequencies in the range of 250 kHz-350 kHz were validated experimentally in a 1.0 m long tube. There was a good agreement between FE amplitudes and the times of flight with those of experimental ones. The maximum errors in the amplitudes and the times of flight turned out to be ~10% and 1.2  $\mu$ s, respectively. Further, there was an excellent agreement between the experimental and

theoretical group velocities. The long-range propagation of the L(0,2) mode generated by the developed in-bore magnetostrictive transducer was observed to be 51 m.

- ❖ A full circumferential defect of 0.46 mm depth (20% WT), axial defects (20% WT and 40% WT depths) and a pinhole of 1.5 mm dia. were considered and detected experimentally using the magnetostrictive transducer.
- ❖ The SNR obtained using the magnetostrictive transducer for the pinhole was compared with that obtained using a piezo-based ultrasonic transducer. The SNR for the piezo based transducer is found to be only ~6 dB better as compared to that for the magnetostrictive transducer.
- ❖ To test the validity of the FE model developed, an axi-symmetric circumferential defect was included in the model and the amplitudes and the times of flight of the defect signals were compared. There was a good agreement between the normalized amplitudes (within 10% variation) and the times of flight (difference of 0.75  $\mu$ s) between FE and experiment.
- ❖ A feasibility test was conducted in SG tubes of mockup SG test facility with SG tubes welded to the tubesheet through spigot welds, using the developed in-bore magnetostrictive transducer. The experimental results were noisy and hence, were de-noised using the Discrete Wavelet Transform (DWT) with the optimized wavelet (sym12). The de-noised signals clearly showed that multiple half and full circumferential grooves were detected with the SNR of approx. 5-10 dB. The sensitivity obtained was 20% WT (0.46 mm) deep and 1 mm wide half circumferential

groove based on a 6 dB criterion. The maximum error in locating a defect was found to be approximately 10 mm.

- ❖ Cross-correlation based de-noising was also used, which provided a good representation of the multiple defect signals without any ambiguity in reading defect signals amidst multiple inter-reflections and noise.
- ❖ Furthermore, to understand the influence of a thermal expansion bend on L(0,2) mode, FE simulations were performed. It showed that L(0,2) mode is influenced by the thermal expansion bend in two ways, namely showing up of maximum amplitudes at the extrados and minimum amplitudes at the intrados and mode conversion to a weak flexural mode. The sensitivity variation is also observed throughout the bends both linearly and circumferentially.
- ❖ Experimentally, a half circumferential groove (non-axi-symmetric) at the extrados of the thermal expansion bend was observed to exhibit a higher amplitude. The variation of sensitivity across the bend observed by the FE simulations with pinholes were also observed to be in line with the experimental observations made in the mock up SG tubes with half circumferential defects. The effect of the thermal expansion bend on axi-symmetric defects (full circumferential groove) is seen masked due to the integration of the reflected energy from the full circumference of the defect.
- ❖ Furthermore, there is a delay of 1.7  $\mu$ s in the arrival of the end reflected signal observed for the bent tube in comparison to the straight tube of the same length. This can be used to correct defect signals corresponding to locations in/ beyond the bend.

However, it was also observed that irrespective of the location of a defect in the bend, the defect can be detected with good sensitivity.

- ❖ The effects of tubesheet thickness and the presence of spigot weld on the reflection of guided waves have also been studied using FE simulation. The results indicated that spigot-tubesheet transitions provide 10% reflection of the incident energy. Further,  $L(0,2)$  mode in the SG tube undergoes mode conversion to longitudinal, shear and Rayleigh waves in the tubesheet. It has been observed that signals from heat exchanger tubes with thicker tubesheets are easier to interpret than those of thinner ones. Based on the study, two locations have been proposed for the inspection of SG tubes of PFBR and they are 190 mm and 1270 mm from the top of the tubesheet.

## 7.2 Significant Contributions

The following are the significant contributions from this research,

- ❖ Development of a single  $L(0,2)$  mode guided wave-based methodology for long-range inspection of SG tubes of PFBR and detection of multiple circumferential, axial, pinholes, tapered and sodium impingement defects lying along the same line.
- ❖ Development of transmitter-receiver magnetostrictive FE models for the generation of  $L(0,2)$  mode.
- ❖ Development of an in-bore longitudinal magnetostrictive transducer for the examination of a 23 long SG tube of PFBR of ID 12.6 mm. It can be readily extended to other similar applications where IDs are small.

- ❖ Study of the influence of a multiple thermal expansion bend on L(0,2) mode and its varying sensitivity across the bend.
- ❖ Study of the influence of the tubesheet on L(0,2) mode indicating that thicker tubesheets are better from the inspection point of view.

### **7.3 Future works**

The study undertaken in the thesis leaves a scope for investigating the following:

- ❖ To study the detection and sensitivity of defects in spigot welds.
- ❖ To understand the scattering of L(0,2) mode from defects from the perspective of wave mechanics.
- ❖ To study the linear and circumferential variation of sensitivity in the thermal expansion bend using wave mechanics
- ❖ To study long-range defect detection.
- ❖ To further improve SNR provided by the in-bore magnetostrictive transducer.
- ❖ Exploring the reduction of dead zone/ringing of the magnetostrictive transducer.
- ❖ Design and development of a torsional mode magnetostrictive transducer for generating a completely non-dispersive mode for aiding inspections and compare its response with that of the L(0,2) mode for detection of different types of defects in the SG tube

## Synopsis

The thesis aims at developing a non-contact ultrasonic guided wave technique and methodology for inspection of steam generator (SG) tubes of the Prototype Fast Breeder Reactor (PFBR). Towards this, ultrasonic longitudinal guided wave L(0,2) mode in the frequency range of 250 kHz-350 kHz is optimized in terms of long-range propagation of 46 m length of an SG tube, negligible dispersion, low attenuation and detection of multiple circumferential, axial, pinhole, tapered and sodium impingement defects in SG tubes. Furthermore, detection of multiple circumferential defects in the thermal expansion of an SG is also found to be successful. All the experiments were performed by coupling ultrasonic transducers to the ends of the tubes. Finite element simulations were performed side-by-side for the multiple defect scenarios and the results were validated experimentally. The defect parameter that influences the reflection is found to be the cross-sectional area of a defect and all types of defects have been detected with the required sensitivity.

However, the developed methodology can be implemented only when free ends of tubes are available for coupling an ultrasonic transducer. SGs of PFBR have a closed structure with only accessibility, for inspection, is through ID of the tubes. In order to extend the methodology developed, L(0,2) mode needs to be generated from the ID of the SG tube. SG tubes are made of Mod. 9Cr-1Mo ferritic steel and are ferromagnetic. It is this ferromagnetic property that was exploited to generate L(0,2) mode through a magnetostrictive means from the ID side. The inner and outer diameters of an SG tube of PFBR are 12.6 mm and 17.2 mm, respectively. Hence, an in-bore magnetostrictive transducer has been developed for generating L(0,2) mode at 300 kHz from 12.6 mm ID of an SG tube. The transducer comprises of a permanent magnet to provide static bias (~0.82 T) and a pair of transmitter and receiver

coils for generating a dynamic magnetic field. Systematic 2D- axi-symmetric FE simulations were performed to optimize the diameter and length of the magnet and the length of the transmitter and receiver coils. The optimized diameter and length of the magnet are 10 mm and 100 mm and the optimized length of the transmitter and receiver coils is half the wave length (=10 mm) of L(0,2) mode at the frequency of 300 kHz. The number of turns is optimized to be 80 turns by using the Thevenin circuit model approach. By considering 75% fill-factor, the width of the coil has been calculated to be 0.46 mm, which corresponds to two layers of 34 SWG copper wire.

With the optimized parameters, an in-bore magnetostrictive transducer has been fabricated and tested experimentally by inserting the transducer in the tube. The in-bore magnetostrictive transducer developed is found to generate L(0,2) mode at 300 kHz. Furthermore, an excellent agreement has been observed between experimental and FE results for the frequency sweep (250 – 350 kHz) and the detection of a circumferential defect. The study of long range propagation using the developed transducer indicates the propagation distance of L(0,2) mode to be 51 m in SG tubes. Besides, the transducer is also found to detect a pinhole of 1.5 mm diameter and axial defects with the required sensitivity. The in-bore magnetostrictive transducer has been found to perform very well in terms of long-range propagation and defect detection.

Finally, trial studies were conducted on the SG tubes welded to the tubesheet of the mock SG test facility using the developed in-bore magnetostrictive transducer. The SG tubes have thermal expansion bends with multiple full and half circumferential grooves. The experimental signals obtained were noisy and hence, they were de-noised using the Discrete wavelet transform (DWT) and the cross-correlation technique. The signals de-noised using

DWT clearly showed that multiple half and full circumferential grooves were detected with the SNR of approx. 5-10 dB. The detection sensitivity obtained was a 20%WT (0.46 mm) deep and 1 mm wide half circumferential groove based on 6 dB criterion. Further, to understand the influence of a tubesheet-spigot structure on L(0,2) mode, 2D-axi-symmetric FE simulations for 25 mm and 150 mm thick tubesheets with spigots were performed. The spigot-tubesheet transitions are found to provide 10% reflection of the incident energy and L(0,2) mode undergoes mode conversion to longitudinal, shear and Rayleigh waves in the tubesheet. The mode converted waves are not seen to complicate interpretation of signals in thicker tubesheets. In fact, thicker tubesheets are found to be better from the perspective of inspection. Based on the analysis, two inspection locations for the actual testing of PFBR SG tubes have been chosen for the placement of the in-bore magnetostrictive transducer and they are 190 mm and 1270 mm from the top of the tubesheet.

## ***Chapter 1. Introduction***

### **1.1 Background context**

Non-destructive testing (NDT) plays an important role in assessing the integrity of engineering components. The test can give information about the presence of flaws, location and the size of flaws. The NDT techniques commonly used are visual testing, magnetic particle testing, eddy current testing, ultrasonic testing, radiography etc. In addition to characterization of flaws, NDT techniques are also used for material characterization and quality control. A planned maintenance of components can avoid catastrophic failures. Areas of application include metal industries, oil industries, gas pipelines, aerospace, defense, nuclear industries, etc. A choice of a particular test depends on the application, material of the specimen, information that is sought for, accessibility of the test component and portability of the equipment. For instance, the ultrasonic testing can provide both local and global information of a component depending on the excitation of wave modes. Conventional ultrasonic testing involves longitudinal and shear waves and provides local information i.e., the region of inspection under the ultrasonic transducer. The conventional testing, in general, is considered to provide good resolution and sensitivity. The two main methods of testing are (a) pulse echo configuration, wherein a single transducer positioned on a sample, which acts as both transmitter and receiver and (b) through-transmission configuration, wherein the transmitter and the receiver are separately positioned on a sample. The parameters used to assess the condition of a test specimen are amplitude, time of flight and attenuation. Further, the range of propagation is limited to hundreds of millimeters. Therefore, it is not suitable for the inspection of large structures, as it may involve heavy labour and large time.

Ultrasonic guided wave testing (GWT) is considered to be advanced and it can provide thorough information about the entire cross-section in plates or plate-like structures and tubes. The main advantages are limited area of insonification and long-range propagation of guided wave fields. The possible guided wave modes in a hollow tube are longitudinal, torsional and flexural. Unlike bulk waves, there is a family of modes in each of the modes. Each mode has characteristic phase and group velocities and is a function of frequency and thickness of a specimen. It is because of this dependence of velocities on frequency, modes are, in general, dispersive. Further, the sensitivity of each mode towards a defect is different for different modes. Hence, there is a flexibility in selecting a mode suitable for inspection. Generally, for long-range inspections, non/less-dispersive modes are selected.

Guided waves are attractive because they are confined within the walls of a tube and hence, can propagate for large distances without much attenuation. It is for these reasons, the time of inspection and labour involved are reduced. Furthermore, they can negotiate curved tube walls (bends), and this property of guided waves makes it even more attractive for inspection of heat exchanger tubes with bends. As mentioned above, the technique involves the placement of an ultrasonic transducer at one location for obtaining the complete information of the tube. The excitation of guided waves can be from the inside of a tube or from the outer diameter (OD) side depending on the accessibility for inspection. The common means of excitation are end coupling of ultrasonic transducers, magnetostrictive transducers and electromagnetic acoustic transducers (EMATs). As mentioned for bulk waves, GWT can be carried out in pulse echo and through-transmission configurations. Any tube inspection requires, in general, long range propagation of guided waves and detection of circumferential, axial and pinholes and fretting-type defects. Commonly used guided wave modes for these purposes are axisymmetric longitudinal modes ( $L(0,m)$ ) and torsional modes ( $T(0,m)$ ). The

frequencies used for this purpose are in the range of 25 kHz- 150 kHz. Earlier researchers have used remote field eddy current testing (RFECT) and internal rotary inspection system (IRIS) for in-bore inspection of tubes. Both techniques can provide only local information, as the scanning unit needs to be guided inside the tube. Moreover, it is time consuming. However, they can be used as complementary techniques.

The present thesis deals with the development of non-destructive ultrasonic longitudinal guided wave based-testing of steam generator (SG) tubes of the Prototype Fast Breeder Reactor (PFBR). The SGs of PFBR are completely closed structures carrying hot liquid sodium on the shell side and steam/water on the tube side. Any failure in the tube may lead to sodium-water exothermic reaction and damaging of neighbouring tubes. As a consequence, smooth operation of the reactor will be affected. Hence, the assessment of the healthiness of the tubes is important. As there is no direct access, only inner diameter (ID) side examination is possible.

The dissertation presents the selection and optimization of a longitudinal guided wave mode, for the inspection of SG tubes of PFBR, using finite element studies and experiments carried out by end-coupling ultrasonic transducers. The studies include long-range propagation and the detection of possible defects in SG tubes, using the optimized mode. Following the feasibility study, the systematic development of an ultrasonic longitudinal guided wave based in-bore (ID side) magnetostrictive transducer for the optimized mode with the aid of the finite element analysis and experiments validating the performance of the developed probe are presented. Finally, the trial studies on the SG tubes of the mockup steam generator set-up of PFBR using the developed in-bore magnetostrictive guided wave transducer, study of the

influence of the tubesheet on the optimized mode for inspection and the location for the placement of the developed probe in SG tubes of PFBR during the actual testing are presented.

## **1.2 Outline of the thesis**

**Chapter 1** discusses the background context for the work carried out in this thesis and a brief introduction to the importance of ultrasonic guided waves in inspection of tubes and to the problem of guided wave-based inspection of SG tubes of PFBR.

**Chapter 2** presents the theories of guided waves in tubes and magnetostriction, electromagnetic concepts related to the study and a brief theory of the finite element (FE) method for guided waves. It also presents the review of the literature in the area of generation and propagation of ultrasonic guided waves in tubes and pipes. This includes the modes used for long-range testing of pipes in terms of frequency, attenuation, dispersion and mode conversion. Various ways of exciting a torsional or longitudinal mode using ultrasonic transducers, EMATs and magnetostrictive transducers and the detection of defects are presented. Furthermore, the sensitivity of modes for particular defects, mode conversion of axi-symmetric to non-symmetric modes due to non-axi-symmetric defects and the reflectivity of  $L(0,1)$ ,  $L(0,2)$  and  $T(0,1)$  modes from defects are provided. Finite element studies carried out for simulating guided wave mode in straight and bent tube segments are given. Since guided wave modes are known to be influenced by bends, the studies related to sensitivity of defects present at different locations across bends are also presented. The chapter also covers signal processing techniques for de-noising guided wave signals using the Discrete Wavelet Transform (DWT) and the cross-correlation technique. One of the main objectives of the thesis is the design of a suitable in-bore magnetostrictive transducer. Therefore, the studies related to the development and the state-of-the-art in the domain are presented as well.

Towards the end, the motivation and objectives of the thesis are presented. The motivation for development of a rapid testing method of SG tubes, using guided waves is presented in detail and the missing elements in the literature are addressed for both specific and general applicability.

**Chapter 3** discusses the numerical routines adopted in the thesis such as Disperse software for the generation of dispersion curves and finite element simulation softwares: ABAQUS for the simulation of the propagation of L(0,2) mode under various defect configurations and COMSOL Multiphysics for the design of an in-bore ultrasonic guided wave magnetostrictive transducer by coupling electromagnetic and acoustic phenomena. Besides, axi-symmetric tubesheet models built in COMSOL with the low-reflecting boundary is also discussed. Furthermore, the details of the finite element models with and without defects, mesh and the temporal and spatial steps used are provided. It also describes the details of the experimental set-up and specimens used, which include short SG tubes and the SG tubes in the mockup SG test facility. Finally, this chapter also includes the details of defects and their dimensions and locations in the SG tubes used.

**Chapter 4** presents the optimization of a guided wave mode ( L(0,2) mode) and the study of feasibility of long-range propagation of 46 m and the detection of the common defects such as multiple circumferential, axial, pinhole, tapered defects and sodium impingement defects lying in the same line in steam generator tubes by end coupling ultrasonic transducers. The FE results and their experimental validation for all the above multiple-defect scenarios are presented. Besides, the detection of multiple defects in the thermal expansion bend of an SG tube is presented. The sensitivities of the defects and a different perspective of sensitivity in terms of the cross-sectional area of a defect are also presented. In addition, the reflectivity of

axial defects, the influence of the curvature of sodium impingement damage on reflectivity, mode conversion of L(0,2) mode due to non-axi-symmetric features and responses of L(0,2) mode to ID and OD defects are discussed in detail.

**Chapter 5** first discusses the need for the design and development of an in-bore magnetostrictive transducer for the generation of the optimized L(0,2) mode, as the technique of end-coupling ultrasonic transducers cannot be directly applied on the tubesheet of an SG. The results of axi-symmetric in-bore magnetostrictive transducer models developed in COMSOL and the optimization of the dimensions of the transmitter and receiver coils, Thevenin circuit models and the fabrication of an in-bore magnetostrictive transducer using the FE results and the related experimental results are presented. Furthermore, the experimental validation of the FE results for a few cases is presented. Besides, a long-range testing, detection of defects in short SG tubes and the sensitivity of the magnetostrictive transducer in the detection of defects are presented. Finally, a comparison of sensitivity obtained using a piezo transducer is given.

**Chapter 6** deals with the application of the developed in-bore magnetostrictive transducer on the SG tubes of mockup SG test facility of PFBR with a tubesheet and spigot welds. The experimental results obtained in the SG tubes with multiple circumferential defects are presented. This chapter also includes wavelet-based and cross-correlation based denoising techniques for de-noising highly noisy raw signals obtained in the mockup SG tubes. Furthermore, it also presents the influence of the thermal expansion bend on L(0,2) mode and subsequent defect detection sensitivity. Finally, the influence of the tubesheet geometry on the actual inspection, studied using FE analysis and the appropriate location for the placement of the transducer in an SG tube for the actual inspection are presented.

**Chapter 7** summarizes the major results obtained, conclusions drawn and the scope for future work.

## ***Chapter 2. Review of Literature, Theory and Motivation***

### **2.1 Chapter overview**

This chapter presents information about steam generator (SG) tubes of PFBR, issues in SG tubes, need for NDE inspection and scope for using ultrasonic guided waves for the examination of SG tubes of PFBR. Furthermore, the review of literature on ultrasonic guided waves, mode selection, dispersion, long range propagation, detection of various defects in tubes, magnetostriction-based guided wave generation and finite element studies on guided waves are presented. Finally, the theory of guided waves, theory of magnetostriction, relevant equations of electromagnetics for magnetostrictive modelling, theory of finite element analysis and signal processing techniques such as short-time Fourier transform (STFT) for time-frequency analysis and the cross-correlation technique and the discrete wavelet transform (DWT) for de-noising are included.

### **2.2 Introduction**

#### **2.2.1 Prototype Fast Breeder Reactor**

The Prototype Fast Breeder Reactor (PFBR) is a 500 MWe (electrical power) sodium-cooled nuclear reactor which is in the advanced stage of commissioning at Kalpakkam, India [1]. PFBR falls in the second stage of Indian nuclear programme. It is a pool-type reactor which uses a mixed uranium-plutonium oxide (MOX) fuel with a burnup of 100 GWdays/ton. The reactor assembly consists of a main vessel, core of fuel sub-assemblies supported on a grid plate, primary sodium circuits and intermediate heat exchangers (IHXs). The main vessel is

enclosed by a safety vessel to provide radial shielding. There is an intervening space of 300 mm between the main vessel and the safety vessel. The gap of 300 mm, filled with nitrogen gas, is used for robotic ultrasonic non-destructive testing to assess the integrity of the main vessel. The prime material of construction is SS 316 LN. The internals of the main vessel are immersed in liquid sodium of weight 1150 t and is blanketed by argon gas at the top. The primary sodium acts as a coolant and is radioactive. The main vessel is welded to the roof slab, which provides top axial shielding while the concrete reactor vault at the bottom provides bottom axial shielding. The main vessel houses an additional vessel called the inner vessel (containing the active core), which separates the hot and cold pools of sodium. Liquid sodium pumped by primary sodium pumps enters the core at 397 °C and leaves the fuel core at 547 °C. The hot liquid sodium being radioactive is not used for steam generation. Instead, non-radioactive secondary sodium circulated through four IHXs by secondary sodium pumps is used for heat transfer. There are two independent secondary sodium loops. Each secondary sodium loop includes two IHXs, sodium pumps and four steam generators (SG). Hence, there are eight steam generators. The secondary sodium circulated through steam generators transfers heat to pre-heated water for steam generation. The steam generated is finally sent to the turbine for power generation.

PFBR involves many critical components, which need to be inspected non-destructively for their integrity as they operate under high temperature, pressure and radioactive environment. Although all the critical components were thoroughly examined as part of pre-service inspection (PSI), they need to be inspected during service, as part of in-service inspection (ISI). For instance, the components that will be subjected to periodic ISI include critical weld joints of the main vessel bearing radioactive core submerged in liquid sodium and steam generator (SG) tubes.

This dissertation deals with ultrasonic longitudinal guided wave-based inspection of steam generator tubes of PFBR. Therefore, discussions about the steam generators of PFBR are essential for the present work and they are presented in the next section.

### **2.2.2 Steam generators of PFBR and scope for ultrasonic guided wave NDE**

SGs of PFBR are one of the most critical components, as secondary sodium and water simultaneously exist in the SGs. This demands a high level of structural integrity. In PFBR, there are eight steam generators of 1.2 m diameter and 26 m vertical height [2]. Each SG houses 547 steam generator tubes made of modified 9Cr-1Mo ferritic steel with tight control on chemistry to avoid scattering of mechanical and creep properties [3]. All 547 tubes are enclosed in a 25 mm thick shell. Each SG tube is of 23 m length with the outer diameter and the wall thickness of 17.2 mm and 2.3 mm, respectively. The SG tubes are welded to tubesheets at the top and bottom of each SG through internal-bore welding (raised spigot type). The tubes are supported by a tube bundle support arrangement made of Inconel 718. The top and bottom tubesheets are protected by thermal shields. SG tubes are provided with a bend of 375 mm radius, to accommodate differential thermal expansion. The thermal expansion bends are in turn made of three successive bends with the expansion length of 1075 mm. The thermal expansion bends start at 5.0 m elevation of SGs. Furthermore, a manhole is provided at water/steam dished heads for in-service inspection and tube plugging and the SGs are mounted vertically [4].

SGs are of counter-flow type with sodium entering shell side through a single sodium inlet nozzle at the top while water enters inside the tubes through the tube-to-tubesheet at the bottom and leaves as steam through the steam outlet at the top [5]. Figure 2.1 shows the

schematic of the SG of PFBR [6]. The operating temperatures and pressures of an SG of PFBR are given in Table 2.1 [7].

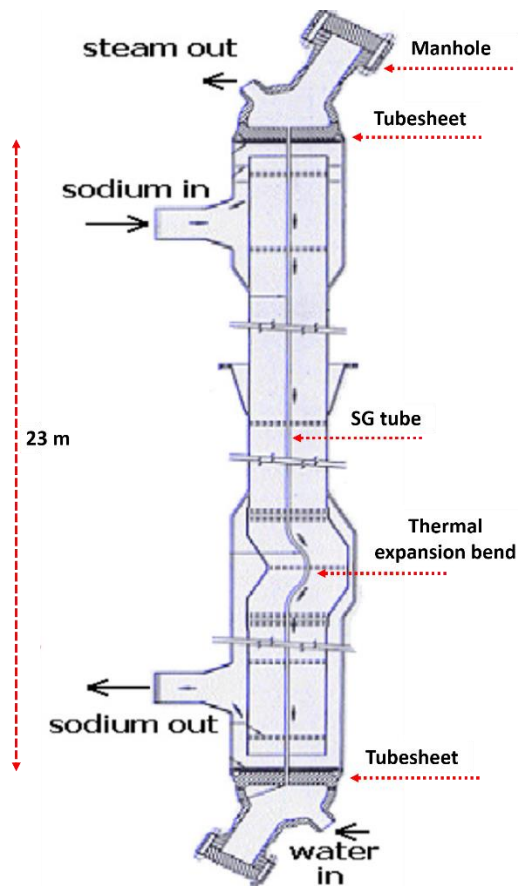


Fig. 2.1. Schematic of steam generator of the Prototype Fast Breeder Reactor [6].

Table 2.1. Operating temperatures and pressures of SGs of PFBR

Process fluid	Inlet temperature, (°C)	Outlet temperature, (°C)	Pressure, MPa
Secondary sodium	525	355	0.8 (Shell side)
Water/steam	235	493 (steam)	17.2 (Tube side)

The reliability of SG tubes of PFBR is ensured right from the selection of materials for the SGs. It is based on the following considerations [8]:

- Good thermal conductivity
- Influence of creep and low cycle fatigue on the high temperature mechanical properties,
- resistance to loss of carbon to liquid sodium leading to reduction in the strength,
- resistance to stress-corrosion cracking in sodium and aqueous media and,
- weldability, workability and cost involved.

Ferritic steels such as 2.25Cr-1Mo, Nb stabilized 2.25Cr-1Mo, 9Cr-1Mo, Modified 9Cr-1Mo, 300 series austenitic stainless steels (AISI 304/316/321) and alloy 800 are some of the candidate materials for SGs [9]. An interesting review of steam generator types and materials for sodium cooled reactors used by different countries is presented in Ref. [10]. 300 series austenitic stainless steels and alloy 800 are not preferred because they are prone to aqueous and chloride stress-corrosion cracking. Among the ferritic steels, Mod. 9Cr-1Mo steel exhibits an excellent combination of high temperature creep strength, ductility and corrosion/oxidation resistance. Hence, it can be used for thinner SG tubes, as given in Ref. [8]. International experience also indicates the use of the steel for SGs [11]. Hence, Mod. 9Cr-1Mo ferritic steel has been chosen for the SGs of PFBR.

If any leakage occurs in an SG tube of PFBR, sodium and high-pressure water/steam can react exothermically leading to the evolution of hydrogen, corrosive products and intense local heat. For instance, a steam leak of 100 mg/s from a crack would result in high pressure waves jetting into the sodium, leading to the cascading failure of the adjacent tubes. This is known as impingement wastage. Besides, it was observed that an experimentally simulated steam

leak under controlled conditions through a 0.1 mm diameter pinhole causes the impingent damage of depth ~ 2 mm [12]. This may disrupt the smooth operation of the reactor.

The possible causes of degradation modes in the SG tubes are stress-corrosion cracks, pitting corrosion, erosion, fretting, arc strikes and spatter on the tube during welding, porosities in the weld and mechanical damage [13, 14].

Therefore, it is essential to ensure the reliability of sodium-water/steam boundaries. In other words, the healthiness of the heat exchanger tubes must be ascertained time-to-time using a suitable and rapid non-destructing testing (NDT) method. NDT methods used for the pre-service examination of heat exchanger tubes are ultrasonic testing, eddy current testing, visual testing and helium and hydro leak testing [15-17]. For in-service inspection of SG tubes of PFBR, remote field eddy current technique (RFEC) is proposed [18].

A major constraint in the inspection of SG tubes of PFBR is accessibility. SGs of PFBR have closed structures, as mentioned above. Hence, only accessibility for inspection is from the ID of the tubes. Given the ID of the SG tube of 12.6 mm (inner area of ~ 125 mm<sup>2</sup>), it is even more difficult. This indicates that there is a scope for ultrasonic guided wave examination from ID side even with limited accessibility. Additional issue that has to be encountered is the excitation of guided waves from inside. A couplant-free non-contact method has to be explored for convenient deployment.

### **2.2.3 International experience on NDE of nuclear steam generator tubes and selection of a rapid NDE technique for PFBR SG tubes**

International experience on the inspection of nuclear steam generator tubes in public domain is scanty. Even the studies reported are mostly eddy current based. For instance, inspection

of CANDU type PHWR (Pressurized heavy water reactor) steam generator tubes involves eddy current transducers with rotating magnetic field [19]. Besides, localized ultrasonic testing from ID side called tiny rotating ultrasonic tube inspection equipment for detection and sizing of defects in SGs of CANDAU is also used [20]. VVER steam generators in Russia uses eddy current testing with bobbin probes and rotating probes [21]. For SG tubes of Superphoenix, France, a 1242 MWe fast reactor, an ultrasonic phased array system is used for inspection [22]. Korean nuclear steam generators (ID of ~19.68 mm) are examined using an array type ultrasonic transducer consisting of five ultrasonic transducers namely one normal and four shear wave transducers at 45 deg angle to detect and characterize axial and circumferential notches [23]. Many countries adopt advanced RFECT over conventional eddy testing for ferromagnetic nuclear generator tubes [24]. However, RFECT also provides only local assessment.

The RFECT technique involves separate exciter and receiver coils, which need to be inserted into a heat exchange tube. Then, a low frequency sinusoidal excitation in the range of a few kHz is applied to the exciter coil which generates eddy currents in the tube. The net magnetic fields generated in the tube are then picked up by the receiver coil nullifying permeability variations. The amplitude and the phase of the induced voltage obtained bear the information of presence of defects [25]. In general, post-processing of RFEC signals necessarily involves advanced signal processing due to the noise picked up by misalignment of coils, probe wobble, welds, permeability variations, residual stresses and bends [26]. The feasibility of RFEC technique for the inspection of ferromagnetic heat exchanger tubes of PFBR has already been studied. It requires the insertion of an RFEC probe all along the length of 23 m of the tube. It is very time consuming and was found susceptible to the above factors. Besides, advanced signal processing techniques should inevitably be used to de-noise and decipher

RFEC signal features. As can be seen that overall studies reported suggest that NDE examination used for nuclear steam generators is a local examination. Given a large number of nuclear steam generator tubes to be inspected at regular intervals at any site, there is a need to develop an alternate method, which should be rapid, reliable and of less labour.

Hence, as an alternate method of examination, ultrasonic guided waves can be explored. It could overcome the above difficulties and can pave way for rapid inspection of the whole SG tube from one end without having to insert and guide a probe all along the length of the tube.

#### **2.2.4 Ultrasonic guided waves in tubes**

Bulk waves are classified as longitudinal or shear based on the nature of particle vibration. It is important to understand that they do not require a boundary for their propagation. Their velocities are purely determined by the elastic properties of the material of a specimen and are mostly independent of frequency. Ultrasonic guided waves are ones that are bounded by the walls of a tube and they are formed by the superposition of fundamental mode converted waves. They are guided by the walls of the tube and can negotiate bends and curves. Since they are bounded, they can propagate for large distances and examine the complete wall thickness, in general. In other words, unlike bulk waves, they show a one-dimensional propagation. These features of a guided wave make it suitable for applications such as oil, gas and petrochemical industries involving long pipelines for rapid examination and global assessment [27]. On the other hand, conventional ultrasonic testing, though more accurate, requires point-by point examination, as the in-sonification is limited only to the small volume of the test piece under the footprint of the transducer. The testing demands enormous labour and time for the examination of a structure of large dimensions. Ultrasonic guided wave-based examination can circumvent the difficulty of moving a probe and limited in-

sonification. Here, an ultrasonic transducer is needed to be placed at a point for obtaining the complete information of healthiness of the structure in question. The cross-section in the direction of wave propagation in the case of plates or plate-like structures and 100% volume in the case of tubes and pipes are covered by guided waves. An increased sensitivity of defects due to the variety of choices in modes and frequency is the additional advantage [28, 29].

#### **2.2.4.1 Dispersion curves and modes in tubes**

Ultrasonic guided waves in tubes propagate in three different modes namely longitudinal modes, torsional modes and flexural modes. Longitudinal ( $L(0,m)$ ) and torsional modes ( $T(0,m)$ ) are axi-symmetric while the flexural mode ( $F(n,m)$ ) is non-axisymmetric. 'n' refers to circumferential order of the mode and 'm' refers to the mode order (counter variable) [30]. Plate modes are called symmetric and anti-symmetric. There are many guided wave modes at a given frequency in plates and pipes and they are in general dispersive (phase velocity is a function of frequency). Modes are the admissible solutions for a given specimen and are represented by dispersion curves, namely phase velocity dispersion curves and group velocity dispersion curves. The latter is the derivative of the former. Group velocity is more meaningful, as the real signals propagate with the group velocity. Figure 2.2 shows typical phase and group velocity dispersion curves of a ferritic steel tube of OD 17.2 mm and wall thickness 2.3 mm. L, T and F in the figure stand for Longitudinal, torsional and flexural modes, respectively. Unlike in plates, there are many modes at low frequencies. The velocities of guided waves are determined by elastic properties and thickness-frequency product. Guided waves have a variety of particle vibration patterns. Hence, one has a flexibility of choosing a mode for achieving a required sensitivity. Many modes at a given frequency can exist at the same time and can make guided wave-based inspection very complex (multi-modal nature). Hence, a successful examination involves selecting a suitable guided wave

mode, a suitable size of transducer, proper instrumentation and signal processing, as mentioned in Ref. [28]. This has led to many studies on optimization of modes [31].

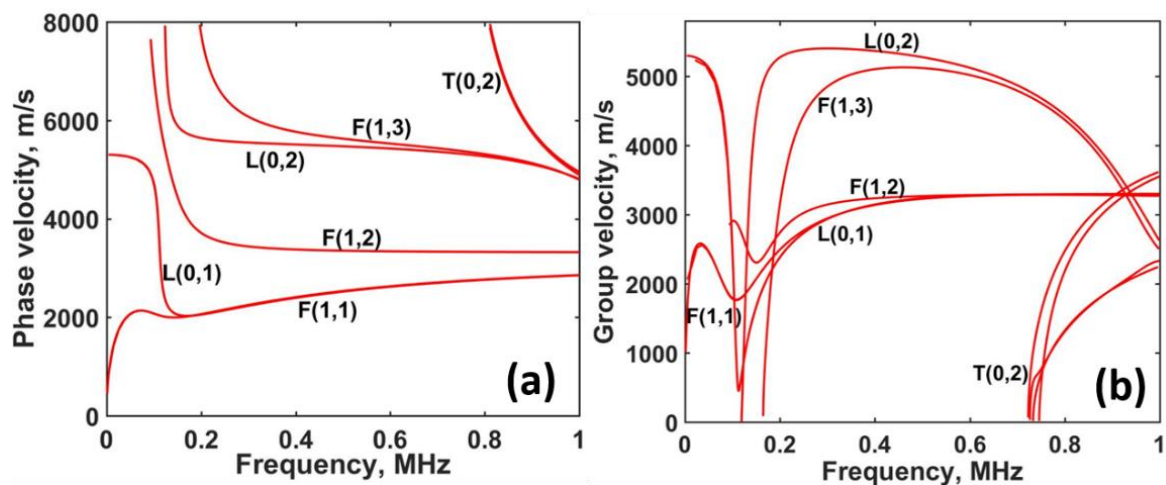


Fig. 2.2 (a) Phase velocity and (b) group velocity dispersion curves of a ferritic steel tube of outer diameter 17.2 mm and wall thickness 2.3 mm.

#### 2.2.4.2 Use of low frequency modes and ways of excitation

The main application of long range ultrasonic guided wave testing (LRUT) is to pipes and tubes. For instance, the use of low frequency axi-symmetric longitudinal modes ( $L(0,m)$ ) and torsional modes ( $T(0,m)$ ) at low frequencies ( $< 200$  kHz) for a long range propagation ( $> 5$  m to 50 m or more) and detection of defects is prevalent in the literature [32, 33].  $L(0,m)$  modes can be easily excited using direct coupling of an ultrasonic transducer to the end of a tube [34, 35], ring transducers wrapped over the tube [36], wedge transducers [37], comb transducers [38], EMATs [39], magnetostriction [40] and phased array based generation [41].  $T(0,m)$  modes can be excited by ring transducers wrapped over the circumference of the tube, EMATs [42] and magnetostrictive methods as well. The low frequency longitudinal and torsional ultrasonic guided wave modes have become very attractive for LRUT because of their nearly uniform stress throughout the wall thickness, less attenuation and high sensitivity

to cross-sectional changes at any location, as mentioned in Ref. [33]. Another advantage is that they are nearly non-dispersive over wide bandwidth.

### 2.2.4.3 Criteria for mode selection

Wilcox et al. [43] mentioned a few criteria for mode selection for LRUT in plates. The criteria can be extended to tubes and they are the following: (1) dispersion, (2) attenuation, (3) sensitivity, (4) excitability, (5) detectability and (6) mode selectivity. First two factors depend on the material, specimen geometry and the selected mode, third factor depends on the mode and partly on the instrument parameters and last three factors depend on transduction mechanism scheme. Dispersion is caused when individual frequencies of a signal propagate with different phase velocities. In other words, when the bandwidth of signal is in a sloping region of dispersion curves, dispersion occurs. As a consequence, there will be a dilatation of the wavepacket in the space-time plane followed by reduction in the amplitude. This will be manifested as increase in the signal duration for various propagation distances. Hence, such a group of waves will have a range of group velocities. The group velocity and the phase velocity are given by Eq. (2.1) [44]:

$$V_{gr} = V_{ph}^2 \left[ V_{ph} - (fd) \frac{dV_{ph}}{d(fd)} \right]^{-1} \quad (2.1)$$

where  $V_{ph}$  is the phase velocity at a particular frequency (f)-thickness (d) product (MHz-mm) and  $V_{gr}$  is the group velocity at the center frequency of the wavepacket. In practice, the group velocity corresponding to the center frequency of a wave packet is considered as the velocity of the group. Dispersion is not desirable in LRUT, as it will first affect the resolution when a defect is close to a geometrical boundary and secondly, it will cause the wavepacket to die

down quickly thereby limiting the propagation distance. Owing to these reasons, generally a mode is chosen in the non-dispersive points (stationary points) of group velocity dispersion curves. However, in practice there is always a finite bandwidth associated with a given input signal of finite duration and therefore, a stationary point cannot be exactly chosen to reduce dispersion. Hence, in practice, all points on the dispersion curves must be considered dispersive. The effect can be minimized by using windowed tonebursts rather than using a pure tone burst. But the major question that remains to be answered is how many cycles one should choose to reduce dispersion. It is known that increasing the number of cycles will make the bandwidth narrow, leading to reduction in dispersion. However, the duration of the wavepacket will be large, which will affect the spatial resolution. On the other hand, using a small number of cycles will involve short duration but may have dominant dispersive effects. This trade-off between spatial resolution and dispersion can be resolved by optimizing the number of cycles for a given mode for a given propagation distance [45]. This involves receiving wavepackets of a given mode of the same center frequency but with different number of cycles each time. The wavepacket received with the minimum time duration (minimum dispersion) is taken as the one containing the optimum number of cycles. Equivalently, the minimum time duration corresponds to the best achievable spatial resolution for the given mode. Similarly, a minimum number of cycles can be obtained for all points of dispersion curves.

However, if one chooses to work with dispersive points, the dispersion can still be corrected using dispersion compensation algorithms [46]. In the study reported, two 5 mm diameter SS rods of lengths 2.85 m and 1.75 m bonded end-to-end were considered and purposefully L(0,1) mode at 250 kHz (highly dispersive) was generated from one end. Then, the dispersion compensation algorithm was applied to remove the dispersion and reduce the spatial duration.

Often in long-range testing for industrial applications, a 5 or 10-cycle Hanning windowed toneburst or a 10-cycle Gaussian window toneburst is used, as mentioned in Ref. [33, 45], to limit the dispersion and suppress the unwanted modes [47, 48]. To generate a specific mode, a narrowband width alone is not sufficient because a finite source size will generate a phase velocity spectrum, in addition to the frequency spectrum, [28, 49].

Furthermore, as regards sensitivity, the use of low frequency guided modes does not preclude the possibility of achieving the sensitivity required. In fact, such low frequency guided modes can detect defects whose depths are much smaller than the wavelength of a particular mode launched [33]. For instance, detection sensitivity of individual Lamb modes to notches depends on frequency-thickness product, mode type (stress distribution across the thickness) and geometry of the notch. Lamb wave modes can be used to detect a notch of depth 40 times smaller than the wavelength provided the width of the notch is much smaller than the wavelength of the Lamb wave mode [50]. This detection sensitivity is much greater than that provided by conventional bulk wave testing at low frequencies. It is clear that detection sensitivity of guided waves is not only governed by wavelength but also by the nature of the mode and the mode shape. A mode shape is the distribution of stresses and displacements across the thickness. It is a general opinion that sensitivity will increase with frequency. However, it may or may not be true for a guided wave because of its dependence on mode shape. That is to say, if a mode exhibits higher stress at the surface, then it will be more sensitive to the surface-breaking features. Thus, each mode on dispersion curves has different sensitivity towards a defect, as implied in Ref. [48]. For instance,  $L(0,m)$  modes are more sensitive to circumferential defects than axial defects and  $T(0,m)$  modes are more sensitive to axial defects [33].

Another factor that needs consideration is attenuation, which is the reduction in amplitude over propagation. There are many sources of attenuation, namely dispersion (spreading of energy in the direction of propagation), beam spreading (energy spreading in perpendicular direction to the wave propagation), frictional losses, scattering due to inhomogeneities, scattering and leakage to the surrounding medium, as in Ref. [43]. If a mode is chosen at a nearly non-dispersive point with a proper bandwidth, the attenuation due to dispersion can be avoided. For a metallic plate or tube in air, leakage losses can be neglected. When it is loaded by liquid or coated with an attenuative material or embedded in solid, the leakage of a particular mode should be considered [35, 43]. For practical purposes, the mode with the least attenuation should be chosen.

Finally, for a single mode excitability, the selection of narrow bandwidth alone is not sufficient. In fact, modal excitability depends on the similarity between the displacement profile across the thickness of a mode and the displacement field impressed by the transducer. For instance, Aristegui et al. [51] used direct end coupling of an ultrasonic transducer of frequency 250 kHz in a copper pipe to generate L(0,2) mode, as it has a uniform axial field. However, for the generation of L(0,1) mode, end coupling was made in a chamfered pipe to excite L(0,1) mode, as its axial field through the wall thickness is not uniform. Bottger et al. [52] demonstrated the modal selectivity of L(0,2) mode and suppression of unwanted modes at 1 MHz- mm in a ferritic steel tube of OD 38 mm and the thickness of 5 mm through EMAT design for L(0,2) mode. Figure 2.3 is extracted from Ref. [53]. Figure 2.3a shows a signal obtained in a plain pipe by a group of transducers attached to a pipe for a full circumference and Fig. 2.3b shows a signal obtained in a long pipe with welds, which are 15 m apart. The signals were obtained in the pulse echo mode using ring transducers with a tight control of narrowband. Ideally in Fig. 2.3a, only two reflections should show up, but many signals show

up because of multimodal excitation and bi-directional propagation. The unwanted modes amount to coherent noise, which cannot be removed by averaging methods. In Fig. 2.3b, reflections corresponding to two welds in a pipe, in early stages of service, are clearly seen along with many smaller signals which could not be removed by averaging, indicating that they are coherent noise of unwanted modes. It is difficult to distinguish a flaw indication from coherent noise in such a situation. The key factor in controlling this is the excitability of a single mode and suppressing bi-directional propagation by means of appropriate excitation.

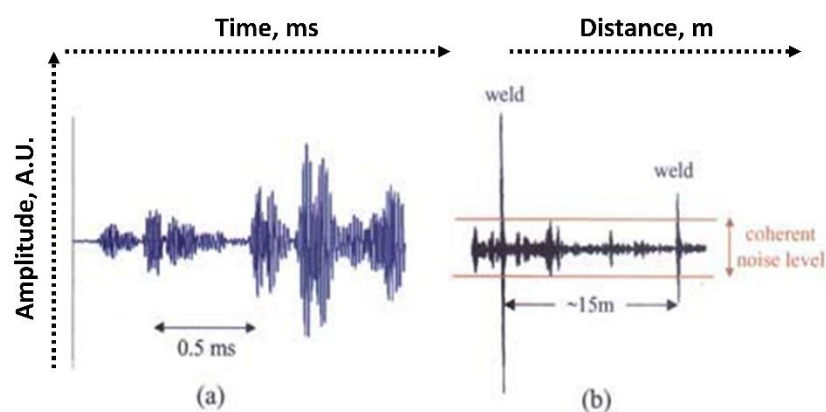


Fig. 2.3 (a) A signal obtained in a plain pipe and (b) a signal obtained in a long pipe with two welds which are 15 m apart by using transducers attached to a pipe for a full circumference [53].

#### 2.2.4.4 $L(0,m)$ and $T(0,m)$ modes: Medium and Long-range propagation, defect detection, effect of bends, reflectivity: Experiments and finite element analysis

The ultimate aim of a mode selection is to derive maximum benefits from the mode in terms of long-range propagation and defect detection with required sensitivity. Numerical analyses can also help in understanding the underlying phenomenon of excitability, propagation and the reflectivity characteristics of a mode with respect to a defect. A successful inspection must necessarily include all the above elements. An interesting work by Allenye et al. [27],

demonstrates the long-range testing of chemical plant pipework for a testing range of 50 m. Wherein, solid ring transducers were used on pipes with diameter ranges of 76 mm- 610 mm for uni-directional generation of T(0,1) mode in the frequency range of 12 kHz- 40kHz. The transducer was an array of piezoelectric crystals connected in the form of a ring to fit the OD of a pipe. The defects detected were corrosion in pipes buried under the road, ID side corrosion in pipes carrying acid and broken bitumen coating on pipes. Furthermore, DAC curves were also used to quantify the size of a defect and the sensitivity achieved was 5-10% of the cross-section area of the pipe at a particular axial location. The study also emphasizes the importance of excitation in controlling a single mode excitation in long-range testing.

It is not only defects which can give indications. There are many pipeline features which may give reflections. Therefore, it becomes difficult to assess an indication amidst these. Allenye et al. [54] showed the influence of standard pipeline features such as welds, supports and flanges on L(0,2) mode at 70 kHz. These features were reported to give reflections and cause mode conversion. The defects detected were crescent-shaped notches of maximum depths 3 mm, 3 mm and 3.5 mm notches of 50 mm, half and full circumferential extents, respectively and a corrosion patch of length 200 mm and 130 deg circumferential extent with the maximum depth of 2.7 mm at the center. All the defects were considered between two welds separated by 0.9 m length in 5.4 m long tube of ID 76 mm and the wall thickness of 6.5 mm. Furthermore, there was also investigation of detection of corrosion under insulation. In another study by Allenye et al. [55], the examination of 80 m long steel pipes with 152 mm OD and 7 mm thickness carrying liquid butane chemical using L(0,2) mode at 70 kHz generated by dry-coupled ring transducers has been reported. The pipes had welds and supporting clamps, which were not welded. Feeble reflections were observed from the support clamps while the reflections from welds were stronger. Furthermore, there are also

studies on examination of cross-country oil pipelines by LRUT [56]. Some applications may involve a pipe of an OD bonded to another pipe of a different OD. It is very challenging to detect defects in such circumstances. For instance, T(0,1) mode generated in the frequency range of 45 kHz- 60 kHz by a ring transducer was used in a complex pipe structure with two 8 m long steel pipes of OD 51 mm and the wall thickness 6 mm welded to a 2 m long middle pipe of 38 mm OD and 5 mm wall thickness. The defects detected were a 4 mm deep and 50 mm long circumferential notch and a 4 mm deep drill hole at the far ends of the tube. The sensitivity achieved was 2~3% cross-sectional loss [57].

Rose et al. [58] studied the influence of water-loaded tube on L(0,1) at  $f_d=1.5$  MHz-mm and applied it to detect a circumferential crack at 8.8 m in a stack of nuclear generator tubes of total length 17.7 m and also used L(0,4) mode at  $f_d=4.4$  MHz-mm for the detection of multiple cracks at OD of a tube of about 1 m length. Liu et al. [59] used T(0,1) mode at 50 kHz in a pipe of length 7.4 mm, OD of 60 mm and the wall thickness of 3.5 mm, excited using nine shear wave elements circumferentially attached to the pipe, to detect the longitudinal defect of 1 mm circumferential extent and 35 mm axial extent. There were four end reflections, shown in the paper, amounting to the propagation distance of 58.92 m. It is further reported that a single mode is not adequate to characterize the axial and circumferential extents of a defect.

All the studies reported above were based on ultrasonic transducers attached to OD. A few studies have reported the use of EMATs and comb transducer for testing of steam generator tubes, though not widely used [60, 61, 62]. There are also studies based on low-frequency magnetostrictive transducers (<500 kHz) for long range guided wave testing [63, 64]. For example, an in-bore magnetostrictive transducer (ID side) has been used to generate L(0,2)

mode at 250 kHz in a ferritic steel tube of ID 24 mm and the length of 15 m for the detection of circumferential, axial and wear type of defects [65]. In-bore magnetostrictive transducers for generating torsional modes  $T(0,1)$  in the frequency range of 32 kHz to 128 kHz have also been used for examining carbon steel heat exchanger tubes of ID ~ 19 mm [66]. Vinogradov et al. [67] used an in-bore magnetostrictive transducer to generate  $L(0,1)$  mode in the frequency range of 18 kHz – 48 kHz in carbon steel heat exchanger tubes of OD 19 mm and length 6.3 m with axial flaws of different extents. Kwun et al. [68] used MsTs encircled on OD to generate a longitudinal mode at 60 kHz in a carbon steel pipeline of 114 mm OD and length of 51 m for the detection of simulated circumferential notches and corrosion patches. The use of Fe-Co-V magnetostrictive strip on the OD of a tube is also reported in the literature. For instance, Cheong et al. [69] investigated the possibility of detection of flaws such as axial, hole, thinning in an elbow pipe of OD 150 mm, thickness 11 mm and length 22 m, using  $T(0,1)$  mode generated by Fe-Co-V magnetostrictive strip pasted on the OD. Even, non-contact magnetostrictive sensors have been used for pipeline inspection from the OD side [70].

Another feature of a pipe that can seriously interfere with a guided wave examination is a bend. The wave propagation in bends is invariably complicated by mode conversion and distortion and it is a real challenge to detect defects in the middle of the complexity. Several studies have been reported on the guided wave propagation in bent tubes. Heinlein et al. [71] studied the areas of detectability in a bend and reported that areas of low detectability were at the intrados while the areas of high detectability were close to extrados. Further, it was also reported that reflected amplitude of  $T(0,1)$  from circumferential cracks in the bend varies roughly with the square of the Von-Mises stress at the location of the defect. Jing Ni et al. [72] studied the propagation of  $L(0,2)$  across various multiple bends using FE analysis and

reported that the characteristics of propagation and the detection sensitivity vary from one bend to another in multiple bends. Verma et al. [73] studied the influence of bends of angles 0 deg (no bend) to 180 deg (U-bend) of mild steel pipes of OD 60 mm and thickness 4.5 mm on 50 kHz L(0,2) mode (generated by a magnetostrictive transducer). The study included both 3D finite element simulation and experimental validation. It was observed that with the increase in the bend angle, there were large mode conversions to flexural modes affecting the transmission of L(0,2) mode across the bend with the reduction in L(0,2) mode velocity.

L(0,2) mode not only undergoes mode conversion but also undergoes asymmetric deformation with the maximum at one circumferential point and the minimum at the opposite point. Demma et al. [74] labelled this mode as L(0,2)<sub>T</sub> mode, as it is obtained from a toroidal model. In this model a bend was modelled as toroid and modal solutions were obtained using finite element analysis for making dispersion curves. The toroid dispersion curves were then compared with the dispersion curves for a straight tube. It has been reported that when an incident L(0,2) mode enters the bend, it splits into F(1,3)<sub>s</sub> and L(0,2)<sub>I</sub> modes and when exiting the bend they again split into L(0,2)<sub>II</sub> and F(1,3)<sub>s</sub> modes. The L(0,2) mode after exit is thus the superposition of L(0,2)<sub>I</sub> and L(0,2)<sub>II</sub> modes and hence, the transit time is reported to depend on the bend length due to the change in velocity. There was no significant reflection observed from the bend. Furthermore, the transmission coefficient was found to be dependent on the ratio of the mean radius of a bend to the diameter and frequency. The same was observed for T(0,1) mode as well. All the FE results were experimentally validated. Qi et al. [75] reported the dependence of the locations of crack-like defects in the elbow region of 2 m long, 70 mm OD and 3.5 mm thick 90 deg mild steel elbow pipe on rates of mode conversion of T(0,1) mode to identify the presence of defects in elbow. The elbow causes reflections, which include the original mode and a mode converted signal. The study included

both FE analysis and experimentation. Elbows not only cause reflections of axi-symmetric modes but also delay the mode negotiating the elbow due to mode conversion into axi-symmetric and non-axi-symmetric modes. However, the mode conversion to another axi-symmetric mode is weak. As a result, substantial energy of the incident mode is lost in mode conversion to non-axisymmetric modes [76]. Given the above difficulties, detection of defects near/in elbows, circumferentially welded to straight tubes using L(0,2) and T(0,1) modes is even more complicated by multiple reflections and mode conversion [77, 78, 79, 80].

There are also studies reported on medium range (< 5 m) testing. They are mainly for studying excitability, mode purity, advantages of using one mode over the other, reflectivity of L and T modes from various defects and to develop a test methodology. Reflectivity studies have been mainly carried out using finite element analysis. Cheong et al. [81] used L(0,1)/ F(m,2) mode at 500 kHz generated by coupling a wedge transducer onto the surface, for detecting axial and circumferential (20% WT and 40% WT and length 25 mm and 50 mm) notches in a feeder pipe (of thickness 6.5 mm, the diameter of 63.5 mm and the length of 1.5 m) in a pressurized heavy water reactor. The short-time Fourier transform was then used to characterize the modes propagating. It is reported that while L(0,1)/ F(m,2) mode at 500 kHz is sensitive to the circumferential notches, it is totally insensitive to the axial notches in straight pipe. However, an axial notch considered in a bent feeder pipe was reported to be detected under the same condition due to the possible circumferential stresses in the bend from F(m,2) mode. Furthermore, circumferential guided waves were also used to detect and quantify the axial notches. Yoon et al. [82] used L(0,1) mode at 2.25 MHz, generated by using a wedge transducer, to detect axial notches (three of length 5 mm each, 1.09 mm, 0.545 mm and 0.218 mm deep and 1 mm wide each) in SG tubes (of length 1.8 m, outer diameter 19.05 mm and wall thickness 1.09 mm each) of Korean nuclear power plant. It is further reported

that the L(0,1) mode at 2.25 MHz is sensitive to surface breaking cracks. T(0,1) mode at 45 kHz, excited using shear wave transducers placed circumferentially, in a 4 m long pipe of OD 60 mm and the wall thickness of 3.5 mm was used to detect the axial defect of dimensions 1 mm width and 35 mm length and the circumferential defect of dimensions 26 mm circumferential extent and 1.2 mm width. It was observed that for the mode, the axial defect is more sensitive than the circumferential defect because of the very dominant circumferential displacement of the mode [83].

Lowe et al. [84] studied the reflectivity of L(0,2) mode at 70 kHz, generated by ring transducers clamped to one end of the tube, from circumferential notches as a function of circumferential extents and depths in steel pipes of length 2.6 m and the diameter of 76 mm. The study involved both FE analysis and experiments for reflectivity. The reflectivity of L(0,2) mode obtained was linear for a fixed depth of the notches with varying circumferential extent. Furthermore, L(0,2) mode incident on an asymmetrical circumferential notch undergoes mode conversion to F(1,3) mode whose axial stress fields are similar to that of L(0,2) mode. It also establishes that F(1,3) mode can serve as a good replacement for L(0,2) mode to detect a non-axi-symmetric defect in the neighbourhood of a full circumferential weld, as L(0,2) mode is strongly reflected by axi-symmetric features. The reflection coefficient of L(0,2) is observed to be a linear function of the ratio of the circumferential extent of the notch to the full circumference of a pipe. It is also a strong non-linear function of depth for a fixed circumferential extent and shoots up rapidly beyond 50% of the wall thickness depth. The observations were made with the assumption that the axial extent is small compared to the wavelength [85]. The axial extent of an axi-symmetric circumferential notch is also seen to influence the reflection coefficient of L(0,2) mode. The reflection coefficients of axi-symmetric part-thickness circumferential notches of different axial extents

exhibit ups and downs with the maxima being at the axial extents of quarter and the three-quarters of the wavelengths while minima being at the axial extents of half and the full wavelengths. The trend of ups and downs was observed for varying frequency. Also, the difference in the reflection coefficients between the maximum and the minimum is large. The ups and downs in the reflection coefficient were observed for through-thickness part-circumferential notches of different axial extents. The difference in the reflection coefficients observed between the maximum and the minimum is small. The trend of ups and downs is reported to occur due to interference of signals reflected from the near and the far edges of a notch. Small difference in the ups and downs of reflection coefficients for through-thickness part-circumferential notches of different axial extents is observed due to negligible transfer of energy from the near edge to the far edge of the notch. Furthermore,  $L(0,2)$  mode also undergoes mode conversion to  $F(1,3)$  mode due to the non-axisymmetric nature of the notches. Also, it has been reported that the reflection coefficients of axisymmetric circumferential notches with small axial extents show increase in the reflection coefficient with the increase in depth and frequency. A steel tube of 76 mm OD and 5.5 mm wall thickness was used and frequency range used in study was less than 100 kHz. The study involved both experiments and FE analysis [86].

Quantitative studies of reflection of  $T(0,1)$  mode in the range of 10-300 kHz from notches of various circumferential extents and depths in 610 mm and 76 mm OD pipes of length 3.1 m with the wall thicknesses of 20 mm and 5.5 mm, respectively, have been carried out using experiments and finite element simulation involving membrane models, axisymmetric models and 3D models. The reflection coefficients of  $T(0,1)$  mode from axisymmetric, 20% wall thickness circumferential notches of different axial extents exhibit ups and downs, with the maxima being at the axial extents of quarter and the three-quarters of the wavelengths

while minima being at the axial extents of half and the full wavelengths. As with  $L(0,2)$  mode, this phenomenon of ups and downs is attributed to interference of signals from the near edge and the far edge. It is also reported that the reflection coefficient of  $T(0,1)$  mode for full wall thickness defects and part-depth circumferential notches with a small axial extent varies approximately linearly with circumferential extent.  $T(0,1)$  mode is found to undergo mode conversion to flexural modes with non-symmetrical defects. It is also reported that the reflection coefficients of axisymmetric circumferential notches with small axial extents show increase in the reflection coefficient with the increase in depth and frequency [87]. Since the reflection of notches with axial extents shows dips at the half and full wavelength axial extents, it is necessary to use two inspection frequencies in practice [88]. Reflection coefficient is seen to be influenced by the axial length of a single defect due to interference. However, such influence of interference has been observed in the case of multiple defects as well.

For instance, a parametric study of through-holes of diameter 5.5 mm placed circumferentially and axially on 76 mm OD pipe with the wall thickness of 5.5 mm was carried out by Lovstad et al. [89] using FE and experiments. The mode used was  $T(0,1)$  mode in the frequency range 40-80 kHz. It was observed that when two holes are taken at different circumferential locations, the reflection coefficient is almost flat with azimuth angles between the two and the reflection coefficient is also seen to vary linearly with frequency. However, when two holes are axially placed, the reflection coefficient exhibits ups and downs with the maxima occurring at the integral multiples of half wavelength and the minima at the integral multiples of three-quarters of wavelength. The phenomenon is attributed to the interference occurring between waves from different defects. This observation was further validated by superposition principle. Furthermore, the maximum of the reflection coefficient in the

circumferential and axial cases was the same. Additional observation was that the reflection coefficient is found to be independent of the circumferentially placed holes when their separation is equal to twice the diameter of the holes and for axially placed holes to exhibit maximum reflection coefficient, their separation should be equal to half wavelength.  $T(0,1)$  mode is also seen to undergo mode conversion to flexural modes of dominant circumferential stress in the given band of frequencies. Another case of practical importance is the interaction of a guided wave mode with a cluster of pits, a multiple defect scenario, over a region, as isolated holes are only of academic interest to understand the underlying phenomenon of scattering and mode conversion. A cluster of pits, simulating pitting corrosion, involves multiple scattering and complex mode conversion. Lovstad et al. [90] studied pit clusters comprising of many holes of diameters in the range of  $1t-2.5t$  in a 3 m long tube (where  $t = 6$  mm, the thickness of the tube) of 114.3 mm OD using FE analysis, superposition principle and experiments.  $T(0,1)$  mode in the frequency range of 0-75 kHz was used. The reflection coefficient exhibited ups and downs with frequency with the maximum reflection coefficient and it was observed to shift with different clusters. Furthermore, the maximum reflection coefficient from pit clusters is found to be a linear function of the total volume fraction removed.

There are studies on reflectivity from dent-type and tapered type defects as well. Usually, to understand the influence of a particular dimension of a defect on reflectivity, the other dimensions of the defect will be fixed. For instance, to study the influence of the depth of an axial defect, the axial length and the width can be fixed and the depth can be varied. Hence, in this case, the reflectivity can be studied with respect to depth. The same is the case with circumferential defects and pin holes but for dents and tapered defects it is not possible to change one dimension alone while retaining the others. Hence, it is difficult to isolate and

identify a particular dimension causing reflection. For instance, Ma et al. [91] studied the reflectivity of single and double dents in an aluminium pipe of OD 16 mm and wall thickness 1 mm and the length of 1250 mm. The depths of the dents were considered in the range of 1.6 – 5.9 mm. L(0,2) mode was used at the frequency of 240 kHz. It is reported that the reflection coefficient increases approximately linearly with depth for single and double dents. It is also reported that L(0,2) mode undergoes mode conversion to F(1,3) mode with smaller amplitudes. Their reflection coefficients of F(1,3) mode for single and double dents also vary approximately linearly with depth. But, the reflection coefficient of F(1,3) mode is observed to be smaller for double dents than that for single dents. Hence, the ratio of reflection coefficients of L(0,2) to F(1,3) modes was proposed to be used as an indicator of single or double dents. These dents were also reported to be located to the accuracy of 2 mm. Carandente et al. [92] studied the reflectivity of T(0,1) mode from a tapered step-up/step-down defects, tapered notches and V-notches in pipes of OD 76 mm and wall thickness of 5.5 mm, in the frequency range of 30- 70 kHz. The study involved FE analysis, semi-analytical analysis and experiments. The depths of the defects were of 20% and 50% wall thickness. It is reported that the two ends of a taper give reflections while the taper region does not give any reflection. The mode shape of T(0,1) inside the taper remains essentially the same, indicating that there is no backward propagating energy from the taper. The reflection coefficient from a tapered step shows ups and downs with frequency for a fixed axial length of the defect. The pattern of ups and downs is explained due to the inference of signals from the ends of the taper. The reflection coefficient showed maximum at low frequencies. The reflection coefficient is observed to be independent of angle of step-up taper. Furthermore, cosine tapers considered were reported to show low ups and downs in the reflection coefficient. The tapered defects with both step-up and step-down pattern exhibit a periodic variation in the reflection

coefficient with respect to the frequency and also display a reduction in the reflection coefficient for lower angles of taper at high frequencies. Hence, there is a difficulty in achieving a good sensitivity for a low-angled tapered defect. The deeper tapered defects are reported to give higher reflections than the shallow ones. The reflection coefficient of V-notch was observed to be consistently lower than that for tapered defects.

It can be seen from thorough literature survey that for long range testing of pipes either low frequency longitudinal ( $L(0,m)$ ) or torsional modes ( $T(0,m)$ ) have been used. The modes have their own advantages and disadvantages. Some researchers recommend the use of  $T(0,m)$  over  $L(0,m)$  or vice-versa [93]. However, it purely depends on the application one deals with and what is sought for. Some researchers recommend the use of both modes for an application [32]. Another point that needs discussion is the signal processing of guided wave signals for mode identification and noise removal.

### **2.2.5 Signal processing techniques**

Signal processing approaches are important to obtain relevant information from a signal. Sometimes, the information to be read from the signal can be direct and other times it can be very difficult. Ultrasonic guided waves are multi-modal and in practice, one often encounters many modes and dispersion. To identify these modes and dispersing of frequencies with respect to time, time-frequency (TF) analyses can be used. Most widely used TF representations are short-time Fourier transform, Wavelet transform, Wigner-ville distribution [94, 95, 96]. Most of the times, NDE signals in practice are corrupted by noise. The sources of noise could be background, electronics, thermal etc. EMAT and magnetostrictive signals are invariably corrupted by heavy noise due to unwanted vibration of a specimen, bi-directional propagation, material noise, electronic noise and EMI [97].

Hence, it is a mixture of coherent and incoherent noise. Therefore, a suitable signal processing technique should be chosen and used to obtain the information of interest with a good signal-to-noise ratio (SNR). Techniques of de-noising include averaging, filters, discrete wavelet transform, S-transform, Hilbert-Huang transform, split-spectrum processing, cross-correlation, empirical mode decomposition (EMD), correlation etc. [97, 98, 99, 100]. The main aim of de-nosing a signal is to improve the SNR of a signal [101].

### **2.2.5.1 Short-time Fourier transform (STFT)**

The frequency content of a stationary signal can be determined by the Fourier transform [102]. If the frequencies of a signal vary with time, the classic Fourier transform cannot determine the evolution of frequencies at a particular instant of time. A signal whose frequency content varies with time is called a non-stationary signal. The fundamental idea behind STFT is to segment a non-stationary signal into many signal segments and obtain the Fourier transform for each of the signal segments [103]. Stationarity of signals is assumed over each of the segments. The spectrum obtained for each of the segments will show the evolution of frequencies with time. The segmentation of a signal is carried out by using windows. The windows used are rectangular, Hanning, Hamming, Kaiser, Gaussian, etc. The issue associated with windowing is spectral leakage, which is an artefact. Rectangular windows exhibit larger leakage while the other windows display smaller leakage [44].

Let the signal to be short-term Fourier transformed be  $f(t)$  and  $w(t)$  be a window function for segmenting  $f(t)$ . The window  $w(t)$  is centered at time ' $\tau$ ' at which the frequency spectrum is desired. The parameter ' $\tau$ ' is used for sliding the window function across the signal  $f(t)$  for segmenting. The signal segmented by Eq. (2.2) which is function of varying time ' $t$ ' and the fixed time ' $\tau$ '. The Fourier transform of the signal segment  $f_w(t, \tau)$  is called the short-time

Fourier transform and is given by Eq. (2.3). Equation (2.5) is the power spectral density centered at time ‘ $\tau$ ’. The assemblage of all the spectra of the segments of  $f(t)$  is called the spectrogram, which will indicate the time evolution of frequencies. In STFT, time localization by windowing will cause a blurring or spread in frequency because signals of short time duration will inherently have wideband spectrum. Hence, a small window in time domain will show a wideband in frequency or vice-versa. Therefore, STFT resolution strongly depends on the size of a window. The resolution that can be achieved in time and frequency domains is limited by Heisenberg inequality, as given in Eq. (2.6). Furthermore, STFT has a fixed resolution in the time-frequency plane.

$$f_w(t, \tau) = f(t)w(t - \tau) \quad (2.2)$$

$$f_w(\omega, \tau) = \frac{1}{2\pi} \int e^{-i\omega t} f_w(t, \tau) dt \quad (2.3)$$

$$f_w(\omega, \tau) = \frac{1}{2\pi} \int e^{-i\omega t} f(t)w(t - \tau) dt \quad (2.4)$$

$$P_w(\omega, \tau) = \left| \frac{1}{2\pi} \int e^{-i\omega t} f(t)w(t - \tau) dt \right|^2 \quad (2.5)$$

$$\Delta t \Delta \omega \geq \frac{1}{2} \quad (2.6)$$

Many researchers have applied STFT to characterize ultrasonic signals. For instance, Yoon et al. [82] have applied STFT on guided wave signals reflected from a through-axial crack to identify the modes generated from the defect. Dong et al. [104] applied STFT on guided wave signals obtained in a steel pipe of OD 42 mm, wall thickness 5 mm and length 5.98 m with a through-hole of 13 mm diameter to identify the modes present. After obtaining a spectrum, dispersion curves can be superimposed on the spectrum to identify modes. Figure 2.4 shows

the spectrogram constructed using signals obtained by a phased array transducer of frequency 1.5 MHz on a 2 mm thick steel plate indicating  $A_1$  and  $S_1$  modes [105].

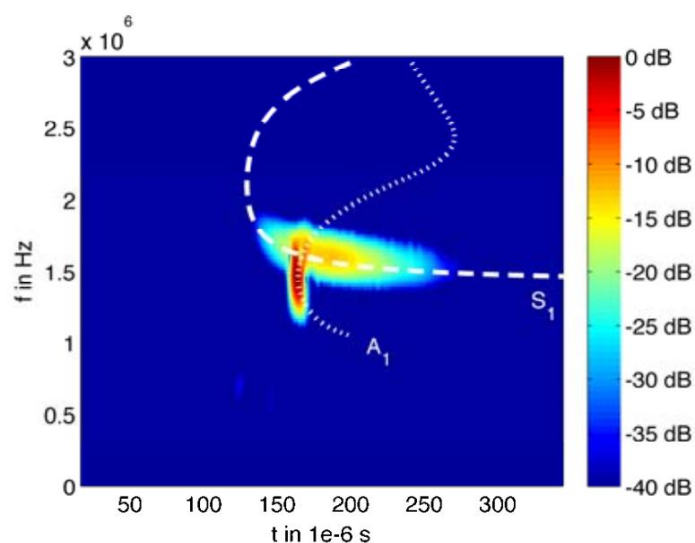


Fig. 2.4. Spectrogram superimposed on dispersion curves of 2 mm thick steel plate [105].

### 2.2.5.2 Cross-correlation

Cross-correlation is a common technique used to obtain the time of flight with a high accuracy [106]. The technique works by matching a reference signal with a received signal. It is achieved by shifting the reference signal in time with respect to the received signal, multiplying and adding the individual data. The output results in the maximum when a maximum degree of similarity is reached. The time of flight corresponding to the maximum correlation is taken as an accurate measure of time of flight. In general, echoes are timed with respect to the time corresponding to the maximum amplitude. This may not yield accurate measurement when dispersion and frequency dependent attenuation are present. In such contexts, cross-correlation can provide a fair measure of the time of flight. The technique can also be used for de-noising applications [107]. However, when the frequency band of the received signal and the noise is the same, the cross-correlation technique exhibits a

correlation. This can be overcome by wavelet based de-noising techniques with suitable thresholding schemes. Equation (2.7) describes the cross-correlation in discrete form, as in [108],

$$G_{xy}(\tau) = \frac{1}{\sqrt{N}} \sum_{k=1}^N X_k(k) Y_k(k + \tau) \quad (2.7)$$

where ‘X’ is the received signal, ‘Y’ is the reference signal, ‘G (τ)’ is the cross-correlation function, ‘τ’ is the time lag, ‘N’ is the data length and ‘k’ is the sample index.

### 2.2.5.3 Discrete Wavelet Transform

Wavelet transform (WT) finds applications in the fields of data encryption, data compression, and signal denoising [109]. The different forms of wavelet transforms are continuous wavelet transform (CWT), Discrete wavelet transform (DWT) and wavelet packet transform [110, 111, 101]. CWT is mostly used for time-frequency analysis to achieve multi-resolution. DWT is mostly used for de-noising, sub-band coding and image compression [108]. A wavelet is an oscillation of short duration centered on a specific time. The WT is discretized as in the case of the Fourier Transform, and is known as the discrete wavelet transform (DWT). Using DWT, a discrete signal  $s(n)$  is decomposed into various levels with different band of frequencies or scales, as given in Eqs. 3 and 4 [112].  $\psi_{j,k}(n)$  and  $\phi_{j,k}(n)$  are basis functions used to decompose a signal into approximations and details, respectively, as given in Eqs. (2.8 and 2.9):

$$\psi_{j,k}(n) = \frac{1}{\sqrt{2^j}} \psi\left(\frac{n - 2^j k}{2^j}\right) \quad (2.8)$$

$$\phi_{j,k}(n) = \frac{1}{\sqrt{2^j}} \phi\left(\frac{n - 2^j k}{2^j}\right) \quad (2.9)$$

$$W_\psi(j, k) = \frac{1}{\sqrt{M}} \sum_n s(n) \psi_{j,k}(n) \quad (2.10)$$

$$W_\phi(j_0, k) = \frac{1}{\sqrt{M}} \sum_n s(n) \phi_{j_0,k}(n) \quad (2.11)$$

where  $j \geq j_0$ ,  $n = 0, 1, \dots, M-1$ , and  $\psi_{j,k}(n)$  and  $\phi_{j,k}(n)$  are wavelets in discrete variables given Eqs. (2.8 and 2.9), respectively. Equation (2.10) computes the detailed coefficients,  $W_\psi$  (high frequency) and Eq. (2.11) computes the approximate coefficients,  $W_\phi$  (low frequency). The approximations are only successively decomposed. General decomposition of approximation for the the  $n^{\text{th}}$  level into the approximation and the detail contains the bands of frequencies as given in Eqs. (2.12 and 2.13) [113]:

**$n^{\text{th}}$  level approximation:**

$$\frac{1}{(N/F_s)} \text{ to } \left(\frac{1}{2}\right)^n \cdot \frac{F_s}{2} \quad (2.12)$$

**$n^{\text{th}}$  level detail:**

$$\left(\frac{1}{2}\right)^n \cdot \frac{F_s}{2} \text{ to } \left(\frac{1}{2}\right)^{n-1} \cdot \frac{F_s}{2} \quad (2.13)$$

where  $F_s$  is the sampling frequency,  $N$  is the number of samples and  $n$  is the level of decomposition. Given the wavelet coefficients, the signal can be reconstructed using the following Eq. (2.14) [114]:

$$s(n) = \frac{1}{\sqrt{M}} \left( \sum_j \sum_k W_\psi(j, k) \psi_{j,k}(n) + \sum_k W_\phi(j_0, k) \phi_{j_0,k}(n) \right) \quad (2.14)$$

The time of occurrence of a specific frequency component in the signal is limited by the time-frequency uncertainty. The DWT along with thresholding techniques can be utilized in extraction and removal of unwanted frequency components present in a signal. In this context, the signal is first decomposed using several wavelets and level-based thresholding is applied to wavelet decomposition coefficients. Threshold is of paramount importance in noise reduction. The threshold value for each level is estimated using various schemes such as Stein's unbiased risk estimator (SURE), minimax threshold, universal threshold etc. [115-117]. For instance, the universal fixed threshold selection proposed by Donoho and Johnstone [118] is given by Eq. (2.15). After the calculation of a threshold, it is applied on each level based on the rules called soft thresholding and hard thresholding, as given in Eqs. (2.16 and 2.17), respectively. In hard thresholding, amplitudes below the estimated threshold are made zero whereas in soft thresholding, amplitudes below the estimated threshold are made zero and the noise amplitudes above the threshold are reduced by the magnitude of the threshold [119].

$$T = \sigma_{std} \times \sqrt{2 \log(n)} \quad (2.15)$$

where  $\sigma_{std} = \frac{\text{Median of wavelet coefficients}}{0.6745}$  is the standard deviation of wavelet coefficients divided by the third quartile of the normal distribution and 'n' is the total number of wavelet coefficients for a given level.

$$X_T^{\text{Hard}} = \begin{cases} 0 & |x| \leq T \\ x & |x| > T \end{cases} \quad (2.16)$$

$$X_T^{\text{Soft}} = \begin{cases} 0 & |x| \leq T \\ x - T & x > T \\ x + T & x < -T \end{cases} \quad (2.17)$$

Subsequent to thresholding of the coefficients, the signal is reconstructed from all the levels using inverse DWT. All the above can be implemented in Matlab using ‘wden’ function.

Figure 2.5 shows the flowchart of DWT technique.

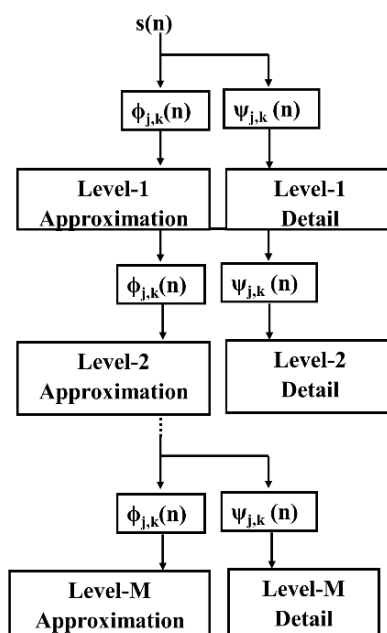


Fig. 2.5. Flowchart of Discrete Wavelet Transform.

As regards the application of DWT, the success in achieving desirable results depends on choice of wavelets. The choice of a mother wavelet purely depends on the application. Different wavelets are used for applications of different nature based on certain estimators, algorithms and optimization [120]. Matz et al. [121] have reported that the mother wavelet

selected should be similar in shape to the ultrasonic signal obtained for de-noising. Furthermore, it has to satisfy the criteria of symmetry and orthogonality. It is also recommended to use DWT for de-noising as it ensures zero-time shift of ultrasonic signals. For the study, discrete Meyer wavelet was used to denoise simulated flaw echoes with noise. Siqueira et al. [122] used dB6 wavelet to de-noise guided wave signals obtained in a mild steel pipe of 152 mm OD, 8 mm thickness and 1850 mm length with notches of depths 4 mm, 7 mm and a through-notch using a comb transducer excited at 500 kHz. The signals obtained were very noisy and de-noising using WT improved the SNR by 12 dB. Kreidl et al. [123] used wavelets from families of Daubechies, Symlet, Coiflet and Biorthogonal pairs to de-noise ultrasonic signals with noise. It is reported that the wavelets of Symlet family are suitable for noise reduction in ultrasonic signals followed by Coiflet and Biorthogonal pairs. The noise reduction was observed to be 12 dB.

#### **2.2.5.3.1 Practical implementation of DWT**

DWT is implemented through filter banks, which consist of high pass and low pass filters [114]. The approximation coefficients are obtained through low pass filters and the detail coefficients are obtained through high pass filters. Then, the filter outputs are downsampled by 2. At each stage only approximation coefficients are filtered using low pass filters and detailed coefficients are retained. The downsampling reduces the time resolution by 2 and increases the frequency resolution by 2. Figure 2.6 shows the schematic of DWT implementation.  $S(n)$  is the input signal.  $h(n)$  and  $g(n)$  are known unit impulse responses of low pass and high pass filters for a given wavelet.  $A$ 's and  $D$ 's are approximation and detail coefficients.

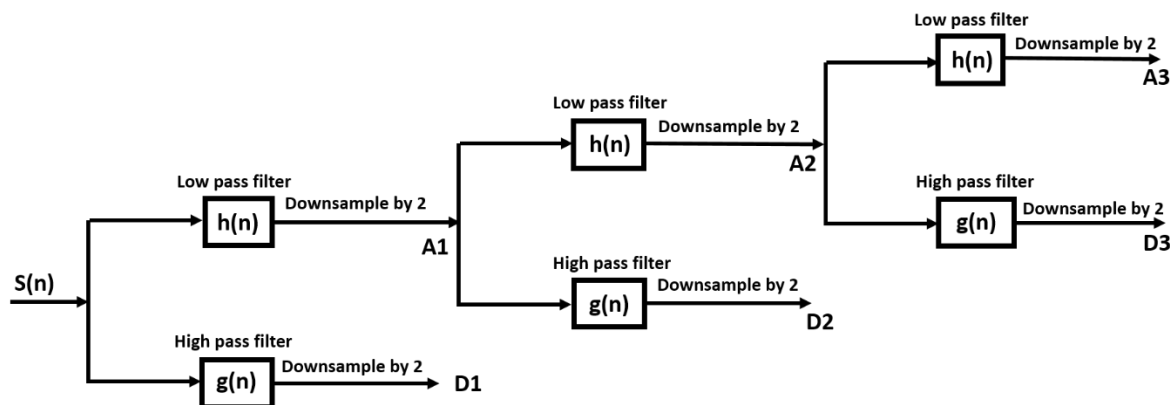


Fig. 2.6. Implementation of Discrete Wavelet Transform using filter bank.

## 2.3 Theory

### 2.3.1 Theory of guided waves in hollow cylinders

Ultrasonic guided waves are formed by multiple reflections of shear and longitudinal waves occurring between boundaries of a specimen. The propagation of ultrasonic guided waves in a specimen is governed by Navier's equation of motion [44], as shown in Eq. (2.18):

$$(\lambda + 2\mu)\nabla(\nabla \cdot \bar{U}) - \mu\nabla \times \nabla \times \bar{U} = \rho \frac{\partial^2 \bar{U}}{\partial t^2} \quad (2.18)$$

where  $\lambda$  and  $\mu$  are Lamé constants,  $\rho$  is the density of the solid and  $\bar{U}$  is the displacement vector. The equation is solved with an assumption that a hollow cylinder is infinitely long, homogeneous and isotropic with traction free boundary conditions at the inner radius and the outer radius [124]. Towards this,  $\bar{U}$  is expressed in terms of the dilatation scalar potential  $\phi$  and the equivolume vector potential  $\bar{H}$  as Eq. (2.19),

$$\bar{U} = \nabla\phi + \nabla \times \bar{H} \quad (2.19)$$

with the gauge condition,

$$\nabla \cdot \bar{H} = 0 \quad (2.20)$$

The gauge invariance condition is known as equal volume condition, which is true for the assumption of the cylinder with an infinite length and volume. Substitution of Eq. (2.19) and Eq. (2.20) in Eq. (2.18) gives:

$$C_p^2 \nabla^2 \phi = \frac{\partial^2 \phi}{\partial t^2} \quad (2.21)$$

$$C_s^2 \nabla^2 \bar{H} = \frac{\partial^2 \bar{H}}{\partial t^2} \quad (2.22)$$

where  $C_p^2 = (\lambda + 2\mu)/\rho$  and  $C_s^2 = \mu/\rho$  are longitudinal and shear wave speeds, respectively. The potentials are then expressed in separable variables in cylindrical coordinates as:

$$\phi = f(r) \cos m\theta \cos(\omega t + kz) \quad (2.23)$$

$$H_r = g_r(r) \sin m\theta \sin(\omega t + kz) \quad (2.24)$$

$$H_\theta = g_\theta(r) \cos m\theta \sin(\omega t + kz) \quad (2.25)$$

$$H_z = g_z(r) \sin m\theta \cos(\omega t + kz) \quad (2.26)$$

where the integer ‘m’ is known as the circumferential order of a wave mode, ‘k’ is the wavenumber,  $H_r$ ,  $H_\theta$  and  $H_z$  are the components of  $\bar{H}$ ,  $g_r(r)$ ,  $g_\theta(r)$  and  $g_z(r)$  are functions of r. The functions H and g are unknowns. Substitution of Eqs. (2.23-2.226) into Eqs. (2.21 and 2.22) yields:

$$(\nabla^2 + \omega^2/C_p^2)\phi = 0 \quad (2.27)$$

$$(\nabla^2 + \omega^2/C_s^2)H_z = 0 \quad (2.28)$$

$$(\nabla^2 - 1/r^2 + \omega^2/C_s^2)H_r - (2/r^2) (\partial H_\theta/\partial\theta) = 0 \quad (2.29)$$

$$(\nabla^2 - 1/r^2 + \omega^2/C_s^2)H_\theta + (2/r^2) (\partial H_r/\partial\theta) = 0 \quad (2.30)$$

Introducing the notations for easy representation,

$$\alpha^2 = \omega^2/C_p^2 - k^2, \quad \beta^2 = \omega^2/C_s^2 - k^2, \quad \alpha_1 r = |\alpha r| \text{ and } \beta_1 r = |\beta r|$$

The most general solution of the Eqs. (2.27-2.30) for guided waves in a hollow cylinder is expressed in terms of Bessel functions (Z): J and I and K and Y with the arguments  $\alpha_1 r$  and  $\beta_1 r$  as in Eqs. (2.31-2.34).  $\alpha$  and  $\beta$  can be either real or imaginary. A, B, A<sub>1</sub>, B<sub>1</sub>, A<sub>2</sub>, B<sub>2</sub>, A<sub>3</sub> and B<sub>3</sub> are unknown constants.

$$f = AZ_m(\alpha_1 r) + BW_m(\alpha_1 r) \quad (2.31)$$

$$h_3 = g_z = A_3 Z_m(\beta_1 r) + B_3 W_m(\beta_1 r) \quad (2.32)$$

$$h_1 = (ig_r - g_\theta)/2 = A_1 Z_{m+1}(\beta_1 r) + B_1 W_{m+1}(\beta_1 r) \quad (2.33)$$

$$h_2 = (ig_r + g_\theta)/2 = A_2 Z_{m-1}(\beta_1 r) + B_2 W_{m-1}(\beta_1 r) \quad (2.34)$$

Two of the constants can be eliminated by using the gauge invariance condition. Substituting Eqs. (2.31-2.34) into Eq. (2.19) yields the displacement components. Furthermore, with the aid of the components and the stress-strain relationship, stress fields for longitudinal waves can be derived. Then, by imposing the stress-free boundary conditions (Eq. (2.35)) at the inner and outer radii, a linear system of six homogeneous equations in six unknowns is

obtained. To obtain a non-trivial solution, the determinant is equated to zero. Then, the eigenvalue problem is solved to obtain the very complicated characteristic equation of the form (Eq. (2.36)). The implicit transcendental equation is solved numerically to obtain dispersion curves (guided-wave solutions).

$$\sigma_{rr} = \sigma_{r\theta} = \sigma_{rz} = 0 \text{ at radii, } r = r_1 \text{ and } r = r_2 \quad (2.35)$$

$$D(r_1, r_2, \lambda, \mu, fd, c) = 0 \quad (2.36)$$

where  $r_1$  and  $r_2$  are inner and outer radii, respectively,  $\lambda$  and  $\mu$  are Lamé' constants,  $f$  is the frequency,  $d$  is the wall thickness and  $c$  is the phase velocity of a mode.

Equation (2.36) is solved using global matrix method [125]. The solution has three different families of guided waves. The three families are termed as the longitudinal (L(0,n)), torsional (T(0,n)) and flexural (F(m,n)) modes, where 'n' is the circumferential order and 'm' is the mode number [126]. Within each family there are infinite numbers of modes with respective phase velocities. These modes are entirely determined by material properties, inner and outer radii of the tube and the frequency-wall thickness (fd) product. The zero order (m=0) longitudinal and torsional modes are axisymmetric. L(0,n) modes have fields such as displacement and stresses as functions of axial (z) and radial (r) coordinates but are independent of the angular coordinate ( $\theta$ ). T(0,n) modes have the displacement field across the cross-section. Flexural modes have all three components of displacement and are non-axisymmetric. Every mode has its respective phase and group velocities. The modes can be dispersive or non-dispersive depending on the location on the dispersion curves. Dispersion curves are ones plotted between phase and group velocities versus frequency, which will aid in understanding the behaviour of a mode.

### 2.3.2 Magnetostriction

Magnetostriction refers to change in the dimensions of a ferromagnetic material when it is subjected to a magnetic field. This phenomenon is called the Joule effect and the strains generated are volume conserving [127, 128]. On the other hand, a ferromagnetic material induces a magnetic field when it is strained. This reverse phenomenon is known as the Villari effect [129]. The first and second effects are used for the generation and reception of elastic waves, respectively. Figure 2.7 shows the schematic of the Joule and the Villari effects. A ferromagnetic material can expand or contract in the direction of application of magnetic field. Accordingly, they are called positive or negative magnetostrictive materials, respectively [130]. Generally, magnetostrictive transducers (MsTs) are a pair of RF coils for transmission and reception of ultrasonic guided waves [131]. The principle behind the transduction mechanism is the alternate expansion and contraction of a ferromagnetic specimen subjected to a time varying magnetic field and that for the reception mechanism is through the alteration of a magnetic state of the specimen by the stresses caused by the wave.

Magnetostrictive transducers for non-destructive applications are fabricated in the low frequency range of less than 500 kHz [131-133]. The limited frequency range comes from reduced efficiency due to dominant skin effect at high frequencies. They can be used for examination of ferromagnetic plates, tubes/pipes and rods. By choosing the proper combination of biasing and the dynamic fields, any desired mode can be generated [132]. Figure 2.8 shows schematic of the bias (static) and the dynamic fields applied in the axial direction of a ferromagnetic tube for the generation of a longitudinal guided wave mode. Even for non-ferromagnetic specimens with the advent of magnetostrictive patch transducers (MPTs), ultrasonic waves can be generated [133]. Unlike in ferromagnetic specimens, strains get generated only in MPTs and they are transmitted to a non-ferromagnetic specimen via

mechanical bonding to the tube. Magnetostrictive phenomenon is described by piezomagnetic equations, which according to IEEE standard [134] are given by Eqs. (2.37 and 2.38)

$$[\varepsilon] = [S^H][\sigma] + [d][H] \quad (2.37)$$

$$[B] = [d]^T[\sigma] + [\mu^\sigma][H] \quad (2.38)$$

Equations (2.37 and 2.38) represent the Joule and the Villari effects, respectively. These equations are derived based on thermodynamic considerations of free-energy [135]. In Eqs. (2.37 and 2.38),  $[\sigma]$  is the stress tensor,  $[\varepsilon]$  is the strain tensor,  $[\mu^\sigma]$  is the permeability matrix at a given stress,  $[S^H]$  is the compliance matrix at a given magnetic field and  $[d]^T$  is the transpose of piezomagnetic matrix at a given stress.  $[d]$  is a crucial parameter that provides a link between elastic and magnetic phenomena. The quantity ‘d’ is given by the slope of the magnetostriction strain curve versus the applied magnetic field at a bias point (point A in Fig. 2.9). A phenomenon associated with a ferromagnetic material is that the strain is exhibited in the same direction regardless of the direction of the applied magnetic field. Thus, a dynamic magnetic field applied to generate elastic waves at origin O in Fig. 2.9 will lead to the doubling of the frequency considered and low amplitudes. Whereas the dynamic field applied at point A (DC bias) will generate strain waves of the applied frequency about the positive static strain. In principle, the magnitude of a dynamic field applied should be smaller than the static bias because Eqs. (2.37 and 2.38) are linearized under that assumption. Thus, a small dynamic field around a large bias point will form a minor B-H loop without much variation in the permeability, and hence the local linearity is ensured. Therefore, the hysteresis losses can be neglected [135, 136]. Higher dynamic fields will generate harmonics of the excitation frequency [137]. Furthermore, external stresses applied will also affect the permeability via

magnetization [138]. Owing to magneto-elastic coupling, there will also be a change in the elastic modulus of the material which is known as  $\Delta E$  effect. Thus, a ferromagnetic material will become stiffer near the saturation. The effect is small in nickel and is very large in Terfenol-D and Metglass, which are known to display large magnetostriction [139]. Moreover, magnetostrictive forces in ferromagnetic materials are more dominant than Lorentz forces [140]. Hence, the generation of ultrasonic waves in a ferromagnetic specimen is largely due to magnetostrictive forces. Figure 2.10 shows the magnetostrictive forces and Lorentz force in a ferromagnetic specimen. Furthermore, there are many applications of MsS such as torque sensors, stress sensor, strain sensor, position sensors etc. [141].

There are also finite element simulation-based studies reported for the design of magnetostrictive transducers. The modeling involves the coupling of magnetic and elastic phenomena. For instance, Kim et al. [142] modelled a magnetostrictive sensor using finite element analysis taking into account the non-linear behaviour of the material for underwater applications. Time-harmonic magnetostrictive models were also developed to study the effect of arbitrarily oriented static magnetic field in a magnetostrictive strip on radiation patterns of guided waves in a plate [143]. Finite element modelling of magnetostrictive phenomena for the generation and reception of L(0,1) and L(0,2) modes at the frequencies of 20 kHz and 80 kHz, respectively was reported by Jiang Xu et al. [39]. The authors thoroughly investigated the effect of lift-off of the receiver coil on the induced voltage.

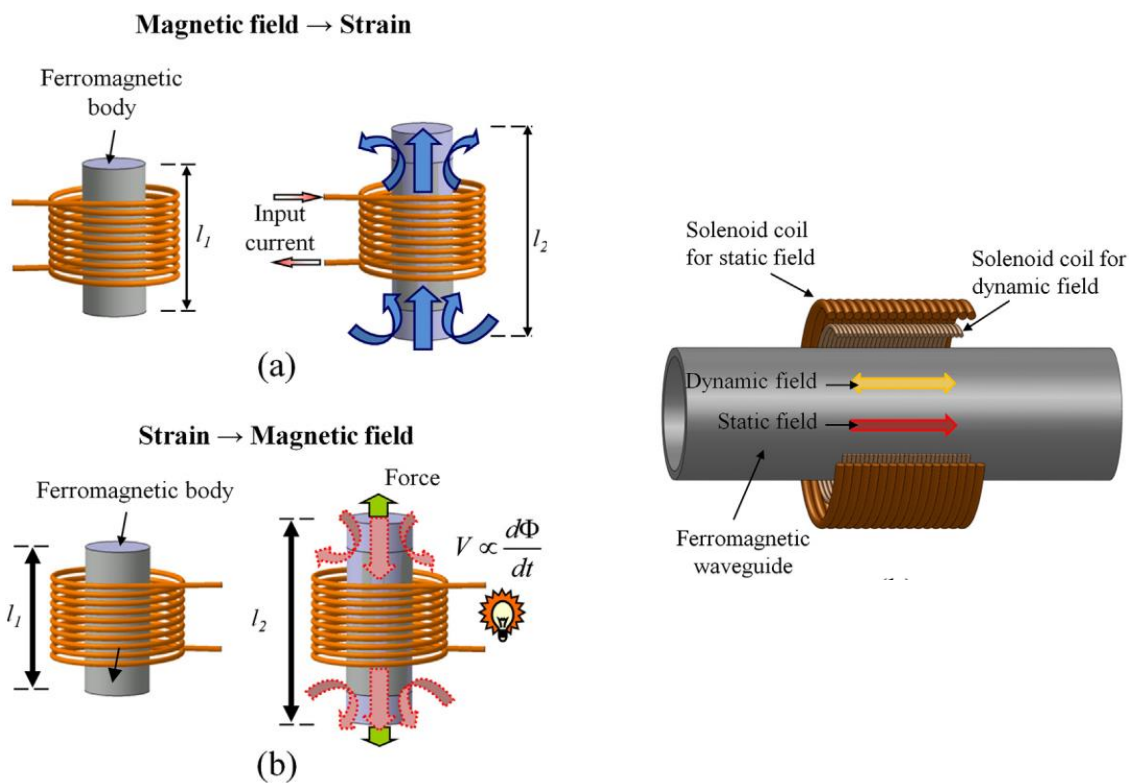


Fig. 2.7. Schematic of (a) Joule effect and (b) Villari effect [135].

Fig. 2.8. Generation and sensing of a longitudinal wave in a ferromagnetic pipe using magnetostrictive phenomena [135].

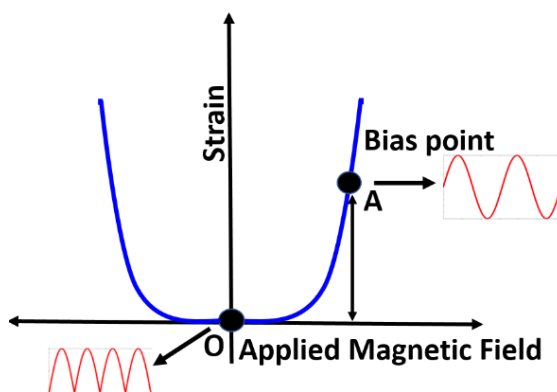


Fig. 2.9. Schematic of magnetostrictive strain versus applied magnetic field.

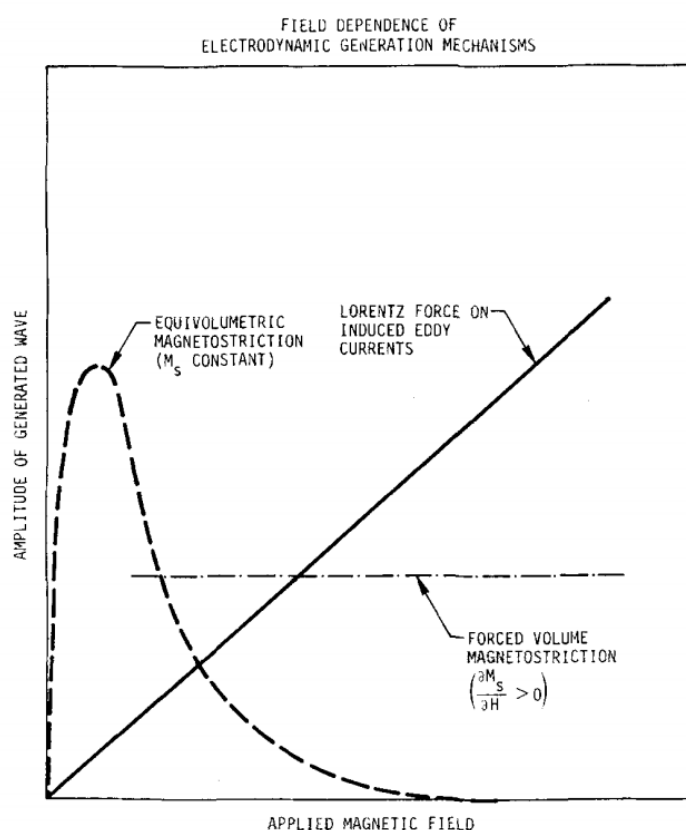


Fig. 2.10. Amplitude of the generated wave in a ferromagnetic specimen due to Lorentz force and magnetostrictive force [140].

### 2.3.2.1 Setting-up of mathematical framework for generation of axi-symmetric longitudinal guided wave mode using magnetostrictive principle

The present thesis deals with the generation of an axi-symmetric longitudinal guided wave mode in SG tubes of PFBR. SG tubes of PFBR are made of Mod. 9Cr-1Mo ferritic steel and are ferromagnetic. Hence, the magnetostrictive principle was used in the generation of elastic guided waves in SG tubes of PFBR. A sequence of mathematical steps followed to achieve the generation of axi-symmetric longitudinal guided wave using magnetostrictive principles is presented below and the same steps were adopted in FE based magnetostrictive modelling

in FE simulation software COMSOL. The details of which are presented in Chapter 3. The procedure given below is applicable to transmitter-receiver coils encircled on a tube or that placed in-bore.

As mentioned above, for the generation of an axi-symmetric longitudinal guided wave mode in an SG tube both applied static magnetic field and applied dynamic field should point along the z-axis of the tube. Additionally, both fields should be axi-symmetric. The application of the large static field alters the magnetization of the material. Thus, the overall pre-dominant static magnetization is along the z-axis of the tube, thereby the magnetic permeability is pre-dominant along the z-axis. This in turn will cause a large static strain along the z-axis. A small dynamic magnetic field applied causes a small dynamic strain riding over the large static strain. As a consequence, an axi-symmetric ultrasonic guided wave is generated. All the above processes are captured by the transmitter equation. On the other hand, the dynamic stress caused by the propagating guided waves alters the magnetic state of the SG tube. Thus, the dynamic magnetic field in turn induces a voltage in the coil. This process is captured by the receiver equation.

For the present problem, the applied strain is zero ( $[\boldsymbol{\varepsilon}] = 0$ ). Hence, the transmitter equation becomes as given in Eq. (2.41). For the sake of clarity, the second term of Eq. (2.39) is denoted as  $\sigma_{mag}$ , i.e., the equivalent stress generated by the dynamic magnetic field. Similarly, when the applied dynamic magnetic field intensity ( $\mathbf{H}$ ) is zero, on the receiver side, the receiver equation becomes as Eq. (2.42). Equations (2.41 and 2.42) jointly describe the transmit-receive phenomenon. For this, the constitutive equations are written for stress ( $\boldsymbol{\sigma}$ ) and magnetic induction ( $\mathbf{B}$ ):

**Transmitter equation:**

$$[\sigma] = [C][\varepsilon] - [C][d][\mu^\sigma]^{-1}[B] \quad (2.39)$$

**Receiver equation:**

$$[B] = [d]^T[\sigma] + [\mu^\sigma][H] \quad (2.40)$$

where  $C$  is the stiffness matrix of the SG tube,  $[\varepsilon]$  is the strain matrix,  $[\sigma]$  is the stress matrix,  $[d]$  is the piezomagnetic coefficient matrix for the case of applied magnetic field along the  $z$ -axis of the tube. It is seen in the literature, the  $[d]$  matrix takes this particular form when the magnetic field is applied along the  $z$ -axis [144]. If the field is applied along a different direction, the  $[d]$  matrix takes a different form and  $[\mu^\sigma]^{-1}$  is the inverse of the permeability matrix at the given stress in the tube. Since, magnetization is pre-dominant along the  $z$ -axis, only  $\mu_{rr}$  and  $\mu_{zz}$  are present in the permeability matrix.  $[B]$  is the dynamic magnetic induction in the tube,  $S$  is the piezomagnetic coefficient along the  $z$ -axis of the tube and  $St$  is the total strain and  $H$  is the applied magnetic field. All the quantities are defined below.

For axi-symmetric cases, the axes of coil and tube are in coincidence, the induced current in the tube will have only circumferential component. Hence,  $B_\phi$  will be zero, a predominant  $B_z$  component and a small  $B_r$  component will be present. It can be seen in the Eq. (2.43) that only  $B_r$  and  $B_z$  components contribute to the axial stress  $\sigma_{zz}$  and the radial stress  $\sigma_{rr}$  for transmission, as required by the symmetry of the mode. Furthermore, it can be observed in Eq. (2.44) that the axial stress  $\sigma_{zz}$  and the radial stress  $\sigma_{rr}$  caused by the longitudinal guided wave contribute to the time varying axial magnetic field  $B_z$ , which is picked by the receiver coil as an induced voltage. The shear stresses  $\sigma_{rz}$  and  $\sigma_{r\phi}$  are zero for the axi-symmetric longitudinal guided wave modes and hence, they do not contribute to  $B_r$  and  $B_\phi$  for the

induced voltage in the receiver coil. This eventually makes the receiver equation, as given in Eq. (2.45).

**Transmitter equation:**

$$[\sigma_{mag}] = -[C][d][\mu^\sigma]^{-1}[B] \quad (2.41)$$

**Receiver equation:**

$$[B] = [d]^T[\sigma] \quad (2.42)$$

In cylindrical coordinates,

$$\varepsilon = \begin{bmatrix} \varepsilon_{rr} \\ \varepsilon_{\varphi\varphi} \\ \varepsilon_{zz} \\ \varepsilon_{rz} \\ \varepsilon_{r\varphi} \\ \varepsilon_{z\varphi} \end{bmatrix}, \sigma = \begin{bmatrix} \sigma_{rr} \\ \sigma_{\varphi\varphi} \\ \sigma_{zz} \\ \sigma_{rz} \\ \sigma_{r\varphi} \\ \sigma_{z\varphi} \end{bmatrix} \quad B = \begin{bmatrix} B_r \\ 0 \\ B_z \end{bmatrix} \quad H = \begin{bmatrix} H_r \\ 0 \\ H_z \end{bmatrix} \quad \mu = \begin{bmatrix} \mu_{rr} & 0 & 0 \\ 0 & 0 & 0 \\ 0 & 0 & \mu_{zz} \end{bmatrix}$$

$$C = \frac{E}{(1+\nu)(1-2\nu)} \begin{bmatrix} (1-\nu) & \nu & \nu & 0 & 0 & 0 \\ \nu & (1-\nu) & \nu & 0 & 0 & 0 \\ \nu & \nu & (1-\nu) & 0 & 0 & 0 \\ 0 & 0 & 0 & (1-2\nu) & 0 & 0 \\ 0 & 0 & 0 & 0 & (1-2\nu) & 0 \\ 0 & 0 & 0 & 0 & 0 & (1-2\nu) \end{bmatrix} \text{ GPa}$$

$$d = \begin{bmatrix} 0 & 0 & -0.5S \\ 0 & 0 & -0.5S \\ 0 & 0 & S \\ 0 & 3St/H & 0 \\ 3St/H & 0 & 0 \\ 0 & 0 & 0 \end{bmatrix} \text{ m/A}$$

$$\sigma_{mag} = \begin{bmatrix} \sigma_{rr} \\ \sigma_{\varphi\varphi} \\ \sigma_{zz} \\ \sigma_{rz} \\ \sigma_{r\varphi} \\ \sigma_{z\varphi} \end{bmatrix} = \frac{-E}{(1+\nu)(1-2\nu)} \begin{bmatrix} \frac{S(\nu-0.5)}{\mu_{zz}} B_z \\ \frac{S(\nu-0.5)}{\mu_{zz}} B_z \\ \frac{S(1-2\nu)}{\mu_{zz}} B_z \\ \mu_{zz} \\ 0 \\ 0 \\ 0 \end{bmatrix} \quad (2.43)$$

$$\begin{bmatrix} B_r \\ B_\varphi \\ B_z \end{bmatrix} = \begin{bmatrix} \frac{3St}{H} \sigma_{r\varphi} \\ \frac{3St}{H} \sigma_{rz} \\ S(\sigma_{zz} - 0.5(\sigma_{rr} + \sigma_{\varphi\varphi})) \end{bmatrix} \quad (2.44)$$

$$\begin{bmatrix} B_r \\ B_\varphi \\ B_z \end{bmatrix} = \begin{bmatrix} 0 \\ 0 \\ S(\sigma_{zz} - 0.5\sigma_{rr}) \end{bmatrix} \quad (2.45)$$

### 2.3.2.2 Electromagnetic equations used for the computation of magnetic field induction

Equation (2.46) is the Gauss law for magnetism and the static magnetic fields can be computed by introducing a scalar magnetic potential  $V_m$ . By substituting Eq. (2.47) in Eq. (2.46), one gets a Laplace equation (Eq. (2.50)), which holds good for a current-free region [145]. With this, the magnetic field set up by permanent magnets can be obtained.  $\bar{B}$  is the magnetic induction vector,  $\bar{H}$  is the magnetic field intensity and  $\mu(\bar{H})$  is the magnetic permeability. Equation (2.51) is the Ampere law for computing  $\bar{H}$  when the current density is present.  $J^e$  is the source current density and  $J^{\text{induced}}$  is the eddy current density [146]. Displacement current density is neglected because it is dominant only at very high frequencies. It is the combination of these current densities that generates the net magnetic

fields. Equation (2.52) relates electric field ( $\bar{E}$ ) to the induced current density in the specimen of conductivity ( $\sigma$ ) and the source current density ( $J^e$ ) is obtained through input current through the coil per the area of the coil. Equation (2.53) relates the gradient of the electric potential and the time-varying magnetic vector potential ( $\bar{A}$ ) to the electric field. The term  $\nabla V$  can be dropped when there is no static electric field in the system (no static charge accumulation). By substitution of Eqs. (2.52 and 2.53) into Eq. (2.51), the governing equation (Eq. (2.54)) for  $\bar{H}$  in terms of  $\bar{A}$  is obtained [146]. By solving the equation for  $\bar{A}$  and taking the curl of  $\bar{A}$  will result in  $\bar{B}$  in the specimen due to the application of current in the transmitter coil. Equation (2.55) is the governing equation of axi-symmetric case obtained by simplifying Eq. (2.54) [146]. Equation (2.56) is Faraday's law for computing the induced voltage in the receiver coil with the flux of  $\bar{B}$  through it.

**Gauss' law:**

$$\nabla \cdot \bar{B} = 0 \tag{2.46}$$

$$\bar{B} = \mu \bar{H} \tag{2.47}$$

$$\mu(\bar{H}) \nabla \cdot \bar{H} = 0 \tag{2.48}$$

$$\bar{H} = -\nabla V_m \tag{2.49}$$

**Governing equation:**

$$\mu(\bar{H}) \nabla \cdot \nabla V_m = 0 \tag{2.50}$$

**Ampere's law:**

$$\nabla \times \bar{H} = J^e + J^{induced} \quad (2.51)$$

$$J^{induced} = \sigma \bar{E} \quad (2.52)$$

$$\bar{E} = -\nabla V - \frac{\partial A}{\partial t} \quad (2.53)$$

**Governing equation:**

$$\sigma \frac{\partial A}{\partial t} + \nabla \times (\mu^{-1} \nabla \times \bar{A}) = J^e \quad (2.54)$$

**Axi-symmetric case:**

$$\frac{\partial^2 A_\phi}{\partial r^2} + \frac{1}{r} \frac{\partial A_\phi}{\partial r} + \frac{\partial^2 A_\phi}{\partial z^2} - \frac{A_\phi}{r^2} = -\mu J^e + \sigma \mu \frac{\partial A_\phi}{\partial t} \quad (2.55)$$

$$V_{ind} = -N \frac{d}{dt} \int \bar{B} \cdot d\bar{s} \quad (2.56)$$

### 2.3.3 Finite element analysis

Finite element (FE) analysis is widely used for solving wave equations numerically. FE analysis can solve problems with complex geometries and can provide accurate results. Accurate modelling requires a good understanding of a physical phenomenon, mathematical modelling to obtain governing equations, representation of geometries (1D, 2D and 3D) based on the physical phenomenon and approximations, and appropriate boundary conditions. It is very useful when there are no analytical solutions available to the problem. It can yield information, for example, such as interaction of waves with defects, visualization of modes,

which experiment cannot provide. However, the results of FE analysis should always be verified experimentally.

There are other modelling tools such as the finite difference method and the boundary element method for wave propagation problems [147, 148]. The finite difference method, though simple, has practical issues in the implementation of stress-free boundary conditions [149] and the boundary element method converts volume integrals into surface integrals, thereby reducing the dimension of the problem [150]. Hence, it is advantageous over FE analysis but there is no readymade code available for that. However, there are many commercial packages available for FE. Hence, in this thesis FE method was chosen for modelling wave propagation.

FE method works by discretizing a domain into elements [44, 151]. Elements are building blocks for FE models and analysis. Each element is connected by nodes. Sometimes, in addition to corner and side nodes, mid-nodes can also be present. The assemblage of elements is called mesh. Elements can be line, quadratic, triangular, hexahedra, tetrahedral, etc. depending on the dimension of a model. Loading functions are applied at nodes. FE methods calculate required fields at the nodes of an element from a governing equation using assumed trial functions. Then, suitable interpolation functions called shape functions are used to obtain a field variation over an element with the field values calculated at nodes. Usually, polynomial functions are used for interpolation and the degree of the polynomial depends on the number of nodes in an element. Finally, elemental level algebraic equations are assembled and solved to obtain the global solution. The governing equation for dynamics is given by Eq. (2.57) [151]:

$$[M]\{\ddot{D}\} + [C]\{\dot{D}\} + [K]\{D\} = \{F^{\text{ext}}\} \quad (2.57)$$

where  $\{\ddot{D}\}$ ,  $\{\dot{D}\}$  and  $\{D\}$  are the acceleration, velocity and the displacement,  $[M]$  is the mass matrix and  $[K]$  is the stiffness matrix. There are two methods to obtain  $\{D\}$  from the dynamic equation and they are implicit and explicit methods.

### 2.3.3.1 Explicit and Implicit Methods

Equation (2.57) should be time integrated to obtain displacement. To this aim, the time variable is discretized using finite difference approximations of time derivatives. Accordingly, it is classified as an explicit or implicit method. Equations (2.58 and 2.59) are functional forms for the time step  $n+1$  for explicit and implicit methods, respectively [151]. It can be observed that in the explicit method (Eq. (2.58)), the displacement at  $n+1$  time level depends only on the time history of the displacements.

$$\{D\}_{n+1} = g(\{D\}_n, \{\dot{D}\}_n, \{\ddot{D}\}_n, \{D\}_{n-1}, \dots) \quad (2.58)$$

$$\{D\}_{n+1} = g(\{\dot{D}\}_{n+1}, \{\ddot{D}\}_{n+1}, \{D\}_n, \{\dot{D}\}_n, \{\ddot{D}\}_n, \dots) \quad (2.59)$$

In the explicit scheme, the central difference method is used for computation of  $\{D\}_{n+1}$ . With the use of the central difference method, the governing equation of dynamics (Eq. (2.57)) can be written as in Eq. (2.60) [152]. It can be seen that the computation of  $\{D\}_{n+1}$  requires only the history of  $\{D\}_n$ . In practice, a lumped mass matrix scheme is used. In this scheme, elemental mass matrices are diagonal and hence, the global mass matrix is also diagonal. Hence, it involves only a few operations to invert the diagonal mass matrix. Besides, the diagonal mass matrix can be stored as a vector, which saves memory space. Therefore, computationally it is very efficient.

Furthermore, with the central difference approximations of time derivatives, velocities and accelerations can be found out. However, the explicit method is conditionally stable [153]. It indicates that the time step ( $\Delta t$ ) has to be smaller than the critical time step ( $\Delta t_r$ ) for the convergence of the solution. For an undamped system, it is determined by the highest frequency ( $\omega_{max}$ ) of the smallest element and is given by Eq. (2.61) [154]. For wave propagation problems, the critical time step is taken as the time for the longitudinal waves to travel through the smallest element, as given in Eq. (2.62) in which  $\Delta x$  is the smallest distance between the nodes and  $C_p$  is the velocity of the longitudinal wave. During an explicit analysis modelling in ABAQUS, a thumb rule for choosing  $\Delta x$  for wave propagation problems is that  $\Delta x$  should be around  $1/20^{\text{th}}$  wavelength of the shear wave [155, 156]. There is another derived parameter called CFL (Courant-Friedrichs-Lewy) number, which is the ratio of the actual time step to the critical time step (Eqs. (2.63 and 2.64)) [154]. The CFL should be chosen less than unity.

Equation (2.65) is the Newmark method for solving the dynamic equation (Eq. (2.57)) implicitly [152].  $\gamma$  and  $\beta$  are numerical damping parameters. The implicit method involves inversion of matrices  $[K]$ ,  $[C]$  and  $[M]$  at every time step. Hence, the method is time consuming. Unlike the explicit method, the implicit method is unconditionally stable if  $\gamma \geq 0.5$  and  $\beta \geq (1 + \gamma)^2/16$ . Hence, the size of  $\Delta t$  will not influence the stability of the solution. However,  $\Delta t$  should be chosen properly from accuracy considerations.  $\Delta x$  can be chosen as mentioned above. FE simulation software COMSOL uses the implicit method to solve the dynamic equation. In general, the same CFL condition is also used for implicit FE analysis for the purpose of accuracy and in practice, CFL number is taken to be less than or equal to 0.2 for accuracy [157]. As regards a 2D-axisymmetric case (Eq. (2.55)) for

computing induced magnetic fields in COMSOL, the time integration implicit method is used similarly [146].

$$(1/\Delta t^2)[M]\{D\}_{n+1} = \{F^{ext}\}_n - [K]\{D\}_n + [(2/\Delta t^2)[M] - (1/\Delta t)[C]]\{D\}_n - [(1/\Delta t^2)[M] - (1/\Delta t)[C]]\{D\}_{n-1} \quad (2.60)$$

$$\Delta t < \Delta t_r = 2/\omega_{max} \quad (2.61)$$

$$\Delta t < \Delta t_r = \frac{\Delta x}{C_p} \quad (2.62)$$

$$CFL = \frac{\Delta t}{\Delta t_r} < 1 \quad (2.63)$$

$$CFL = \frac{\Delta t \times C_p}{\Delta x} \quad (2.64)$$

$$[K] \{ \{D\}_n + (\Delta t)\{\dot{D}\}_n + (\Delta t^2)[(0.5 - \beta)\{\ddot{D}\}_n + \beta\{\ddot{D}\}_{n+1}] \} + [C] \{ \{\dot{D}\}_n + (\Delta t)[(1 - \gamma)\{\ddot{D}\}_n + \gamma\{\ddot{D}\}_{n+1}] \} + [M] \{\ddot{D}\}_{n+1} = \{F^{ext}\}_{n+1} \quad (2.65)$$

## 2.4 Motivation and Objectives

It is seen from thorough literature survey that for long range testing of pipes either low frequency longitudinal (L(0,m)) or torsional modes (T(0,m)) have been used. The defects that have been dealt with are mostly circumferential or axial and a very few studies have been reported on detection of holes. Detection of extended shallow defects, simulating corrosion, has also been reported and they are considered to be uniform. No non-axisymmetric tapering defect such as wear scar, arising due to rubbing of a tube with its supports, has been reported

so far. The defects considered in studies have been on the outside of pipes, no inside defect has been considered even in numerical simulations. A few studies have shown the detection of multiple circumferential defects machined not along the same line of sight. There are no studies that report detection of multiple axial and circumferential defects, circular holes, wear scars and combination of these defects along the same line of sight. It is also seen that different modes are chosen depending on the nature of defects, that is to say that a mode chosen for detecting axial defects may not be suitable for circumferential defects. Moreover, there has been no study that reports the influence of multiple bends on L(0,2) mode and detection of multiple defects in bends (multiple bends). Besides, the frequency used for long-range testing is less than 100 kHz and the sizes of defects considered were large and they were based on the industrial need.

Furthermore, as discussed previously, the excitation of guided waves in SG tubes of PFBR can be only from ID side of the tubes due to constraints in accessibility and it should be couplant-free. This indicates that the only possibility of such an excitation is through magnetostriction, as the SG tubes of PFBR are ferromagnetic. It can be seen in the literature that there are only a few studies that discuss non-contact generation of guided waves from the ID side of the tube. Most of the magnetostrictive transducer-based inspection are carried out from the OD sides of tubes. Thus far, in-bore magnetostrictive transducers for torsional modes and longitudinal modes have been developed for tubes larger than 19 mm ID. No commercial magnetostriction based guided wave transducer for examination of the tube with the ID of 12.6 mm is available. Hence, an in-bore magnetostriction, for the present application, needs to be developed. Furthermore, information pertaining to the design of coils, optimization of coil parameters and the placement of coils is scarce in the open domain. Moreover, there is

no ready-made software package available for the magnetostriction problem for the generation of ultrasonic guided waves.

The present study aims at using a single mode  $L(0,2)$  at 250-350 kHz for long range propagation and detection of multiple circumferential defects, axial defects, pinholes, wear scars and sodium impingement damage as well. The same mode  $L(0,2)$  will also be used for the bent segment of an SG tube for detection of defects. The study also aims at achieving the required sensitivity for all the defects. The study also involves carrying out finite element simulation to gain insight into the nature of the mode, its propagation, interaction with multiple defects in the same line of sight and finally, the design of an in-bore magnetostrictive transducer for the generation of  $L(0,2)$  mode from the ID side of the tube.

The study of multiple defects in the context of SG tubes is meaningful for the reasons, as explained below: (a) given the 23 m length of an SG tube of PFBR, there is a possibility of occurrence of multiple defects along its length, (b) error in locating a defect in multiple defect scenario, (c) to gain insight into interaction of  $L(0,2)$  mode with different defects and mode conversion, (d) spatial resolution that can be achieved and (e) the effect of shadowing of one defect by another. The dimensions of the defects considered in the study are much smaller than that reported in the literature.

Another major challenge encountered is the development of an in-bore magnetostrictive transducer for the generation of  $L(0,2)$  mode in the steam generator tubes of PFBR for the ID of 12.6 mm, which has not been reported so far, and its placement beyond the spigot weld. All the above are the motivating factors for the thesis with the need for development of a suitable transducer, technique and inspection methodology for SG tubes of PFBR and to address the missing elements in the literature. The overall objective of the study is to develop

a suitable guided wave-based inspection methodology and to develop an ultrasonic longitudinal guided wave mode in-bore magnetostrictive transducer for the inspection of SG tubes of PFBR meeting certain requirements. The scope of the investigation and specific objectives of the thesis are thus set as follows:

- ❖ optimization of a guided wave mode for a long-range propagation of 46 m (up and down travelling distance of the guided waves) using ultrasonic transducers in the frequency range of 250-500 kHz,
- ❖ detection (means sensitivity of detection not sizing, which applies throughout the thesis) of 10% WT deep circumferential, 10% WT deep axial defects, 2.3 mm diameter through-pinholes and 10% WT deep (max.), 15 mm length and 27 mm circumferential tapered defects, 40% WT deep, 8.6 mm long, 7.74 mm wide sodium impingement damage,
- ❖ detection of flaws in thermal expansion bends,
- ❖ studying the influence of the thermal expansion bend on L(0,2) mode using FE models,
- ❖ studying the influence of the tubesheet and spigot on L(0,2) mode using axisymmetric FE models
- ❖ design and the development of an in-bore magnetostrictive transducer for the generation of L(0,2) guided wave mode in the frequency range of 250-350 kHz,

- ❖ to propagate the L(0,2) mode for a distance of 46 m (up and down travel in an SG tube) using the magnetostrictive transducer,
  
- ❖ to demonstrate the detection sensitivity as per the requirement mentioned above,
  
- ❖ detection of circumferential grooves in the SG tubes of a mockup SG test facility with the SG tubes welded to a tubesheet through a spigot weld using the in-house developed in-bore magnetostrictive transducer and
  
- ❖ improving SNRs of defect signals using denoising techniques.

## ***Chapter 3. General Methods: Experiments and Simulation***

### **3.1 Chapter overview**

This chapter covers the details of the experimental set-ups, finite element simulation and the SG tube specimens used. First, the experimental set-ups used for the generation and reception of an ultrasonic longitudinal guided wave in SG tubes using ultrasonic transducers and an in-house developed in-bore magnetostrictive transducer are presented. Then, Disperse software used for the generation of dispersion curves and the parameters used for the thesis are discussed. Furthermore, the details of the SG tube specimens used along with the dimensions and locations of defects considered are presented. The chapter also gives a brief description about the finite element simulation software ABAQUS and COMSOL Multiphysics. The details of the FE models of SG tubes such as dimensions, properties, mesh, elements and spatial and time steps are presented. Finally, the coupling of acoustic and electromagnetic equations using COMSOL for the magnetostriction based generation of longitudinal guided waves is also discussed.

### **3.2 Experimental set-up**

Figure 3.1a shows the photograph of the experimental set-up in which an ultrasonic transducer is coupled to one end of an SG tube segment and Fig. 3.1b is schematic of the experimental set up. Figure 3.2a shows the photograph of an in-bore magnetostrictive transducer developed in-house and Fig. 3.2b shows the photograph of the experimental set up in which the in-bore magnetostrictive transducer is inserted into an SG tube segment. Figure 3.2c shows the in-

bore magnetostrictive transducer inserted in a tubesheet hole of the mockup SG setup. Figure 3.2d shows the schematic of the experimental set up.

To generate the L(0,2) mode, an ultrasonic broadband transducer (M/s. Panametrics) of center frequency 250 kHz and the diameter of 40 mm was directly coupled to the one end of the tube and excited by a high power pulser-receiver (Ritec rpr-4000), using a 5-cycled toneburst.

The signals received were transferred to the oscilloscope through the pulser-receiver. The oscilloscope used was of 12-bit resolution and 350 MHz bandwidth. The signals were then sampled at 2.5 MHz, averaged 16 times and stored as ASCII data for post-processing. All the experiments were carried out along the same lines.

As the mode L(0,2) is axi-symmetric, the symmetric coupling of an ultrasonic transducer on the end face should be ensured. To achieve this, the transducer axis was made coincident with the axis of the tube during the end coupling of the ultrasonic transducer.

To generate the L(0,2) mode using the principle of magnetostriction, an in-bore magnetostrictive transducer (developed in-house as discussed in Chapter 5 of the thesis) of center frequency 300 kHz was inserted in one end of an SG tube segment. For efficient generation of L(0,2) mode, the magnetostrictive transducer axis and the axis of the tube should be in co-incidence. This was achieved by providing rubber O-rings to the transducer during the examination of tubes.

The transmitter coil was excited by a high power pulser-receiver (Ritec rpr-4000), using a 5-cycled toneburst. The signals were picked up by a receiver coil placed 10 mm apart from the transmitter coil and sent to the oscilloscope through the pulser-receiver. The signals were then sampled at 3.5 MHz, averaged 64 times and stored as ASCII data for post-processing. All the

experiments were carried out in the same manner. The excitation voltage was set to 100 V. The bandpass filter used was 50 kHz-1.6 MHz.

Figure 3.3 shows the photograph of the strain measurement system in which a strain gauge of length 10 mm and width 4 mm was pasted on an SG tube segment of length 100 mm. The instrument is capable of providing strain directly. The static magnetostrictive strains generated by the insertion of permanent magnets of different strengths (1 T and 1.48 T) into the tube segment were measured using the strain gauge and subsequently, piezomagnetic coefficient (S) was calculated.

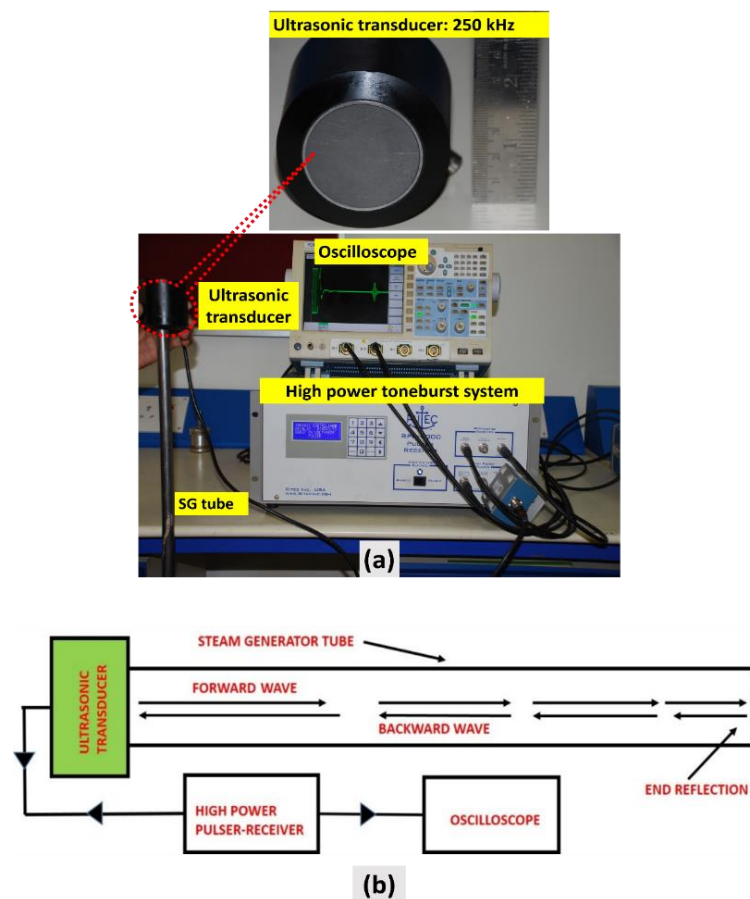


Fig. 3.1 (a) Photograph of experimental set-up with an ultrasonic transducer coupled to the end of an SG tube and (b) schematic of the experimental set-up.

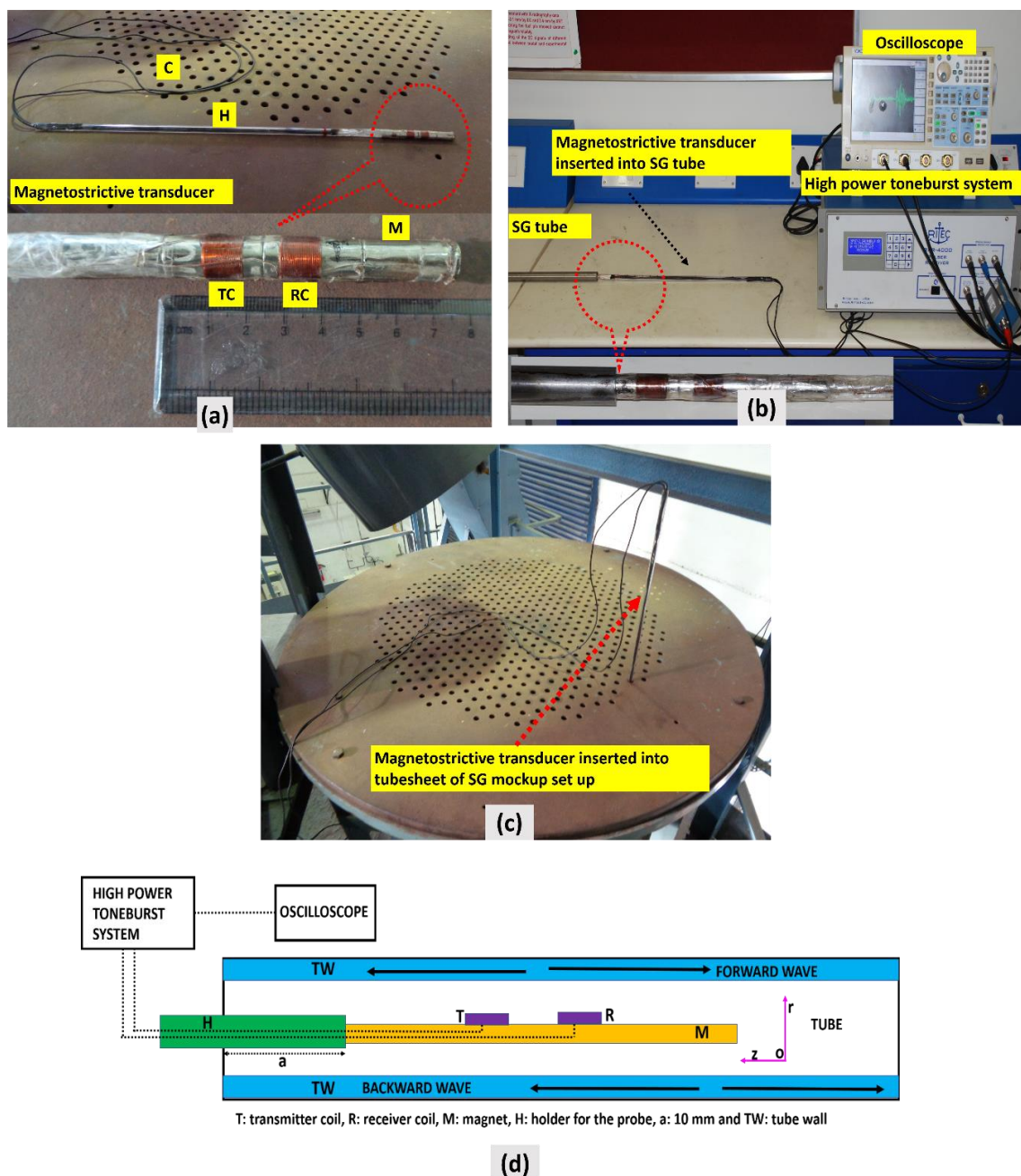


Fig. 3.2 (a) Photograph of in-house developed in-bore magnetostrictive transducer, (b) photograph of the experimental set-up with the magnetostrictive transducer inserted into an steam generator tube segment, (c) photograph showing the in-bore magnetostrictive transducer inserted in a tubesheet hole of the mockup SG setup and (d) the schematic of the experimental set-up.

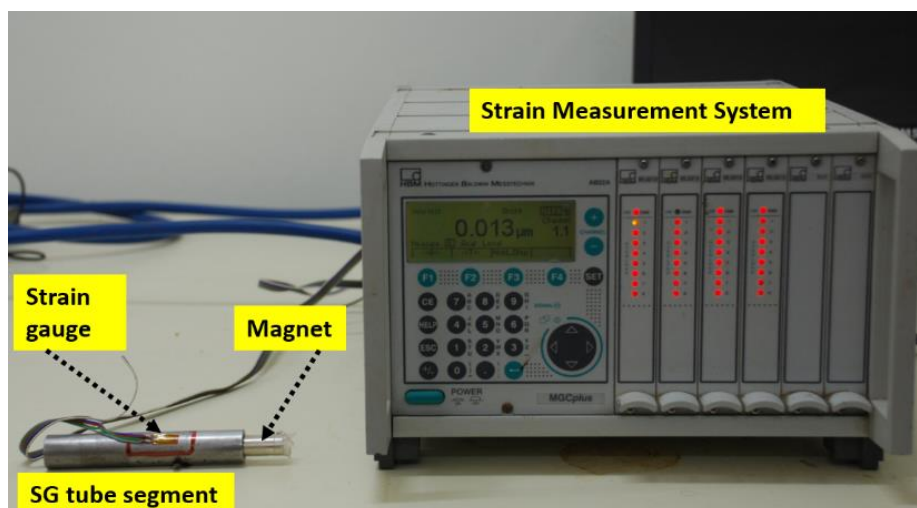


Fig. 3.3. Photograph of the experimental set-up for magnetostrictive strain measurement.

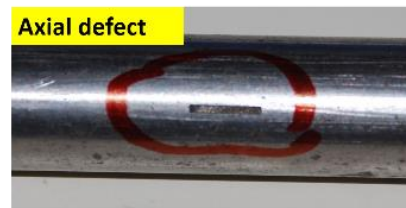
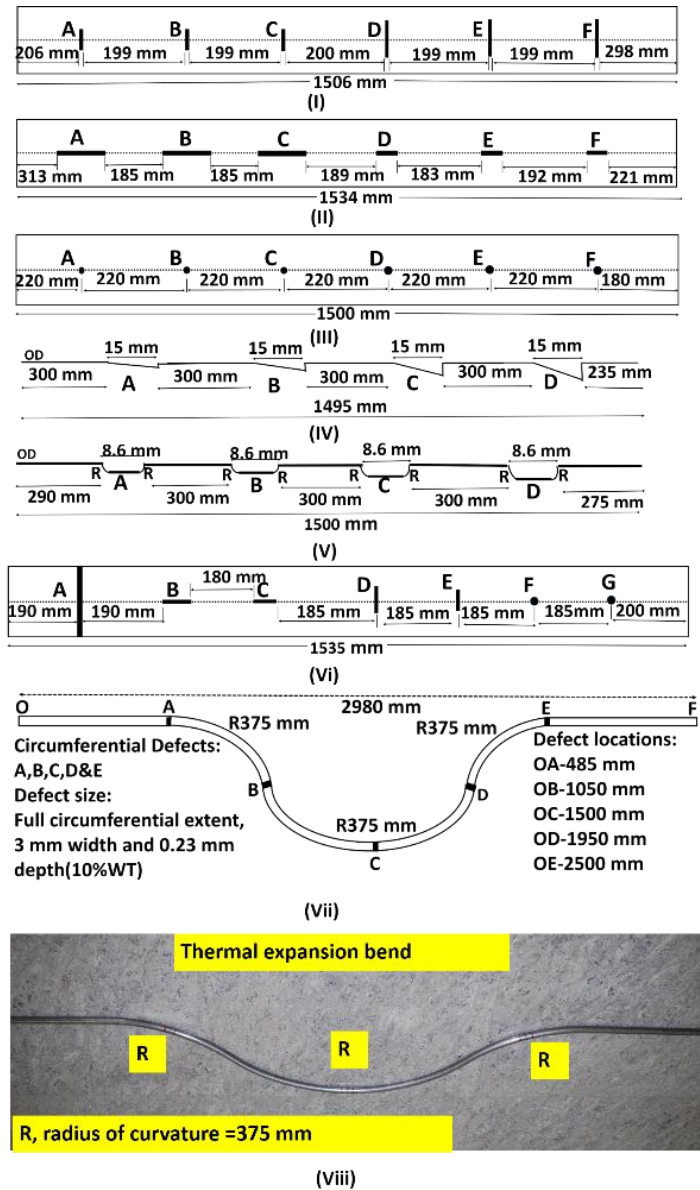
### 3.3 Specimen details

The four types of defects that can possibly occur in steam generator (SG) tubes are circumferential and axial defects due to stress-corrosion cracking [158, 159], pinholes due to pitting corrosion [160] and tapered defects due to fretting [161]. A pinhole in this dissertation is considered as a cylindrical defect of smaller diameter (1-2 mm) and length (0.46-1.86 mm) as compared to the wall thickness (2.3 mm) of the SG tube. A circumferential defect is considered as a defect whose circumferential length (7 and 15 mm) is larger than the wall thickness and the width (1 mm) is much smaller than the wall thickness (2.3 mm) of the SG tube. An axial defect is considered as a defect whose axial length (7 and 15 mm) is larger than the wall thickness of the SG tube and the width (1mm) is smaller than the thickness (2.3 mm). The dimensions of the defects are shown in Table 3.1. The dimensions of the defects are chosen in accordance with the requirement [26]. The defects were machined using the Electrical Discharge Machining (EDM) technique. In samples with multiple defects, all the

defects were chosen to lie along the same line to study shadowing effect, if any. Following were the specimens used in the thesis:

- (a) a 1 m long SG tube segment,
- (b) a 1.5 m and 3.8 m long SG tube segments for long-range testing,
- (c) a 1.5 m long tube with a full circumferential defect of depth 0.46 mm (20% WT) and width 1.5 mm located at 840 mm,
- (d) a 1060 mm long tube with a through pinhole of diameter 1.5 mm located at 600 mm,
- (e) a 1.5 m long tube with six partial circumferential defects lying along the same line,
- (f) a 1.5 m long tube with six axial defects lying along the same line,
- (g) a 1.5 m long tube with six partial pinholes lying along the same line,
- (h) a 1.5 m long tube with a combination of circumferential defects, axial defects and pinholes,
- (i) a 3 m long SG tube with a thermal expansion bend with five circumferential defects and,
- (j) mockup SG setup with 4.6 m long tubes with thermal expansion bends with full and partial circumferential defects.

The dimensions, locations and type of defects are shown in Table 3.1 and 3.2. The schematic of the tubes with various defects is shown in Fig. 3.4. The schematic of the mockup SG setup with the tubesheet, spigot welds and thermal expansion bends with defect locations is shown in Fig. 3.5.



(a)

(b)

Fig. 3.4 (a) A set of specimens used: (i) six partial circumferential defects, (ii) six partial axial defects, (iii) six partial pinholes, (iv) four tapered defects, (v) four sodium impingement defects, (vi) a combination of circumferential, axial and pinhole defects, (vii) thermal expansion bend and (viii) photograph of a thermal expansion bend and (b) photographs of circumferential, axial and pinhole defects. The dimensions and locations of the defects are given in Table 3.1.

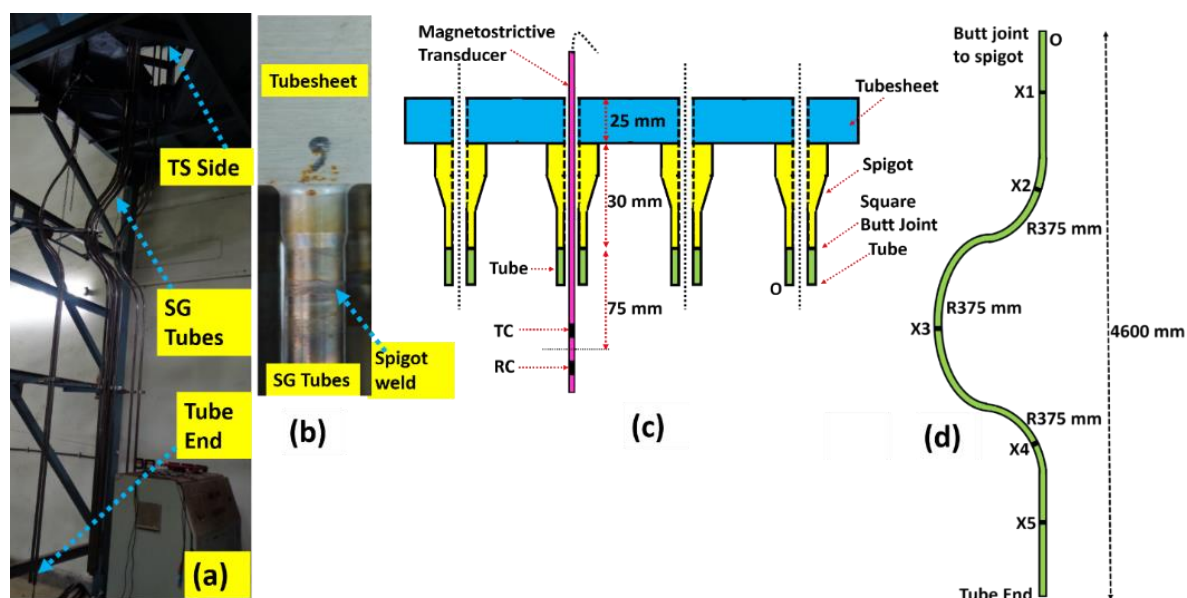


Fig. 3.5 (a) Photograph of mockup steam generator (SG) test facility, (b) photograph of tube-to-tubesheet joints with spigot welds, (c) side view of tubesheet with SG tubes and (d) schematic of a mockup SG tube in the mockup SG test facility. TS: Tubesheet, TC and RC: transmitter and receiver coils of length 10 mm each. X1-X5 stand for half and full circumferential grooves, as given in Table 3.2.

Table 3.1. Types of defects, locations and their dimensions in SG tube segments

S. No.	Defect label	Circumferential defects (1 mm width)			Axial defect (1 mm width)			Pinhole defects (partial)			Tapered defects (27 mm CE, 15 mm AL)		Locations of Circumferential defects in thermal expansion bend, mm (CE 360 deg, width 3 mm and 0.23 mm depth)	Sodium impingement defects with the radius of curvature: 3.175 mm				Sodium impingement defects with the radius of curvature: R= 3.175 mm				Combination of circumferential defect (CD), axial defect (AD)&pinholes (PH)
		CE, mm	D, mm	OL, mm	AL, mm	D, mm	OL, mm	Dia. mm	D, mm	OL, mm	D, mm	OL, mm		D, mm	AL, mm	W, mm	OL, mm	D, mm	AL, mm	W, mm	OL, mm	
1	A	7	0.23	206	15	0.69	313	1	0.92	220	0.23	300	485	0.23	8.6	3.9	294.3	0.23	8.6	3.9	600	CD: Full, 3 mm width, 0.23 mm D
2	B	7	0.46	406	15	0.46	513	1	1.38	440	0.46	615	1050	0.46	8.6	5.55	602.9	0.69	8.6	6.75	600	AD: 10 mm AL, 2 mm Width, 0.92 mm D
3	C	7	0.69	606	15	0.23	713	1	1.84	660	0.69	930	1500	0.69	8.6	6.75	911.5	1.15	8.6	8.6	600	AD: 10 mm AL, 2 mm Width, 1.38 mm D
4	D	15	0.23	807	7	0.69	917	2	0.46	880	0.92	1245	1950	0.92	8.6	7.74	1220.1	1.61	8.6	10	600	CD:10mm CE, 3 mm Width, 0.92 mm D
5	E	15	0.46	1007	7	0.46	1107	2	0.92	1100	-----	-----	2500									CD:10mm CE, 3 mm Width, 1.38 mm D
6	F	15	0.69	1207	7	0.23	1306	2	1.38	1320	-----	-----	-----									PH: 3 mm dia., 0.92 mm D
7	G																					PH: 3 mm dia., through-and-through hole

CE: Circumferential extent, D: depths of axial, circumferential, pinhole, sodium impingement and tapered defects, AL: axial length of axial and tapered defects, Dia.: diameters of pinholes and OL: locations of the respective defects w.r.t. the left ends of the tubes. CD: Circumferential defect, AD: Axial defect and PH: pinholes. All the defects were made on the outer dia.(OD) of the tubes.

**Table 3.2. Circumferential defects, locations and their dimensions in mockup SG test facility**

S. No.	Tube Label	Defect Label	Dimensions and locations of circumferential defects			
			CE, mm	W, mm	D, mm	Locations of defects (OL), m
1	T#1	A1-A5	54	1	0.69	0.825, 1.82, 2.27, 2.68 and 3.9
2	T#2	B1-B5	54	1	0.46	0.825, 1.82, 2.27, 2.74 and 3.73
3	T#3	C1-C5	54	2	0.23	0.825, 1.82, 2.240, 2.74 and 3.77
4	T#4	D1-D5	27	1	0.69	0.825, 1.82, 2.28, 2.74 and 3.77
5	T#5	E1-E5	27	1	0.23	0.825, 1.84, 2.280, 2.74 and 3.74
7	TR is a tube for reference					
CE: Circumferential extent, D: depths of circumferential defects, W: width of circumferential defects and OL: locations of the respective defects w.r.t top of the tubesheet,						

## 3.4 Generation of Dispersion curves

### 3.4.1 Disperse Software

Disperse software has been developed by Imperial College, London for generating dispersion curves [162]. The software has the capability of handling a range of materials, which can be isotropic or anisotropic. It can generate dispersion curves for specimens (under various conditions) such as plates, loaded plates, multilayered structures, solid cylinders and hollow tubes. The input parameters include material properties such as density, Young's modulus and Poisson's ratio. In addition, the thickness of a specimen and the loading, if any, can be provided. The routine has automatic tracing and manual tracing features wherein any desired curves, for instance, fundamental and higher order Lamb wave modes in plates and tube modes such as longitudinal, torsional and flexural can be traced. The display can be of phase velocity versus frequency-thickness products and group velocity versus frequency-thickness products. The plots can be made in terms of angle of incidence as well. In the case of loaded

specimens, attenuation versus frequency/group velocity curves can be obtained for individual modes. It is this feature that makes it very attractive when selecting a less attenuating mode for inspection. The software also has the provision for displaying mode shapes, stresses generated by modes, power flow and strain energy density. There are also animated displays of modes to enhance our understanding. In general, the shape of a wave packet of dispersive signals changes as it propagates. To visualize this, it has a feature with a range of excitation signals with a tunable number of cycles in a wave packet. The wave packet can be modulated by window functions such as Hanning, Hamming, Gaussian, rectangular, triangular, taper, flat top sin etc., to control the bandwidth. Once a mode is chosen, its propagation characteristics for various distances can be studied. There is also a provision for visualization of interference of modes that can possibly be excited for a given band of frequencies.

For this dissertation, the dispersion curves for an SG tube of PFBR made of Mod. 9Cr-1Mo ferritic steel were generated using Disperse software. The inner and outer radii of an SG tube are 6.3 mm and 8.6 mm, respectively and the wall thickness is 2.3 mm. The density of 7800 kg/m<sup>3</sup>, Young's modulus of 220 GPa, the Poisson ratio of 0.2805 were used [163]. The dispersion curves were generated using the above parameters for an SG tube of PFBR. The curves were obtained by specifying air interfaces at the inner and outer interfaces of the tube. The dispersion curves generated depend on the elastic properties, inner radius and the wall thickness.

## **3.5 Finite element (FE) simulation details**

### **3.5.1 3D-FE models developed in FE simulation software ABAQUS**

ABAQUS is a commercial software for performing finite element analysis (FEA) [164]. It provides a complete environment for defining geometry, materials, loads, contact conditions,

boundary conditions and mesh. The main advantage is the capability of the software to handle complex geometries. There are separate modules for each of the steps. It also has a module for visualization of results. ABAQUS can handle static and quasi-static stress analyses, buckling and collapse analyses, forming analyses, fracture and damage, dynamic stresses, tire and vehicle analyses, crash analyses, eigen frequency/mode analyses, mechanisms, heat transfer and thermal-stresses, fluid dynamics, fluid structure interaction, simple electromagnetic analysis, mass diffusion, acoustic and shock analyses, soil analyses etc. Researchers in the field of NDT have used ABAQUS for elastic (ultrasonic) wave propagation in structures and many applications have been benchmarked. This fact provided the motivation for using ABAQUS for the generation of ultrasonic guided waves in tubes, for the dissertation. Ultrasonic wave propagation problems are solved using both implicit and explicit methods, as mentioned in Chap. 2. In the present dissertation, the finite element simulation software ABAQUS/Explicit was used to simulate the wave propagation utilizing explicit time domain algorithm. The FE models developed are as follows:

- (a) L(0,2) mode propagation in a 1.0 m and a 3.0 m long steam generator tubes,
- (b) 1.5 m long tubes with six OD circumferential defects, six OD axial defects, six OD pinholes of various dimensions, four sodium impingement damage and four tapered defects,
- (c) 750 mm long tube with a pinhole at ID and OD at 375 mm,
- (d) L(0,2) mode propagation in a 1.0 m long SG tube with full circumferential defects of depth 0.92 mm and width 1 mm at one of the following locations in each simulation: 250 mm, 350 mm, 400 mm, 450 mm, 500 mm, 550 mm, 650 mm and 750 mm,
- (e) Further, to study the shadowing effect of a defect on the signal amplitude of a neighbouring defect, a circumferential defect was fixed at 250 mm and the other circumferential defect was placed at one of the following locations in each simulation: 252

mm, 257.5 mm, 260 mm, 275 mm, 300 mm, 325 mm, 350 mm, 400 mm, 450 mm, 500 mm, 550 mm, 650 mm and 750 mm,

(f) L(0,2) mode propagation in a 3 m long tube with a thermal expansion bend and

(g) pinholes at the extrados and intrados of a 3 m long tube with a thermal expansion bend.

The locations and the dimensions of the defects are mentioned in Table 3.1

The properties used for FE analysis were the density  $7800 \text{ kg/m}^3$ , Young's modulus 220 GPa and the Poisson ratio 0.28. The spatial step was chosen as  $1/30^{\text{th}}$  of the wavelength ( $\lambda=13 \text{ mm}$ ) of the shear wave at 250 kHz which is 0.45 mm and the time step of  $10^{-8} \text{ s}$  was chosen based on the time required for the longitudinal wave velocity ( $C_L$ ) of 6008 m/s to travel the spatial step of 0.45 mm. The time step was chosen smaller than the critical time step based on Eq. (2.45) in Chap. 2. Both time and spatial steps were sufficient for convergence.

The wavelength of the mode L(0,2) at 250 kHz is 21.5 mm and hence, there are nearly 50 elements across one wavelength. The number of through-thickness elements was chosen to be 6. Figures 3.6a and b show the FE model of an SG tube with excitation and reception location at one end of the tube and the excitation signal of a five cycle hanning windowed toneburst at the center frequency of 250 kHz. To excite L(0,2) mode, this excitation pulse was applied axi-symmetrically on the end face of the tube, as an axial displacement ( $U_z$ ). In addition, a five cycle hanning windowed toneburst of center frequency 300 kHz was also used. The spatial and time steps were chosen along the similar lines. All the FE programs were run in two steps, namely the excitation step and the wave propagation step in ABAQUS/Explicit solver.

Figure 3.7 shows various defects modelled in SG tubes in ABAQUS. The mesh elements used in the FE models were four-node linear tetrahedron (C3D4), eight-node linear brick with

reduced integration (C3D8R) and six-node linear triangular prism (C3D6) elements. Figure 3.8 shows the meshes used in the FE models.

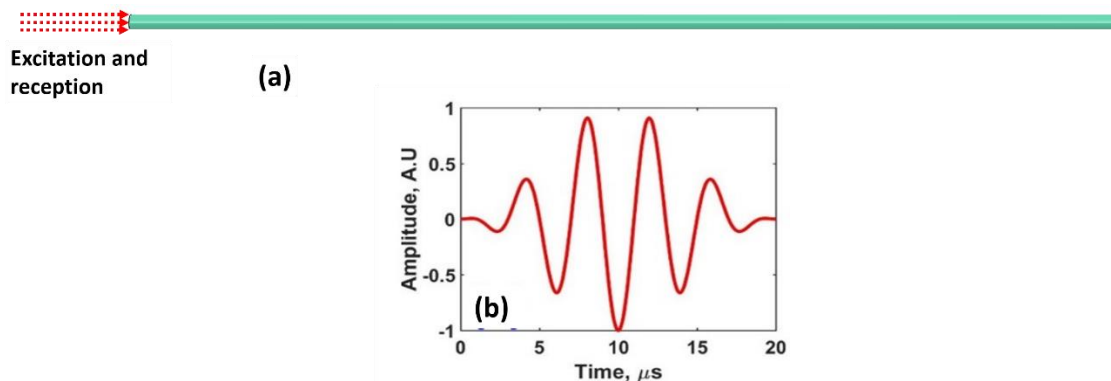


Fig. 3.6. ABAQUS finite element model: (a) Excitation along z-axis of a steam generator tube and (b) excitation signal used in finite element simulation.

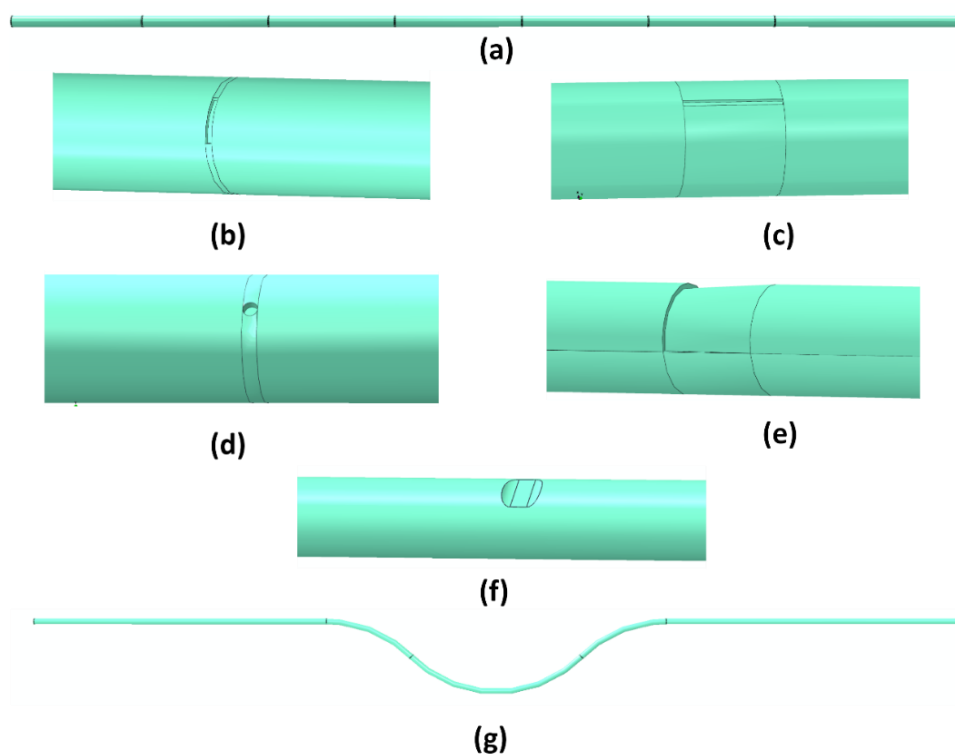


Fig. 3.7. ABAQUS finite element models with defects in steam generator tubes: (a) defects considered in the same line, (b) partial circumferential defect, (c) axial defect, (d) partial pinhole, (e) tapered defect, (f) sodium impingement damage and (g) thermal expansion bend.

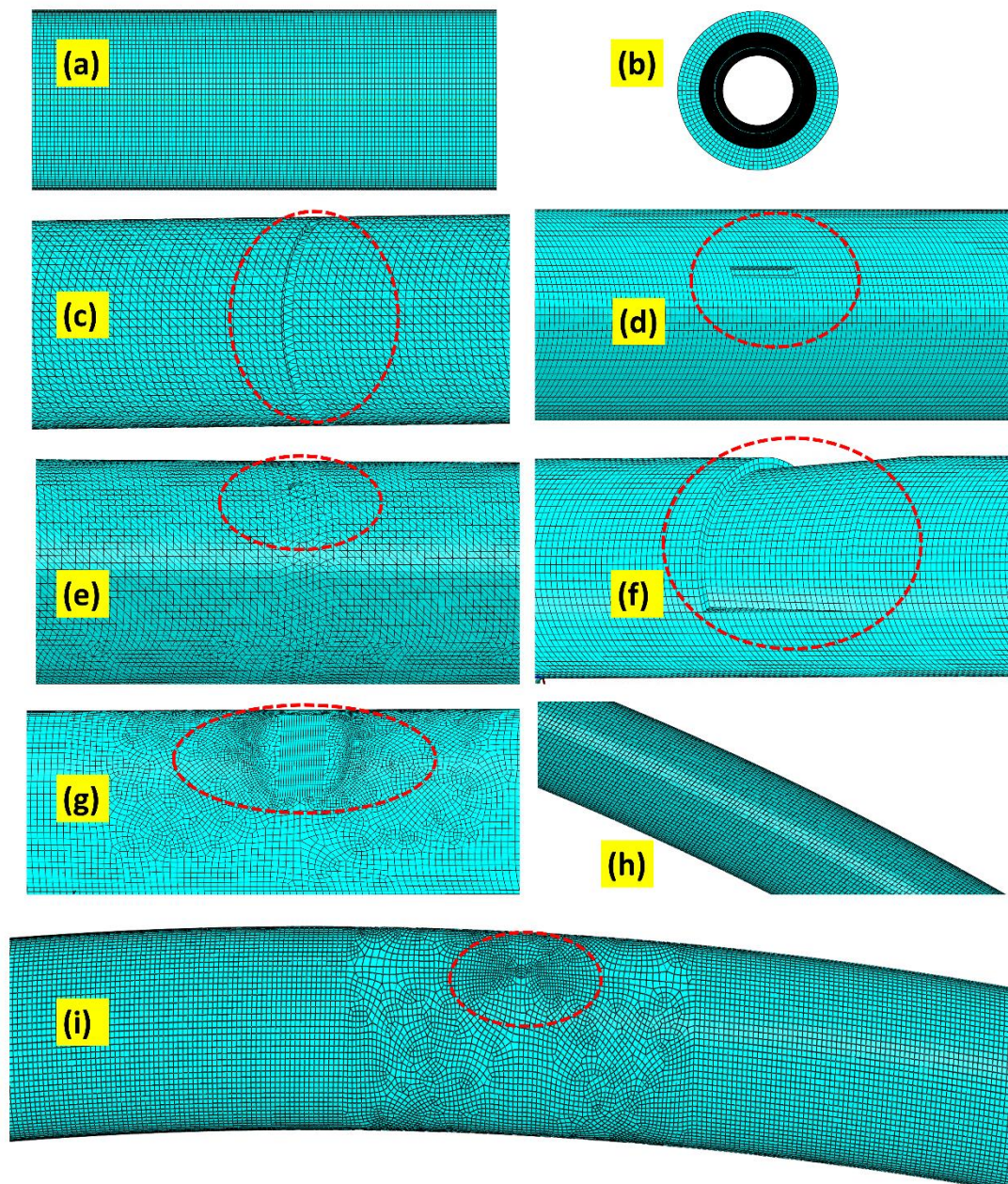


Fig. 3.8. Mesh details: (a) defect-free tube with hexahedral mesh, (b) tube end mesh, (c) circumferential defect with tetrahedral mesh, (d) axial defect with hexahedral mesh, (e) pinhole with triangular prism mesh, (f) tapered defect with triangular prism mesh, (g) sodium impingement damage with hexahedral mesh, (h) thermal expansion bend with hexahedral mesh and (i) thermal expansion bend with a pinhole with hexahedral mesh.

### 3.5.2 FE models developed in FE simulation software COMSOL

COMSOL Multiphysics is a finite element analysis-based software, which gives different interfaces for physics-based users [165]. The applications handled by COMSOL include solid mechanics, electromagnetic problems, thermal analysis, fluid mechanics etc. The major advantage of the software is coupling of different physical phenomena. Besides, it also has the provision for feeding in complex partial differential equations and boundary conditions.

#### 3.5.2.1 2D-axi-symmetric FE modelling of tubesheet-spigot SG tube structures

2D-axisymmetric FE models of tubesheet-spigot structures were developed and studied in COMSOL because low reflection boundaries can be implemented readily in the model and they are essential in understanding the role of boundaries in reflection. Figures 3.9a and b show the axi-symmetric FE models of tubesheets of thickness 25 mm and 150 mm with tubesheets and spigots, respectively

The tubesheets of 25 mm and 150 mm thicknesses correspond to the ones of the mockup SG setup and actual SGs of PFBR, respectively. The axi-symmetric FE simulations were performed for the cases with low reflecting boundary (LRB) at the right edges of the tubesheets. Besides, for the case of 25 mm thick tubesheet, LRB at the top and right edges of the tubesheet was also imposed. The elements used were quadrilateral elements. The time and spatial steps used were  $3 \times 10^{-8}$  s and 1 mm and they were determined by the Courant–Friedrichs–Lewy (CFL) number, as given by Eq. (2.47) in Chap. 2. For the present study, CFL used was 0.18. Both steps were seen to be sufficient for convergence. The relative tolerance used in the model was  $10^{-8}$ .

The excitation of center frequency of 300 kHz with a five cycle Hanning windowed toneburst was provided at the bottom end (Fig. 3.9c). A receiver point named R1 in Figs. 3.9a and b was used in the models to record the axial displacement ( $U_z$ ). R1 is located at 200 mm from the excitation end. Additionally,  $U_r$  (radial) and  $U_z$  (axial) components were also recorded at R2 and R3 in 150 mm thick tubesheet model. R2 and R3 are located at 960 mm and 930 mm, respectively from the excitation end.

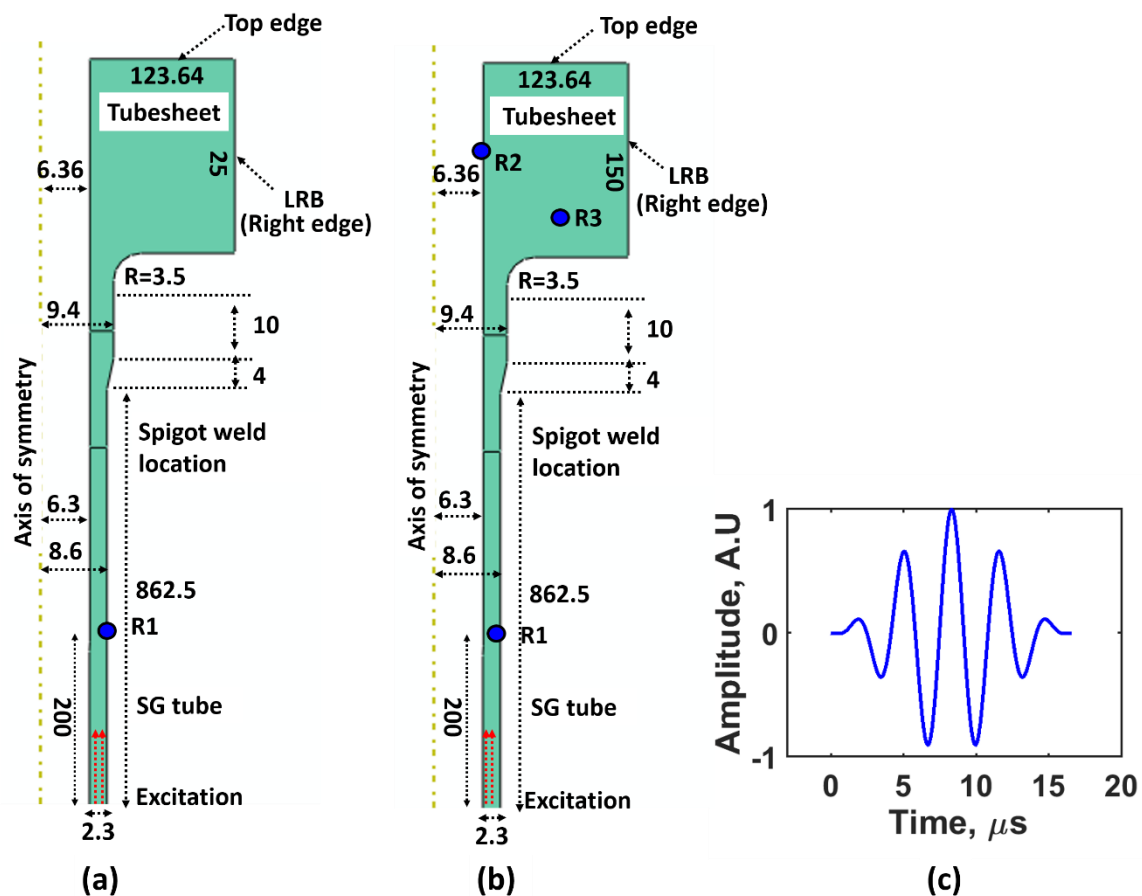


Fig. 3.9. 2D-axisymmetric finite element models: (a) tubesheet of thickness 25 mm, as in tubesheet of the mockup steam generator, (b) tubesheet of thickness 150 mm, as in the actual tubesheet of the Prototype Fast Breeder Reactor and (c) excitation signal of 300 kHz center frequency. The only difference in Figs. 3.9a and b is the tubesheet thickness, which is 25 mm in Fig. 3.9a and 150 mm (not shown to the scale) in Fig. 3.9b. R1, R2, and R3 are receivers located at 200 mm, 960 mm and 930 mm, respectively from the excitation end. In Figs. 3.9a and b, all the dimensions are in mm.

### 3.5.2.2 Finite element modelling of in-bore magnetostrictive transducer for L(0,2) mode generation, propagation and reception in FE simulation software COMSOL

The fundamental idea behind the in-bore magnetostrictive FE model is to insert the coils wound on permanent magnets into the ID of an SG tube and excite them with the time varying current. This in turn will generate a time varying magnetic field to which ID side of the tube is exposed. The region exposed to the magnetic field will introduce dynamic strains, which in turn will generate the desired mode. The mode L(0,2) is axi-symmetric. Hence, an axi-symmetric FE model for generating L(0,2) guided wave mode from the ID side of the tube based on magnetostrictive phenomenon was developed. The objectives of the FE models are to optimize the dimensions of the transmitter and receiver coils and to design an in-bore magnetostrictive transducer for L(0,2) mode generation based on the FE results.

A magnetostrictive phenomenon involves coupling of applied magnetic fields to stresses generated in a specimen. The coupling can be achieved using COMSOL as it has the provision for coupling both magnetic and acoustic phenomena. To be specific in the FE model, AC/DC and solid mechanics modules were coupled for guided wave generation (Joule effect) and solid mechanics and AC/DC modules were coupled for wave reception (Villari effect). COMSOL utilizes implicit algorithm, as discussed in Chap. 2. 2D-axi-symmetric magnetostrictive FE models were sequentially developed as follows:

(1) First, an axi-symmetric model of an SG tube segment of length 200 mm was designed.

Then, an axisymmetric model of a permanent magnet of length 50 mm was made on the ID of the tube. Finally, the entire model was enclosed in a 2D- air box of dimensions: 300 mm x 250 mm. The triangular elements were used with varying size from 0.08 mm to 2

mm. Towards, optimizing the diameter of the magnet, the diameter ( $D$ ) was varied from 2 mm to 12 mm in the step of 2 mm and stationary analysis was carried out. The B-field generated by the magnet was obtained along the central line of the tube for the length of 20 mm. Finally, with the optimized diameter, the length ( $L$ ) of the magnet was varied from 25 mm to 150 mm in the step of 25 mm. With the B-field in the tube wall, the length of the magnet was optimized. The schematic of the model with dimensions and different domains is given in Fig. 3.10a.

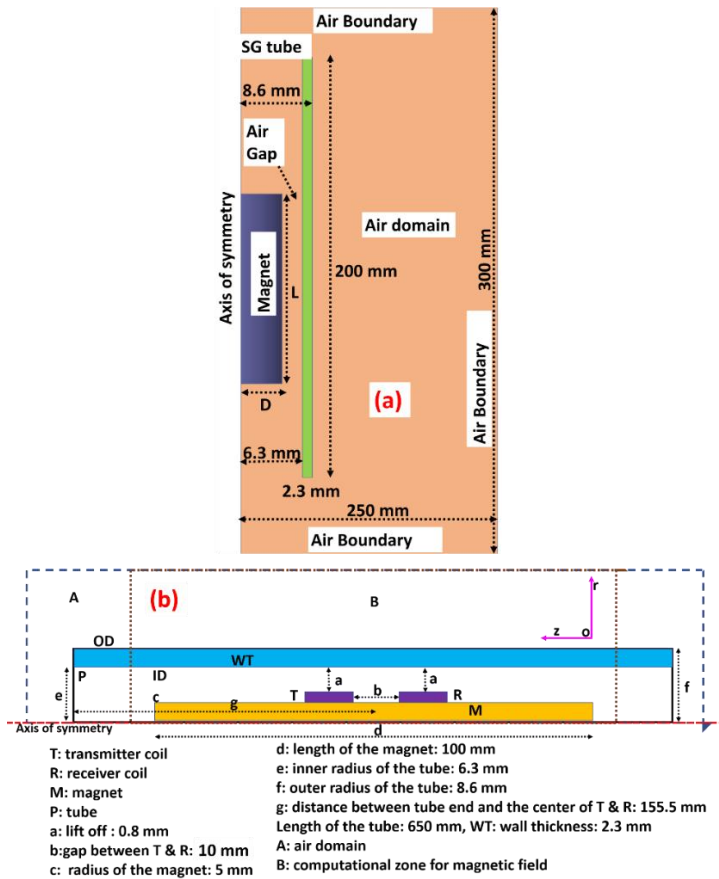


Fig. 3.10 (a) Schematic of the finite element axi-symmetric model for optimizing diameter and length of the magnet and (b) 2D-finite element axisymmetric model of an in-bore magnetostrictive transducer with optimized magnet dimensions and coil parameters.

(2) Secondly, with the permanent magnet of optimized dimensions, an axi-symmetric model of an SG tube segment of length 650 mm was designed with the magnet on the ID of the tube. Towards performing dynamic analysis for L(0,2) mode generation and reception, 2D-axisymmetric transmitter and receiver coils were included in the model. The transmitter coil was placed at 147.5 mm from one end of the tube. The receiver coil was placed at 167.5 mm from the end of the tube. The distance between the coils was 10 mm. Finally, the entire model was enclosed in a 2D-air box of dimensions: 700 mm x 100 mm. Figure 3.10b shows the schematic of the model with the optimized dimensions of the magnet and coils.

(3) Axi-symmetric models along the same lines with a 1.0 m long tube were designed for validating FE amplitudes with the experimental amplitudes of the tube end reflections for frequencies in the range of 250 kHz-350 kHz. The distance between the center of the transmitter-receiver coils to the near end of the tube was set at 57.5 mm and,

(4) Finally, an axi-symmetric model with a full circumferential defect of depth 0.46 mm and width 1.5 mm in a 1.5 m long tube was designed. The distance between the center of the transmitter-receiver coils to the near end of the tube was set at 90 mm.

The models were assigned the electrical and elastic properties in the respective regions, as given in Table 3.3. The tube was meshed with quad elements of size 1 mm. The coils, intervening space between the coils and the tube, and 0.6 mm layer ID of the tube was meshed with quad elements of size 0.01 mm to capture skin effect in the tube. There are nearly 18 elements across the wavelength and 10 elements across the thickness of the tube. The air

domain was meshed with triangular elements of size 0.2 mm-5 mm. The time and spatial steps used were  $3 \times 10^{-8}$  s and 1 mm and they were determined by the Courant–Friedrichs–Lewy (CFL) number, as given by Eq. (2.47) in Chap. 2. Accurate results are obtained when CFL is less than 0.2. For the present study, CFL used was 0.18. Both steps were seen to be sufficient for convergence. The relative tolerance used in the model was  $10^{-8}$ . To excite L(0,2) mode, a five cycle Hanning windowed toneburst of 1 A peak current at 300 kHz center frequency was applied to the transmitter coil, as shown in Fig. 3.11. The problem was solved using the implicit method, as mentioned in Chap. 2

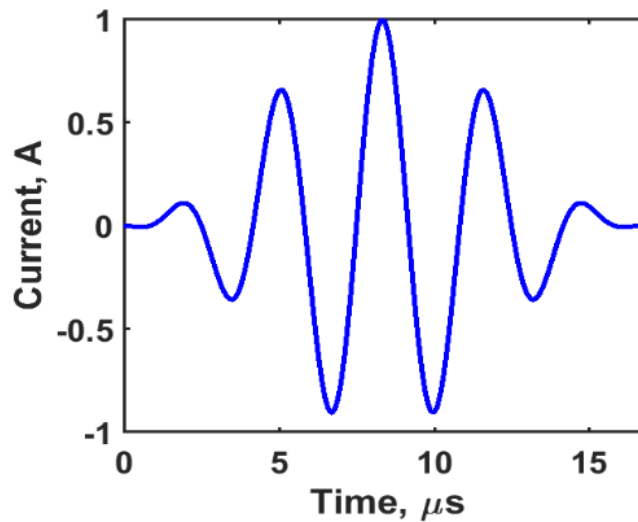


Fig. 3.11. Excitation with center frequency at 300 kHz

Table 3.3. Parameters used in COMSOL FE models

Object	Parameters	Value
SG tube (Mod. 9Cr-1Mo steel)	Electrical conductivity	1.5e6 S/m
	Relative permittivity	1
	Density ( $\rho$ )	7800 kg/m <sup>3</sup>
	Young's modulus (E)	220 GPa
	Poisson's ratio ( $\nu$ )	0.28
	Inner diameter	12.6 mm
	Outer diameter	17.2 mm
	Wall thickness	2.3 mm
	Length	650 mm
Transmitter (TC) & Receiver coils (RC)	Relative permittivity	1
	Relative permeability	1
	Electrical conductivity	5.9e7 S/m
	Gauge used for coils	34 SWG (=0.2337 mm)
	TC & RC length (different combinations studied)	4.5 mm, 10 mm, 13.5 mm, 18 mm and 22.5 mm
	Lift-off (gap between coils and ID of the tube)	0.83 mm
Bias: Permanent Magnet (Neodymium)	Relative permittivity	1
	Relative permeability	1
	Electrical conductivity	0.667e7 S/m
	Strength	1.48 T
	Dimensions	Dia. used: 2, 4, 6, 8, 10 and 12 mm and Length used: 25, 50, 75, 100, 125 and 150 mm
Air	Relative permeability	1
	Electrical conductivity	1e-4 S/m
	Relative permittivity	1

### 3.5.2.2.1 Analyses used in COMSOL for L(0,2) mode generation, propagation and reception

- Static analysis:** The magnetic field strength of the permanent magnet used in the present study was measured in air as 1.48 T in the axial direction using a Hall probe. To obtain the magnetic permeability matrix, as given in § 2.2.2.1 in Chap. 2, in the SG tube due to the presence of permanent magnets of strength 1.48 T inside the tube, ‘Magnetic field no current node’ in AC/DC module was used. Electrical properties (Table 3.3) and B-H curve [166] (Fig. 3.12) for the material (Mod. 9Cr-1Mo steel) of the SG tube of PFBR were provided as the input to the model. A stationary study was used to compute the stationary magnetic field in the region of the tube. The magnetic field was computed using Gauss’ law for magnetic fields, as given in Eq. (2.33). The boundary conditions used were magnetic insulation (Eq. (3.1)) and axial symmetry (Eqs. (3.2 and 3.3)) [146]. The interface between air and the ID of the tube was defined using Eqs. (3.4 and 3.5) [145] and the permeability matrix was obtained using the magnetic field in the tube.  $\bar{B}_r$  and  $\bar{B}_z$  are radial and axial components of  $\bar{B}$ ,  $\bar{H}_1$  and  $\bar{H}_2$  are magnetic field intensities in air (ID side) and the tube, respectively, and  $\bar{B}_1$  and  $\bar{B}_2$  are the magnetic field induction on the ID side and the tube,  $\bar{n}_2$  is the outward normal from the tube pointing inward and  $J_s$  is the source current density, which is zero for this case.

#### Boundary conditions:

$$\bar{n} \cdot \bar{B} = 0 \text{ (exterior air boundary)} \quad (3.1)$$

$$\bar{B}_r = 0 \text{ (axis of symmetry)} \quad (3.2)$$

$$\frac{\partial \overline{B_z}}{\partial r} = 0 \text{ (axis of symmetry)} \quad (3.3)$$

**Interface conditions:** ID side air gap and ID of the tube interface, coil-magnet interface and tube OD-air interface

$$\overline{n}_2 \times (\overline{H}_1 - \overline{H}_2) = \mathbf{J}_s \quad (3.4)$$

$$\overline{n}_2 \cdot (\overline{B}_1 - \overline{B}_2) = 0 \quad (3.5)$$

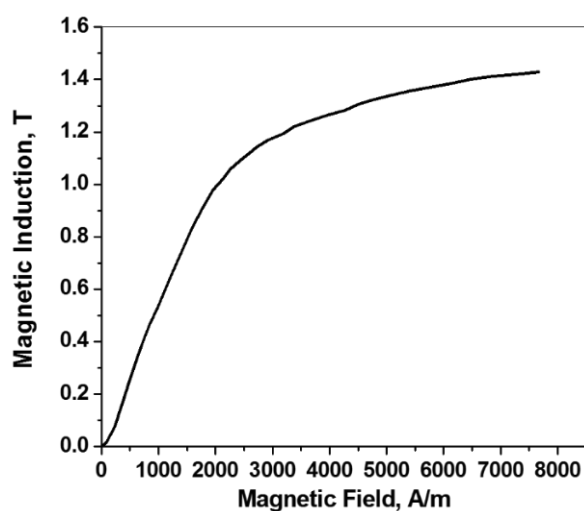


Fig. 3.12. B-H curve for Mod. 9Cr-1Mo ferritic steel.

**Dynamic analysis:** To generate a dynamic magnetic field in the tube, magnetic field node in AC/DC module was used. The permeability matrix obtained in the previous step was defined in the region of the tube above the magnets. A five cycle Hanning windowed toneburst of 1 A peak current (Fig. 3.11) was applied to the transmitter coil considered as a multi-turn coil. The governing equation is Ampere's law given by Eqs. (2.37 and 2.38). The boundary conditions used were magnetic insulation on the exterior boundaries (Eq. (3.6)) and the axial symmetry was defined using Eqs. (3.7 and 3.8) [146]. The interface conditions defined using Eqs. (3.4 and 3.5) are valid here as well. The only difference is

that now the fields are dynamic and the source current density  $J_s$  in the tube is non-zero due to the formation of eddy current in the tube because of time-varying magnetic fields. Dynamic magnetic field ( $\bar{B}$ ) components  $B_r$  and  $B_z$  were computed and the circumferential magnetic field component ( $B_\phi$ ) is zero due to axi-symmetry.  $\bar{A}$  is the time dependent vector magnetic potential used for computing dynamic  $\bar{B}$ .

**Boundary conditions:**

$$\bar{n} \times \bar{A} = 0 \text{ (exterior air boundary)} \quad (3.6)$$

$$\bar{B}_r = 0 \text{ (axis of symmetry)} \quad (3.7)$$

$$\frac{\partial \bar{B}_z}{\partial r} = 0 \text{ (axis of symmetry)} \quad (3.8)$$

- **Guided wave mode L(0,2) generation:** The magnetic field [B] obtained in the previous step was fed as an equivalent magnetic stress in solid mechanics module through a magnetostrictive constitutive equation (Eq. (2.26)) in the region of the magnetic field. The procedure to arrive at equivalent stress generated by magnetic field is given in § 2.2.2.1. The boundary conditions used were stress-free (Eq. (3.9)). Thus, the stress input fed generates a wave.  $\sigma_{rr}$ ,  $\sigma_{zz}$  and  $\sigma_{rz}$  are radial stress, axial stress and the shear stress.

**Boundary conditions:** ID and OD interfaces

$$\sigma_{rr} = \sigma_{zz} = \sigma_{rz} = 0 \quad (3.9)$$

- **Guided wave mode L(0,2) reception in receiver coil:** The stresses generated by the L(0,2) mode in the region below the receiver coil was fed as the input to obtain the time varying magnetic field through the magnetostrictive constitutive equation given by Eq. (2.28), which represents the Villari effect. This in turn was used to calculate the induced voltage in the receiver coil using Faraday's law (Eq. (2.39)). All the above steps are summarized in a flowchart, as given in Fig. 3.13.

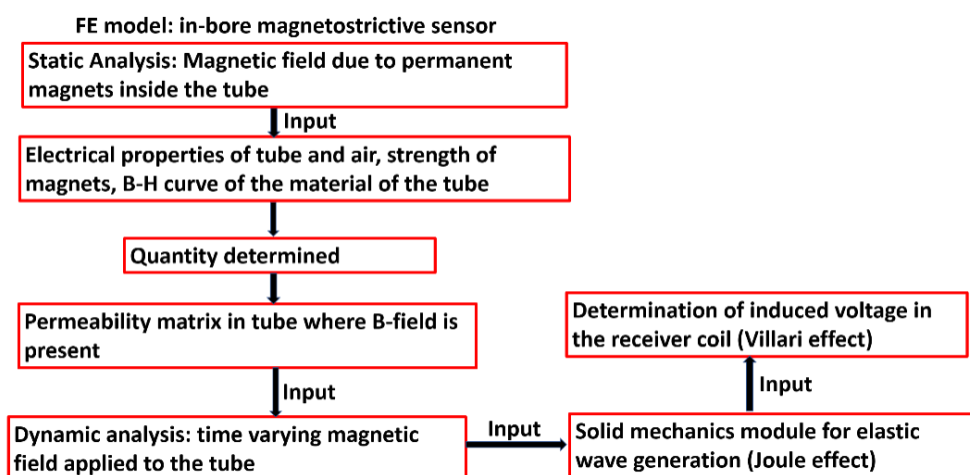


Fig. 3.13. Flowchart for steps followed in a finite element model for designing an in-bore magnetostrictive guided wave transducer.

## ***Chapter 4. Optimization of Guided Wave Mode for Long-range Propagation and Study of Feasibility for Detection of Common Defects in SG Tubes of PFBR***

### **4.1 Chapter overview**

This chapter discusses the optimization of L(0,2) mode using dispersion curves, mode shapes, finite element simulation using ABAQUS and experiments by end-coupling ultrasonic transducers to SG tubes. This includes the study of long-range propagation of L(0,2) mode and the detection of various commonly found defects such as circumferential, axial, pinhole, tapered and sodium impingement defects lying along the same line, in SG tubes. The chapter also presents the experimental validation of most of the FE results. Furthermore, the defect parameter influencing reflectivity and shadowing of one defect by another are also presented. Besides, the responses of the L(0,2) mode to ID and OD axial and pinhole defects are discussed. Finally, the chapter presents the experimental result of multiple axi-symmetric circumferential defects in a thermal expansion bend of an SG tube.

### **4.2 Mode selection through Disperse software and FE simulation**

#### **4.2.1 Guided mode properties and mode selection using Disperse software**

The SG tubes of PFBR are made of modified 9Cr-1Mo ferritic steel with the properties: density of 7800 kg/m<sup>3</sup>, Young's modulus of 220 GPa, the Poisson ratio of 0.2805, the longitudinal wave velocity of 6008 m/s and the shear wave velocity of 3319 m/s. The inner

and outer diameters of the tube are 12.6 mm and 17.2 mm, respectively and the wall thickness is 2.3 mm. With the inner radius, wall thickness and the elastic properties of the material of the tube, the phase velocity and the group velocity dispersion curves were obtained using Disperse software. Figures 4.1a and b show the phase velocity and the group velocity dispersion curves. Figure 4.1c shows the mode shape of L(0,2) mode at the center frequency of 250 kHz.

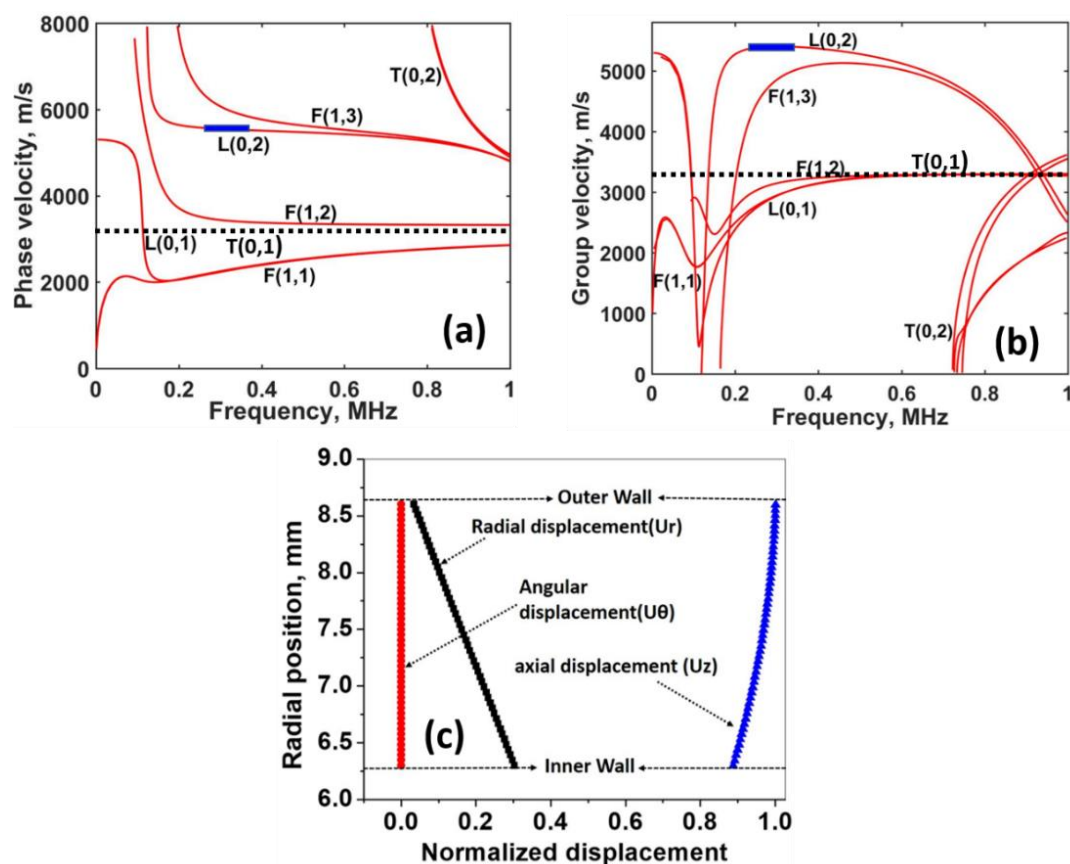


Fig. 4.1. (a) Phase velocity dispersion curves and (b) group velocity dispersion curves for SG tubes of the Prototype Fast Breeder Reactor, made of mod. 9Cr-1Mo ferritic steel with the inner diameter of 12.6 mm and the wall thickness of 2.3 mm and (c) mode shape of L(0,2) at 250 kHz. (Disperse software)

It can be seen in Fig. 4.1a that flexural mode F(1,2) and longitudinal mode L(0,2) are nearly non-dispersive in the range of frequencies: 250 kHz-1 MHz and 200 - 650 kHz, respectively.

The torsional mode  $T(0,1)$  is fully non-dispersive in the bandwidth of 0-1 MHz. The cut-off frequency of  $L(0,2)$  mode is around 150 kHz. From ~150 kHz to ~200 kHz,  $L(0,2)$  mode is highly dispersive.  $F(1,3)$ ,  $F(1,1)/L(0,1)$  modes in this frequency range are also dispersive and hence, are discounted with. Furthermore,  $T(0,2)$  mode is also dispersive. As mentioned earlier, either  $L(0,2)$  or  $T(0,1)$  mode is used for long range inspection. Between  $T(0,1)$  and  $L(0,2)$  modes,  $L(0,2)$  mode at 250 kHz has been chosen for the examination of SG tubes of PFBR.  $L(0,2)$  mode has the following advantages over  $T(0,1)$  mode: the highest group velocity, good separation from neighboring modes, fairly uniform axial stresses indicating fairly equal sensitivity and easy excitability using ultrasonic transducers and magnetostrictive principles.

As mentioned earlier, only accessibility for actual testing is from the inside of the SG tube whose inner area of cross-section is  $\sim 125 \text{ mm}^2$ . Owing to this constraint, couplant-free, non-contact magnetostrictive method has been chosen for guided wave generation. Both  $L(0,2)$  and  $T(0,1)$  modes can be generated using the magnetostriction principle. To be specific, the magnetostrictive based generation of  $L(0,2)$  mode requires axial magnetic fields, while  $T(0,2)$  mode requires circumferential magnetic fields. Given the above constraint of space for examination, it was found that generating axial magnetic fields of required strength from the inside of an SG tube is easier than generating a circumferential magnetic field from inside. Hence, a magnetostrictive transducer generating  $L(0,2)$  mode is easier to fabricate. Apart from the advantages mentioned above, it is the primary reason that  $L(0,2)$  mode has been chosen for inspection of SG tubes.

$L(0,2)$  modes at higher frequencies in the range 250 - 650 kHz could be chosen for better sensitivity and resolution but there are two possible disadvantages. First,  $L(0,2)$  mode in the

higher frequency end will result in higher attenuation, which is not desirable for long-range propagation. Secondly, high frequencies also exhibit reduced skin depth and consequently, the effective volume of the distribution of magnetostrictive forces will be very low. This will result in inefficient generation of the wave mode. Thus, a wave frequency of 250 – 350 kHz has been selected from the perspective of lower attenuation and efficient magnetostrictive generation.

The blue-filled markers in Fig. 4.1a and b show the bandwidth used (~170 -330 kHz). It can be seen in the figure that the axi-symmetric longitudinal mode (L(0,2)) is nearly non-dispersive and its group velocity is 5380 m/s. The mode shape of L(0,2) mode at 250 kHz shown in Fig. 4.1c indicates that the axial displacement fairly uniform across the wall thickness, a small radial displacement and zero angular displacement component. Hence, the axial stress across the thickness is also uniform indicating nearly equal sensitivity for ID, OD and internal defects. Modes in the dispersion curves are theoretically possible solutions. Hence, to check the excitability of L(0,2) mode, FE simulation has been performed.

### **4.2.2 Mode excitability using FE simulation**

A 3D-FE simulation was performed in ABAQUS with a 1.0 m long defect-free tube, as mentioned in Chap. 2. The left end face of the tube was imposed a five-cycle Hanning windowed toneburst with the center frequency of 250 kHz. The bandwidth of the excitation was in the range of 170-330 kHz at 20 dB down point. The dominant displacement component in the mode shape of L(0,2) mode is the axial displacement and it is nearly uniform across the wall thickness. Imposing an axial displacement of similar kind to the tube is expected to generate a pure L(0,2) mode. Further, it is easy to impress such a displacement in experiments by end coupling an ultrasonic transducer to the tube.

The FE parameters such as mesh, spatial step and the time step were chosen, as described in Section 3.5. Figure 4.2a shows the FE signal of the averaged axial displacement ( $U_z$ ) signal picked up at the excitation end. The end reflection from the tube is clearly seen in the figure. Figure 4.2b shows the screenshot of the propagation of L(0,2) mode at the time of 65  $\mu$ s. The group velocity of the end reflected signal was calculated by taking the time corresponding to the maximum of the envelop of the signal, which travels a distance of 2.0 m. The group velocity turned out to be 5367 m/s, which compares very well with 5380 m/s provided by Disperse. Figure 4.2c shows the magnitude plot of the axial displacement in the cross-section of the tube.  $U_z$  magnitudes over the cross-section were normalized with the  $U_z$  magnitude at the OD. It can be seen that  $U_z$  is slightly larger at the OD than that at the ID and the variation is very small. This fact is also in complete agreement with the mode shape obtained from Disperse software (Fig. 4.1c). This confirms that the mode generated in the FE simulation by end excitation is L(0,2) mode. Furthermore, the radial displacement in the simulation was observed to be very small and the angular displacement was virtually zero. These components were not considered because the ultrasonic transducer used in the experiment works on the longitudinal mode and it will be insensitive to the radial component.

Further, it can be noticed in the signal (Fig. 4.2a) that there is a low-frequency oscillation between the initial signal and the end reflected signal. The appearance of the low-frequency oscillation is explained as follows. Figure 4.3a shows the excitation signal of a five-cycle Hanning window tone burst of the center frequency 250 kHz. Figure 4.3b is the frequency spectrum of the five-cycle Hanning window tone burst. The peak frequency in the spectrum is 250 kHz and the bandwidth at 20 dB down point is 170 -330 kHz. There are also frequencies of smaller amplitudes to the left and right of the peak. Figure 4.3c shows the axial displacement signal ( $U_z$ ) obtained at the excitation end in the FE simulation for the SG of 1.0

m length (same as Fig. 4.2a). The inset in Fig. 4.3c shows the ringing of lower frequency between the initial signal and the end reflected signal. The amplitude of the ringing is of 0.006 A.U. Figure 4.3d shows the frequency spectrum of the ringing in Fig. 4.3c. The peak frequency turns out to be 115 kHz. The frequency of 115 kHz is very close to that of 116.5 kHz of L(0,2) mode with the zero group velocity, as indicated by a dotted circle in the group velocity dispersion curves ( Fig. 4.3d). It can be observed that this frequency of 115 kHz is present in the spectrum of the excitation at the lower end (Fig. 4.3b). Hence, the zero group velocity of L(0,2) mode is the cause of the ringing. Actually, the zero group velocity of L(0,2) mode sets up a resonance in the tube, which consequently makes the tube to continuously vibrate, even after the duration of excitation.

In order to establish this fact, FE simulations were performed with various number of cycles, say 5, 10, 15, 20 25 of the excitation signals in a 1.0 m long defect-free tube. The increase in

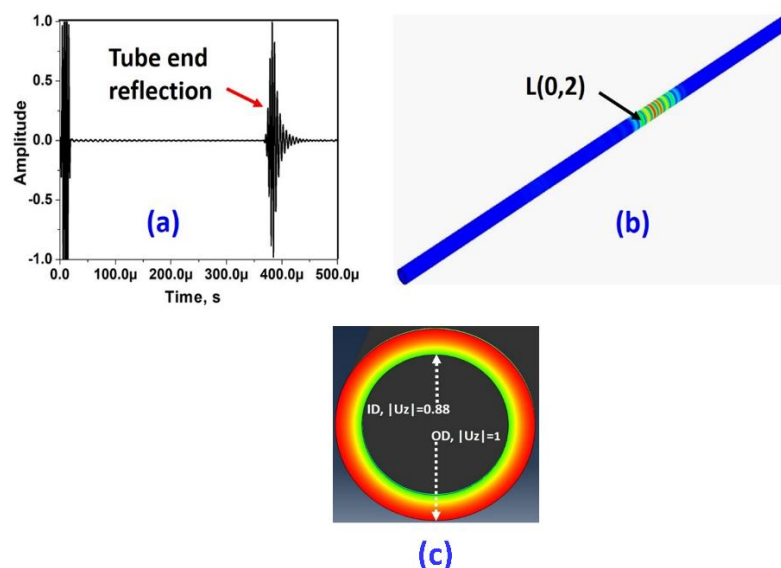


Fig. 4.2. (a) Axial displacement signal ( $U_z$ ) obtained at the excitation end and (b) a snapshot of L(0,2) mode at  $65 \mu\text{s}$  and (c) magnitude plot of axial displacement in the cross-section (Finite element simulation).

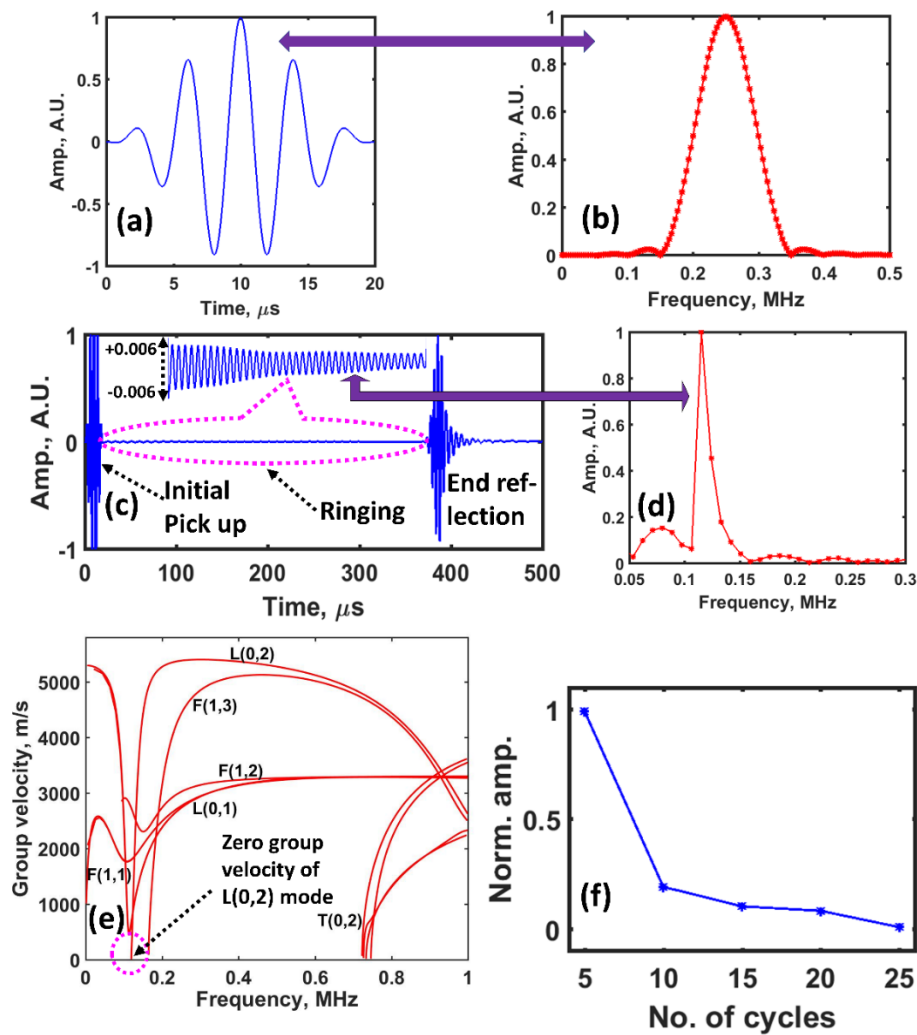


Fig. 4.3 (a) A five cycle Hanning window toneburst at the center frequency of 250 kHz, (b) frequency spectrum of (a), (c) axial displacement obtained in a 1.0 m long tube (same as Fig. 4.2a) with ringing shown in the inset, (d) frequency spectrum of the ringing shown in (c), (e) group velocity dispersion curves of SG tubes showing the zero group velocity of L(0,2) mode and (f) amplitudes of the ringing for various cycles of excitation (Finite element simulation).

the number of cycles leads to the narrowing of bandwidths. As done before, the signals were excited at one end and the reflections from the other were recorded at the same end. Figure 4.3f shows the plot of the amplitude of ringing versus the number of cycles of excitation. It can be clearly seen that as the number of cycles increases in the excitation, the ringing dies down completely. Mathematically, the increase in the number of cycles amounts to

reducing/narrowing the bandwidth of signals. Consequently, the lower end of the spectrum found in Fig. 4.3a drifts away from the resonant frequency of 115 kHz. As this frequency of the zero group velocity is gone past, there is no other frequency of L(0,2) mode that can cause the ringing. Hence, for a large number of cycles, the ringing is absent, as shown in Fig. 4.3f. Furthermore, it can be noticed that its effect is small and hence, it will not affect actual signals in any way. Therefore, the number of cycles for this dissertation was chosen to be a maximum of five, which may yield a better resolution.

## **4.3 Results and discussion**

### **4.3.1 Experimental results for a 1.0 m long SG tube**

To generate L(0,2) mode at 250 kHz center frequency, an experiment was conducted on a tube of 1.0 m length by end coupling an ultrasonic transducer of the center frequency of 250 kHz, as described in Chap. 3. Figure 4.4 shows the experimental time signal obtained in the tube of 1.0 m length. It can be seen that the experimental signal closely resembles to that obtained from simulation (Fig. 4.2a). The times of flight of the FE and the experimental signals agree well. To ascertain the modes present, time–frequency plots (spectrogram) were made using the short time Fourier transform and overlaid on the dispersion curves. Figures 4.5a and b show the group velocity-frequency plots for the experimental (Fig. 4.4) and FE simulation signals (Fig. 4.2a) overlaid on dispersion curves, respectively. They agree very well. It can be seen that the mode present is only L(0,2) mode covering the frequency range of 175 kHz-350 kHz. It can also be seen in the figure that the lower end of the bandwidth comprises of frequency components that propagate slightly slower than the higher frequency components. For practical purposes, the group velocity corresponding to the center frequency can be considered and it was found to be 5387 m/s. The group velocities obtained in the

experiment and the FE model were 5387 m/s and 5367 m/s, respectively and that obtained using Disperse software was 5380 m/s. There is a good agreement between the observed group velocities and that provided by Disperse software. The relative errors in the group velocity with respect to 5380 m/s are about 0.1% and 0.2% for the experimental and FE predicted group velocity, respectively.

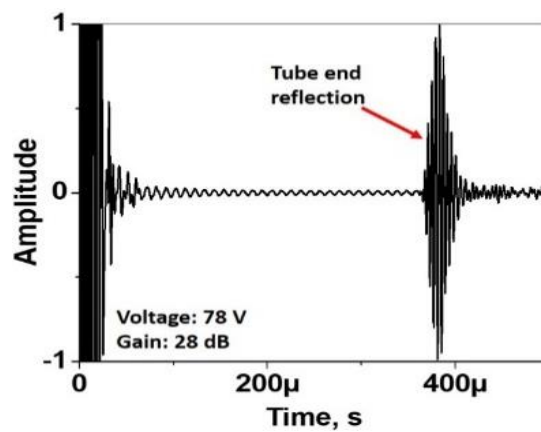


Fig. 4.4. Experimental signal obtained from the end of the SG tube segment of 1.0 m length.

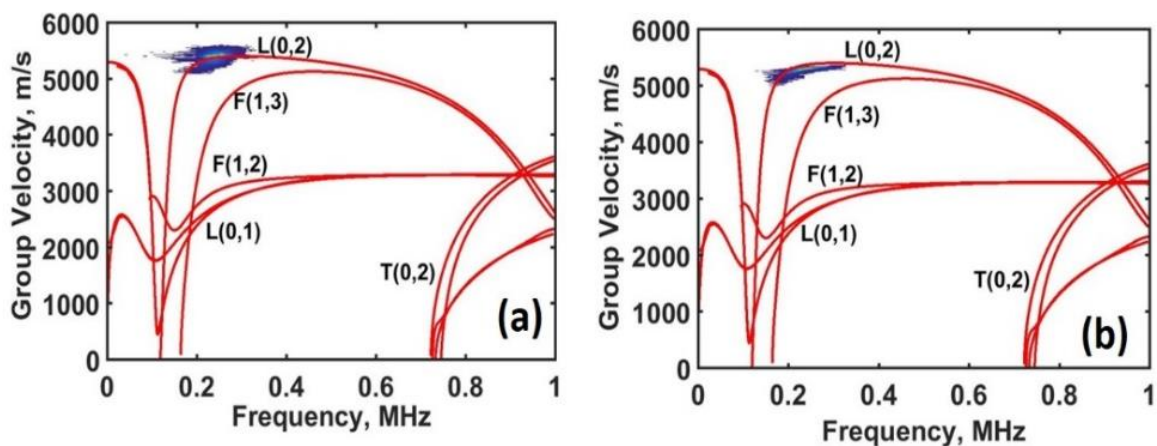


Fig. 4.5. Dispersion curves overlaid on spectrograms: (a) experimental signal (Fig. 4.4) and (b) the axial displacement signal (Fig. 4.2a (FE simulation)).

### 4.3.2 Long range propagation of L(0,2) mode at 250 kHz in a 3.8 m long SG tube segment

The excitability of L(0,2) mode was checked using FE simulation and validated by the experiment, as mentioned above. To check the long-range propagation of L(0,2) mode, experiments were conducted on a 3.8 m long SG tube segment. Figure 4.6a and b show the experimental time signal and the corresponding spectrogram, respectively obtained in a 3.8 m long SG tube using the ultrasonic transducer of center frequency 250 kHz.

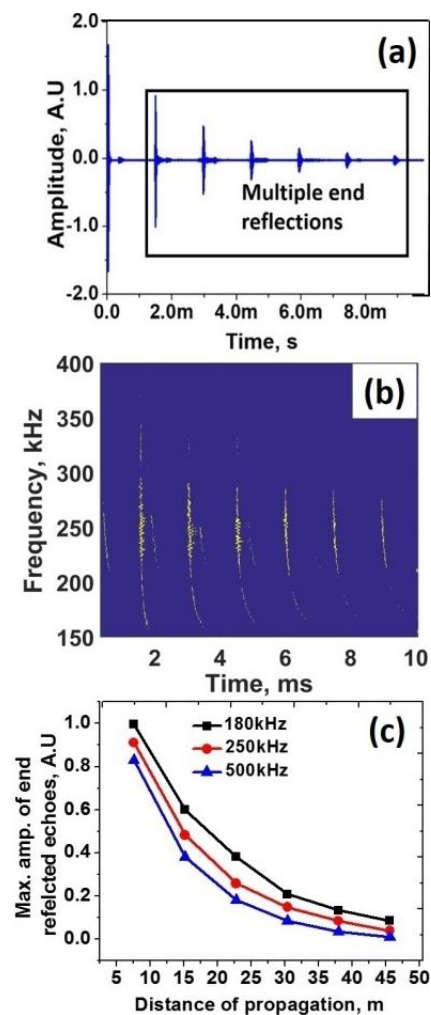


Fig. 4.6. (a) Experimental signal obtained in a 3.8 m long tube, (b) frequency versus time of propagation and (c) maximum amplitudes of end reflections obtained with transducers of frequencies 180 kHz, 250 kHz and 500 kHz.

The experimental parameters used were a five cycle of toneburst with the center frequency of 250 kHz, excitation voltage of 100 V and the gain of 28.0 dB. It can be seen in Fig. 4.6a that there are six multiple reflections, which amount to the propagation distance of 45.6 m against the required 46 m. The maximum distance of propagation was limited by the pulse repetition frequency of the equipment used. It can be observed that though slight dispersion is present, its effect is not very severe in the long range, but it may have a consequence on the resolution of closely spaced defects. This is due to the dispersive lower frequencies in the bandwidth (Fig. 4.5a) and it can be avoided by increasing the number of cycles. Figure 4.6b clearly shows that the frequency components at the lower end of the bandwidth separate out with time, trail the higher frequencies and eventually, die out due to dispersion of frequencies lower than 250 kHz. However, the majority of the higher frequency components reach a distance of 45.6 m, as indicated in Fig. 4.5.

Further, to examine L(0,2) mode at 250 kHz in comparison with nearby L(0,2) modes, experiments were also conducted on the same tube with the frequencies of 180 kHz and 500 kHz. Figure 4.6c shows the plots of maximum amplitudes obtained from time plots for 180 kHz, 250 kHz and 500 kHz frequencies. The attenuations were calculated for the signals in the frequency domain at the corresponding frequencies. The average attenuations for 180 kHz, 250 kHz and 500 kHz were found to be 0.56 dB/m, 0.72 dB/m and 1.01 dB/m, respectively. However, the modes generated for all three frequencies were able to propagate for the distance of 45.6 m. The highest attenuation is exhibited by 500 kHz followed by 250 kHz and 180 kHz. This can be attributed mainly to scattering, as the wavelength is much larger than grain size [167]. There are also contributions due to dispersion and absorption. However, absorption at low frequencies are very small and hence, it can be neglected.

The time duration of wavepackets with the center frequency of 180 kHz is large indicating a poor spatial resolution of defects and this frequency also falls in the dispersive region of L(0,2) mode. Moreover, the mode at 500 kHz centre frequency exhibits highest attenuation and the skin depth (~0.03 mm) necessary for magnetostrictive based generation becomes very small. Hence, this will result in the generation of the mode with low energy, which may not be sufficient for long range propagation of 46 m. On these grounds, the L(0,2) mode at 250 kHz with the bandwidth of 170- 330 kHz has been selected for all the study, discounting with the other frequencies. Further, the FE results for 1.0 m long tube indicated that L(0,2) mode gets reflected almost entirely without mode conversion losses. There could be an additional loss if the ends of the tube are not cut exactly perpendicular to the tube axis. Hence, the attenuation calculated can be considered to be the upper bound. The mode L(0,2) at 250 kHz has been found to be satisfactory in terms of ease in its excitability and a long-range propagation and acceptable dispersion. However, the suitability of this mode for the application can be judged only based on its response to defects. The following sections discuss the capability of defect detection of the L(0,2) mode at 250 kHz, in specific, multiple defects lying in the same line.

### **4.3.3 Finite element simulation for tubes with defects and experimental validation**

FE simulation studies were carried out for 1.5 m long tubes with six OD circumferential defects, six OD axial defects, six OD pinholes of various dimensions, four sodium impingement defects and four tapered defects. The schematic of the specimens used for the experiments is shown in Fig. 3.4. The FE models of the tubes with the defects are shown in Fig. 3.7 in Chap. 3. Furthermore, FE simulations were also performed in short tubes with different dimensions of axial and sodium impingement defects to obtain reflectivity. In

addition, FE simulations were performed to understand the response of one circumferential defect in the vicinity of another. Finally, FE models with ID and OD partial-pinholes and axial defects in 750 mm long tubes were also considered and studied.

#### **4.3.3.1 Circumferential defects, axial defects, partial pinholes, tapered defects and sodium impingement damage**

Figures (4.7-4.10) show FE simulated and experimental axial displacement-time signals obtained for multiple circumferential defects (Fig. 3.4a(i)), axial defects (Fig. 3.4a(ii)), partial-pinholes (Fig. 3.4a(iii)), and sodium impingement defects (Fig. 3.4a(v)), respectively obtained in 1.5 m long SG tubes. Figure 4.11 shows the FE time signal for the case of non-axisymmetric tapered defects (Fig. 3.4a(iv)), in a 1.5 m long SG tube. Figure 4.12 shows the experimental time signal obtained in a 1.5 m long tube with a combination of circumferential, axial and pinhole defects. The dimensions and locations of the defects are given in Table 3.1 in Chap. 3.

Figures 4.13a, c and e show the amplitudes of the individual defect signals in Figs. 4.7-4.9. The reasonable measures of the amplitudes were obtained by taking the maxima of the envelopes of the signals. The times of flight corresponding to the maximum amplitudes were used as the measure of the times of flight. The experimental and FE amplitudes show a good correlation for all the cases. In Figs. 4.7-4.9, all the amplitudes were normalized with respect to the highest amplitude of defects. It can be observed that all six circumferential and axial defects were detected with good SNR. In the case of partial-pinholes, all but the 1 mm diameter and 0.92 mm deep pinhole were detected with a good SNR. Figures 4.13b, d and f show the difference in times of flight (a measure of error) observed in the FE and experimental defect signals in Figs. 4.7-4.9. The data for defect A is corrupted by noise and hence, it is not

shown in Fig. 13e and f. Furthermore, the experimental and FE amplitudes and times of flight for sodium impingement defects compare well for all four defects (Fig. 4.10). The SNR of the highest response in all four cases turns out to be approximately 20 dB (Figs. 4.7-4.10).

The maximum deviation between the experimental and FE amplitudes for the circumferential defect, axial and pinhole cases are  $\sim 0.25$  A.U. (Fig. 4.13a, c and e). The amplitudes of signals in experiments are generally influenced by excitation voltage, gain, attenuation and the dimensions of a defect and its profile. The first two parameters are in experimenters' control while the second two parameters are not. In other words, a slight deviation from the dimensions of the modelled defect and the actual one may have a definite influence on amplitude. Furthermore, a slight asymmetry in the end coupling of the ultrasonic transducer may result in a slight non-uniformity of the mode generated. In FE simulations, this can be 100% ensured whereas in experiments, this can only be made as close to 100% uniform excitation as possible. The deviation in the amplitudes between experimental and FE signals could have resulted from the above reasons.

The maximum difference in experimental and FE times of flight for the circumferential defect, axial and pinhole cases are  $\sim 1 \mu\text{s}$ ,  $1.5 \mu\text{s}$  and  $1 \mu\text{s}$ , respectively (Fig. 4.13b, d and f). The highest deviation is exhibited by the axial defect case. This could have resulted from the slight deviation ( $\sim 5$  mm) of the actual defect locations and the modelled ones. Another factor that could have caused the deviation is the slight difference in the elastic properties used for the models and the actual tubes.

Further, it can be seen in Figs. 4.7-4.12 that the reflected amplitudes increase or decrease in accordance with the size of the defect. The amplitudes corresponding to the circumferential defects (Fig. 4.13a) show an increasing response with depth and circumferential extent due

to the increased area of interaction. Besides, the reflected amplitude should be influenced by width as well. The reflected amplitudes for axial defects (Fig. 4.13b) show an increasing response with depth and are also influenced by the axial length due to the interference happening between the signals reflected from the start and the end of the axial defect. Hence, it is always recommended to use two inspection frequencies [88], in the case of axial defects. For the case of pinholes, the reflected amplitudes (Fig. 4.13e) increase both with the diameter and the depth. Understanding of the behaviour of the reflection coefficient from a defect requires a detailed study of wave scattering from a defect in terms of stresses and displacements. As the objective of the thesis is the development of guided wave-based inspection methodology and a suitable in-bore magnetostrictive transducer, the study of wave scattering is beyond the scope of the thesis. However, it will form one of the future studies.

It is also worth mentioning that the low frequency oscillations found in the FE signals (Fig. 4.8 and Fig. 4.10) are due to the ringing effect caused by the zero group velocity  $L(0,2)$  mode at 115 kHz, as discussed earlier. The signals reflected from axial defects and sodium impingement damage are weak and they require high amplification to be seen. Consequently, the low frequency oscillations are also seen more pronounced. In the FE models for circumferential, axial, pinhole and sodium impingement defects, no damping was provided. This can be avoided by artificial damping, as is the case for FE models in the latter chapters. Furthermore, the low-frequency and low-amplitude oscillation can be filtered using a suitable high pass filter as well.

A comparison of Figs. 4.7-4.10 can convey an impression that the amplitudes are similar for all the defect cases studied. However, it is not, because the sizes of the defects are different. In fact, the amplitude scale in each figure (Figs. 4.7-4.12) is normalized with respect to the highest response in that figure, for the signals to be seen clearly. The experimental parameters:

excitation voltage and gain used for circumferential, axial, pinhole and sodium impingement damage were 274 V and 30 dB gain, 520 V and 32.8 dB, 575 V and 42.8 dB and 500 V and 40 dB, respectively.

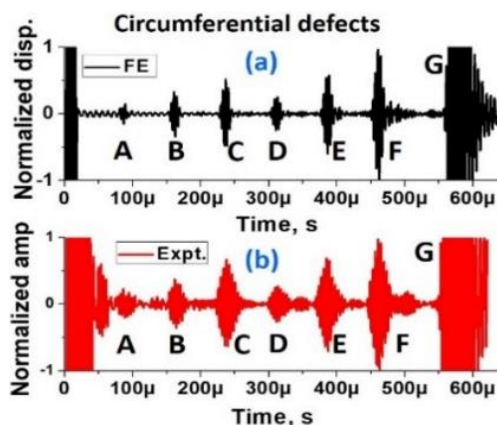


Fig. 4.7. Comparison of circumferential defect signals obtained using (a) finite element (FE) simulation and (b) experiment. **A-F** are defect labels, as in Table 3.1. **G**, the tube end reflection.

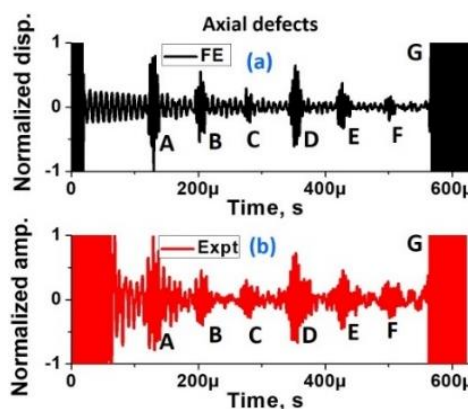


Fig. 4.8. Comparison of axial defect signals obtained using (a) finite element simulation (FE) and (b) experiment. **A-F** are defect labels, as in Table 3.1. **G**, the tube end reflection.

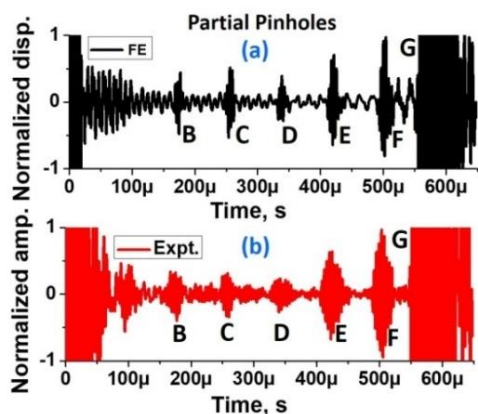


Fig. 4.9. Comparison of pinhole defect signals obtained using finite element (FE) simulation and experiment. **B-F** are defect labels, as in Table 3.1. **G**, the tube end reflection.

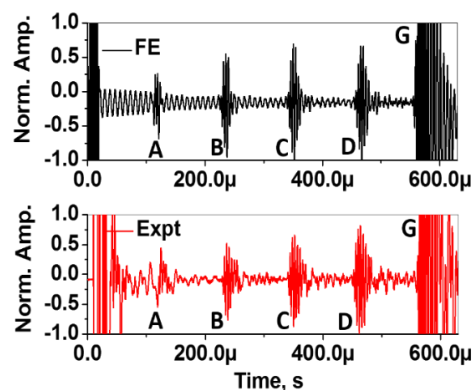


Fig. 4.10. Comparison of sodium impingement damage signals obtained using finite element (FE) simulation and experiment. **A-D** are defect labels, as in Table 3.1. **G**, the tube end reflection.

Figure 4.11 shows the FE time signal for the case of non-axisymmetric tapered defects (Fig. 3.4a(iv)), in a 1.5 m long SG tube. The FE time signals (Figs 4.11a and b) for non-axisymmetric tapered defects obtained by left excitation and right excitation of the sample (Fig. 3.4a(iv)) show that the reflected amplitudes from left to right and vice-versa increase and decrease, respectively because of the order of defects seen by L(0,2) mode. The responses in the two cases are similar but for the multiple reflections between the tube end and defect D in Fig. 4.11b (seen between D&C, C&B and B&A). It can be seen that the flat part of a tapered defect is more effective in interaction than the tapered part. For instance, defect D when it is seen by L(0,2) mode from the right, it sees the flat of the defect first and hence, gives more reflected amplitude than when it sees the tapered part from the left. It is reported in the literature [92] that there will be separate reflections from the start and end of a taper. It is not noticed here because the linear dimension of the defect is smaller than the width of the excitation signal (five times the wavelength of L(0,2) mode (21.5 mm)) and hence, the reflections will merge to a single signal. In the case of the combination of different defects such as circumferential, axial and pinhole defects (Fig. 3.4a(vi)), all seven defects are detected with good sensitivity, as shown in Fig. 4.12. The amplitudes in the figure were normalized with the highest response of defects. Importantly, Fig. 4.12 indicates that irrespective of the nature of defects and their order, L(0,2) mode can detect them.

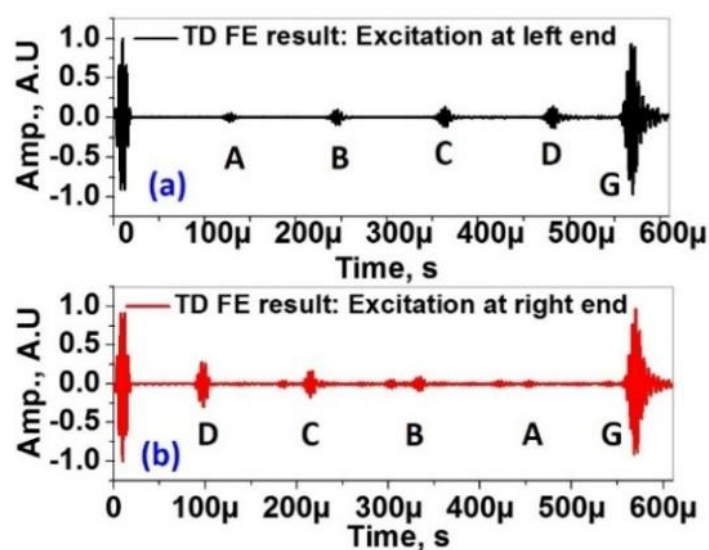


Fig. 4.11. Axial displacement signals obtained for excitation at (a) left and (b) right ends of a tube with tapered defects (TD). **A-D** are defect labels, as in Table 3.1. **G**, the tube end reflection. (Finite element (FE) simulation)

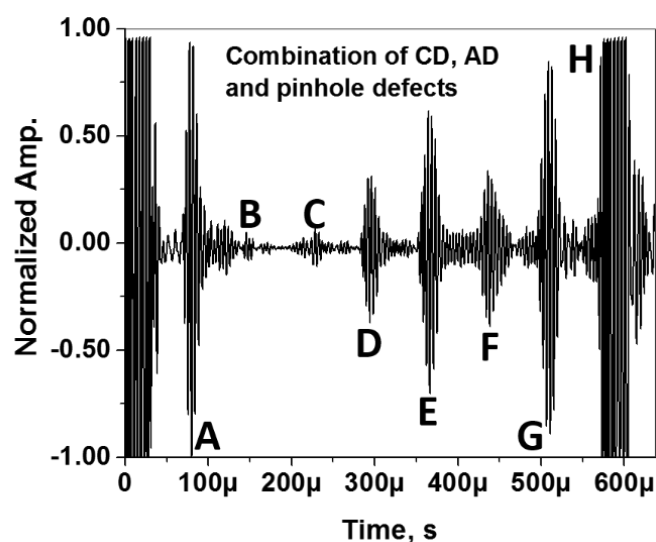


Fig. 4.12. Experimental signals obtained in a tube with the combination of circumferential defects (CDs), axial defects (AD) and pinholes (PHs). Labels **A-G** represent defects whose dimensions are given in Table 3.1 and **H** represents end reflection. **A**: Full circumferential defect, **B and C**: Axial defects, **D and E**: Part-circumferential defects and **F and G**: Pinholes, as shown in Fig. 3.4a(vi).

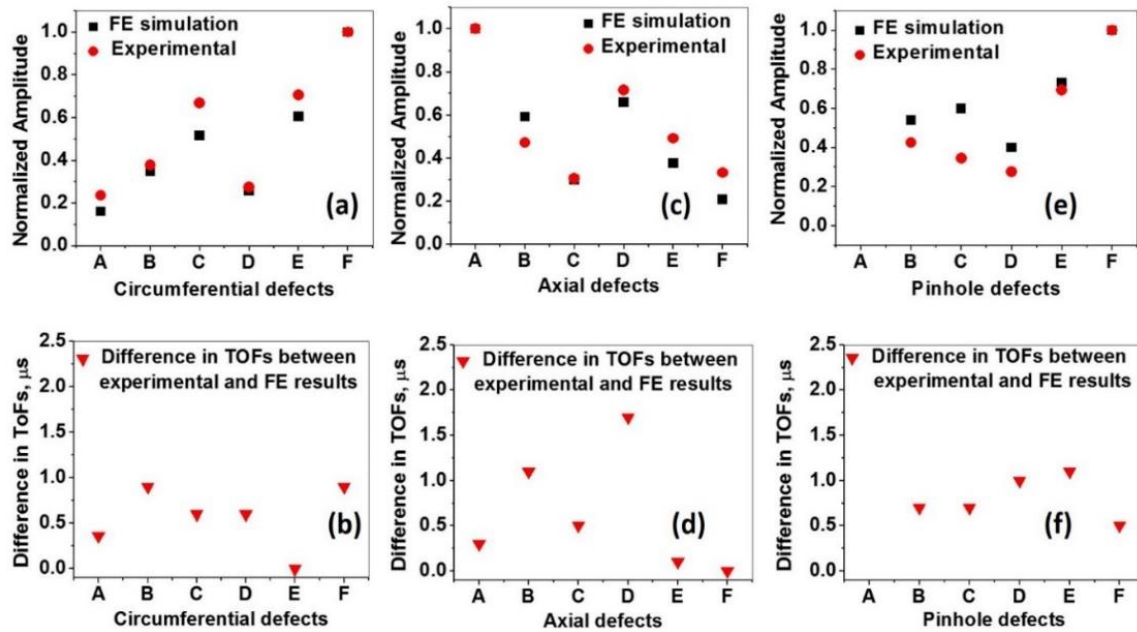


Fig. 4.13. A comparison of amplitudes and times of flight for finite element (FE) simulation and experimental time signals: (a and b) circumferential defects, (c and d) axial defects and (e and f) partial pinholes. A-F represent defect labels, as given in Table 3.1.

Figure 4.14 shows the plot of reflected amplitudes from non-axisymmetric tapered defects for the right and left excitation. The reflected amplitudes increase non-linearly with the depth of the non-axisymmetric tapered defects. The amplitude profiles in Fig. 4.14 are not symmetric in both cases which is attributed to different shape of the defects seen by  $L(0,2)$  when propagating from left to right and vice-versa. Further, as the reflected amplitude from the first defect encountered is different, the remaining amplitude propagating further is also different. Figure 4.15a shows the comparison of FE reflected amplitudes for the tapered defect, circumferential defect, axial defect and partial-pinhole with all having the same 0.46 mm depth but with different percentages of cross-section. The response of the tapered flaw is the highest followed by the circumferential defects, axial defects and the pinhole for the same depth of 0.46 mm. It substantiates that the area presented by the defect to the mode  $L(0,2)$  governs the reflection. Figure 4.15b shows the error in locating a defect for all four defect

types. It can be seen that a defect can be located within the accuracy of max. 10 mm even when multiple defects are present. The maximum errors in locating a defect are for axial and tapered defects having larger axial extent due to the superposition of reflected signals arising from the start and the end of the defects.

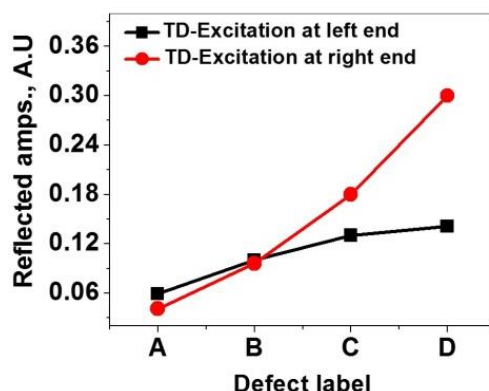


Fig. 4.14. Reflected amplitudes from tapered defects (TD): right and left excitation. (Finite element simulation)

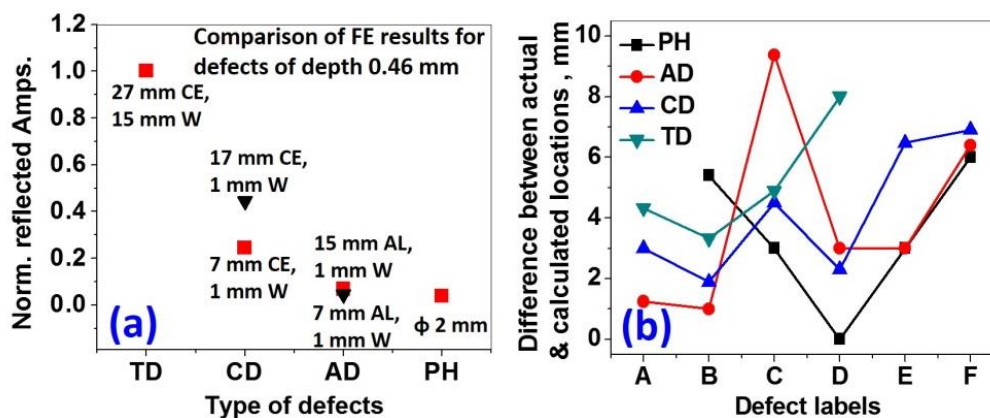


Fig. 4.15. (a) A comparison of amplitudes for a tapered defect (TD), circumferential defects (CD), axial defects (AD) and pinholes (PH) of the same 0.46 mm depth and (b) error between FE estimated locations of the defects and the original locations of the defects Vs. defects. All the amplitudes are normalized with respect to the amplitude of the tapered defect. CE: circumferential extent, AL: axial length and W: Width. (Finite element simulation)

The response of L(0,2) mode at 250 kHz to various defects such as circumferential, axial, pinhole, sodium impingement and tapered defects has been studied. It is found to be satisfactory in terms of the requirement for sensitivity (6 dB from noise level). For instance, the background noise level for experimental pinhole defect signals is in the range of  $\pm 0.1$  V and a 6 dB criterion is used for fixing the sensitivity which means a pinhole defect signal greater than  $\pm 0.2$  V will represent a defect signal. In the present case, the pinhole of dimensions: 1.38 mm (60% WT) depth and 1 mm diameter shows  $\sim 0.35$  V and the pinhole of dimensions: 0.46 mm (20% WT) depth and 2 mm diameter shows  $\sim 0.25$  V. The percentages of cross-section for the first and the second defects (mentioned here) can be obtained as 1.38% and 0.85%, respectively by assuming the equivalent reflecting areas (rectangular) for the curved surface. Hence, a pinhole with 1.38% cross-section has been considered for the sensitivity due to its smaller volume occupied by the defect than the 2 mm dia. pinhole. It can be seen that the reflected amplitude is governed more by the depth and less by the diameter of the pinhole because of the curved reflecting area.

Furthermore, to check if any mode conversion occurred during the interaction of L(0,2) mode with the defects  $U_r$  and  $U_\theta$  components were recorded in addition to  $U_z$  in the FE simulations. The results show that there are indeed, mode conversions occurring due to the interaction of L(0,2) mode with the non-axisymmetric defects chosen in the study. This fact is reported in the literature that when a symmetric mode like L(0,2) is incident on a non-axisymmetric feature, there will be a mode conversion to F(1,3) and F(2,3) [86]. Since the ultrasonic transducer arrangement (symmetric system) used in the study can pick up only axial displacements, mode conversion to the angular and the radial displacements is not observed.

### **4.3.3.2 Reflectivity of L(0,2) mode from axial and sodium impingement defects**

As seen above, the reflected amplitude from a circumferential defect increases with circumferential extent and depth when the width is small in comparison with wavelength. The reflected amplitude from a pinhole increases with depth and diameter. The reflected amplitudes from axial and sodium impingement defects increase with depth but are also strongly influenced by the axial extents. Furthermore, it is also important to understand the influence of the curvature of a sodium impingement defect on reflectivity.

To this end, FE simulations were performed with axial defects having different depths and axial extents. Figure 4.16 shows the plot of reflected amplitude versus the ratio of axial lengths of axial defects to wavelength ( $\lambda$ ). It can be seen that the reflected amplitude is not monotonic with the axial length but exhibits ups and downs. It is maximum at the quarter wavelength and three-quarters of the wavelength and is minimum at half and full wavelength. This phenomenon is due to the interference occurring between the reflected signals from the start and end of an axial defect. It indicates that when an axial defect is of axial extents half and full wavelength, the defect will not be detected. However, this can be overcome by using a different inspection frequency.

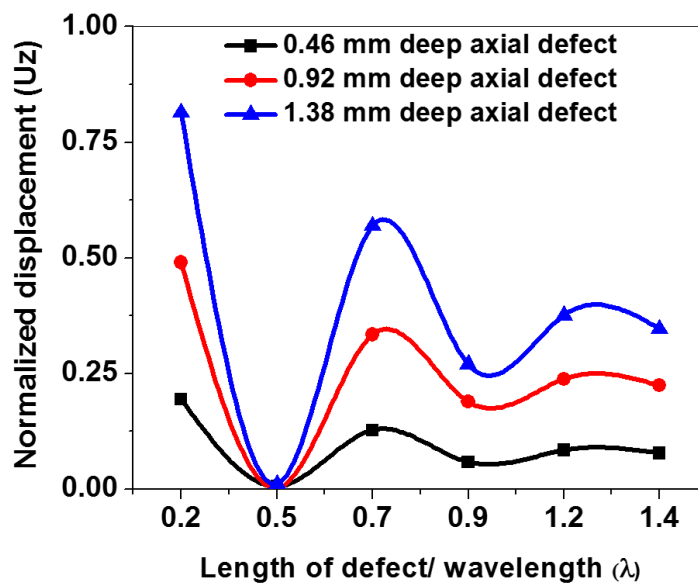


Fig. 4.16. Reflectivity of L(0,2) mode from axial defects of different lengths vs. ratio of length of the defect to the wavelength. (Finite element simulation)

The influence of the axial extent of a sodium impingement defect on reflectivity is also expected to follow a similar trend as that of the axial defects. Hence, sodium impingement defects of different depths and widths for the same axial length and the radius of curvature were studied using FE simulation. The dimensions and locations of the defects used were shown in Table 3.1. Figure 4.17 shows the reflectivity of L(0,2) from the defects. The amplitudes are normalized with respect to the highest response of the defects. It can be seen that the reflectivity increases monotonically with the depth. The only varying parameters from one defect to another are depth and width. The reflection from the defects can be understood in terms of percentages of cross-section. This was arrived at by considering the ratio of the product of the width and depth of the defects to the tube wall cross-sectional area. The defects A-E in the figure have increasing percentages of cross-section as 0.8%, 4.3%, 9.2% and 21.5%. It is clear that the reflectivity of a sodium impingement defect increases with the effective area.

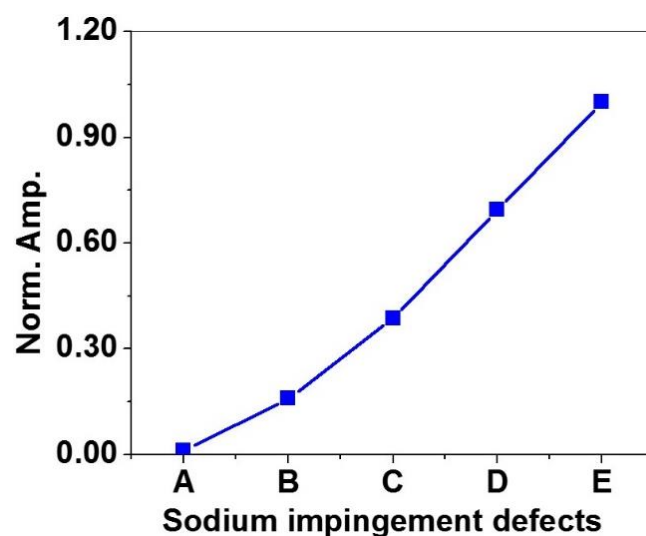


Fig. 4.17. Reflectivity of L(0,2) mode for defects with different depths and widths for the same radius of curvature  $R=3.175$  mm. **A-E** stand for different defects. (Finite element simulation)

Further, to study the influence of the curvature of the defects, FE simulations were performed with 50% WT deep defects with the different radii of curvature  $R= 3.175$  mm, 5 mm and 7 mm. Figure 4.18 shows the reflectivity of L(0,2) mode from the defects with the different radii of curvature. All the amplitudes were normalized with the maximum amplitude of the end reflected signal. It can be observed that the amplitudes of defect signals, indicated by G in the figure, are almost the same. This could be due to the smoothness of the curvature and small values of curvature from the perspective of L(0,2) mode at 250 kHz. However, in practice, the curvature of a sodium impingement damage is expected to be smaller than the wavelength and hence, its influence will be negligible.

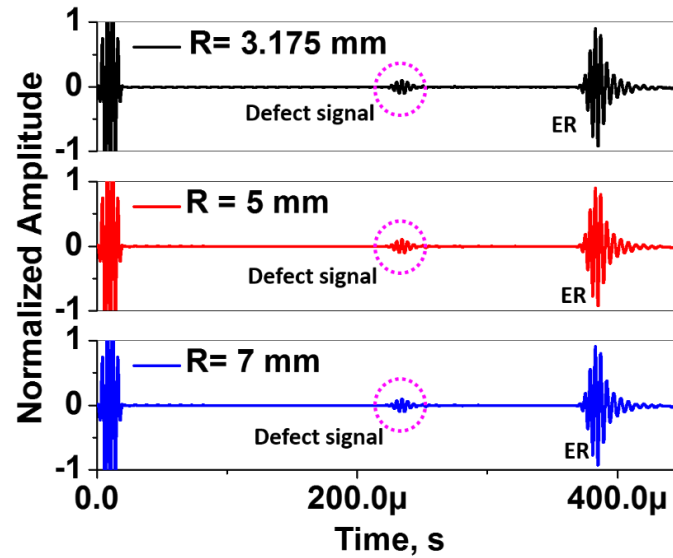


Fig. 4.18. Axial displacement signals obtained for 50% WT deep defects with the radii of curvature: (a)  $R=3.175$  mm, (b)  $R=5$  mm and (c)  $R=7$  mm, respectively. ER stands for the end reflection. (Finite element simulation)

#### 4.3.3.3 Mode conversion of $L(0,2)$ mode

To check the mode conversion of  $L(0,2)$  mode, after its interaction with a non-axisymmetric sodium impingement defect, FE simulation was performed with a 50% WT deep defect with the radius of curvature,  $R=3.175$  mm located at 600 mm in a 1.0 m SG tube. The axial ( $U_z$ ), radial ( $U_r$ ) and angular displacement ( $U_\theta$ ) components were recorded at the receiver points at the end face of the tube and averaged. Figure 4.19 shows the time signals of the axial, radial and the angular displacement components. All the amplitudes were normalized with the maximum of the end reflected axial component. It can be seen that  $U_z$  component contains a defect signal and the end reflection and both of which correspond to  $L(0,2)$  mode. However,  $U_r$  and  $U_\theta$  components show mode converted signals of  $F(1,3)$  and  $F(1,2)$  modes. The end reflections of the flexural modes do not show up due to their slower propagation than  $L(0,2)$  mode. They can be observed on a larger time scale than that shown in the figure.  $L(0,2)$  mode has a dominant axial displacement and a small radial displacement. Therefore, it undergoes

mode conversion to nearby flexural modes whose displacements fields are similar. The percentages of amplitude of F(1,3) and F(1,2) modes for the angular displacement ( $U_\theta$ ) with respect to the amplitude of the defect signal of  $U_z$  are 20% and 40% , respectively. While, the percentages of amplitude of F(1,3) and F(1,2) modes for the radial displacement ( $U_r$ ) with respect to the amplitude of defect signal of  $U_z$  are 0.097% and 0.03% , respectively. Even though mode conversion is addressed only for non-axisymmetric sodium impingement damage, it can also be observed in the cases of pinholes, axial defects and partial circumferential defects. As mentioned earlier, this also substantiates the fact that an axisymmetric mode like L(0,2) mode incident on a non-axi-symmetric defect, undergoes mode conversion to non-axi-symmetric flexural modes.

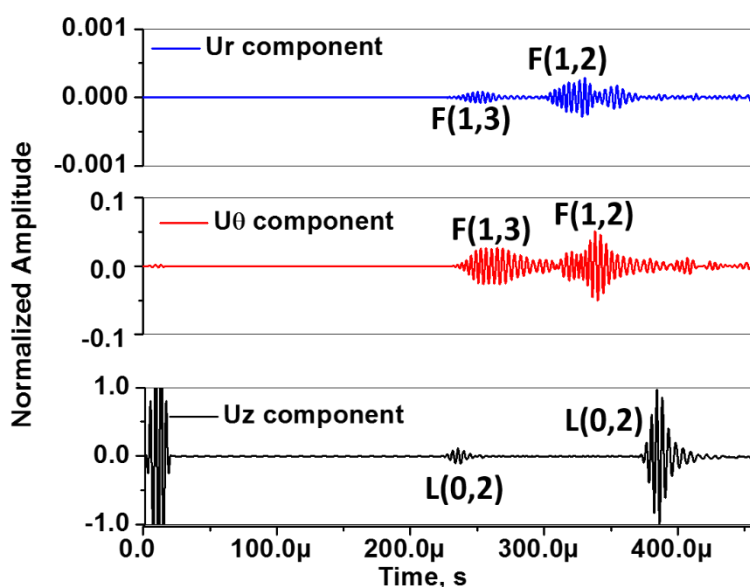


Fig. 4.19. Axial ( $U_z$ ), radial ( $U_r$ ) and angular displacement ( $U_\theta$ ) signals obtained for 50% WT deep sodium impingement defects with the radius of curvature,  $R=3.175$  mm (Finite element simulation)

#### 4.3.3.4 Shadowing of defects

The influence of one circumferential defect on the reflected amplitude from the second circumferential defect has been studied using FE simulation. Towards this, a 3D-finite

element models were developed in ABAQUS to simulate L(0,2) mode propagation in a 1.0 m long SG tube with a full circumferential defect of depth 0.92 mm and width 1 mm at one of the following locations: 250 mm, 350 mm, 400 mm, 450 mm, 500 mm, 550 mm, 650 mm or 750 mm in each simulation. Further, to study the shadowing effect of the defect, a circumferential defect was fixed at 250 mm and another circumferential defect was placed at one of the following locations: 252 mm, 257.5 mm, 260 mm, 275 mm, 300 mm, 325 mm, 350 mm, 400 mm, 450 mm, 500 mm, 550 mm, 650 mm and 750 mm in each simulation. Therefore, in one model, two defects were taken at a time. Figures 4.20a and b show the FE model with one circumferential defect and two circumferential defects, respectively.

Figures 4.21a and b show the averaged time signals for the cases of a circumferential defect (CD) at 500 mm and circumferential defects (CD1 & CD2) at 250 mm and 600 mm in 1.0 m long tubes, respectively. The reflected amplitude for CD2 at 600 mm is reduced in the presence of CD1 at 250 mm, as shown in Fig. 4.21b, due to the partial reflection from CD1. Figure 4.22 shows the maximum reflected amplitudes for CD at various locations and the max. reflected amplitudes for CD2 at various locations in presence of CD1 at 250 mm. In Fig. 4.22, it can be seen that there is a reduction of the reflected amplitude as the distance of the CD increases due to the small attenuation of the L(0,2) mode. It can be seen that (the red curve in Fig. 4.22) there is a reduction in the reflected amplitude corresponding to CD2 which is partly due to the presence of CD1 and attenuation. However, the reduction is not smooth as compared to that of the first case. The regions far away from CD1 (300 mm) follow the trend observed as in the first case (black curve). And in the regions close to the defect CD1, the reflected amplitudes corresponding to CD2 are much lower than the reflected amplitudes corresponding to a single CD at respective locations followed by a sudden peaking of the reflected amplitude with CD2 at 260 mm. It is due to the interference of the signals from the

two defects. At the separations of 2 -7.5 mm, the reflected amplitudes for the two-defect case is slightly lower indicating the destructive interference between the signals from the CD1 and CD2. At the separation of 10 mm, the reflected amplitude becomes double due to constructive interference. For distances more than 10 mm, the interference effect gradually reduces. There is a kink in the reflected amplitude at 500 mm separation due to the constructive interference between the signals from reflected CD1 and CD2: The signal from CD1 at 250 mm undergoes four reflections between the near end of the tube and CD1 and travels the path length of 1 m while the signal reflected from CD2 at 500 mm also travels the path length of 1 m.

At small separations of the defects, it is evident that two defects are seen as a single defect with a smaller size. In other words, the presence of the second defect is shadowed by the first defect. For instance, the drop in the reflected amplitude from CD2 at 252 mm with respect to that from CD at 250 mm is 4.7 dB. Even though, the technique is successful in detecting multiple defects lying along the same line, the detection may be limited by this. Hence, in such cases, a complimentary localized ultrasonic technique namely internal rotary inspection system can be used.

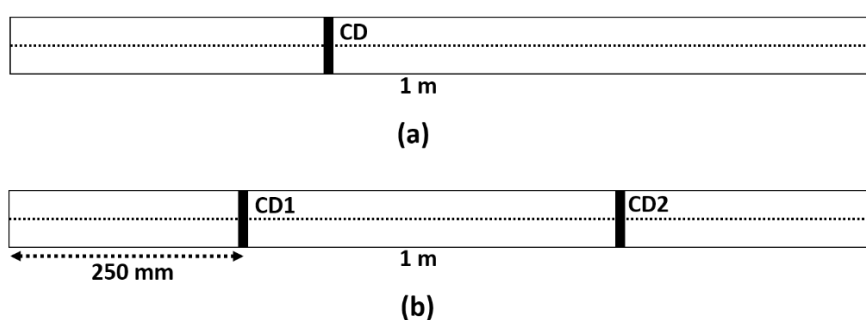


Fig. 4.20. (a) Finite element model with a full circumferential defect (CD) and (b) finite element model with CD1 fixed at 250 mm and CD2 at different locations.

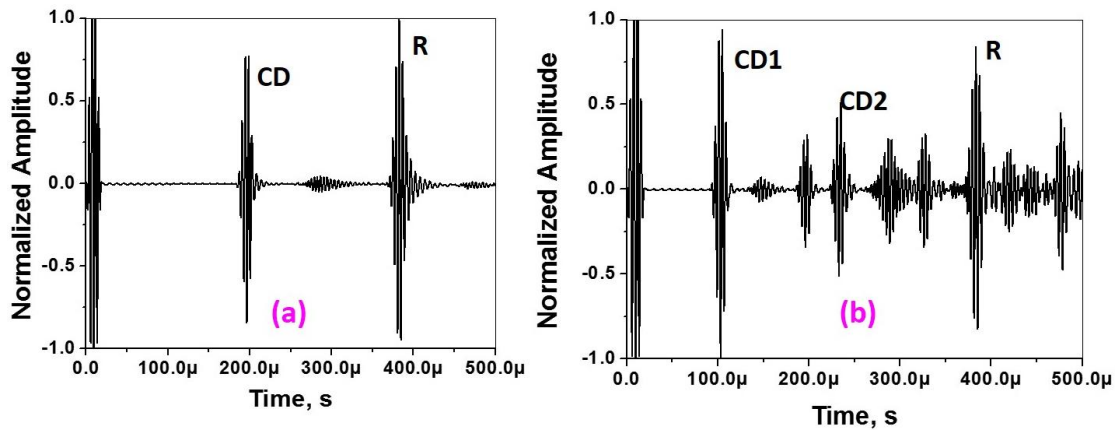


Fig. 4.21. Axial displacement signals: (a) for the case of circumferential defect (CD) at 250 mm and (b) for circumferential defect (CD1) at 250 mm and CD2 at 600 mm in a 1 m long tube. **R** denotes the tube end reflection. (Finite element simulation)

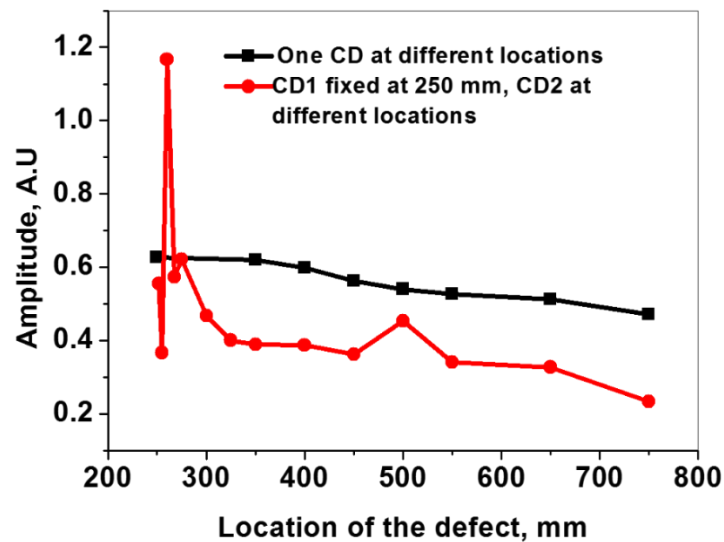


Fig. 4.22. Maximum reflected amplitudes obtained for the case of a single circumferential defect (CD) at various distances and the maximum amplitudes obtained for the case with a circumferential defect (CD1) fixed at 250 mm and with the second circumferential defect (CD2) moved for different distances in 1 m long tubes. The dimensions of the CDs are 0.92 mm depth, 1 mm width and full circumference. (Finite element simulation)

### 4.3.3.5 FE results for ID and OD pinhole and axial defects

It is difficult to fabricate an ID defect. Hence, to study the response of an ID defect to L(0,2) mode at 250 kHz, FE simulations have been performed with both ID and OD pinholes and axial defects. The defects were placed at 375 mm in 750 mm long tubes. Figures 4.23a and b show the FE signals for the cases of ID and OD pinholes, respectively. It can be clearly seen that the ID and OD pinhole defects are obtained with the signals of similar amplitudes (normalized with respect to OD pinhole amplitude) due to the nearly uniform axial stress of L(0,2) mode throughout the thickness. Figure 4.24 shows the plot of reflected amplitudes from ID and OD axial defects having depths of 0.46 mm and 1.38 mm and axial lengths of 5 mm to 30 mm in the step of 5 mm. Even for this case, ID and OD responses are similar. It thus indicates that irrespective of the radial and angular locations for a fixed axial location, a defect can be detected with similar SNR. The observation was found to be true for circumferential defects as well.

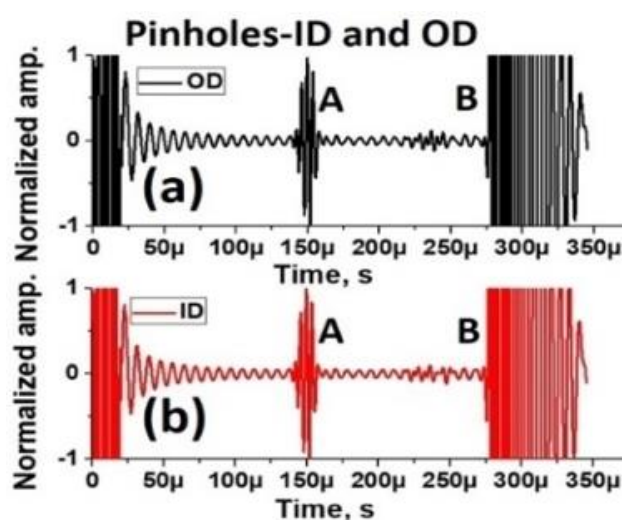


Fig. 4.23. A comparison of (a) inner diameter (ID) and (b) outer diameter (OD) pinhole signals. **A** refers to the defect signal and **B**, the tube end reflection. The diameter and the depth of the pinhole are 1 mm and 1.38 mm, respectively. (Finite element simulation)

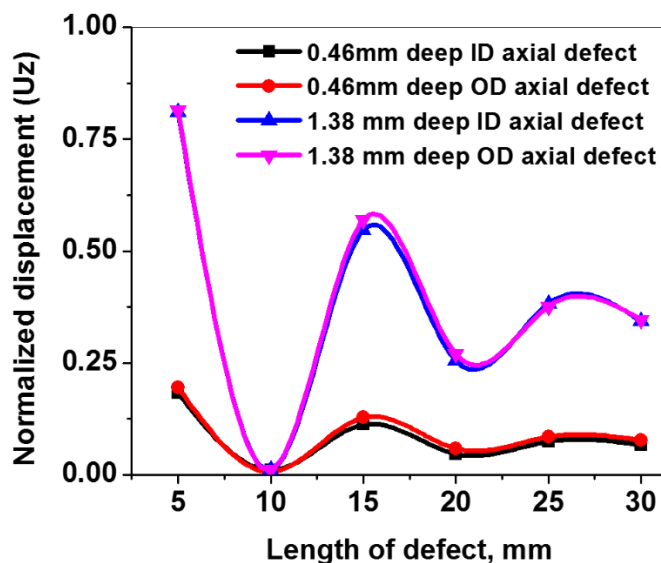


Fig. 4.24. Plot of inner diameter (ID) and outer diameter (OD) axial defects' response for various axial lengths. Axial defects have depths 0.46 mm and 1.38 mm. (Finite element simulation)

#### 4.3.4 Experimental results for circumferential defects in the thermal expansion bent section of the steam generator tube

It is a known fact that propagation of guided waves in bends is complicated by dispersion and mode conversion. This can lead to a further complication when a defect is present in the bend. Hence, it can be very challenging or involved task to detect a defect in a bend region. Figure 4.25 shows the experimental results obtained for a bent tube with five full circumferential defects, as shown schematically in Fig. 4.3a(vii). The labels A, B, C, D and E in the figure represent defect signals and the label F represents the end reflection. It can be observed that the response of the defects in the bend to L(0,2) mode is good and the mode is able to negotiate the bend without much dispersion. The circumferential defects considered were of the same size and this fact is also evidently brought out by the relative amplitudes of the defects **A-E**. It is reported in the literature that the reflected amplitudes strongly depend on the location of a defect in the bend. However, it can be observed that the reflected amplitudes do not vary

much with the location of an axi-symmetric defect in the three successive bends. The reasoning for this observation is addressed in detail in Chap 6. The locations of the defects are found to be accurate to within 10 mm.

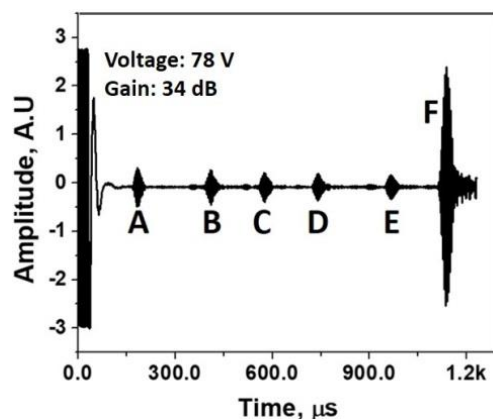


Fig. 4.25. Experimental signal obtained in a bent tube. **A-E** are circumferential defect labels, as in Fig. 3.4a(Vii) (and the dimensions and the locations of which are given in Table 3.1), representing corresponding defect signals. **F** stands for the tube end reflection.

## 4.4 Summary

The findings of the chapter are summarized as follows:

- An axisymmetric longitudinal mode  $L(0,2)$  is optimized in the frequency range, 170 kHz- 330 kHz using finite element simulation and experiments, for inspection of SG tubes of PFBR. Experiments were carried out with an ultrasonic transducer of center frequency 250 kHz coupled to the ends of the tubes.
- The group velocity of the mode is found to be 5387 m/s and the attenuation exhibited by the mode is 0.72 dB/m.

- The mode L(0,2) was examined for its long range propagation in a 3.8 m long tube and the maximum distance of propagation achieved was 45.6 m based on multiple reflections.
- The detection of multiple defects namely circumferential, axial, pinhole and sodium impingement defects lying in the same line of sight was examined using FE simulation and experiments. The experimental and simulation results agreed well. The multiple defects lying in the same line could be located fairly accurately.
- Following are the smallest defects detected:
  - (a) Circumferential defect: 0.23 mm (10%WT) depth, 7 mm circumferential extent and 1 mm width.
  - (b) Axial defect: 0.23 mm (10%WT) depth, 7 mm axial length and 1 mm width.
  - (c) Pinhole defect: 1.38 mm (60%WT) depth and 1 mm diameter.
  - (d) Sodium impingement defect: 0.23 mm (10%WT) deep defect of 8.6 mm length and 3.9 mm width
  - (e) Tapered defect: 0.23 mm maximum depth (10%WT), 15 mm length and 27 mm circumferential extent.
- FE simulations for the reflectivity showed that it is dependent on the effective area presented by the defect. Reflectivity of axial defects is found to be strongly dependent on the axial length with the maxima at quarter and three-quarters of the wavelength and minima at half and full wavelength. Furthermore, it was also found that there is a shadowing of one defect by another for small inter-separations.

- FE simulations for the cases of ID and OD axial and pinhole defects showed the similar ID and OD responses for L(0,2) mode.
- All the axisymmetric circumferential defects in the multiple bend were detected with good sensitivity. The influence of the thermal expansion bend of an SG on L(0,2) mode and detection sensitivity of non-axisymmetric defects in the bend are presented in Chap 6.
- Hence, the mode L(0,2) chosen meets all the requirement of long range propagation and detection of defects in the straight section and in the bend in terms of sensitivity.

## ***Chapter 5. Development of In-bore Magnetostrictive Transducer for Generating Optimized Ultrasonic Longitudinal Guided Wave Mode in SG Tubes***

### **5.1 Chapter overview**

This chapter covers the development of an in-bore magnetostrictive transducer for the generation of the optimized L(0,2) mode from ID side. This includes a systematic 2D axisymmetric FE modelling of an in-bore magnetostrictive transducer using FE simulation software COMSOL. The approach involves arriving at the optimum dimensions of permanent magnets and transmitter and receiver coils. Furthermore, it also presents equivalent circuit-based models for arriving at the optimum number of turns of the transmitter and receiver coils and their gauge. Further, it also presents the actual design of an in-bore magnetostrictive transducer with the optimized parameters from the FE results and the equivalent circuit models. The chapter also covers the study of long range propagation of L(0,2) mode and the detection of circumferential, axial and pinhole defects achieved using the developed in-bore magnetostrictive transducer. In addition, experimental validation of FE results for a frequency sweep and the circumferential defect case is presented.

### **5.2 Need for in-bore magnetostrictive transducer**

The experimental results presented in the previous chapter were obtained by coupling an ultrasonic transducer to the ends of SG tube segments. However, in actual testing there is no access to the tube end. The coupling of an ultrasonic transducer can only be made with the tubesheet. Figure 5.1a shows the ultrasonic transducer placed on the tubesheet of a mockup

SG facility with the SG tubes of length 4.6 m and Fig. 5.1b shows the signal obtained using the ultrasonic transducer placed on the tubesheet. It can be seen that there is a complete absence of reflection from the end of the tube. The loss of signal is due to the tubesheet geometry and it can be understood from Fig. 5.2.

Figure 5.2a shows an ultrasonic transducer directly coupled to the free end of the tube resulting in L(0,2) mode generation. Figure 5.2b shows an ultrasonic transducer directly placed on the tubesheet, as there is no access to the tube. It can be easily understood from Fig. 5.2b that the tubesheet-to-spigot-weld region is all together a different structure with many thickness variations than a free end of the tube. Therefore, L(0,2) mode is not generated. Since, SG tubes of PFBR are ferromagnetic, alternate means of generating L(0,2) mode using magnetostriction is investigated. Figure 5.2c shows the conceived model of such an in-bore magnetostrictive transducer that can be designed to generate L(0,2) mode from ID side. The model considered is symmetric about the central axis of the tube since fields of L(0,2) mode are symmetric about the central axis. Once the mode is generated efficiently by this means, every aspect of propagation and defect detection, as discussed in the previous chapter, remains the same.

To develop a suitable in-bore magnetostrictive transducer for SG tubes of PFBR, finite element models in FE simulation software COMSOL Multiphysics were built and studied. The following sections discuss the results of the models, fabrication of an in-bore transducer using the FE results for the generation of L(0,2) mode and necessary experimental validation.

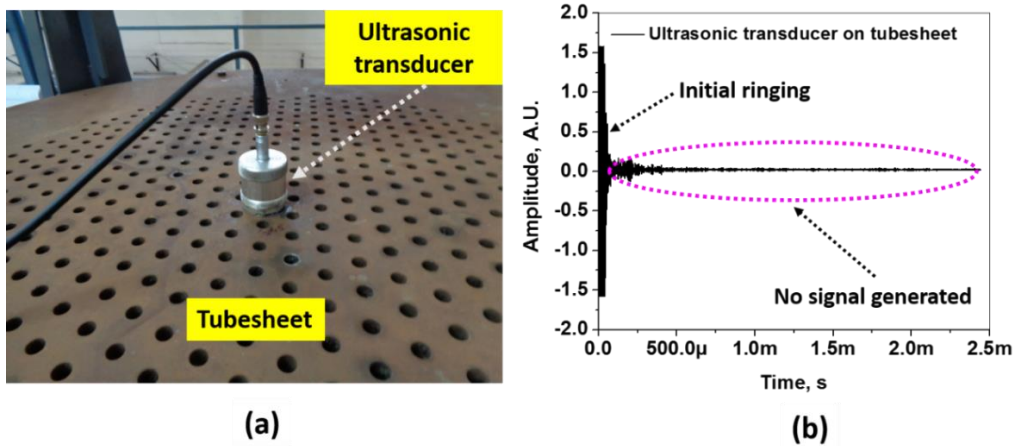


Fig. 5.1. (a) Photograph showing an ultrasonic transducer placed on the tubesheet of the mockup steam generator (SG) facility and (b) a signal obtained using the ultrasonic transducer placed on the tubesheet.

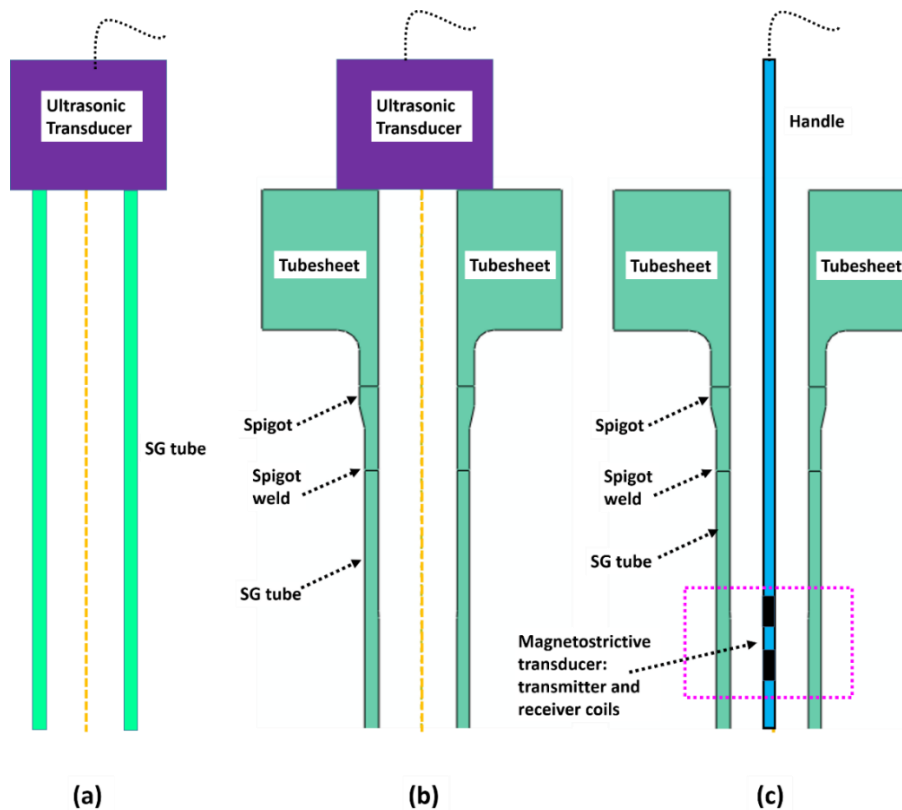


Fig. 5.2. 2D section of SG tube and tubesheet: (a) an ultrasonic transducer coupled to the free end of a tube, (b) an ultrasonic transducer coupled to the tubesheet and (c) a conceived model of a magnetostrictive transducer placed beyond the spigot of the tube sheet in the tube region.

## 5.3 Results and discussion

This section is divided into two parts, namely (a) FE simulation for optimization of the transmitter and receiver coil parameters and (b) design of a magnetostrictive transducer and experimental validation of the FE results.

### 5.3.1 FE simulation in COMSOL

The aim of the study is to optimize the dimensions of the transmitter and receiver coils for magnetostrictive based generation of L(0,2) mode. The schematic of the FE model is shown in Fig. 3.10 in which a magnetostrictive transducer is modelled in-bore to fit the bore diameter of 12.6 mm (ID of the SG tube). Various dimensions of the transmitter and receiver coils considered were given in Table 3.3 of Chapter 3. The FE models developed in COMSOL were 2D-axisymmetric and the related FE parameters are given in Section 3.5.4. The FE models were axi-symmetric, as L(0,2) mode is axi-symmetric. Four studies were carried out in sequence to achieve transmission (Joule effect) and reception (Villari effect), as described in Section 3.5.5 and Flowchart (Fig. 3.13).

#### 5.3.1.1 Stationary study

##### 5.3.1.1.1 Optimization of length and diameter of permanent magnets

FE studies were carried out in a 200 mm long tube, as mentioned in Section 3.5.2.2. Initially, 2D- axisymmetric permanent magnets of high strength (1.48 T) were modelled inside the tube to obtain the magnetic field in the wall of the tube. The diameter of a permanent magnet is parametrized from 2 mm to 12 mm in the step of 2 mm for a fixed length of 50 mm, as the ID of the SG tube is 12.6 mm. The electrical and magnetic properties used in the FE models are given in Table 3.3 of Chapter 3. The objective of the study is to optimize the diameter and

length of a permanent magnet and obtain the magnetic permeability in the tube using the magnetic induction generated by the optimized permanent magnet. The governing equation for this stationary study is given by Eq. (2.50). The boundary and interface conditions applied were given in Section 3.5.2.2.1.

Figure 5.3 shows the arrow plot of the magnetic field vector in the magnet, air gap and the tube. It can be seen that the magnetic field emanated from the magnet curves and goes inside the tube and enters the other end through the tube. Thus, a magnetic circuit is formed between the north pole, a small segment of the SG tube, and the south pole of the magnet, as the path has lower reluctance than a circuit through the air gap. The magnetic field in the air gap is almost zero. Figures 5.4a and b show the line plots for the radial component ( $B_r$ ) for the permanent magnet of diameter 10 mm and the axial ( $B_z$ ) components along the central line passing through the tube wall for diameters 2 to 12 mm in the step of 2 mm, respectively. The  $B_r$  component is quite small ( $\sim 0.8$  mT) in the tube except for the regions near the poles ( $\sim 0.2$  T) of the magnet because the flux lines become dense (concentrate) and curve to enter and exit the tube. The  $B_z$  component is nearly uniform and axial for the length of 50 mm. The maximum values of the  $B_z$  components obtained for various diameters are superimposed on the B-H curve of Mod. 9Cr-1Mo steel (Fig. 5.4c). It can be seen in Fig. 5.4c that as the diameter of a magnet increases, the magnetic induction in the tube also increases due to the increase in the magnetic flux emanating from the magnets of fixed strength (1.48 T).

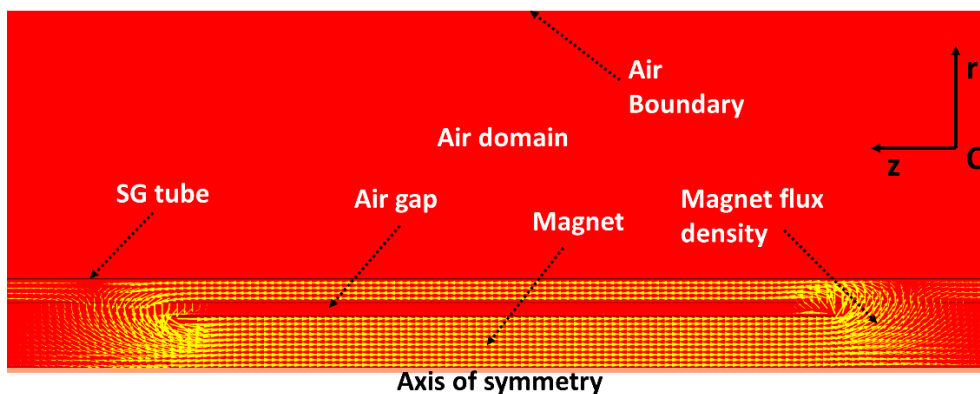


Fig. 5.3. Arrow plot showing magnetic field lines. (Finite element simulation)

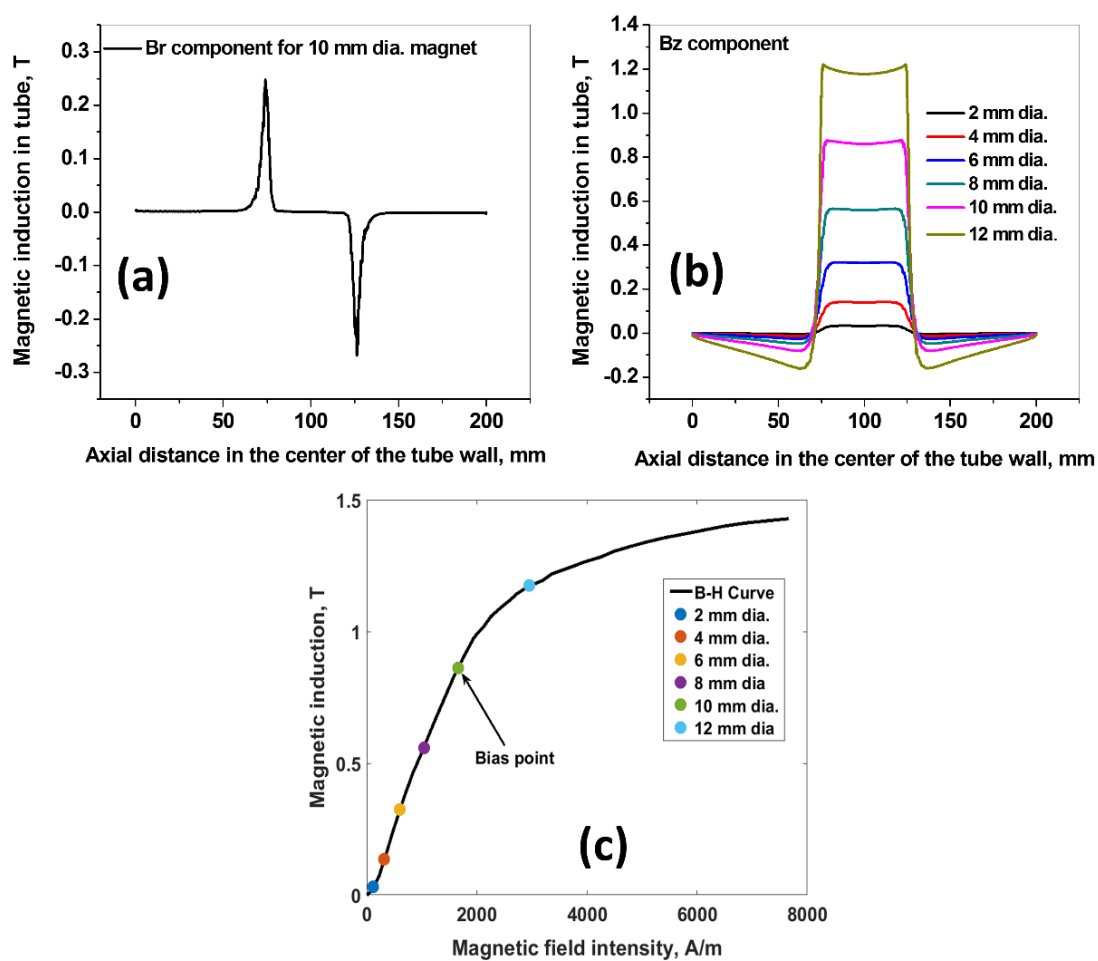


Fig. 5.4 (a) Br component along the central line of the tube wall for the magnet of diameter 10 mm and length 50 mm, (b) Bz component along the central line of the tube wall for magnets of various diameters and fixed length of 50 mm and (c) magnetic induction in the tube for the diameters in Fig. 5.4b superimposed onto the experimental B-H curve for Mod. 9Cr-1Mo steel. (Finite element simulation)

The maximum magnetic induction of  $\sim 1.2$  T for the magnet with the diameter of 12 mm, shown by a blue marker in Fig. 5.4c, is in the non-linear region of the B-H curve [166]. This point is not chosen as a bias point because it may lead to inefficient generation of L(0,2) mode and undesirable modes. Moreover, the constitutive equations (Eqs. (2.37 and 2.38) used for the study hold good only for the linear region of B-H curve. Hence, the maximum magnetic induction of 0.82 T in the linear region of the B-H curve (green marker) corresponding to 10 mm diameter of the magnet is chosen as a bias point. Elastic stresses generated in a specimen depend on the applied magnetic fields, as indicated by Eq. (2.43). Hence, the bias point for the magnet of 10 mm diameter will provide larger stresses for efficient generation of L(0,2) mode than the other lower points of lower magnetic induction corresponding to smaller magnet diameters.

With the optimized magnet diameter of 10 mm and the strength of 1.48 T, the influence of the length of the magnet in the magnetic induction in the tube was studied by parametrizing the length from 25 mm to 125 mm in the step of 25 mm. Figure 5.5a shows the axial magnetic induction in the central line of the tube wall for various lengths of magnets with the optimized diameter of 10 mm. The axial magnetic induction remains almost uniform in the projected lengths of the magnets. The variation of magnetic induction in the concave up regions for the cases of 25 mm to 150 mm lengths of the magnets is less than 0.1 T. Furthermore, the dip slightly increases with the increasing magnetic length because of the increased reluctance for the increasing lengths of the magnets. Figure 5.5b shows the plots of the gradient of the axial magnetic induction shown in Fig. 5.5a versus the axial distance in the tube wall. The large positive and negative gradients indicate the regions near the poles of the magnet, whereas the mid-flats represent regions between the poles and their gradients are almost zero. Hence, it can be concluded that the length of the magnet does not have much influence on the magnetic

induction in the tube. Considering the space required for the transmitter and receiver coils to be wound over the magnet and cross-talk between the coils, any length of the magnet over 50 mm can be chosen. For the thesis, a magnet of 100 mm length was chosen. The variation of  $B_z$  corresponding to the magnet of 100 mm from the extremes to the midpoint is  $\sim 0.05$  T. This ensures that  $B_z$  is almost uniform ( $\sim 0.82$  T) in the projected length of the 100 mm long magnet in the tube wall. The uniformity of  $B_z$  is the requirement for the generation of an axisymmetric  $L(0,2)$  mode.

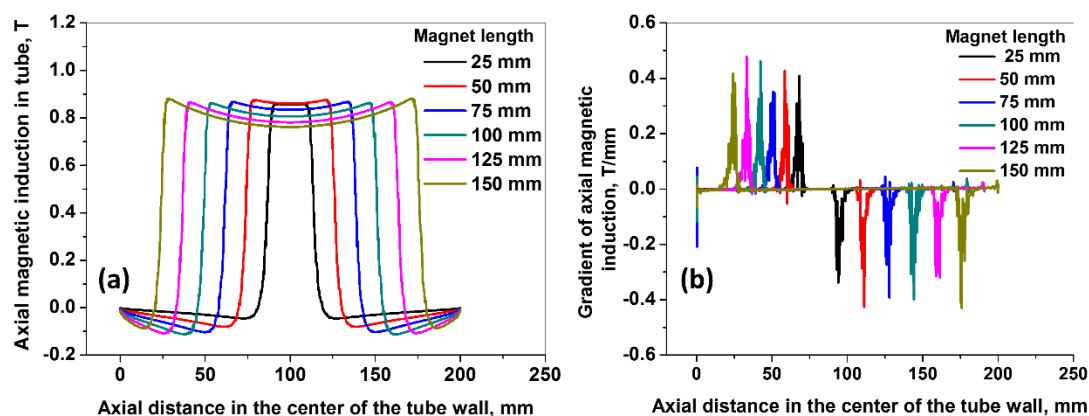


Fig. 5.5 (a) Axial magnetic induction along the central line of the tube for magnets of various lengths and for a fixed diameter of 10 mm and (b) their gradients. (Finite element simulation)

With  $B_r$  and  $B_z$  values obtained for the optimized magnet length and the diameter of 100 mm and 10 mm, respectively, the corresponding equivalent applied magnetic fields ( $H$ ) were obtained from the B-H curve (Fig. 5.4c) under the assumption that the same B-H curve holds good for both radial and axial directions. The radial and the axial permeabilities of the tube corresponding to the bias were calculated using the formula:  $B = \mu H$ . Equation (5.1) is the permeability matrix formed with the radial and the axial components of the magnetic permeability. The magnetic permeability components in the other directions are zero as the

magnetization is predominantly along the axial direction. Equation (5.1) was ascribed to the region of the tube for dynamic analysis.

$$\mu_r = \begin{bmatrix} 66 & 0 & 0 \\ 0 & 0 & 0 \\ 0 & 0 & 422 \end{bmatrix} \quad (5.1)$$

### 5.3.1.2 Dynamic Analysis

The objective of this analysis is to generate dynamic  $B_r$  and  $B_z$  fields in the region of the tube with the permeability defined by Eq. (5.1). To this end, a five Hanning windowed toneburst having peak current 1 A and 300 kHz center frequency was applied to the transmitter coil of 10 mm length and 0.4674 mm width, as shown in Fig. 3.11. The center of the transmitter coil was chosen at 147.5 mm from one end of the tube. The description of the FE model is given in Section 3.5.2.2 and the schematic of the model is shown in Fig. 3.10b. The governing equations for this dynamic study are given by Eq. (2.55 and 2.56) and the boundary and interface conditions applied were given in Section 3.5.2.2.1.

The magnetic field generated in the tube due to the application of time-varying current to the coil at time 8.33  $\mu\text{s}$  is shown as a contour plot in Fig. 5.6. It can be clearly seen that the magnetic field concentrates at the ID of the tube for a depth of 0.25 mm due to the skin effect. The maximum field at the ID is 0.18 T whereas that at 0.25 mm depth is 0.0003 T. Figures 5.7a and b show the plots of  $B_r$  and  $B_z$  at the ID of the tube below the center location of the transmitter coil. The magnitude of  $B_r$  is very small and is of the order of  $\mu\text{T}$  and that of the  $B_z$  is 0.18 T. It can be concluded that the dynamic field existing in the tube is predominantly  $B_z$ . Figure 5.7c shows the variation in the maximum of  $B_z$  at ID along the length of the tube in the vicinity of the transmitter coil. It can be seen that  $B_z$  component is nearly uniform in

the central region and then drops off to zero on both sides due to the fall of field with distance from the source. The variation in the field from the center to the ends of the projection of the coil onto ID is around 0.065 T. The field in the tube drops off to nearly-zero value at a distance of 5 mm from the ends of the transmitter coil. Hence, to minimize the cross-talk, the separation between the transmitter and receiver coils can be chosen as 5 mm or more. For the thesis, the gap was chosen as 10 mm.

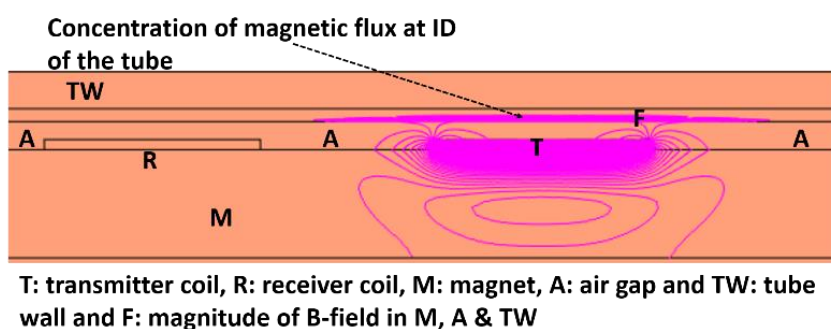


Fig. 5.6. The magnitude of magnetic field at  $8.33 \mu\text{s}$ , shown as contour plot (Finite element simulation).

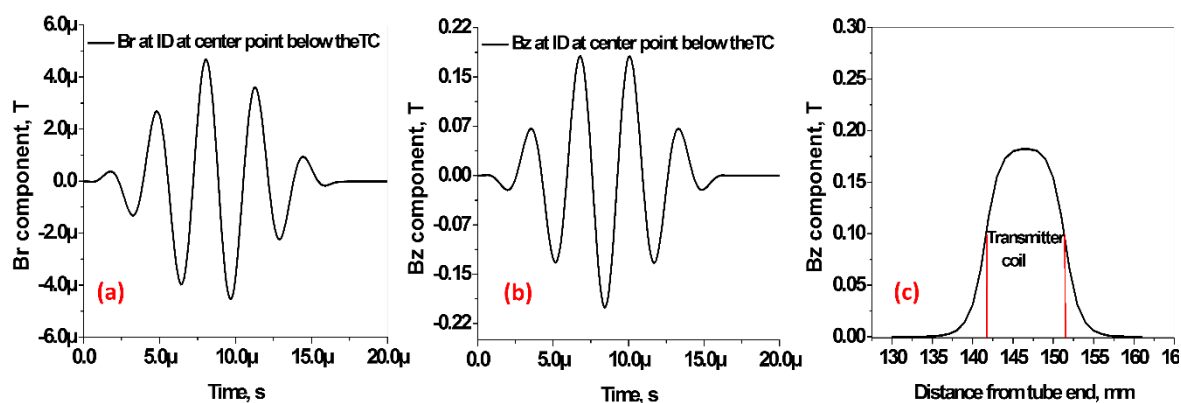


Fig. 5.7 (a)  $B_r$  and (b)  $B_z$  components at the ID of the tube at the center point below the transmitter coil (TC) and (c) the variation in the maximum of  $B_z$  at the ID of the tube with distance at  $8.33 \mu\text{s}$ . (Finite element simulation)

### 5.3.1.3 Generation of L(0,2) mode at 300 kHz

The objective of this analysis is to generate L(0,2) mode at 300 kHz using the dynamic magnetic fields ( $B_r$  and  $B_z$ ) as inputs in a tube of length 650 mm. The connection of the

dynamic magnetic fields and the stress fields was achieved by using constitutive relation (Eq. (2.43)). With the dynamic stresses generated by the applied magnetic field as an initial stress, the governing equation given by Eq. (2.18) was solved using the boundary conditions given by Eq. (2.35).

First, the length of the transmitter and receiver coils was taken to be 10 mm with the end-to-end separation of 10 mm, as arrived above. The center of the transmitter and receiver combination was chosen to be located at 157.5 mm from one end of the tube. The coupling of the dynamic  $B_z$  fields for elastic wave generation was performed, as mentioned in Eq. (2.43). The value of piezomagnetic coefficient ( $S$ ) used was  $6.8e-9$  m/A. The displacement fields of the wave were captured in the tube of length 650 mm at the center location of the receiver coil at 167.5 mm. Secondly, the magnetic field caused by the stresses of  $L(0,2)$  mode was calculated using Eq. (2.45) and using the magnetic field, the voltage induced in the receiver coil was computed using Eq. (2.56).

Figures 5.8a and b show the radial and axial components of the displacement picked up at 167.5 mm in the tube of 650 mm length. The radial component is smaller than the axial component, which is in conformity with the mode shapes of  $L(0,2)$  at 300 kHz (Fig. 4.1c). The group velocity of the mode is found to be 5386 m/s as against 5380 m/s, obtained from Disperse simulation software. Thus, the mode generated is indeed,  $L(0,2)$  mode at 300 kHz. The error in the velocity is 0.1%. The wave generated by this means is bi-directional. Label A is the signal reflected from the low reflection boundary at the near end. It can be seen that the amplitude of  $U_z$  is higher and  $U_z$  is non-dispersive, as predicted by dispersion curves. Furthermore, it can also be observed that the axial displacement is approximately three times the radial displacement component at ID of the tube, as predicted by Disperse mode shape

(Fig. 4.1c). Figure 5.9 shows the induced voltage in the receiver due to L(0,2) mode propagation in the tube, i.e., above the receiver coil. Figure 5.9 essentially bears the same information as Fig. 5.8b.

Besides, FE simulations were also performed for the frequencies 250 kHz and 350 kHz. Figure 5.10 shows a fall of the induced voltage (corresponding to end reflected signal) in the receiver coil due to the dominant skin effect at higher frequencies at the transmission. This leads to the reduction in the volume of the magnetostrictive energy and in turn, the particle displacement. However, the reduction in the induced voltage is from 10 mV to 5 mV, which is small and it can be compensated by slightly increasing the current driving the transmitter coil. Hence, for the study, the middle frequency of 300 kHz in the frequency range of 250 - 350 kHz was selected.

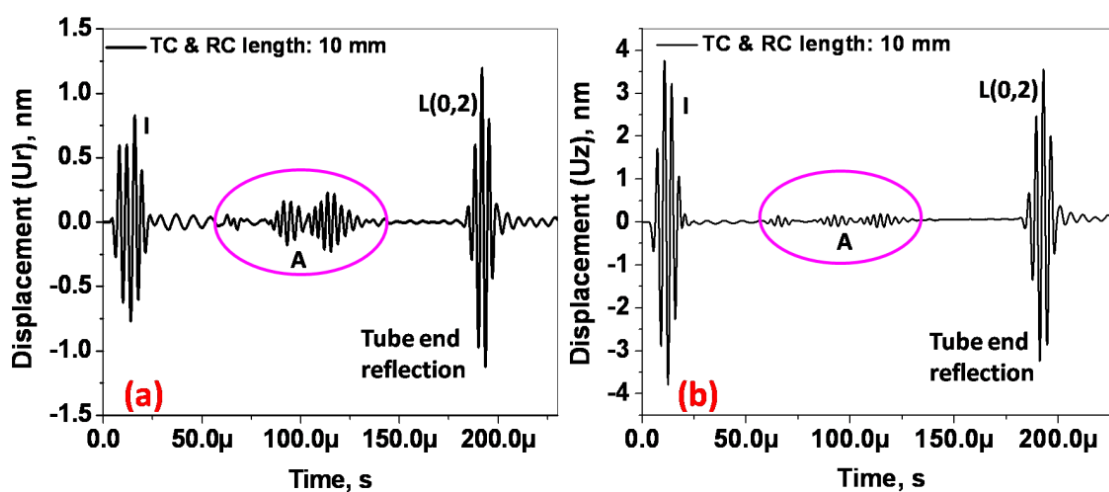


Fig. 5.8. Displacement signals at 300 kHz: (a) radial component ( $U_r$ ) and (b) axial component ( $U_z$ ) picked-up at 164.5 mm (center location of the receiver coil) in the tube of 650 mm length. Labels I: initial pick-up of L(0,2) mode and A: reflections from the left low-reflection boundary. (Finite element simulation)

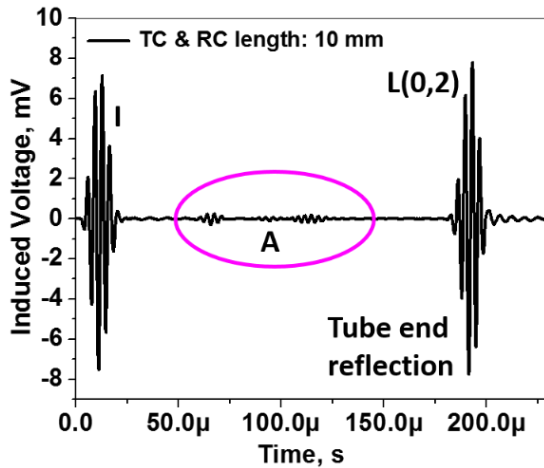


Fig. 5.9. Induced voltage in the receiver caused by L(0,2) mode at 300 kHz (Villari effect). Labels **I**: initial pick-up of L(0,2) mode and **A**: reflections from the left low-reflection boundary. (Finite element simulation)

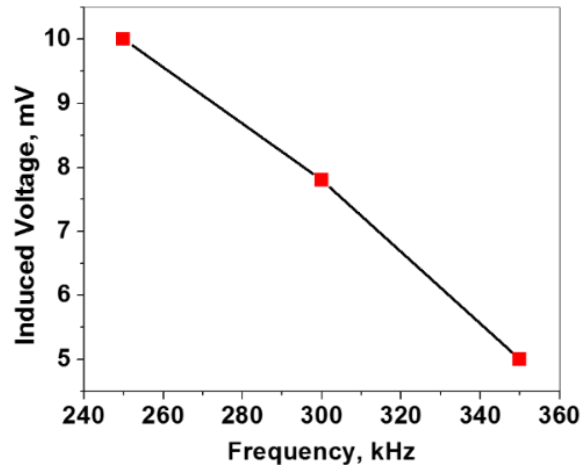


Fig. 5.10. Induced voltages caused by L(0,2) mode in the frequency range: 250 kHz – 350 kHz. (Finite element simulation)

### 5.3.1.4 Optimization of coil parameters

In the previous section, the length and the width of the transmitter and receiver coils were chosen based on rough estimations and L(0,2) mode was shown to be generated and received. However, to obtain the most efficient transmission, generation and reception, the parameters of the coils such as length, width, number of turns and a suitable wire gauge have to be optimized.

#### 5.3.1.4.1 Optimization of length

To optimize the length of the transmitter and receiver coils, FE simulations were performed with the transmitter and receiver lengths as 4.5 mm, 10 mm, 13.5 mm, 18 mm and 22.5 mm. Towards this, 34 SWG (0.2337 mm) wires of 2 layers were chosen initially. All the

simulations were performed with the same excitation of 1 A current at the peak frequency of 300 kHz.

Figure 5.11 shows the plots of the maximum induced voltage corresponding to the end reflected echo in a 650 mm long tube for various receiver and transmitter coil lengths. It can be seen that for a fixed length of the transmitter coil, the induced voltage in the receiver coil increases and reaches the peak at the receiver length of 10 mm and then decreases, followed by a small increase. This behaviour of increase and decrease in the maximum of the induced voltage is the consequence of constructive and destructive interference of transient magnetic fields with varying phases. It can also be seen that for small transmitter lengths, the induced voltage in the receiver coil is also small due to the reduction in the magnetostrictive stresses generated. Out of the three cases, the highest response is exhibited for the length of the transmitter and receiver of 10 mm which corresponds to approximately half the wavelength (18 mm). This clearly brings out the general idea of the dependence of the length of coils on the wavelength. This also indicates that the highest stresses are generated when the transmitter is of half-wavelength and a large net magnetic flux passes through the receiver coil when it is of half-wavelength. Hence, the length of the transmitter and receiver is chosen as 10 mm.

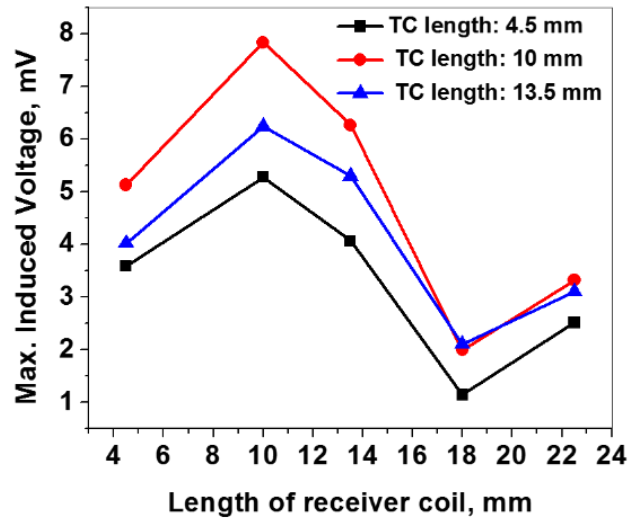


Fig. 5.11. Maximum induced voltage in the receiver coil for different transmitter and receiver coil lengths. TC: transmitter coil. (Finite element simulation)

#### 5.3.1.4.2 Optimization of number of turns ( $N$ ) of transmitter and receiver coils

In order to optimize the number of turns of the coils, Thevenin equivalent circuit models of the transmitter and receiver coils were considered. A typical experiment with coils will involve an instrument with a certain source and load resistance for excitation and reception. The Thevenin equivalent circuits for the transmitter and receiver coils are shown in Fig. 5.12a and b, respectively [168]. Figure 5.12a represents a transmitter with an inductance of  $L_T$  excited by a conventional Thevenin voltage ( $V_S$ ) with a source resistance ( $R_S$ ). In Fig. 5.12b,  $V_i$  represents the induced voltage in the receiver coil,  $L_R$  is the receiver coil inductance, and  $R_L$  is the load resistance.

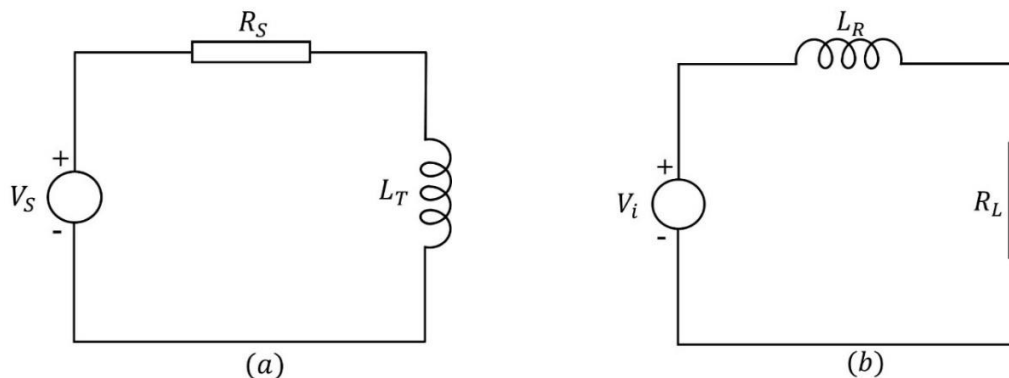


Fig. 5.12. Thevenin equivalent circuits of (a) transmitter coil and (b) receiver coil.

The gain of the transmitter  $G_T(\omega)$  and gain of the receiver  $G_R(\omega)$  can be written as Eqs. (5.2 and 5.3), respectively.

$$G_T(\omega) = \frac{j\omega L_T}{R_S + j\omega L_T} = \frac{j\omega}{j\omega + \frac{R_S}{L_T}} \quad (5.2)$$

$$G_R(\omega) = \frac{R_L}{R_L + j\omega L_R} = \frac{\frac{R_L}{L_R}}{j\omega + \frac{R_L}{L_R}} \quad (5.3)$$

The maximum gain of the transmitter (Eq. (5.2)) occurs at the frequency  $\omega_T$  as given by Eq. (5.4) and the maximum gain of the receiver (Eq. (5.3)) occurs for the induced voltage frequency  $\omega_R$  as given by Eq. (5.5)

$$\omega_T = \frac{R_S}{L_T} \quad (5.4)$$

$$\omega_R = \frac{R_L}{L_R} \quad (5.5)$$

By maximizing the gain in transmitter, the voltage across the inductance ( $L_T$ ) is maximized for a given source voltage thereby maximum energy is transferred to the magnetic field.

Maximizing gain in the receiver ensures the maximum voltage drop across the data acquisition unit ( $R_L$ ) for a given induced voltage in the receiver.

The inductance of a coil having a large length compared to the thickness can be written as given in Eq. (5.6) [169].

$$L = \frac{(25.4 \times 10^{-6})r^2N^2}{9r + 10l} = KN^2 \quad (5.6)$$

where  $r$  is the mean radius of the coil,  $N$  is the number of turns,  $l$  is the length of the coil and  $K$  is a geometrical constant. Substituting for  $L_T$  from Eq. (5.6) into Eq. (5.4) gives the number of turns of a transmitter ( $N_T$ ) for the maximum gain in the transmitter, as given by Eq. (5.7).

$$N_T = \sqrt{\frac{R_S}{\omega_T K}} \quad (5.7)$$

By substituting for  $L_R$  in Eq. (5.6) from Eq. (5.5), the optimum number of turns of receiver coil ( $N_R$ ) for a maximum gain can be written as Eq. (5.8)

$$N_R = \sqrt{\frac{R_L}{\omega_R K}} \quad (5.8)$$

With the optimized coil length of 10 mm and the optimized magnet radius of 5 mm considered as the inner radius of the coils, the geometrical constant ( $K$ ) was calculated for the typical source and load resistance of 50  $\Omega$ . The geometrical constant turns out to be  $4.37 \times 10^{-9}$ . With the values of  $K$ , load and source resistance, the optimum number of turns for the transmitter and receiver was calculated using Eqs. (5.7 and 5.8) in the frequency range of 200 to 400 kHz. Figure 5.13 shows the variation of the optimum number of turns with respect to the

excitation frequency. The optimum number of turns for the transmitter and receiver coils at the frequency of 300 kHz turns out to be about 80 turns. The figure also shows the optimum number of turns for other frequencies when the length and inner radius are 10 mm and 5 mm, respectively. It can be seen that the optimum number of turns reduces with frequency due to the reduction in the wavelength and thus, exhibits an inverse relation.

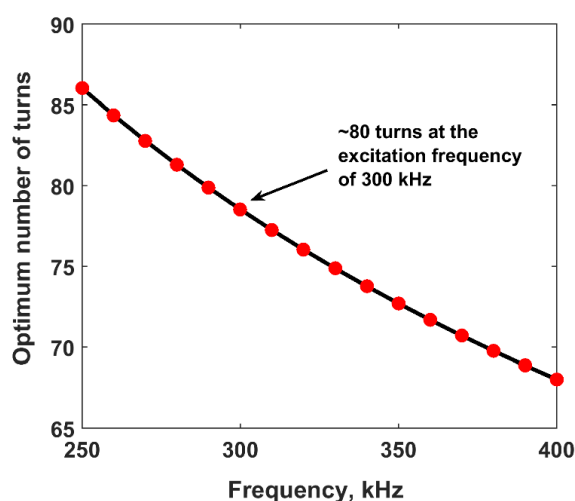


Fig. 5.13. Variation of optimum number of turns (N) with excitation frequency.

#### 5.3.1.4.3 Optimization of wire size for transmitter and receiver coils

The electromagnetic coupling between a tube and coil on the ID is expressed in terms of fill-factor. Fill-factor is a dimensionless parameter defined as the ratio of the area covered by coil to the area covered by the tube and is usually expressed in terms of percentage [170]. For achieving maximum sensitivity, the fill-factor should be equal to 100%, which is practically not feasible. However, for reliable inspection, the targeted value of a fill-factor should be as close to 100 % as possible [171]. Considering the ease of insertion/withdrawal of the probe and ensuring sufficient magnetic coupling between the probe and the tube wall, a fill-factor of 75 % was considered. For a given fill-factor, the outer diameter of the coils (OD) can be

estimated. As the coils are wound over the permanent magnet, the inner diameter of the coils (ID) is the same as the optimized magnet diameter. The diameter of the wire to be used for coil fabrication can be estimated using the expression given by Eq. (5.9):

$$\text{wire diameter} = \sqrt{\frac{L \times T}{N}} \quad (5.9)$$

where, L is the optimized length of the coil (=10 mm), N is the optimized number of turns (=80) and T is the coil thickness,  $T = 0.5 \times (\text{OD-ID})$ . The parameters, L =10 mm and N=80, were obtained for the frequency of 300 kHz. The ID of the coil is 10 mm, which is the same as the diameter of the permanent magnet. The OD of the coil can be calculated using the fill-factor. The ID of an SG tube is 12.6 mm. For 100% fill-factor, the ID of the tube becomes the OD of the coil. The ID of the coil is 10 mm and the OD of the coil is now 12.6 mm and T value calculates to be 1.3 mm. For the considered fill-factor of 75 % and the ID of an SG tube of 12.6 mm, the OD of the transmitter and receiver coils was calculated to be 10.9 mm. And the T value turns out to be 0.456 mm. By substituting L (=10 mm), N (=80) and T value of 0.456 mm in Eq. (5.9), the wire diameter was found to be 0.2387 mm. This wire diameter of 0.2387 mm corresponds to that of 0.2337 mm of 34 SWG and the 80 turns of 34 SWG for 10 mm will consist of 2 layers of 34 SWG.

**Table 5.1. Optimized parameters of an in-bore transducer to generate L(0,2) mode at 300 kHz**

Geometrical parameter	Estimated value
Diameter of the permanent magnet	10 mm
Length of the permanent magnet	$\geq 50$ mm, selected as 100 mm
Length of the transmitter/receiver coils	10 mm
Number of turns of transmitter/receiver coils	80 turns
Inner diameter of transmitter/receiver coils	10 mm
Outer diameter of transmitter/receiver coils	10.9 mm
Wire gauge	34 SWG (=0.2337 mm)
Number of layers	2 layers

### 5.3.2 Experimental validation

With the optimized coil parameters from FE simulations, an in-bore magnetostrictive transducer was fabricated (Fig. 3.2) and experiments were performed by inserting the magnetostrictive transducer in tubes. Figure 3.2a shows the photograph of the transducer and the enlarged view of the transmitter and the receiver coils wound over permanent magnets of length 100 mm. The transducer has transmitter and receiver coils of length 10 mm each and they are separated by a gap of 10 mm. The assembly of magnets and coils was wrapped in a thick adhesive tape and supported by a Perspex tube of OD 10 mm to form an integrated probe of 480 mm length for conveniently inserting the transducer in the SG tube.

The signals were acquired, as mentioned in Section 3.2. Five cases were considered: (a) 1 m long tube to check the generation of L(0,2) mode in the frequency range of 250 kHz to 350 kHz, (b) long range propagation of an L(0,2) mode, (c) detection of a full circumferential

defect of depth 0.46 mm (20% WT) and width 1.5 mm in a 1.5 m long tube, (d) detection of axial defects of depths 0.46 mm and 0.92 mm and width 15 mm and (e) detection of a pinhole of 1.5 mm diameter in a 1060 mm long tube. Comparison of the results obtained for the pinhole with that obtained using a piezoelectric ultrasonic transducer. FE simulation studies were performed for the cases (a) and (c). Since the FE model developed is axi-symmetric, the cases of the pinhole and the axial defect were not studied using FE analysis.

### **5.3.2.1 Frequency response (FE and experiment) and long-range propagation**

First, the frequency of excitation was swept in the range of 250 kHz to 350 kHz in the step of 10 kHz in a 1 m long tube. Figures 5.14a and b show the FE and the experimental signals for the frequencies: 280 kHz, 300 kHz, 320 kHz and 340 kHz. The signals were normalized with the amplitude of the first end reflection corresponding to the frequency of 280 kHz in all the cases. There is a good correlation between FE and experimental times of flight and amplitudes indicating the good performance of the designed transducer. In the figures, two end reflections, labelled R1 and R2, are shown. In each reflection, three wave packets appear as a result of bi-direction propagation of the waves generated.

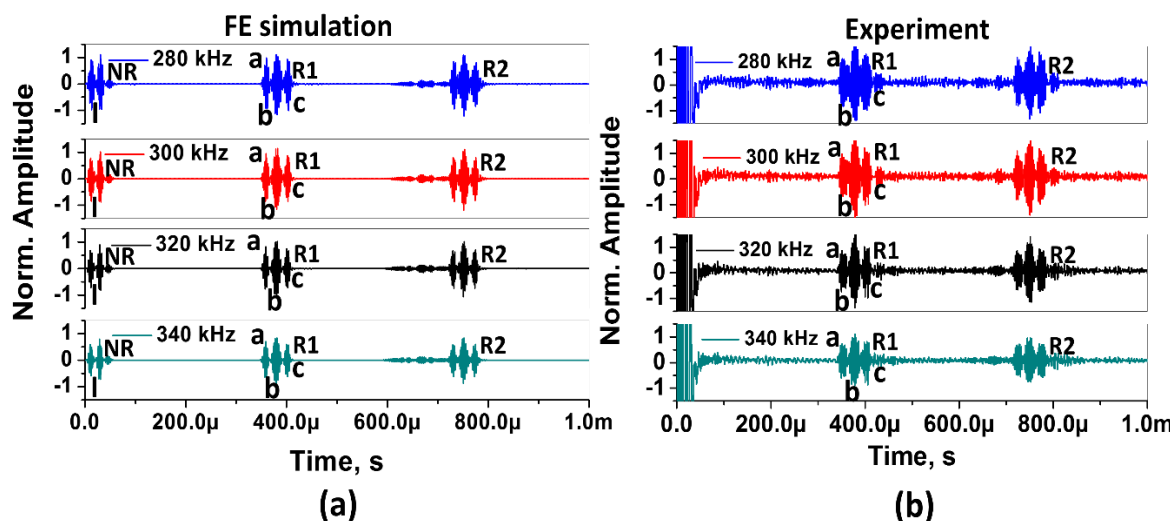


Fig. 5.14 (a) Finite element (FE) simulation and (b) experimental signals obtained in a tube of 1 m length, respectively, for frequencies: 280 kHz, 300 kHz, 320 kHz and 340 kHz. Labels a, b & c indicate wave packets resulting from bi-directional propagation of L(0,2) mode and R1 & R2 represent the first and second end reflections (Gain used: 60.8 dB). I: initial pick up and NR: near end reflection.

The formation of three wave packets is explained in Fig. 5.15. Signal labelled 'a' is due to forward propagation and far end reflection, signal 'b' is due to the constructive interference of backward propagated signal b' after its round trip with the near end reflection of a, labelled a' and signal 'c' is the reflection of signal 'b' from the near end. The time difference between a, b & c corresponds to twice the travel time between the transducer and the left end of the tube. The signal to noise ratio corresponding to the case of 300 kHz frequency is about 15 dB. The noise level was considered in the region between the initial ringing and the first end reflection.

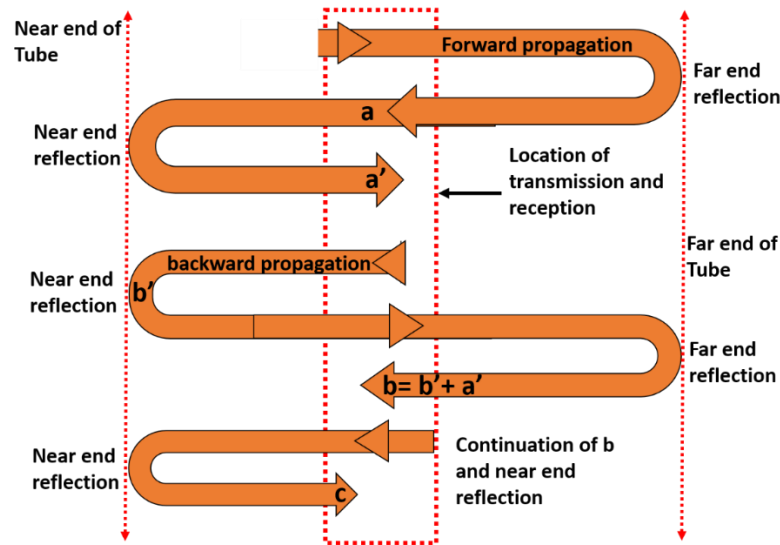


Fig. 5.15. Schematic of reflection pattern obtained in a tube with free ends due to bi-directional propagation (formation of three-echo pattern).

Figure 5.16a shows the FE and experimental amplitudes of the first end reflections (a in R1 of Figs. 5.14a and b) for the frequencies in the range of 250 kHz-350 kHz. The amplitudes were normalized with the amplitude of the first end reflection corresponding to the frequency of 250 kHz for all the cases. It can be observed that the amplitudes fall with increasing frequency due to the skin effect. There is a good agreement between FE and experimental amplitudes with the maximum error of less than 10% in the normalized amplitude (Fig. 5.16b). This shows the accuracy of the FE models in capturing the phenomenon very well. Figure 5.16c shows the difference in the times of flight between FE and experiment of the first end reflections. The first end reflection (a in R1 of Figs. 5.14a and b) was considered because of its direct path. FE times agree well with the experimental times. It can be seen in the figure that the maximum absolute error in time is about  $1.2 \mu\text{s}$ . The factor that could have caused the deviation is the slight difference in the elastic properties used for the models and the actual tubes.

Figure 5.17 shows the calculated experimental group velocity superimposed on the group velocity dispersion curves. The experimental group velocities are found to fall on the non-dispersive region of the dispersion curve for L(0,2) mode in the frequency range of 250 kHz-350 kHz. There is an excellent agreement between the experimental and the theoretical values. Hence, it is confirmed experimentally that the in-bore magnetostrictive transducer designed, indeed, generates L(0,2) mode in this frequency range. This is in absolute conformity with the predictions of the FE models. The range of errors in the velocity is between 0.3% to 1.2%.

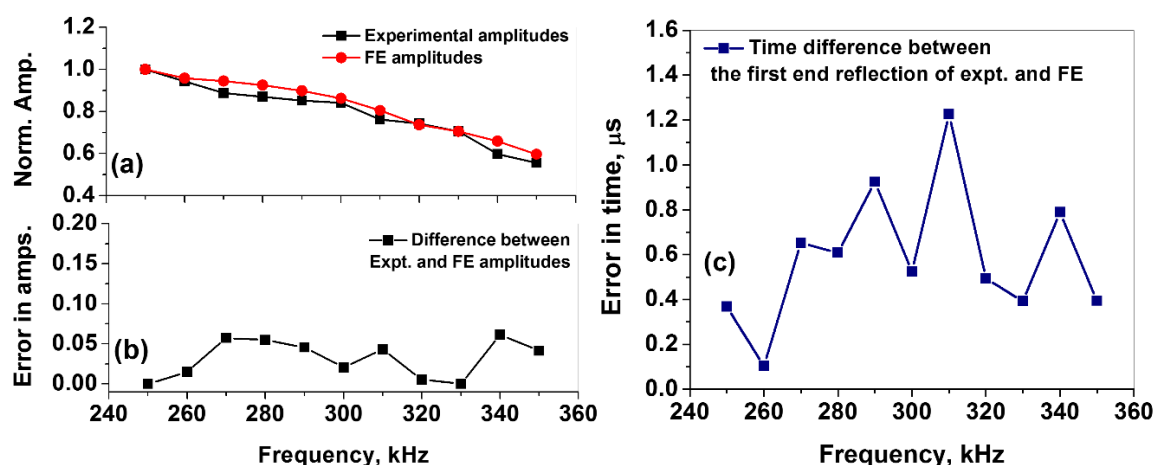


Fig. 5.16 (a) A comparison of Finite Element (FE) simulation and experimental amplitudes of the first end reflections obtained in a tube of 1 m length for different frequencies, (b) the difference in the amplitudes of the first end reflections between FE and experiment vs. frequency and (c) the difference in the times of flight of the first end reflections between FE and experiment vs. frequency. Amplitude values in (a) are normalized with the corresponding amplitudes at 250 kHz for both experimental and FE simulation.

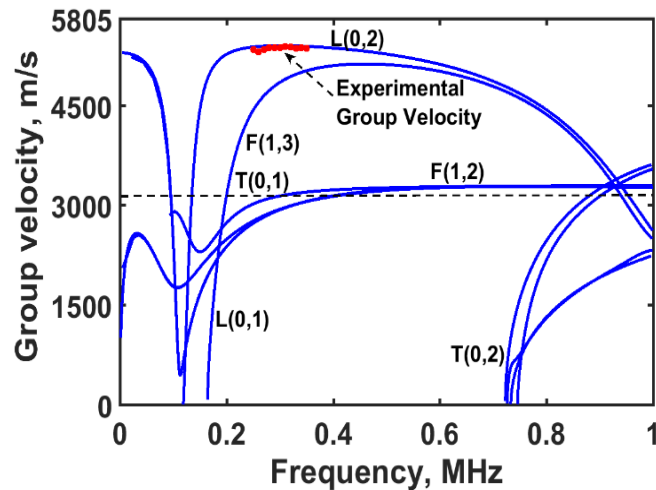


Fig. 5.17. Experimentally obtained group velocity superimposed on the group velocity dispersion curves.

To test the efficiency of the transducer for the long range propagation of L(0,2) mode, experiments were conducted on a 1.5 m long tube by inserting the transducer to the length of 110 mm. Figure 5.18 shows the signal obtained at the frequency of 300 kHz in the 1.5 m long tube. There are 17 end reflections in the figure, which amount to the propagation distance of 51 m. Thus, the L(0,2) mode at 300 kHz is able to propagate for a long range without much dispersion, as predicted. In other words, the widths of the multiple end reflections were calculated and it was found to be fairly constant. It indicates that there is no dilatation of the signals and hence, they are non-dispersive. The loss in amplitude from the first echo to the last echo is ~10 dB.

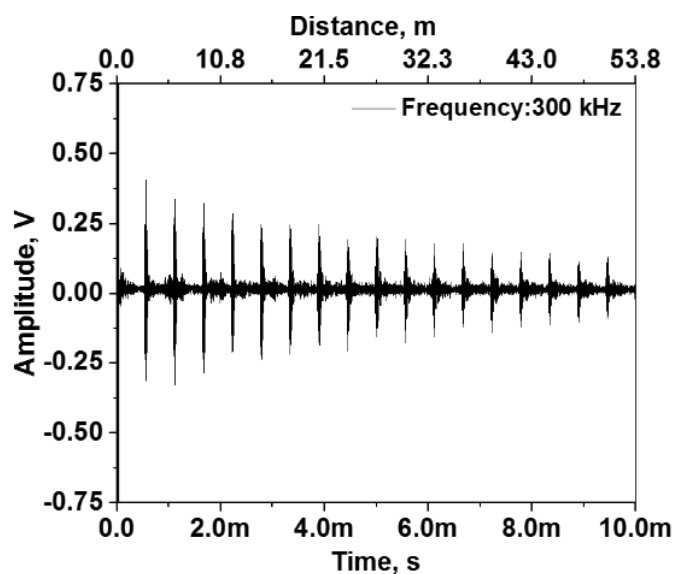


Fig. 5.18. Experimental signal, showing multiple end reflections, obtained in a 1.5 m long tube for the frequency of 300 kHz (Gain: 62.8 dB).

### 5.3.2.2 Detection of circumferential defect, axial defect and pinhole

Finally, to evaluate the sensitivity of the transducer in detecting defects, experiments were conducted on tubes for the frequency of 300 kHz for the cases: (a) 1.5 m long tube with a full circumferential defect of depth 0.46 mm (20% WT) and width 1.5 mm located at 840 mm from one end, (b) of 1.5 m long tube with axial defects having 20% WT and 40% WT depths, 15 mm length and 2 mm width, and (c) 1060 mm long tube with a pinhole of diameter 1.5 mm located at 600 mm from one end.

Figures 5.19a and b show the FE and experimental signals obtained at the frequency of 300 kHz in the tube with the circumferential defect. The FE and experimental amplitudes and times of flight compare well. The signals from the defect and the end reflections are clearly seen in the figure. The signals were normalized with the maximum amplitude of the first end reflection. The ratios of amplitudes of the first defect reflection to the first end reflection in FE and experiment respectively are 0.195 and 0.212. These values indicate a linear

relationship between the reflecting area (20%) and the reflected amplitude. The times of flight corresponding to the defect signals in FE and experiment respectively are 283.98  $\mu\text{s}$  and 283.24  $\mu\text{s}$ . With the use of the group velocity of 5386 m/s, the error in locating the defect is found to be about 1.7%.

Figure 5.20 shows the experimental signal obtained in a 1.5 m long tube with two axial defects. AD1 and AD2 with the inter-separation of 386 mm. AD1 is 40%WT deep, 2 mm wide and 15 mm long and located at 592 mm from the inspection end and AD2 is 20% WT deep, 2 mm wide and 15 mm long and located at 993 mm from the inspection end. It can be seen that the axial defects are detected with good sensitivity. The SNR of defect signal with respect to the noise between AD2 and the end reflection turns out to be 5 dB. The defects can be located within the relative error of 3%. The error in locating the defects is due to the interference occurring between the signals reflected from the front and back ends of the axial defects. Further, in addition to defect signals, there are small echoes resulting from mode conversion due to the axisymmetric nature of the defect.

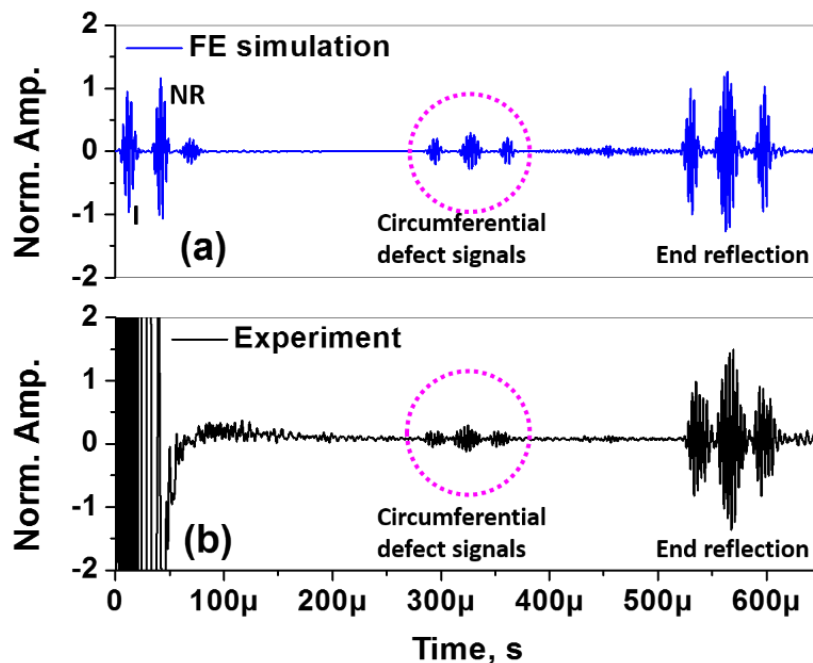


Fig. 5.19 (a) Axial displacement signal obtained in Finite element (FE) simulation and (b) experimental signals obtained in a 1.5 m long tube with a circumferential defect located at 840 mm, for frequency of 300 kHz. Gain used: 65.0 dB. I: initial pick up and NR is near end reflection.

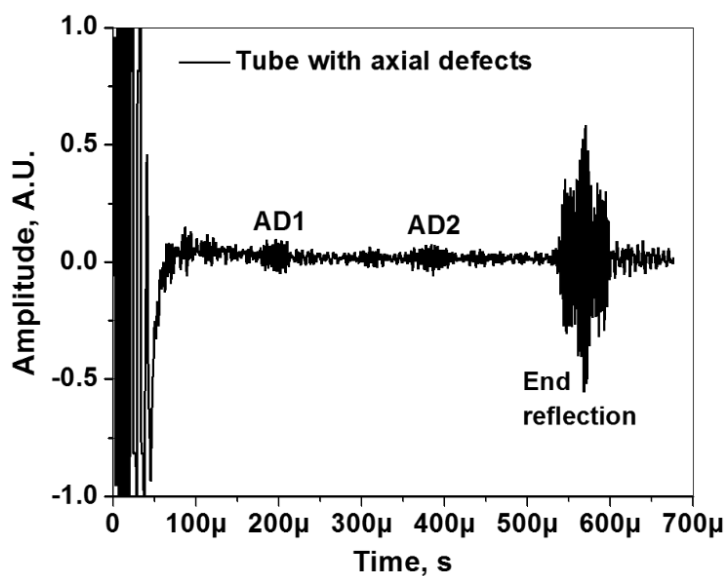


Fig. 5.20. Experimental signals obtained at the frequency of 300 kHz in a 1.5 m long tube with 20% WT and 40% WT deep axial defects. AD1 & AD2: axial defects. Gain used: 64.8 dB

Figure 5.21a shows the signal obtained in a 1060 mm long tube with a pinhole of diameter 1.5 mm using the magnetostrictive transducer. The gain used was 85 dB. The signals from the pinhole and the far end can be clearly seen in the figure. The initial ringing covers the time span of nearly  $175 \mu\text{s}$  and it is much amplified because of high gain. With the use of the group velocity of 5386 m/s, the error in locating the defect is found to be about 2%. The signal to noise ratio of the defect signal with respect to the noise between the defect signal and the end reflection is 6 dB.

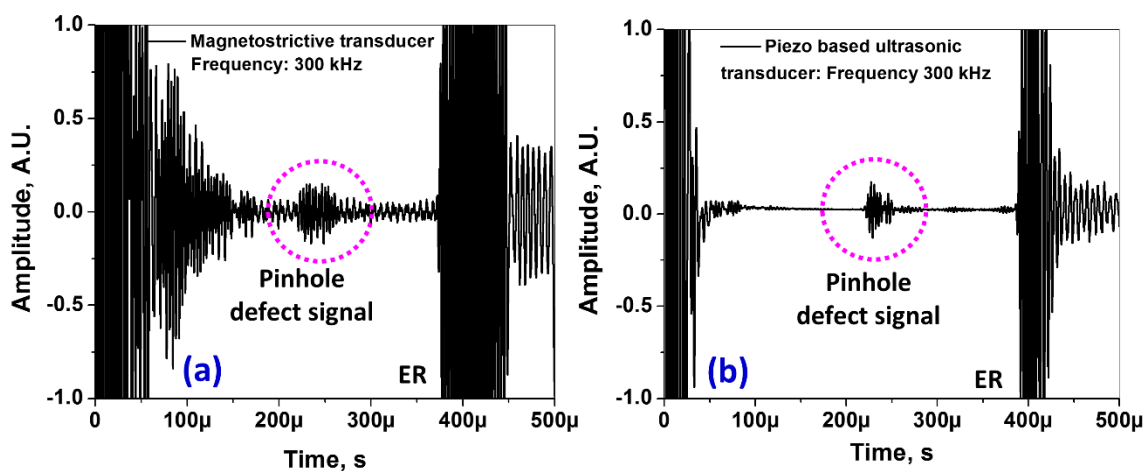


Fig. 5.21. Experimental signals obtained in a 1060 mm long tube with a 1.5 mm dia. pinhole for the frequency of 300 kHz: (a) Magnetostrictive transducer (Gain used: 85.0 dB) and (b) a piezo based ultrasonic transducer (Gain used: 32.0 dB). ER stands for end reflection.

Further, the sensitivity and the SNR for the magnetostrictive transducer in picking up the pinhole were compared with that for a piezo based ultrasonic transducer for the same 300 kHz frequency. To this aim, an experiment using the piezo-based ultrasonic transducer was conducted with the same parameters but for the gain of 32.0 dB, as mentioned in Section 3.2. Figure 5.21b shows the signal obtained using the ultrasonic transducer on the same 1060 mm long tube with a pinhole of 1.5 mm diameter. The amplitude of the defect signal ( $\sim 0.15 \text{ V}$ ) is

approximately the same in both cases. The gain required to achieve this amplitude was 32 dB and is smaller than that used for the magnetostrictive transducer (85 dB). It can be seen in Fig. 5.21b that the end reflection saturates for the gain used. There is a difference in the gain of 53 dB between the magnetostrictive and the piezo transducer for the same excitation voltage of 100 V. This can be improved by increasing the static bias magnetic field in the linear region of the B-H curve. The SNR of the defect signal turns out to be approximately 12 dB with respect to the noise between the defect signal and the end reflection.

## 5.4 Conclusions

In this chapter, the design of an in-bore magnetostrictive transducer for the generation of longitudinal ultrasonic guided waves for the inspection of steam generator (SG) tubes of PFBR has been presented systematically. First, finite element studies using axi-symmetric models were carried out to optimize the diameter and the length of the permanent magnet. The magnetic field induced in the tube increases with the diameter of the magnet and the influence of the length of the magnet on the field in the tube is small. The optimized diameter was 10 mm and the optimized length of the magnet was found to be equal to more than 50 mm. The bias or operating point was chosen as 0.82 T in the tube, which corresponds to the induced magnetic field generated by a magnet of strength 1.4 T and the optimized diameter of 10 mm. The corresponding axial permeability was calculated and used for transient analysis.

In order to optimize the length of the transmitter and receiver coils, FE simulations were carried out for the generation of L(0,2) mode in the frequency range of 250 kHz to 350 kHz. L(0,2) mode was found to be generated and propagated and received in the coil as an induced voltage. The transmitter and receiver length of half wavelength (~10 mm) was found to the

best combination. The challenging aspect of the dynamic FE simulations was the coupling of the elastic and magnetic phenomena. It was achieved using constitutive equations. After obtaining the optimum length of the transmitter and receiver coils, the number of turns of receiver and transmitter coils was optimized by considering the Thevenin circuit model. The model predicted the optimum number of turns of the transmitter and receiver coils to be 80 turns of 2 layers of 34 SWG wire of diameter 0.2337 mm. In arriving at the optimum wire diameter, 75% fill-factor was used.

With the optimized coil parameters, a magnetostrictive transducer was designed and checked for the L(0,2) mode generation. Further, FE results obtained for frequencies in the range of 250 kHz-350 kHz were validated experimentally. There was a good agreement between FE amplitudes and the times of flight with those of experimental ones. The maximum errors in the amplitudes and the times of flight turned out to be ~10% and 1.2  $\mu$ s, respectively. Further, there was an excellent agreement between the experimental and theoretical group velocities. The long-range propagation of the L(0,2) mode generated by the developed in-bore magnetostrictive transducer was observed to be 51 m with a minimal loss.

Towards defect detection, a full circumferential defect of 0.46 mm depth (20% WT), axial defects (20% WT and 40% WT depths) and a pinhole of 1.5 mm dia. were considered. To test the validity of the FE model developed, axi-symmetric circumferential defect was included in the model and the amplitudes and the times of flight of the defect signals were compared. There was a good agreement between the normalized amplitudes (within 10% variation) and the times of flight (difference of 0.75  $\mu$ s) between FE and experiment. The transducer developed is also capable of picking up a pinhole of 1.5 mm diameter with a good SNR of 6 dB, as per the requirement. Finally, the SNR obtained for the pinhole using the

magnetostrictive transducer was compared with that obtained using a piezo based ultrasonic transducer. The SNR for the piezo based transducer is found to be only ~6 dB better as compared to that for the magnetostrictive transducer. Thus, the couplant-free generation and reception of L(0,2) guided wave mode from ID side of the tube using magnetostrictive principle has been developed successfully.

## ***Chapter 6. Studies on SG Tubes of Mockup SG Test Facility using the Developed In-bore Magnetostrictive Transducer and Influence of Thermal Expansion Bend and Tubesheet on L(0,2) Mode***

### **6.1 Chapter overview**

This chapter presents the results of the trial studies conducted on the SG tubes of mockup SG test facility using the developed in-bore magnetostrictive transducer. The results include raw signals from several multiple axi-symmetric and non-axisymmetric circumferential defects in the SG tubes. It also presents the de-noising of the noisy raw signals using the Discrete Wavelet Transform and the cross-correlation technique. Further, the chapter presents the results of 3D-FE simulation, performed in ABAQUS, of L(0,2) mode propagation in the thermal expansion bend to understand the influence of the bend on L(0,2) mode and the sensitivity of defects at different locations of the bend. Further, it also presents the results and discussion of 2D- axisymmetric FE simulation studies, performed with low reflecting boundaries in COMSOL, of L(0,2) mode propagation in an SG tube segment attached to the tubesheet to understand the influence of the tubesheet geometry on L(0,2) mode for the actual examination.

### **6.2 Results and Discussion**

To test the feasibility for the prospective use of the developed in-bore magnetostrictive transducer in actual trials, experiments were conducted on the mockup SG test facility by inserting the transducer in the tubesheet holes, as shown in Fig. 3.2c and as mentioned in

Section 3.2. The dimensions of the transducer are mentioned in Section 5.3.2. The SG tubes in the mockup facility are welded to a tubesheet with spigot welds. The SG tubes have thermal expansion bends made of three successive bends. The radius of curvature of each bend is 375 mm. The mockup SG tubes are of 4.6 m length. There are six SG tubes. Out of six tubes, three have axi-symmetric full circumferential grooves and two have non-axi-symmetric half circumferential grooves. The circumferential defects have been machined using saw cutting. One of the tubes is defect-free and was used for reference. The locations and the dimensions of the defects are given in Table 3.2. Figure 3.5a shows the photograph of the mockup facility. Figures 3.5b and c show the cut view of the tubesheet with a spigot and the schematic of tube-to-tubesheet joints through spigot welds, respectively. Figure 3.5d shows the schematic of a mockup SG tube of length 4.6 m with circumferential grooves (X1-X5) at five different locations. Figure 3.5c also shows the location of the transducer placed in the SG tubes beyond the spigot welds.

### **6.2.1 Response of axi-symmetric full circumferential grooves in SG tubes of mockup SG set-up**

Experiments were carried out on the mockup SG tubes with axi-symmetric defects, as mentioned above. Figures 6.1a, 6.1c and 6.2a show the raw experimental signals corresponding to the tubes (T#A, T#B and T#C) with five full circumferential defects of depths 0.69 mm (30% WT), 0.46 mm (20% WT) and 0.23 mm (10% WT), respectively. In Figs. 6.1 and 6.2, the indices 1 and 5 stand for defects in the straight portions of the tubes while the indices 3-5 stand for defects in the bend. ERs in the figures represent the end reflections. There are multiple echoes due to bi-directional propagation. These signals look similar to the signals obtained using an ultrasonic transducer coupled to the end of the tube in a 3.0 m long bent tube with axi-symmetric circumferential grooves (Fig. 4.25), but for the multiple echoes.

It was also seen that the effect of bend was not evident when axi-symmetric defects are present in the bend (Sec. 4.3.4). Figure 6.3a shows the raw experimental signal corresponding to the defect-free tube (T#R) used for reference and its SNR is 19 dB. It can be seen in Figs. 6.1a, 6.1c and 6.2a that the raw signals are very noisy. The SNRs of the raw signals in Figs. 6.1a, 6.1c and 6.2a are 10.5 dB, 9.5 dB and 5 dB, respectively. Despite the presence of noise, the defect signals can be seen in Figs. 6.1a and c. However, in Fig. 6.2a for T#C, the defect signals are buried in the noise. Hence, the signals were de-noised using the discrete wavelet transform (DWT) and the cross-correlation technique. They are discussed below.

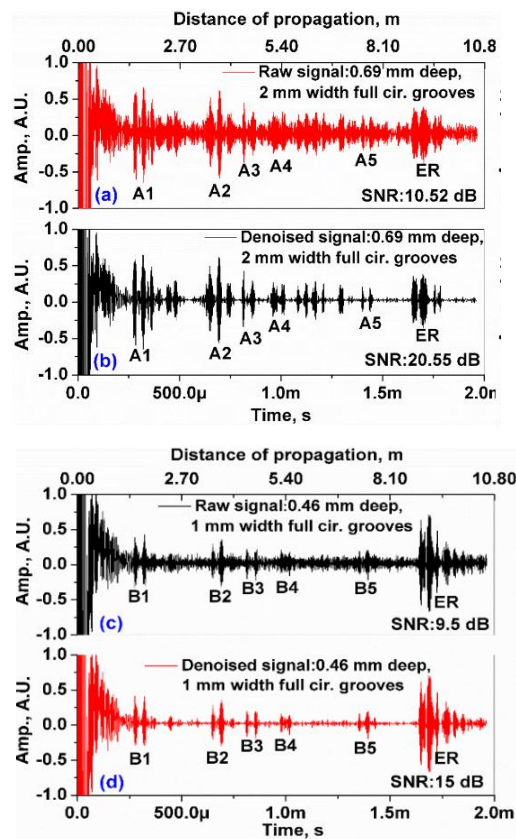


Fig. 6.1. Experimental signals obtained in steam generator (SG) tubes of mockup SG test facility: (a) raw and (b) processed signals corresponding to 0.69 mm deep and 2 mm wide full circumferential grooves (T#A) and (c) raw and (d) processed signals corresponding to 0.46 mm deep and 1 mm wide full circumferential grooves (T#B). The labels An-Bn stand for defects and T#(A-B) for tubes, as given in Table 3.2. Where, n=1,2,3,4 and 5. ER; End reflection. Gain used: 85 dB

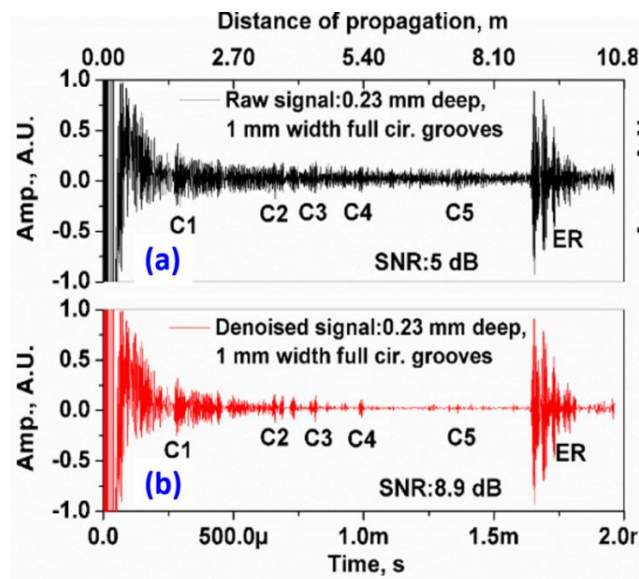


Fig. 6.2. Experimental signals obtained in steam generator (SG) tubes of mockup SG test facility: (a) raw and (b) processed signals corresponding to 0.23 mm deep and 1 mm wide full circumferential grooves (T#C). The labels C<sub>n</sub> stand for defects and T#C for tube, as given in Table 3.2. Where, n=1,2,3,4 and 5. ER: End reflection. Gain used: 85 dB

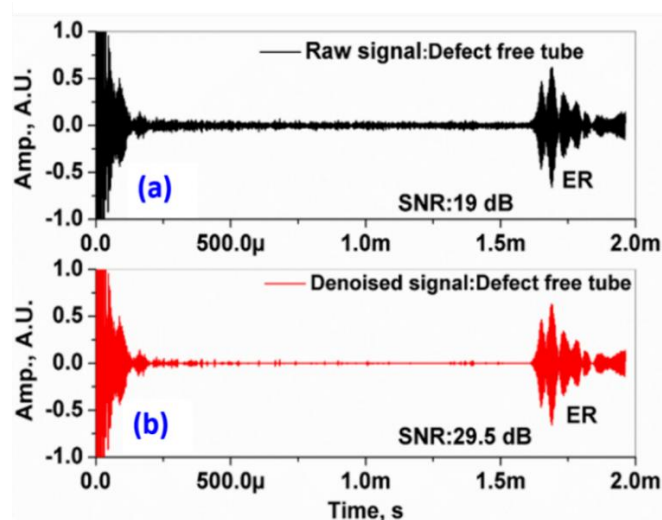


Fig. 6.3. Experimental signals obtained in steam generator (SG) tubes of mockup SG test facility: (a) raw and (b) processed signals for the case of defect-free tube (T#R). Gain used: 85 dB and ER: End reflection.

### 6.2.1.1 De-noising using DWT and optimization of wavelet

The raw signals (Figs. 6.1a, 6.1c and 6.2a) were processed using the DWT to denoise the signals [119, 122, 172]. The procedure for denoising and application of suitable thresholds were discussed in Section 2.2.5.3. Towards this, first the raw signal corresponding to the full circumferential grooves of depth 0.69 mm of SNR of 10.5 dB, as shown in Fig. 6.1a was used as a test signal to de-noise with several wavelets. Then, a wavelet was optimized by choosing a one with the best SNR.

Table 6.1 shows various wavelets used and the SNRs obtained for different decomposition levels for the signal corresponding to the full circumferential grooves of depth 0.69 mm of SNR of 10 dB, as shown in Fig. 6.1a. The SNRs were calculated by considering the maximum amplitudes of the second defect echo (A2) and the maximum noise level between the fifth defect echo and the end reflection (ER) in Fig. 6.1a for different decomposition levels. It can be seen in the table that sym12 wavelet gives the highest SNR of 20.55 dB at the 10<sup>th</sup> level decomposition.

At each of the decomposition levels, universal hard thresholding, as discussed in Section 2.2.5.3, was applied and the signals were reconstructed using sym12 wavelet. The sym12 wavelet yields the best results probably due to the similarity of its shape with the ultrasonic signals received. Figure 6.4 shows the sym12 wavelet. Mallet et al., as discussed in Ref. [107], have used a symmlet wavelet for wavelet de-noising of dispersive guided wave signals obtained in a long range ultrasonic guided wave testing of a pipe.

A significant improvement in SNR is observed when the signal was reconstructed from levels up to level-5, after which there was not much improvement. This occurs due to the segregation of signals in the detailed coefficients of 4<sup>th</sup> and 5<sup>th</sup> levels. Decomposing the raw signals to

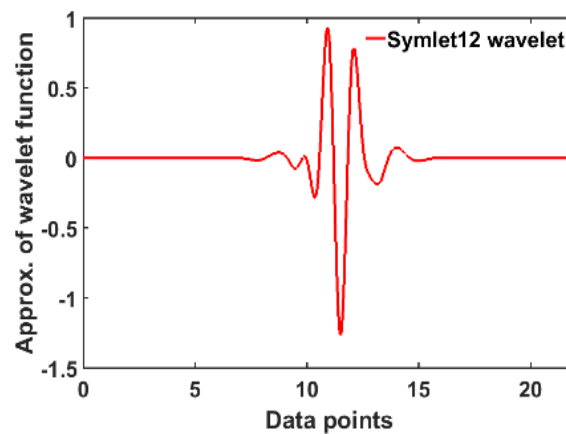
higher levels leads only to the separation of low frequency noise with small amplitudes. Hence, thresholding of levels above level-5 did not yield much improvement in SNR. In other words, wavelet de-noising removes low-amplitude signals present in each of the decomposition levels by thresholding. Hence, the signals reconstructed from all the decomposition levels appear with reduced noise.

Figure 6.1b shows the DWT denoised signal corresponding to the tube with full circumferential grooves of depth 0.69 mm (T#A) with the SNR of 20.55 dB. There is an improvement of SNR by  $\sim 10$  dB. The denoising using the optimized sym12 wavelet was extended to the signals corresponding to the other cases. Figures 6.1d and 6.2b show the DWT processed signals (with sym12 wavelet) corresponding to the tubes (T#B and T#C) with five full circumferential defects of depths 0.46 mm (20% WT) and 0.23 mm (10% WT). The SNRs of the DWT denoised signals in Figs. 6.1d and 6.2b are 15 dB and 8.9 dB, respectively. After denoising, the SNRs improve by approximately 5-10 dB. All the defects are detected with good sensitivity.

In the defect-free reference tube (T#R), the SNR improved by  $\sim 10$  dB (Fig. 6.3b). From Fig. 6.3b, the group velocity was calculated using the end reflection and it turns out to be 5398 m/s, which again confirms that the mode generated is L(0,2) mode. The L(0,2) mode detects all the defects with good sensitivity but for the defect C5 whose depth could be less than that considered (Fig. 6.2b). Besides, the defects can be located with the accuracy of approximately 10 mm.

**Table 6.1. SNRs for different decomposition levels of the signal corresponding to 0.69 mm deep and 2 mm wide full circumferential grooves**

S. No.	Wavelets	SNR for various decomposition levels		
		Level 3	Level 5	Level 10
1	Db4	10.93	17.76	17.83
2	Db6	10.74	18.47	18.86
3	Db8	10.62	18.19	18.31
4	Db10	10.60	19.45	19.77
5	Db12	10.78	19.76	20.27
6	Sym2	11.60	18.01	18.07
7	Sym4	11.01	19.85	20.00
8	Sym8	10.70	18.56	18.91
9	Sym12	10.63	20.34	20.55
10	Coif1	11.55	17.73	17.93
11	Coif2	10.94	17.98	18.03
12	Coif3	10.84	18.80	19.03



**Fig. 6.4. Symmlet 12 wavelet.**

### 6.2.1.2 Cross-correlation based de-noising

The three-echo features in Figs. 6.1a may cause ambiguity in practice to identify a defect signal in the middle of multiple signals. For example, the signals between A4 and A5 in Fig. 6.1b. Even though the DWT performs well in removing the noise, there are many echoes present in Fig. 6.1b due to the bi-directional reflection of L(0,2) mode from a defect on the one side and the tubesheet on the other. To resolve this, the raw signal (Fig. 6.1a) was cross-correlated to de-noise the signals, as discussed in Section 2.2.5.2. To this aim, raw signals were first bandpass filtered in the frequency range of 100 to 400 kHz and then cross-correlated with a three-echo signal obtained from an end of a defect-free tube (Fig. 6.3a).

Figures 6.5a and b are the same as Figs. 6.1a and b for the case of the full circumferential grooves of depth 0.69 mm and they are presented here for easy comparison. Figure 6.5c is the cross-correlated signal. All five defects are clearly seen as peaks with the inter-reflections suppressed. Further, the times of flight between correlated signals and the de-noised signals compare well. The SNR of the signal is ~13 dB, which is less than that provided by DWT denoised signal of 20.55 dB. However, the cross-correlation de-noises the signals and they can be interpreted without ambiguity. The results for the other cases exhibited a similar feature and hence, are not presented.

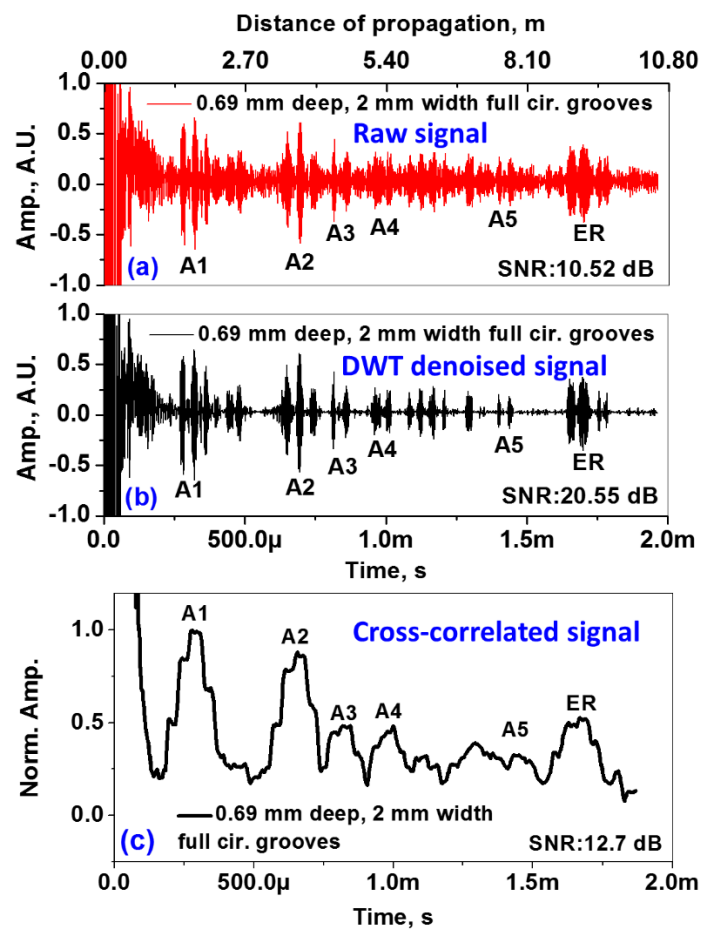


Fig. 6.5. Experimental signals obtained in the steam generator (SG) tubes of the mockup SG test facility: (a) raw and (b) Discrete Wavelet Transform (DWT) processed signals corresponding to 0.69 mm deep and 2 mm wide full circumferential grooves (T#A) and (c) cross-correlated signal normalized with respect to the maximum response. The labels A1-A5 stand for defects and T#A for tube, as given in Table 3.2. ER: end reflection.

## 6.2.2 Response of non-axi-symmetric defects in SG tubes of mockup SG set-up

In the case of axi-symmetric defects, the effect of bend was completely masked as the reflection from the defect is integrated over the full circumference of the defect. In order to understand the effect of bend on detection sensitivity, response of non-axisymmetric half-circumferential defects at various locations of the bend was studied.

Figures 6.6a and c show raw experimental signals while Figs. 6.6b and d show the-DWT processed signals corresponding to the tubes (T#D and T#E) with five half-circumferential defects of depths 0.69 mm (30%WT) and 0.46 mm (20%WT), respectively. The locations of the defects are given in Table 3.2. The SNRs of the raw signals in Figs. 6.6a and c are 4.6 dB and 3.7 dB, respectively. However, the SNRs of the DWT denoised signals in Figs. 6.6b and d are 9.62 dB and 10.9 dB, respectively. After de-noising, the SNRs improve by approximately 5 and 6 dB.

In Figs. 6.6, the indices 1 and 5 stand for defects in the straight portions of the tubes while the indices 3-5 stand for defects in the bend. Figure 6.6b shows the signals for half circumferential defects D2 and D4 located at the intrados of the bend while D3 at the extrados of the bend. It can be noticed in Fig. 6.6b that the reflected amplitudes from D3 is higher than that for D2, even though wave interacts first with D2. The same phenomenon is observed for the half-circumferential defect E3 (Fig. 6.6d).

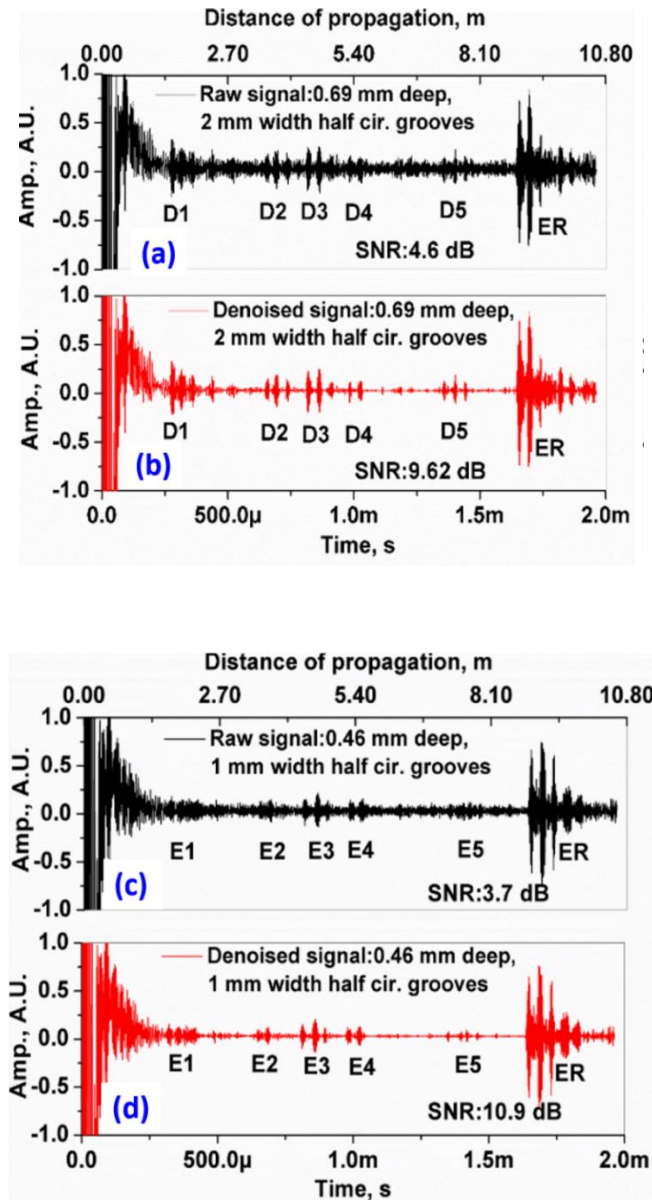


Fig. 6.6. Experimental signals obtained in steam generator (SG) tubes of mockup SG test facility: (a) raw and (b) processed signals corresponding to 0.69 mm deep and 2 mm wide half circumferential grooves (T#D) and (c) raw and (d) processed signals corresponding to 0.46 mm deep and 2 mm wide full circumferential grooves (T#E). The labels D<sub>n</sub>-E<sub>n</sub> stand for defects and T#(D-E) for tubes, as given in Table 3.2. Where, n=1,2,3,4 and 5. ER: End reflection. Gain used: 85 dB.

Figure 6.7 shows the plot of the reflected amplitudes from full and half circumferential grooves of depth 0.69 mm (Figs. 6.1b and 6.6b). The reflected amplitudes corresponding to

the full circumferential grooves gradually fall with the locations of the defects due to partial transmission of energy from one defect to another in the bend and attenuative losses. The reflected amplitudes corresponding to the half circumferential grooves show reduction in the amplitudes for the grooves located in the intrados and increase in the amplitude in the extrados. This clearly shows the dependence of detection sensitivity on the location of the bend and the effect can be attributed to the bend. Furthermore, it can also be inferred that irrespective of the location of a defect in the bend, it can be detected with good sensitivity. Further, the reflected amplitudes seem to be proportional to the cross-sectional area of the defect. Besides, the defects can be located with the accuracy of approximately 10 mm, which can be improved further by applying a suitable correction in the time of flight of the signals received from beyond the bend. The sensitivity can thus be stated as 20% WT (0.46 mm) deep and 1 mm wide half circumferential groove based on a 6 dB criterion. The influence of bend on L(0,2) mode propagation and the aspect of amplitude reduction at the intrados is addressed in the next section using FE analysis.

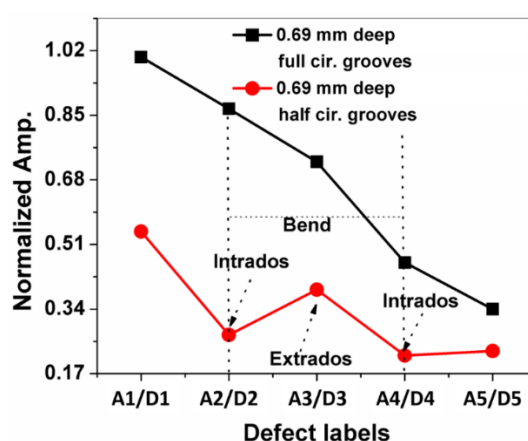


Fig. 6.7. Reflected amplitudes versus defect locations in steam generator (SG) tubes of the mockup SG test facility with 0.69 mm depth full and half circumferential grooves. A and D correspond to full and half circumferential defects, respectively.

### 6.2.2.1 Finite element simulation to study the influence of thermal expansion bend on L(0,2) mode

Finite element simulation was performed in ABAQUS to study the influence of the thermal expansion bend of an SG tube, as mentioned in Section 3.5. To this end, three cases were considered: (a) propagation of L(0,2) mode in a 3 m long straight tube, (b) propagation of L(0,2) mode in a 3 m long tube with the thermal expansion bend and (c) propagation of L(0,2) mode in a 3 m long tube with the thermal expansion bend having pinholes of diameter 1.5 mm considered at the intrados and the extrados of the bend.

Figures 6.8a and b show the FE time signals obtained for a 3 m long straight tube and a 3 m long tube with a bend. The signals were normalized with respect to the maximum amplitude of the end reflection from the straight tube. The reflections from the tube ends are marked in the figures. The group velocity of the mode turns out to be 5370 m/s against the Disperse software predicted group velocity of 5380 m/s. This ensures that the mode propagating is a L(0,2) mode. There is a delay of 1.7  $\mu$ s in the arrival of the end reflected signal of the bent tube with respect to the end reflected signal from the straight tube. This indicates that the error in locating a defect in/beyond the bend will be of  $\sim$ 10 mm, if the delay is not accounted.

Figures 6.9a and b show the spectrograms of the signals (Figs. 6.8a and b) for the cases of the straight and the bent tubes, respectively. It can be clearly seen in Fig. 6.9a for the case of the straight tube that L(0,2) mode is non-dispersive. However, both non-dispersive and dispersive signals can be seen in Fig. 6.9b for the case of the bend. The non-dispersive signal corresponds to L(0,2) mode while the dispersive signals correspond to F(1,3) mode due to mode conversion in the bend. The low frequency components of F(1,3) modes propagate slower than higher frequency components in the bandwidth of 250 kHz – 380 kHz. This

conforms well with the group velocity dispersion curve for F(1,3) mode in this range (Fig. 4.1b). It can also be seen that the amplitude of F(1,3) mode is much smaller than that of L(0,2) mode and hence, it presents no complexity in the signal interpretation. Owing to this mode conversion, there is an amplitude loss of about 4 dB for the L(0,2) mode propagating in the thermal expansion bend with respect to that propagating in the straight tube.

Furthermore, the transmission across the bend is governed by the ratio (R/D) of the bend radius (R) to the diameter (D). For the SG tube of PFBR, R/D ratio is 21.8. The ratio (D/t) of the pipe diameter (D) to the wall thickness (t) is 7.5. There will not be any mode conversion for any D/t ratio, as long as L(0,2) mode propagates in the straight tube. However, in the bend, the ratio R/D affects the transmission across the bend. For a large ratio of R/D (>25), the bend (shallow) essentially behaves similar to a straight tube [74]. However, for small ratios, different transmission coefficients are obtained for the same frequency. Even for the same R/D ratio, the transmission is seen to be frequency dependent. Because of the large R/D ratio in the present application, the transmission is not badly affected by the bend. Another useful parameter is the ratio of the bend radius (R) to the wavelength ( $\lambda$ ) [73]. For shallow bends,  $R/\lambda$  is much greater than 1. For the thermal expansion bend,  $R/\lambda$  is 20.8. Hence, the thermal expansion bend of an SG tube of PFBR can be considered to be shallow and only mild effects are observed in terms of mode conversion and asymmetry in the bend region. Furthermore, no noticeable reflection from the shallow bend is observed.

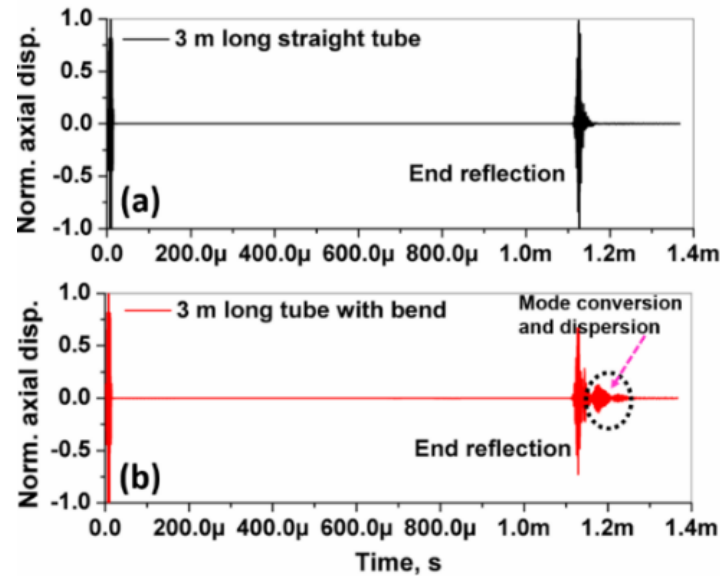


Fig. 6.8. Axial displacement signals obtained at the frequency of 300 kHz: (a) a 3 m long straight SG tube and (b) 3 m long SG tube with a thermal expansion bend. (Finite element simulation)

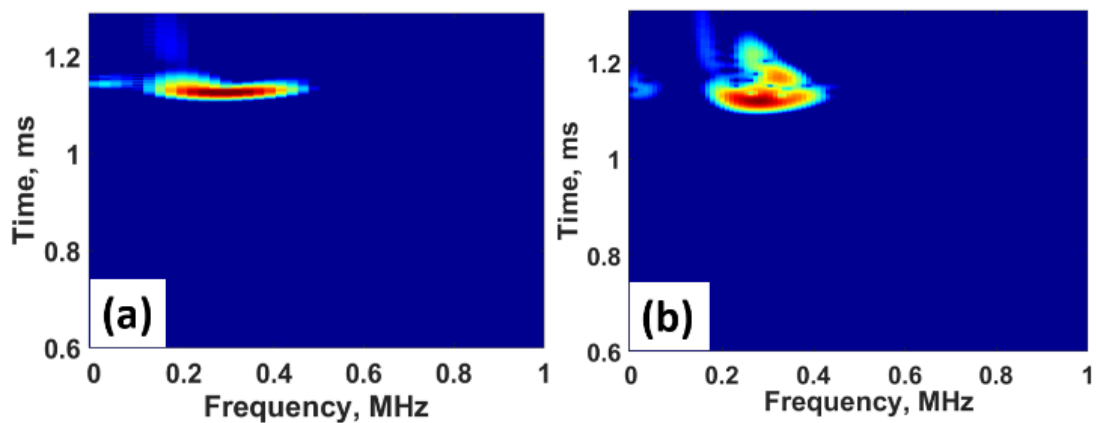


Fig. 6.9. Spectrograms for the cases of the finite element signals obtained in (a) a 3 m long straight SG tube and (b) a 3 m long SG tube with a thermal expansion bend. (Finite element simulation)

Figures 6.10(a-d) show the snapshots of L(0,2) mode propagating from left to right for different instants, in a 3 m long SG tube with a thermal expansion bend. The mode conversion in the third bend can be clearly seen in Figs. 6.10d and e. L(0,2) mode in the bend becomes non-axi-symmetric in the bend with the maximum at the extrados and the minimum at the

intrados. It is clear that the gradual fall of amplitudes in the case of full circumferential defects of depth 0.69 mm (T#E) in the mockup SG tube is due to the mode conversion of L(0,2) mode to F(1,3) mode, partial transmission of energy upon interacting with a defect and small attenuative losses (Black curve in Fig. 6.7).

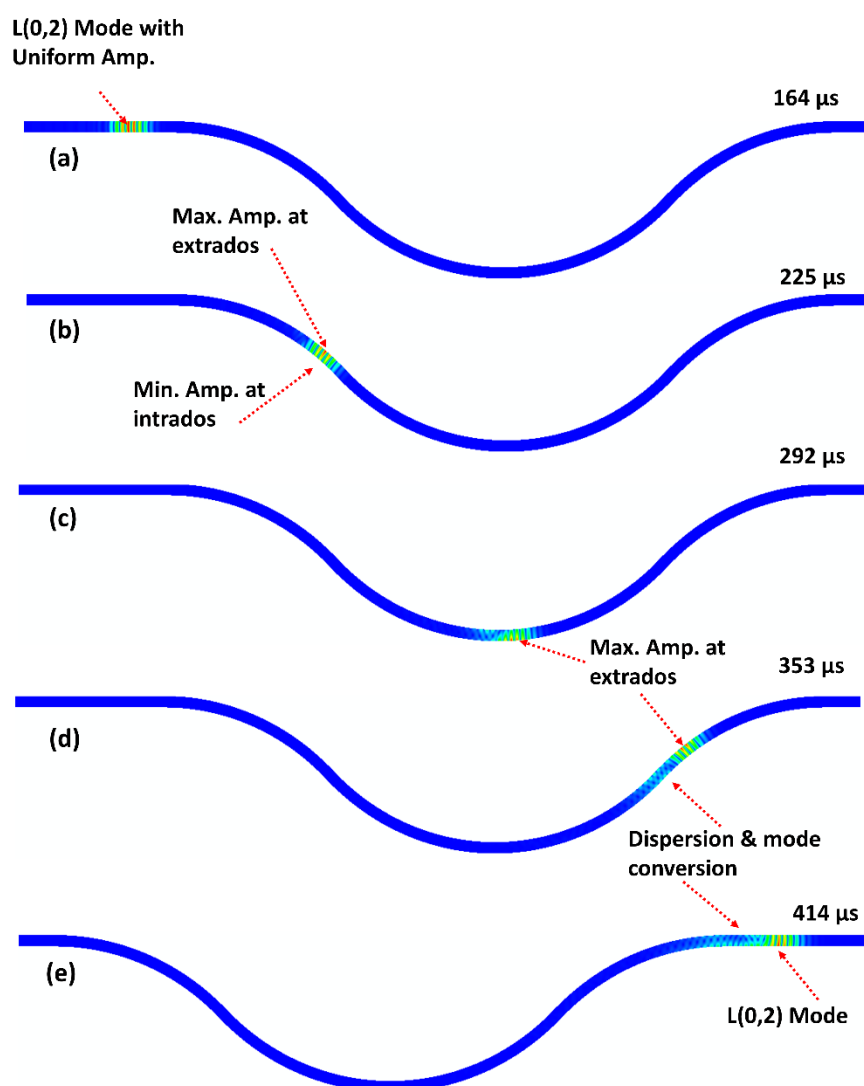


Fig. 6.10. Snapshots of L(0,2) mode propagation in the bend at different time instants. L(0,2) wave mode propagates from left to right. (Finite element simulation)

To study sensitivity, FE simulations were performed by considering pinholes at different locations of the bend and also in the straight portions. Figure 6.11a shows the schematic of a

bent tube with pinhole locations (A-I). Figures 6.11b and c show the FE signals corresponding to pinholes located at 1.502 m distance from the end and it is marked as 'E' in Fig. 6.11a. Reflections from pinholes located at extrados and intrados are clearly seen. The calculated location turns out to be 1.509 m. Further, the amplitude of reflection for a pinhole at the extrados point is higher than that for the intrados point. The amplitude of the intrados signal is about -7 dB as compared to that of the extrados signal.

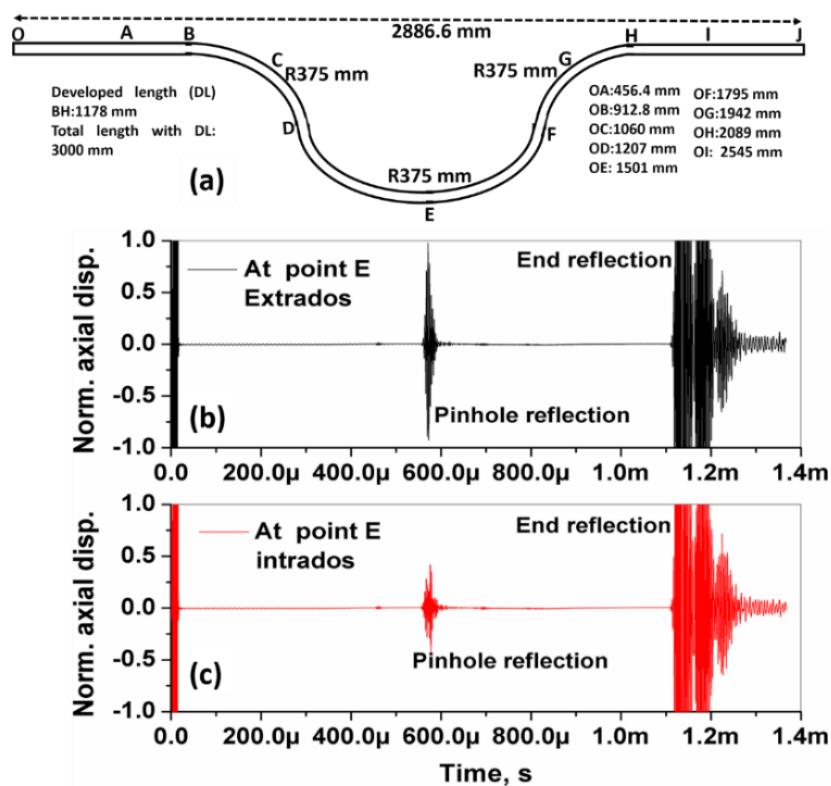


Fig. 6.11 (a) Schematic of thermal expansion bend. Axial displacement signals obtained from pinholes at 1.5 m at the frequency of 300 kHz in a thermal expansion bend for (b) a 1.5 mm dia. pinhole at extrados and (c) a 1.5 mm dia. pinhole at intrados. (Finite element simulation)

Figure 6.12a shows the variation in the axial displacement in a defect-free bend obtained by recording the displacement at the designated locations, as shown in the top figure. Figure 6.12b shows the variation in the reflected axial displacement from the pinholes, which are

placed at the designated locations, as shown in the top figure, obtained by recording the displacement at the excitation face. Figure 6.12c shows the variation of axial stresses in the thermal expansion bend.

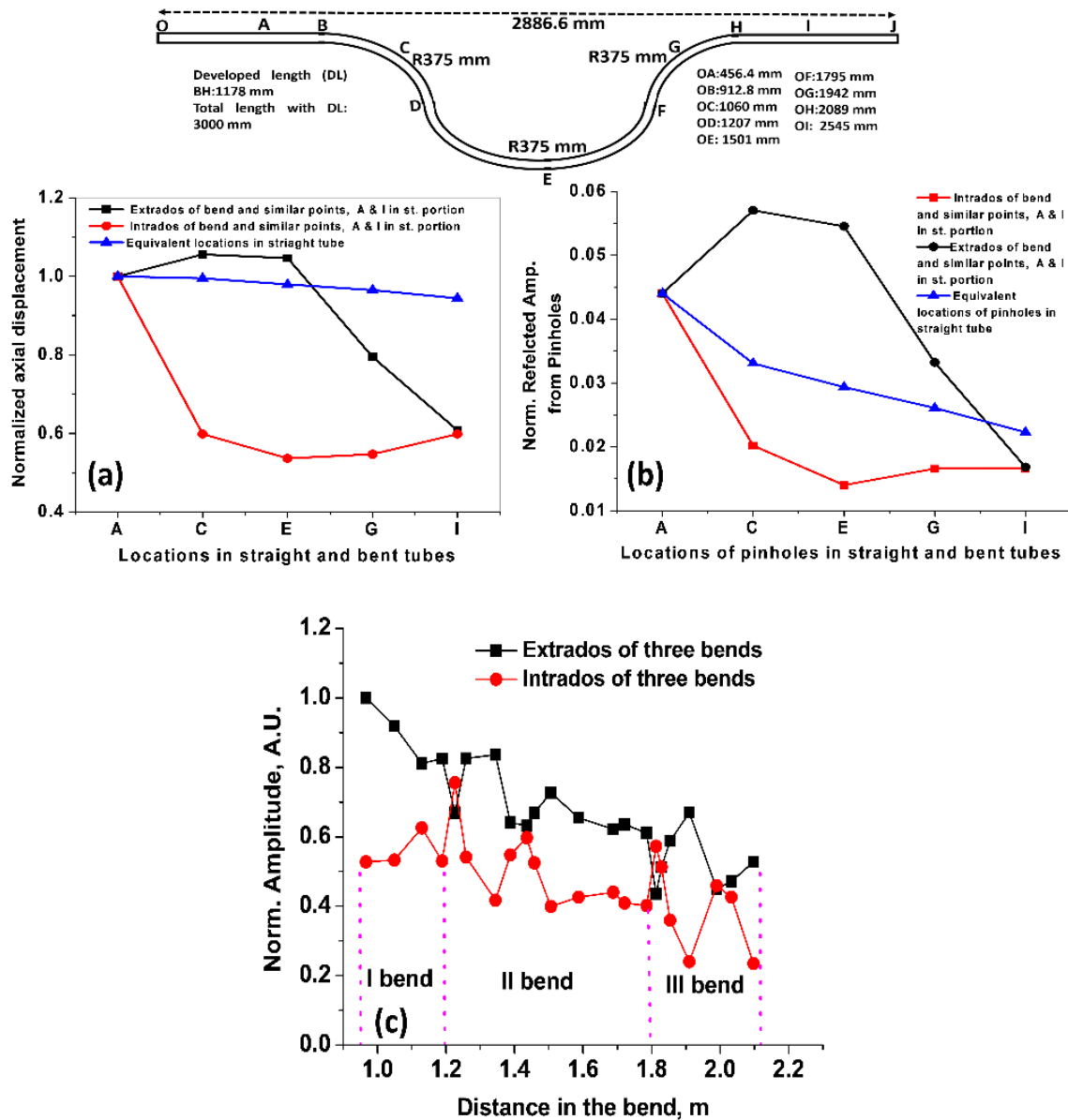


Fig. 6.12. (a) Amplitudes of time signals (axial displacement) at different locations of a 3.0 m long defect-free thermal expansion bend, (b) reflected amplitudes received at the excitation end from 1.5 mm dia. pinholes at locations A, C, E, G and I and (c) variation of axial stress amplitudes across the bends. (Finite element simulation result)

In Figs. 6.12a and b, all the amplitudes were normalized with the maximum incident amplitude. It can be seen in Figure 6.12a that when  $L(0,2)$  mode propagates from the straight portion A to C, there is an increase in the amplitude at the extrados and reduction in the amplitude at the intrados. There is a slight reduction from C to G. Again, in the straight portion at location I, there is essentially no difference in amplitudes at the two opposite points, indicating axi-symmetry. However, the amplitude dropped by about 4 dB after crossing the bend, as also observed in Fig. 6.8b. Figure 6.12b clearly shows that the reflected amplitudes from pinholes at these locations (A, C, E, G, and I) follow a similar trend with a difference in magnitude. This essentially means that sensitivity of a defect is not uniform across the bend. The axial displacements in Fig. 6.12a were picked up at A, C, E, G and I while the axial displacements in Fig. 6.12b were picked up at the excitation end. They are reflections from the pinholes located at A, C, E, G and I. In the latter case,  $L(0,2)$  mode travels twice the forward propagation path. In addition, a pinhole of 1.5 mm diameter is a small cylindrical reflector. Hence, the amplitudes are smaller in Fig. 6.12b.

To compare the amplitudes corresponding to the bend locations A, C, E, G and I, equivalent straight tube locations were chosen in a 3.0 m long straight tube. These plots are shown by the blue curves in Figs. 6.12a and b. It can be seen that the amplitudes for the case of the straight tube gradually fall (0.3 dB/m) with increasing distance due to the mild damping with increasing distance and they are between the amplitudes corresponding to the extrados and intrados of the bend and they are between the amplitudes corresponding to the extrados and intrados of the bend. For instance, the amplitudes corresponding to the extrados and intrados at point E with respect to the amplitude at point E of the straight tube is 0.5 dB and -5 dB, respectively. The loss of amplitude at point I is 4 dB. This clearly brings out the non-symmetric nature of the mode in the bend with the maximum stress field being at the extrados

while the minimum being at the intrados. It is due to this fact the half circumferential defect at the extrados (point A3/D3) shows a sudden increase in amplitude (red curve of Fig. 6.7). Further, the reflected amplitudes corresponding to pinholes in Fig. 6.12b also show a fall with increasing distance of the pinholes from the transducer. As observed in Fig. 6.12a, the pinhole reflected amplitudes are between those for the extrados and intrados of the bend. The amplitudes corresponding to the extrados and intrados at point E with respect to the amplitude at point E of the straight tube is 2 dB and -9 dB, respectively. The loss of amplitude at point I is 7 dB.

Furthermore, it can be seen in Fig. 6.12c that the axial stresses in the bends are not uniform. The axial stresses vary in the extrados from 1 - 0.6 A.U. while in the intrados the axial stresses vary from ~0.8 - 0.3 A.U. There are locations in the bends where the axial stresses in the extrados and intrados are nearly the same. These are transition zones from one bend to another and the regions close to the middle of the second and third bends. In the other locations, the axial stresses at the extrados and the intrados are well separated. At the transition zones, the extrados of one bend becomes the intrados of another. Hence, it takes some time for the reversal of stresses from maximum to minimum or vice-versa at the transition zones. Owing to this, the stresses at the extrados exhibit minimum while that at the intrados exhibit maximum at the transition zones. It is not clear why the mode becomes uniform near the center of the second and third bends. It can also be noticed that there is one highest value of the axial stresses at the extrados in each of the bends. There are local minima at the extrados of the second and third bends. Local minima are observed at the intrados as well. All this points out to the fact that there is a variation of sensitivity along the bend and at the extrados and the intrados of the bends. Furthermore, the presence of two lobes of maxima close to the extrados with minima in the middle of a 1D bend, reported by Heinlein et al. [71]

is not observed in the present case because of the large radius to diameter ratio ( $R/D$ ) of 22, which again the article also reports for 3D, 5D, 7D and 20D bend radii. In fact, in the case of a large  $R/D$  ratio, the two lobes merge into one, as is observed in the present case.

Experimental results from mockup SG tubes with axi-symmetric and non-axi-symmetric were discussed. Influence of the bend on  $L(0,2)$  mode and detection sensitivity were studied. The bend is understood to influence  $L(0,2)$  mode in two ways namely, mode conversion to  $F(1,3)$  mode and maximizing stresses at the extrados and minimizing at the intrados. The second aspect of influence was clearly brought out in the experiment by considering non-axi-symmetric defects in the bend (T#D and T#E). Further, sensitivity across whole bend was also studied. Another feature of an SG tube that can influence  $L(0,2)$  mode is the tubesheet-spigot structure and spigot weld and it is discussed in the next section.

### **6.2.3 Influence of tubesheet thickness and spigot weld on guided wave signal**

Three-echo pattern features when the tube under examination has free ends (Fig. 5.14). The formation of three-echo pattern is clearly explained using a schematic (Fig. 5.15) and it is due to the bi-directional propagation of  $L(0,2)$  mode in a tube with free ends (Sec. 5.3.2.1). In actual SG set up, SG tubes are bounded by tubesheets through spigot welds. Hence, it is important to study the influence of tubesheets and spigot on end echoes for actual testing. To this aim, 2D-axisymmetric FE simulations were performed, as mentioned in Section 3.5.2.1. The dimensions of the models and the location of the receiver points (R1, R2 and R3) are shown in Fig. 3.9. The two models were considered to have tubesheet thicknesses 25 mm and 150 mm. In the models, the spigot weld was assumed to be a perfect joint. The spigot weld is of full penetration butt-joint type without any noticeable weld cap with the width of  $\sim 3$  mm.

Due to the fine-grain structure of the ferritic steel weld, the weld exhibits negligible change in elastic properties from the parent metal. This fact was also evidenced in the experimental signals from the mockup SG setup.

The FE simulations were performed with and without the low reflecting boundary (LRB) condition at the right edge of the tubesheet-air interface (Fig. 6.13b). This assumes that the horizontal extent of the tubesheet is infinitely long or in other words, the right edge is assumed to be at infinity. This assumption will be justified in the fore-going discussions. Figure 6.13 shows the snapshots of the axial displacement at different time instances in 150 mm and 25 mm thick tubesheets. Figures 6.13a and b show L(0,2) mode approaching the spigot-tubesheet transition. Figure 6.13c shows the mode conversion happening in the tubesheet. Figure 6.13d shows the mode conversion of L(0,2) mode into longitudinal, shear, Rayleigh and head waves at 196  $\mu$ s. Figure 6.13e shows the colour plot of the axial displacement superimposed on the arrow plot of the displacement vector in the tubesheet.

The arrows in the figure clearly indicate that the polarizations of the modes in the tubesheet are the longitudinal, shear, Rayleigh and head waves. The wavelengths of the longitudinal, shear, Rayleigh waves, respectively turn out to be 20.0 mm, 10.4 mm and 9.6 mm and the corresponding velocities turn out to be 6000 m/s, 3120 m/s and 2880 m/s. Figure 6.13f shows the waves in 25 mm thick tubesheet at 196  $\mu$ s. It can be seen that the waves are highly distorted and there is no formation of wave fronts due to the small thickness.

When the mode enters the tubesheet region, it essentially sees it as a large medium. This entry is analogous to a point load excitation at the point of entry. It is known that a large medium under point load excitation will generate longitudinal waves, shear waves, head waves and Rayleigh waves, in order to satisfy the stress-free conditions at the boundaries of the medium

[173]. Similarly, in order to satisfy the stress-free boundary conditions at the tubesheet edges, the bulk waves must necessarily exist. Furthermore, the wavelength of the L(0,2) mode at 300 kHz in the SG tube is  $\sim 18$  mm, which is much smaller than the width of the tubesheet region ( $\sim 120$  mm) in the r-direction, resulting in the bulk wave formation.

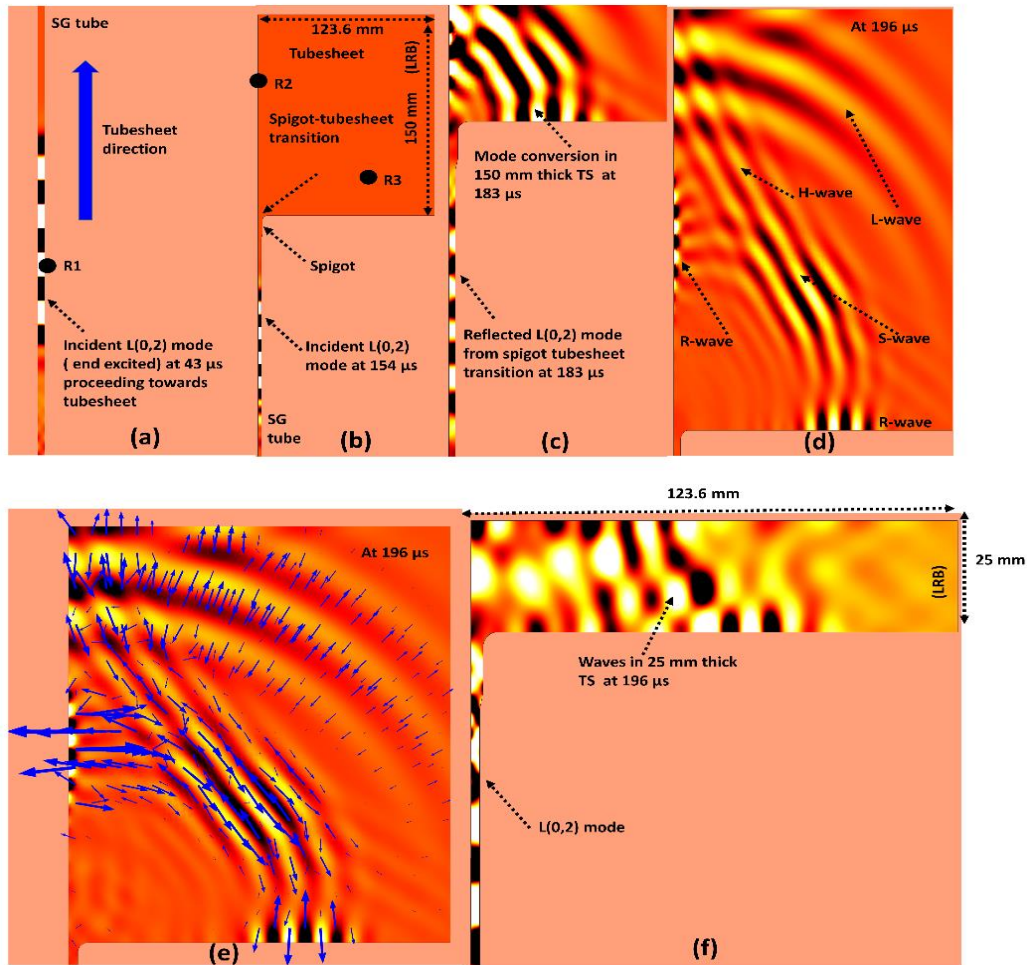


Fig. 6.13. Snapshots of L(0,2) mode and mode converted waves in SG tube and tubesheet (TS): (a) incident L(0,2) mode at R1 at  $43 \mu\text{s}$  in the tube, (b) incident L(0,2) mode approaching spigot-tubesheet transition at  $154 \mu\text{s}$ , (c) mode conversion of L(0,2) mode in the tubesheet of 150 mm thickness at  $183 \mu\text{s}$ , (d) mode converted longitudinal wave (L), shear wave (S), head wave (H) and Rayleigh wave (R) in the 150 mm thick tubesheet at  $196 \mu\text{s}$ , (e) arrow plot of displacement vector superimposed on plot (d), and (f) waves in 25 mm thick tubesheet at  $196 \mu\text{s}$ . LRB stands for low reflecting boundary and it is imposed at the right edge of the tubesheet. The coordinates of the receiver points R1, R2 and R3 are (8.6 mm, 200 mm), (6.36 mm, 960 mm) and (75 mm, 930 mm), respectively with the origin (0,0) at the center of the tube at the excitation end. (Finite element simulation)

Figures 6.14a and b show the magnitude of the displacement normalized with respect to the maximum of the incident mode and picked up at points R2(6.36 mm, 160 mm) and R3 (75 mm, 130 mm), respectively in the 150 mm thick tubesheet (R2 and R3 are shown in Fig. 3.9). The Rayleigh wave exhibits the maximum magnitude of displacement followed by shear and longitudinal waves, as observed in a point load excitation [173].

Figures 6.15a and b show the signals picked up at R1(8.6 mm, -600 mm) with LRB at the right edges of 150 mm and 25 mm thick tubesheets. Figure 6.15c shows the signals picked up at R1 in the tube for 25 mm thick tubesheet with LRB at the right and top edges. Signals (A) in Figs. 6.15(a-c) correspond to the reflection of L(0,2) mode from the spigot-tubesheet transitions due to the thickness variation. The signal (A) is small and is followed by the near end reflections of A and small reflections from the tubesheet. In Fig. 6.15b, there is a higher amplitude signal adjacent to A that corresponds to the reflection from the top of the tubesheet. This becomes evidentially clear in Fig. 6.15c with absorbing top of the tubesheet, there is a considerable reduction in the amplitude of the signal. In the experimental signals (Figs. (6.1-6.3)) for the mockup SG set-up with 25 mm thick tubesheet, the middle and third echoes of the three-echoes for a defect is due to the top of the tubesheet.

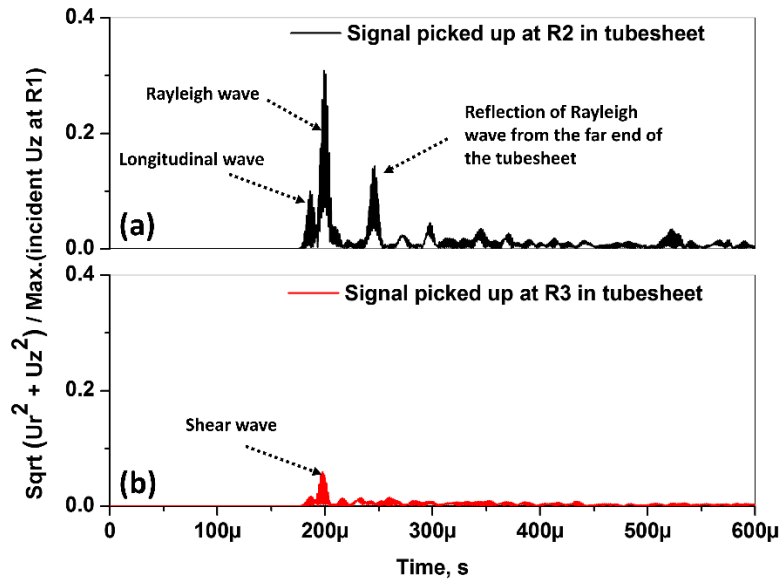


Fig. 6.14. Magnitude of displacement vector in a tube with 150 mm thick tubesheet: (a) at R2= (6.36 mm, 960 mm) and (b) at R3= (75 mm, 930 mm). (Finite element simulation)

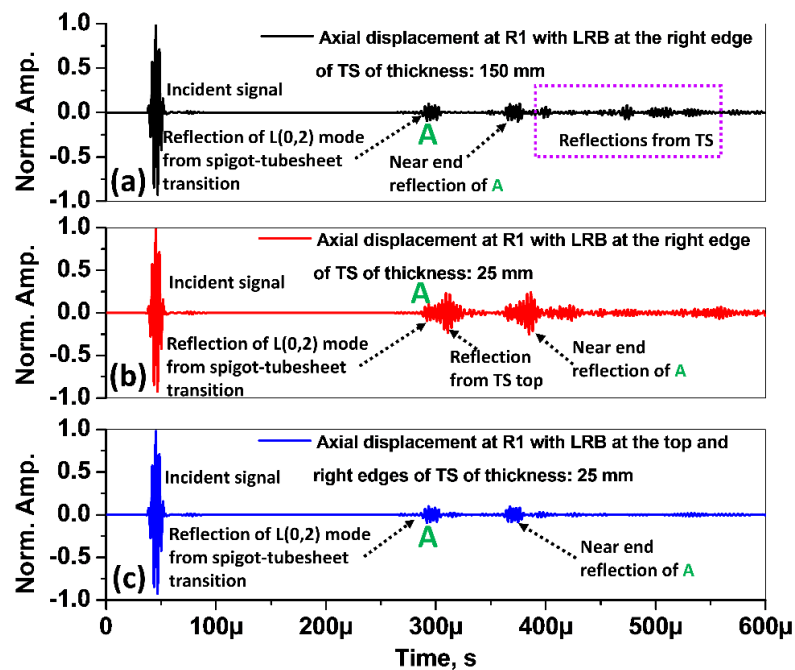


Fig. 6.15. Axial displacement signals picked up at receiver point R1 located at 200 mm from the excitation end and 680 mm from spigot-tubesheet transition for (a) tubesheet (TS) thickness of 150 mm (actual SG of PFBR SG) with low-reflection boundary (LRB) at the right edge of tubesheet, (b) TS thickness of 25 mm (Mockup SG) with LRB at the right edge of the TS and (c) with LRB at the top and right edges of the 25 mm thick TS. LRB stands for low reflecting boundary. (Finite element simulation)

Furthermore, the reflection coefficient of L(0,2) mode (signal (A)) due to spigot-tubesheet transitions for 25 mm and 150 mm thick tubesheets is found to be approximately 10%. For larger horizontal lengths of 150 mm thick tubesheet without LRB, to simulate the actual one, spigot-tubesheet transition signals of the same magnitude and low-amplitude reflections from the tubesheet were observed. Hence, the actual 150 mm thick tubesheet behaves nearly like a large medium with far-off boundaries. Therefore, the use of LRB to simulate such a medium in a small domain is justified. Furthermore, the models assume that the tubesheet is a continuous medium. Conversely, the actual tubesheet has 1.2 m diameter with 547 penetrations of SG tubes. This suggests that there will be a large scattering inside the tubesheet, further reducing the amplitudes of reflections. Hence, it can be concluded that in the actual testing, the role of the tubesheets will be minimal but for low spigot-tubesheet reflections (amplitude). It indicates that only one direct echo from a defect, i.e., the first echo in a three-echo pattern for a tube with free ends is expected to be present. As a consequence, interpretation of experimental signals will become direct and simple.

Since spigot-tubesheet reflections are quite small, even the spigot region can also be inspected thoroughly. The only care that should be taken during the actual inspection is the ringing of the transmitter-receiver unit itself. This corresponds to a dead zone of ~550 mm (Figs. (6.1-6.3)). This may mask indications across the zone. However, since the guided waves generated by the transducer are bi-directional, this can be overcome by inserting the transducer to two different locations of the tube to detect a defect signal falling in the dead zone. This indicates that the length of the transducer unit should be about 1400 mm and data should be acquired at two different probe insertions. The two proposed probe center locations from the top of the tubesheet are 190 mm and 1270 mm from the spigot weld to avoid loss of data due to dead zone.

### 6.3 Conclusions

The effects of two geometrical features viz. thermal expansion bend and tubesheet on the guided wave ultrasonic inspection of SG tubes of a fast breeder reactor using in-bore magnetostriction transducers were studied. To understand the influence of geometry, FE simulations of L(0,2) mode propagation in a 3.0 m long straight tube and defect-free thermal expansion bends and the ones with pinholes were performed. Besides, 2D- axisymmetric FE simulations were also performed for a tubesheet-spigot-SG tube structure. Further, experiments were also conducted using an in-house developed in-bore magnetostrictive transducer in mockup SG test facility with SG tubes welded to the tubesheet through spigot welds.

The experimental signals were noisy and hence, were de-noised using the DWT with the optimized wavelet (sym12). The de-noised signals clearly showed the detection of multiple half and full circumferential grooves with the improved SNR of approx. 5-10 dB. The sensitivity obtained was 20% WT (0.46 mm) deep and 1 mm wide half circumferential groove based on a 6 dB criterion. The error in locating a defect was found to be approximately 10 mm. Irrespective of the location of a defect in the bend, it can be detected with good sensitivity. The magnetostrictive transducer used generates bi-directional waves, which can make signals hard to interpret because of multiple reflections. Therefore, cross-correlation based de-noising was attempted and that provided a good representation of the defect signals. Hence, defect signals amidst multiple inter-reflections and noise could be easily identified without any ambiguity.

Furthermore, FE simulation of axi-symmetric L(0,2) mode in the multiple bends of SG tubes showed maximum amplitudes at the extrados and the minimum amplitudes at the intrados. In

addition, it also undergoes mode conversion to a weak flexural mode. Also, there is a delay of 1.7  $\mu\text{s}$  in the arrival of the end reflected signal for the bent tube in comparison to the straight tube of the same length. This can be used to correct the location of a defect beyond the bend in actual testing.

Experimentally, a half circumferential groove (non-axi-symmetric) at the extrados of the thermal expansion bend was observed to exhibit a higher amplitude. The variation of sensitivity across the bend observed by the FE simulations with pinholes were also observed to be in line with the experimental observations made in the mock up SG tubes with half circumferential defects. The effect of bend on axi-symmetric defects (circumferential groove) is seen to be masked due to the integration of reflected energy from the full circumference of the defect.

Further, 2D-axi-symmetric FE simulations for 25 mm and 150 mm thick tubesheets with spigots were performed. The FE results indicated that the spigot-tubesheet transitions provide ~10% reflection of the incident L(0,2) mode and it was found to undergo mode conversion to longitudinal, shear and Rayleigh waves in the tubesheet. This feature was clearly observed in 150 mm thick tubesheet, whereas wave fronts were highly distorted in 25 mm thick tubesheet. Furthermore, the top of the 25 mm thick tubesheet (mockup SG set up) is understood to cause the second and third echoes in the three-echo pattern while 150 mm thick tubesheet behaves like a large medium with far-off boundaries causing low reflections. Since the actual SG tubes of PFBR are bounded by tubesheets with the thickness of 150 mm and 1.2 m diameter on either side, only one direct echo from a defect in an SG tube (23 m long) can be expected to be present along with a small L(0,2) mode reflection signal from spigot-tubesheet transitions. Consequently, signals can be interpreted without difficulty. It can also be inferred that signals

from heat exchanger tubes with thicker tubesheets are easier to interpret than those of thinner ones.

The developed in-bore magnetostrictive transducer thus generates L(0,2) mode from the inside of an SG tube efficiently and is also capable of detecting defects in SG tubes with the required sensitivity. Therefore, the developed transducer holds a good promise for the actual testing of SG tubes of PFBR which can be also extended to applications thereof.

## References

1. S.C. Chetal, V. Balasubramanian, P. Chellapandi, P. Mohanakrishnan, P. Puthiyavinayagam, C.P. Pillai, S. Raghupathy, T.K. Shanmugham, C. Sivathanu Pillai, The design of the Prototype Fast Breeder Reactor, Nuclear Engineering and Design 236 (2006) 852–860.
2. T.K. Mitra, Aravinda Pai and Prabhat Kumar, Challenges in manufacture of PFBR steam generators, Energy Procedia 7 (2011) 317-322.
3. Baldev Raj, B.K. Choudhary, R.K. Singh Raman, Mechanical properties and non-destructive examination of chromium-molybdenum ferritic steels for steam generator application, Pressure Vessels and Piping 81 (2004) 521-534.
4. S.C. Chetal, S.B. Bhoje, T.K. Mitra, S.R. Paranjpe, G. Vaidyanathan, Design of PFBR steam generator, Proc. of the specialists' meeting on steam generator failure and failure propagation experience, France, INIS 22 (18) 1990, Report No: IWGFR-78.
5. R. Srinivasan, P. Chellapandi and C. Jebaraj, Structural design approach of steam generator made of modified 9Cr-1Mo for high temperature operation, Transactions of the Indian Institute of Metals 63 (2-3) (2010) 629-634.
6. V.A. Suresh Kumar, I.B. Noushad, K.K. Rajan, Steam generator test facility-A test bed for steam generators of Indian sodium cooled fast breeder reactors, Nuclear Engineering Design 248 (2012) 169-177.
7. V. Vinod, L.S. Sivakumar, V.A. Suresh Kumar, I.B. Noushad, G. Padmakumar, K.K. Rajan, Experimental evaluation of the heat transfer performance of sodium heated once through steam generator, Nuclear Engineering and Design 273 (2014) 412–420.

8. Baldev Raj, S L Mannan, P. R. Vasudeva Rao, M. D. Mathew, Development of fuels and structural materials for fast breeder reactors, *Sadhana* 27(5) (2002) 527–558.
9. S.L. Mannan, S.C. Chetal, Baldev Raj, S.B. Bhoje, Selection of materials for prototype fast breeder reactor, *Trans. Indian Inst. Metals* 56(2) (2003) 155–78.
10. S.C. Chetal and G. Vaidyanathan, Evolution of design of steam generator for sodium cooled reactors, *Proc. of 3<sup>rd</sup> Int. Conf. on Heat Exchanger Design, Boilers and Pressure Vessels, Alexandria, Egypt* (1997) 41-57.
11. Y. Dai, Yong, X. Jia, K. Farrell, Mechanical properties of modified 9Cr–1Mo (T91) irradiated at  $\leq 300$  °C in SINQ Target3, *Journal of Nuclear Materials*, 318 (2003)192-199.
12. S. Kishore, A. Ashok Kumar, S. Chandramouli, B.K. Nashine, K.K. Rajan, S. Chetal, P. Kalyanasundaram, An experimental study on impingement wastage of Mod. 9Cr-1Mo steel due to sodium-water reaction, *Nuclear Engineering Design* 243 (2012) 49-55.
13. S. Thirunavukkarasu, B.P.C. Rao, G.K. Sharma, Viswa Chaitanya, C, Babu Rao, T. Jayakumar, Baldev Raj, Arvinda Pai, T.K. Mitra, Methodology for nondestructive assessment of integrity of steam generator shell welds, *International Journal of Structural Integrity* 2(2) (2011) 145-157.
14. S. Bakhtiari, D. S. Kupperman, W. J. Shack, Characterizing steam generator tube degradation mechanisms with eddy current technology, *Technical Letter Report, Argonne National Laboratory* (2007) 1-54.
15. H.M. Sadek, NDE technologies for examination of heat exchangers and boiler tubes-principles, advantages and limitations, *Insight* 48 (2006) 181-183.

16. R.M. Shriwardhankar, P. B. Patil, Mahesh Limaye, Development of helium leak testing system and procedure for testing welds of steam generator, *Energy Procedia* 7 (2011) 638-644.
17. B.S. Yoon, S.H. Yang, Y.S. Kim, H.J. Lee, Steam generator tube inspection of nuclear power plants using ultrasonic testing, *Transactions of the Korean Nuclear Society, Korea* (2006).
18. S. Vaidyanathan, S. Thirunavukkarasu, B.P.C. Rao, T. Jayakumar, P. Kalyanasundaram, Baldev Raj, Development of remote field eddy current technique for in-service inspection of ferromagnetic steam generator tubes, *Journal of Non-destructive Testing & Evaluation* 4(1) (2005) 26-30.
19. R. Grimberg, L. Udpa, A. Bruma, R. Steigmann, A. Savin, S. Udpa, Eddy current examination of steam generator tubes from PHWR power plants using rotating magnetic field transducer, *Proc. NDT for Safety, Czech Republic* (2007) 87-96.
20. Z. Chen, K. Chan, J. Huggins, T. Malkiewicz, Ultrasonic inspection of steam generators at CANDAU power plants, *Proc. of 17th World Conference on Nondestructive Testing, China* (2008) 1-8.
21. Z. Corak, Investigation of reliability of EC method for inspection of VVER steam generator tubes, *Proc. of 5th International Conference on Nuclear Option in Countries with Small and Medium Electricity Grids, Croatia* (2004) 1-8.
22. J. Poguët, G. Fleury, Circular phased array probes for inspection of Superphoenix steam generator tubes, *EPRI Phased Array Inspection Seminar, Portland, USA, 1998*.
23. B. Yoon, Y. Kim, S. Yang, An experimental result on flaw sizing of steam generator tube at nuclear power plants using ultrasonic testing, *Journal of Nuclear Science and Technology* 49 (2012) 760-767.

24. H. Hoshikawa, K. Koyama, Remote field eddy current testing of ferromagnetic double wall tube, *Non destr. Test. Eval* 7 (2009) 337-346.
25. H. Fukutomia, T. Takagib, M. Nishikawa, Remote field eddy current technique applied to non-magnetic steam generator tubes, *NDT&E International* 34 (2001) 17-23.
26. Standard practice for in-situ examination of ferromagnetic heat-exchanger tubes using remote field testing, *ASME Article 26 SE-2096, ASTM Section V* (2010) 556-565.
27. D.N. Alleyne, B. Pavlakovic, M. J.S. Lowe and P. Cawley, Rapid, long range inspection of chemical plant pipework using guided waves, *AIP Conf. Proc, Review of Progress in Quantitative Nondestructive Evaluation* 20 (2001) 180-187.
28. J. L. Rose, A Baseline and Vision of Ultrasonic Guided Wave Inspection Potential, *Journal of Pressure Vessel Technology* 124 (2002) 273-282.
29. J. L. Rose, Guided wave nuances for ultrasonic nondestructive evaluation, *IEEE Transactions on Ultrasonics, Ferroelectrics, and Frequency Control* 47 (2000) 575-583.
30. M.G. Silk, K.F. Bainton, The propagation in metal tubing of ultrasonic wave modes equivalent to Lamb waves, *Ultrasonics* 17(1) (1979) 11-19.
31. M.F. Zhenga, C. Lua, Guo-Zhu Chenb, P. Men, Modelling three dimensional ultrasonic guided wave propagation and scattering in circular cylindrical structures using finite element approach, *Physics Procedia* 22 (2011) 112-118.
32. A Tatarinov, Evgency N. Barkanov, E. Davydov, M. Mihovski, T- and L-types of long-range guided waves for defect detection, *Non-destructive testing and Repair of pipelines, Engineering Materials, Springer International publishing* (2018) 15-29.

33. M.J.S. Lowe and P. Cawley, Long range guided wave inspection usage–current commercial capabilities and research directions, Technical report, Department of Mechanical Engineering, Imperial College, London, UK. (2006)1-40.  
<https://www3.imperial.ac.uk/pls/portallive/docs/1/55745699.pdf>
34. D.N. Alleyne, P. Cawley, The excitation of Lamb waves in pipes using dry-coupled piezoelectric transducers, *Journal of Nondestructive Evaluation* 15(1) (1995) 11-20.
35. C. Aristegui, M.J.S. Lowe, P. Cawely, Guided waves in fluid-filled pipes surrounded by different fluids, *Ultrasonics* 39 (2001) 367-375.
36. P.S. Lowe, Ruth M. Sanderson, Nikolaos V. Boulgouris, Alex G. Haig, Wamadeva Balachandran, Inspection of cylindrical structures using the first longitudinal guided wave mode in isolation for higher flaw sensitivity, *IEEE sensors Journal*, 16(3) (2016) 706-714.
37. H. J. Shin, J.L. Rose, Guided wave tuning principles for defect detection in tubing, *Journal of Nondestructive Evaluation* 17 (1998) 27-36.
38. E. Thomas R. Hay, Joseph L. Rose, Flexible PVDF comb transducers for excitation of axisymmetric guided waves in pipe, *Sensors and Acutators A* 100 (2002) 18-23.
39. J. Xu, Y. Sun, J. Zhou, Research on the lift-off effect of receiving longitudinal mode guided waves in pipes based on the Villari effect, *Sensors* 16(9) 1529(2016) 1-14.
40. A. Cong M, Wu X, Qian C, A Longitudinal Mode Electromagnetic Acoustic Transducer(EMAT) Based on a Permanent Magnet Chain for Pipe Inspection, *Sensors* 16(5) (2016) 1-18.

41. J. Li and J.L. Rose, Implementing guided wave mode control by use of a phased transducer array, *IEEE Transactions on Ultrasonics Ferroelectrics and Frequency Control* 48(3) (2001) 761-768.
42. Samuel Hill, Steve Dixon, Sri Harsha Reddy K, Prabhu Rajagopal, Krishnan Balasubramaniam, A new electromagnetic acoustic transducer design for generating torsional guided wave modes for pipe inspections, *AIP Conference Proceedings* 1806 (2017) 050003-9.
43. P.D. Wilcox, R.P. Dalton, M.J.S. Lowe, P. Cawley, The mode and transducer selection for long Lamb wave inspection, *Key Engineering Materials* 167-168 (1999) 152-161.
44. . J.L. Rose, *Ultrasonic guided waves in solid media*, Cambridge University Press, USA (2014)
45. P.D. Wilcox, M.J.S. Lowe, P. Cawley, Long range Lamb wave inspection: The effect of dispersion and modal selectivity, *Rev. of Progress in Quan. Nondestructive Evaluation* 18 (1999) 151-158.
46. P.D. Wilcox, A rapid signal processing technique to remove the effect of dispersion from guided wave signals, *IEEE Trans. On Ultrasonics, Ferroelectrics, and Frequency Control* 50 (4) (2003) 419-427.
47. A. Demma, The interaction of guided with discontinuities in structures, Ph.D. thesis, Imperial College, London, U.K. (2003).
48. D.N. Alleyne, P. Cawley, Optimization of Lamb wave inspection techniques, *NDT & E*, 25 (1992) 11-22.
49. Y. Li, J. Xu, Q. Li, G. Chen, Analysis of source influence on guided wave excitation in cylindrical structures using spatial Fourier transform method, *Journal of Sensors* (2020) 1-11.

50. D. N. Alleyne, P. Cawley, The interaction of lamb waves with defects, *IEEE Transactions on Ultrasonics, Ferroelectrics, and Frequency Control* 39 (1992) 381-396.
51. C. Aristegui, M.J.S. Lowe, P. Cawley, Guided waves in fluid-filled pipes surrounded by different fluids, *Ultrasonics* 39 (2001) 367-375.
52. W. Bottger, H. Schnider, W. Weingarten, Prototype EMAT system for tube inspection with guided ultrasonic waves, *Nuclear Eng. and Design*, 102 (1987) 369-376.
53. P. Cawley, Practical long-range guided wave inspection — managing complexity, *Review of Progress in Quantitative Nondestructive Evaluation* 22 (2003) 22-37.
54. D.N. Alleyne, P. Cawley, The effect of discontinuities on the long-range propagation of Lamb waves in pipes, *Proc. Instn. Mech. Engrs.* 210 (1996) 217-226.
55. D.N. Alleyne, M. Lowe, P. Cawley, The inspection of chemical plant pipework using Lamb wave: Defect sensitivity and field experience, *Review of Progress in Quantitative Nondestructive Evaluation* 15 (1996) 1859-1866.
56. M. Mokhles, C. Ghavipankeh, A. Tamimi, The use of ultrasonic guided waves for extended pipeline qualification prediction, *International NDT conference & Exhibition, Singapore 2013.*
57. I. Park, Y.K. Kim, H.M. Kim, W.J. Song, Y.S. Cho, Long-range ultrasonic guided wave technique for inspection of pipes, *Key Engineering Materials* 321-323 (2006), 799-803.
58. J.L. Rose, J.J. Diriti, A. Pilarski, K. Rajana, F. Carr, A guided wave inspection for nuclear steam generator tubing, *NDT&E International* 27(6) (1994) 307-310.

59. L. Zenghua, W. Bin, H. Cunfu, Y. Shiming, W. Xiuyan, Detection of longitudinal defect in pipes using torsional modes, *Chinese Journal of Mechanical Engineering* 19 (2006.)146-150.
60. R.B. Thompson, R.K. Elsley, W.E. Peterson, C.F. Vasile, An EMAT system for detecting flaws in steam generator tubes, *Ultrasonic Symposium* (1979) 246-249.
61. J.L. Rose, D. Jiao, J. Spanner, Ultrasonic guided waves for piping inspection, *Review of Progress in Quantitative Nondestructive Evaluation* 16 (1997) 1285-1290.
62. I.K. Park, Y.K. Kim, Y.H. Cho, W.J. Song, Y.S. Ahn, Y.S. Cho, G. Jung, A study on the behaviour of ultrasonic guided wave mode in a pipe using a comb transducer, *Key Engineering Materials* 297-300 (2005) 2182-2186.
63. H. Kwun, K.A. Bartels, Magnetostrictive sensor technology and its applications, *Ultrasonics*, 36 (1998) 171-178.
64. Hegeon Kwun, Sang Y. Kim, and Glenn M. Light, Magnetostrictive sensor technology for long-range guided wave inspection and monitoring of pipe, *NDT Technician*, 10(2) (2011) 6-9.
65. N. Muthu and S. Vinogradov, Application of guided wave technology for screening of SeaCure tubing, Sixth international EPRI conference on NDE in relation to structural integrity of nuclear and pressurized components, Hungary, 2007.
66. Sergey A Vinogradov, Tuning of torsional mode guided wave technology for screening of carbon steel heat exchanger tubing, *Materials Evaluation* (2008) 419-424.
67. Vinogradov Sergey, Jacobs, Bruce, Godwin, Joel, Experimental and theoretical investigation for the use of guided waves to detect and size corrosion/erosion

- defects in heat exchanger tubes, 7th EPRI Balance of Plant Heat Exchanger NDE Symposium, Santa Ana Pueblo, New Mexico (2002) 1-10.
68. H. Kwun and C. Dynes, Long-range guided wave inspection of pipe using the magnetostrictive sensor technology—feasibility of defect characterization, SPIE proceedings 3398 (1998) 28-34.
69. Y. M. Cheong, Shinkim, Acoustic performance of a magnetostrictive strip sensor for a torsional guided wave, Proc. of the International Conference on ANDE 2007, World Scientific, Singapore (2008) 418-423.
70. P. Sun, X. Wu, J. Xu, J. Li, Enhancement of the excitation efficiency of the non-contact magnetostrictive sensor for pipe inspection by adjusting the alternating magnetic field axial length, *Sensors*, 14 (2014) 1544-1563.
71. S. Heinlein, P. Cawley, T.K. Vogt, Reflection of Torsional  $T(0,1)$  waves from defects in pipe bends, *NDT&E International* 93 (2018) 57-63.
72. J. Ni, S. Zhou, P. Zhang, Y. Li, Effect of Pipe Bend Configuration on Guided Waves-Based Defects Detection: An Experimental Study, *Journal of Pressure Vessel Technology* 138(2) (2015) 021203-1 -021203-9.
73. B. Verma, T.K. Mishra, K. Balasubramaniam, P. Rajagopal, Interaction of low-frequency axisymmetric ultrasonic guided waves with bends in pipes of arbitrary bend angle and general bend radius, *Ultrasonics* 54 (2014) 801-808.
74. A. Demma, P. Cawley, M. Lowe, B. Pavlakovic, The effect of bends on the propagation of guided waves in pipes, *Trans. of the ASME* 127 (2005) 328-335.
75. M.X. Qi, P.G. Zhang, J. Ni, S.P. Zhou, Experiment and numerical simulation of ultrasonic guided wave propagation in bent tube, *Procedia Engineering* 130 (2015) 1603-1611.

76. T. Hayashi, K. Kawashima, Z. Sun, J.L. Rose, Guided wave propagation mechanics across a pipe elbow, *Transactions of the ASME* 127 (2005) 322-327.
77. H. Nishino, S. Masuda, Y. Mizobuchi, T. Asano, K. Yoshida, Long-range testing of welded elbow pipe using T(0,1) mode ultrasonic guided wave, *Japanese Journal of Applied Physics* 49 (2010) 116602-1-6.
78. M.V. Predoi, C.C. Petre, Guided waves scattering by discontinuities near pipe bends, *Proc. of Meetings on Acoustics* 19 (2013) 1-9.
79. L. G. Sheng, T.J. Ping, W. Liang, X. Yan, Defects detection in typical positions of bend tubes using low-frequency ultrasonic guided wave, *J. Cent. South. Univ.* 22 (2015) 3860-3867.
80. T.J. Jack, A. Guo, W. Xin, H.J. Hou, Guided ultrasonic waves in steel pipe with welded bend with defect, 21<sup>st</sup> International Congress on Sound and Vibration, China (2014) 1-8.
81. Y.M. Cheong, D.H Lee, H. K. Jung, Ultrasonic guided wave parameters for detection of axial cracks in feeder pipes of PHWR nuclear power plants, *Ultrasonics* 42 (2004) 883-888.
82. B. Yoon, S. Yang, H. Lee, Y. Kim, Detection and mode identification of axial cracks in the steam generator tube of the nuclear power plant using ultrasonic guided wave, *Journal of Nuclear Science and Technology* 47(8) (2010) 754-759.
83. L. Zenghua, B. Wu, H. Cunfu, X. Wang, S. Yang, Circumferential and longitudinal defect detection using T(0,1) mode excited by thickness shear mode piezoelectric elements, *Ultrasonics* 44 (2006) 1135-1138.
84. M.J.S. Lowe, D.N. Alleyne, P. Cawley, Defect detection in pipes using guided waves, *Ultrasonics* 36 (1998) 147-154.

## **References**

85. D.N. Alleyne, M.J.S. Lowe, P. Cawley, The reflection of guided waves from circumferential notches in pipes, *Journal of Applied Mechanics* 65 (1998) 635-641.
86. P. Cawley, M.J.S. Lowe, F. Simonetti, C. Chevalier, A.G. Rossenbrand, The variation of the reflection coefficient of extensional guided waves in pipes from defects as a function of defect depth, axial extent, circumferential extent and frequency, *Journal of Mechanical Engineering Science* 216(11) (2002) 1131-1143.
87. A. Demma, P. Cawley, M. Lowe, A.G. Roosenbrand, The reflection of the fundamental torsional mode from cracks and notches in pipes, *Journal of the Acoustical Society of America* 114(2) (2003) 611-625.
88. M. Ratasepp, S. Fletcher, M.J.S. Lowe, Scattering of the fundamental torsional mode at an axial crack in a pipe, *J. Acoust. Soc. Am.* 127(3) (2010) 730-740.
89. A. Lovstad, P. Cawley, The reflection of the fundamental torsional guided wave from multiple circular holes in pipes, *NDT & E International* 44 (2011) 553-562.
90. A. Lovstad, P. Cawley, The reflection of the fundamental torsional mode from pit clusters in pipes, *NDT & E International* 46 (2012) 83-93.
91. S. Ma, Z. Wu, Y. Wang, K. Liu, The reflection of guided waves from simple dents in pipes, *Ultrasonics* 57 (2015) 190-197.
92. R. Carandente, J. Ma, P. Cawley, The scattering of the fundamental torsional mode from axi-symmetric defects with varying depth profile in pipes, *J. Acoust. Soc. Am.* 127(6) (2010) 3440-3448.
93. D.N. Alleyne, T. Vogt, P. Cawley, The choice of torsional or longitudinal excitation in guided wave pipe inspection, *Insight-Non-Destructive Testing and Condition Monitoring* 51 (2009) 373-377.

94. M. Niethammer and L.J. Jacobs, Time-frequency representations of Lamb waves, *J. Acoust. Soc. Am.* 109(5) (2001) 1841-1847.
95. W. H. Prosser and M. D. Seale, Time-frequency analysis of the dispersion of Lamb modes, *J. Acoust. Soc. Am.* 105(5) (1999) 2669-2676.
96. D. Ta, K. Huang, W. Wang, Y.Y. Wang, H.L. Lawrence, Identification and analysis of multimode guided waves in tibia cortical bone, *Ultrasonics* 44 (2006) 279–284.
97. V. Matz, R. Smid, M. Kreidl, S. Starman, Comparison of de-noising methods used for EMAT signals, *Proc. of 9th European Conference on NDT, Berlin, Germany* (2006) 1-7.
98. Y. Kopsinis and S. McLaughlin, Development of EMD-Based Denoising Methods Inspired by Wavelet Thresholding, *IEEE Transactions on Signal Processing* 57(4) (2009) 1351-1362.
99. M.S.M. Naquiuddin, M.S. Leong, L.M. Hee, M.A.M. Azrieasrie, Ultrasonic signal processing techniques for Pipeline: A review, *MATEC Web of Conferences* 255 (2019), *EAAI Conference 2018*, 1-11.
100. L. Yu, J. Bao, V. Giurgiutiu, Signal processing techniques for damage detection with piezoelectric wafer active sensors and embedded ultrasonic structural radar, *Proc. SPIE 5391, Smart Structures and Materials 2004: Sensors and Smart Structures Technologies for Civil, Mechanical, and Aerospace Systems* (2004) 1-12.
101. L.V. Matz, R. Smid, M. Kreidl, S. Starman, Signal-to-noise ratio enhancement based on wavelet filtering in ultrasonic testing, *Ultrasonics* 49 (2009) 752–759.
102. O.E. Brigham, *Fast Fourier Transform*, Prentice-Hall, Inc. USA (1974).
103. A.D. Poularikas, *Transforms and Applications Handbook*, CRC Press, third Edition, USA (2018).

104. J. Dong, M. Yin, Analysis of Guided Wave Signal Based on LabVIEW and STFT, 2010 International Conference on Computer, Mechatronics, Control and Electronic Engineering (CMCE) (2010) 115-117.
105. J. Prager, C. Hoever, G. Brekow, M. Kreutzbruck, Flaw detection with guided waves using phased array technique, NDT in Progress, 5th International Workshop of NDT Experts 2009, 4 (2010) 1-11.
106. D. Marioli, C. Narduzzi, C. Offelli, D. Petri, E. Sardini, and A. Taroni, Digital time-of-flight measurement for ultrasonic sensors, IEEE Transactions on Instrumentation and Measurement 41(1) (1992) 93-97.
107. R. Mallett, P.J. Mudge, T. H. Gan, W. Balachandran, Analysis of cross-correlation and wavelet de-noising for the reduction of the effects of dispersion in long-range ultrasonic testing, Insight 49(6) (2007) 350-355.
108. Michael Weeks, Digital Signal Processing using MATLAB and Wavelets, Firewall media, India (2007).
109. O. Rioul and M. Vetterli, Wavelets and signal processing, IEEE Signal Processing Magazine 8(4) (1991) 14-38.
110. R. Polikar, The Wavelet Tutorial, 2<sup>nd</sup> Edition, Part 1 (1996) [online].
111. W. Sheng S.F. Wirtz, D. Soffker, Wavelet Packet Transform-Based Feature Extraction for Acoustic Emission Pattern Recognition, 9th European Workshop on Structural Health Monitoring (EWSHM 2018) 1-8.
112. I. Daubechies, Orthonormal bases of compactly supported wavelets, Communications on Pure and Applied Mathematics, 41(7) (1988) 909-996.
113. Zhongqing Su and Lin Ye, Identification of Damage Using Lamb Waves: From Fundamentals to Applications, Springer (2009).

114. I. Fair weather, A. Brummfield, LabView, A Developer's Guide to Real World Integration, CRC Press, USA (2012).
115. D.L. Donoho, De-noising by soft thresholding, IEEE Transactions on Information Theory 41 (1995) 613-627.
116. D.L. Donoho, I.M. Johnstone, Ideal spatial adaptation by wavelet shrinkage, Biometrika 81 (1994) 425-455.
117. D.L. Donoho, I.M. Johnstone, Adapting to unknown smoothness via wavelet shrinkage, J. Amer. Statist. Assoc. 90 (1995) 1200-1224.
118. J.C. Lazaro, Noise reduction in ultrasonic NDT using discrete wavelet transform processing, IEEE Ultrasonics Symposium (2002) 777-780.
119. J.C. Lazaro, J.L.S. Emeterio, A. Ramos, J.L. Fernandez-Marron, Influence of thresholding procedures in ultrasonic grain noise reduction using wavelets, Ultrasonics 40 (2002) 263-267.
120. W.K. Ngui, M.S. Leong, L.M. Hee, A.M. Abdelrahman, Wavelet analysis: Mother wavelet selection methods, Applied Mechanics and Materials 393 (2013) 953-958.
121. V. Matz, M. Kreidl, R. Smid, Signal-to-Noise Ratio Improvement Based on the Discrete Wavelet Transform in Ultrasonic Defectoscopy, Acta Polytechnica 44 (2004) 61-66.
122. M.H.S. Siqueira, C.E.N. Gatts, R.R. da Silva, J.M.A. Rebello, The use of ultrasonic guided waves and wavelets analysis in pipe inspection, Ultrasonics 41 (2004) 785-797.
123. M. Kreidl, P. Houfek, Reducing ultrasonic signal noise by algorithms based on wavelet thresholding, Acta Polytechnica 42(2) (2002) 60-65.

124. V. Giurgiutiu, Structural Health Monitoring with Piezoelectric Wafer Active Sensors, Academic Press, 2<sup>nd</sup> Edition, USA (2014).
125. B. Pavlakovic, M. Lowe, D. Alleyne, P. Cawley, DISPERSE: A general purpose program for creating dispersion curves, Review of Progress in Quantitative Nondestructive Evaluation 16 (1997) 185-192.
126. A. Ghavamian, F. Mustapha, B.T.H.T. Baharudin, N. Yidris, Detection, localization and assessment of defects in pipes using guided wave techniques: A review, Sensors 18 (2018) 1-48.
127. Y. He, P.S. Stamenov, C. Jiang, M. Coey, When does magnetostriction not conserve volume? IEEE International Magnetics Conference (INTERMAG), 2017.
128. S. Tumanski, Handbook of Magnetic Measurements, CRC press, 1<sup>st</sup> edition, 2011.
129. J. Awrejcewicz, Resonance, In Tech, 1<sup>st</sup> edition 2017.
130. Hain Abramovich, Intelligent materials and structures, De Gruyter, 2016.
131. H Kwun, S. Antonio, C.M. Teller, Non-destructive evaluation of pipes and tubes using magnetostrictive sensors, US. Patent, No. 5581037.
132. H. Kwun and C.M. Teller, Magnetostrictive generation and detection of longitudinal, torsional and flexural waves in a steel rod, J. Acoust. Soc. Am. 96(2) (1994) 1202-1204.
133. R. Puthusseri and K. Balasubramaniam, Influence of magnetostrictive strip size in the generation of L(0,2) and T(0,1) wave mode using magnetostrictive patch transducer (MPT), AIP Conference Proceedings 2102 (2019) 050023-1-6.
134. IEEE Standard on Magnetostrictive Materials: Piezomagnetic Nomenclature, IEEE Transactions on Sonics and Ultrasonics (1973) 71-76.

135. Y. Y. Kim, Y. E. Kwon, Review of magnetostrictive patch transducers and applications in ultrasonic nondestructive testing of waveguides, *Ultrasonics* 62 (2015) 3–19.
136. Remo Ribichini, Modelling of electromagnetic acoustic transducers, Ph.D. Thesis, Imperial College, London (2011).
137. Sergey Vinogradov, Adam Cobb, Glenn Light, Review of magnetostrictive transducers (MsT) utilizing reversed Wiedemann effect, *AIP Conf. Proc.* 1806 (2017) 02008-1-9.
138. D.C. Jiles, Theory of the magnetomechanical effect, *J. Phys. D. App. Phys.* 28 (1995) 1537-1546.
139. Marcelo J. Dapino, On magnetostrictive materials and their use in adaptive structures, *Structural Engineering and Mechanics* 17 (2004)1-26.
140. A. Bruce Thompson, Mechanisms of electromagnetic generation and detection of ultrasonic Lamb waves in iron-nickel alloy polycrystals, *J. Appl. Phys.* 48 (12) (1977) 4942-4950.
141. Frederick T. Calkins, Alison B. Flatau and Marcelo J. Dapino, Overview of Magnetostrictive Sensor Technology, *Journal of Intelligent Material Systems and Structures* 18(10) (2007) 1-11.
142. J. Kim, E. Jung, Finite element analysis for acoustic characteristics of a magnetostrictive transducer, *Smart Materials and Structures*, 14(2005) 085007-1-13.
143. J. H. Oh, K. H. Sun and Y. Y. Kim, Time-harmonic finite element analysis of guided waves generated by magnetostrictive patch transducers, *Smart Materials and Structures* 12 (2013) 1273-1280.

144. X.W. Zhang, Z.F. Tang, F.Z. Lv, X.H. Pan, Excitation of axisymmetric and non-axisymmetric guided waves inelastic hollow cylinders by magnetostrictive transducers, *Journal of Zhejiang University-SCIENCE A (Applied Physics & Engineering)* 17(3) (2016) 215-229.
145. D. J. Griffiths, *Introduction to Electrodynamics*, Cambridge University Press, USA (2017).
146. N. Ida, *Numerical Modelling for Electromagnetic Non-Destructive Evaluation*, Chapman & Hall, 1<sup>st</sup> Edition, GB (1995).
147. A.H. Harker, Numerical modelling of the scattering of elastic waves in plates, *Journal of Non-destructive Evaluation* 4(2) 89-106.
148. S.P. Jay, *Application of the Boundary Element Method to Elastic Wave Scattering Problems in Ultrasonic Nondestructive Evaluation*, Ph.D. thesis, Iowa State University, USA (1991).
149. David N. Alleyne, *The Nondestructive Testing of Plates using Ultrasonic Lamb Waves*, Ph.D. thesis, Imperial College of Science, Technology and Medicine, University of London (1991).
150. M. Ameen, *Boundary Element Analysis: Theory and Programming*, Narosa Publishing House, India (2001).
151. R. Cook, D.S. Malkus, M.E. Plesha, R.J. Witt, *Concepts and Applications of Finite Element Analysis*, 4<sup>th</sup> Edition, Wiley, India (2004).
152. G.R. Liu, S.S. Quek, *The Finite element Method: A Practical Course*, Butterworth Heinemann (2003).

153. J.S. Sun, K.H. Lee, H.P. Lee, Comparison of implicit and explicit finite element methods for dynamic problems, *Journal of Materials Processing Technology* 105 (2000) 110–118.
154. Mickael Brice Drozd, Efficient finite element modelling of ultrasonic waves in elastic media, Ph.D. thesis, Imperial College of Science, University of London, UK (2008).
155. F. Mosera, Laurence J. Jacobs, J. Qu, Modeling elastic wave propagation in waveguides with the finite element method, *NDT&E International* 32 (1999) 225–234.
156. M. Gresil, V. Giurgiutiu, Y. Shen, B. Poddar, Guidelines for using the finite element method for modeling guided lamb wave propagation in SHM processes, 6th European Workshop on Structural Health Monitoring, Germany (2012) 1-8.
157. COMSOL Multiphysics, Model library, Ver. 3.4.
158. F. Hasan, J. Iqbal, F. Ahmed, Stress-corrosion failure of high-pressure gas pipeline, *Engineering Failure Analysis* 14 (2007) 801-809.
159. L.J. Berchmans, S. Muralidharan, N.S. Rangaswamy, S. Natrajan, V. Sivan, S. Venkatakrishna Iyer, Stress-corrosion cracking and hydrogen embrittlement susceptibility studies on modified 9Cr-1Mo steel weldments in acidic and neutral media, *British Corrosion Journal* 31(3) (1996) 223-226.
160. J. Paul Guyer, *An Introduction to Liquid Process Piping*, Second Edition, Guyer Partners (2017).
161. Joseph R. Davis, *Stainless Steels*, ASM Specialty Handbook, ASM International (1994).
162. Disperse software, User's manual, Version 2.0 (2000).

163. Anish Kumar, Correlation of microstructure and mechanical properties with ultrasonic parameters in metallic materials, Ph.D. thesis, Indian Institute of Technology, Kharagpur, India (2005).
164. ABAQUS Analysis User's Manual 6.10.
165. COMSOL, User's guide, version 5.2 (2015).
166. S. Thirunavukkarasu, Remote field eddy current based approaches for high - sensitive detection of defects in ferromagnetic steam generator tubes, Ph.D. thesis, Homi Bhabha National Institute, IGCAR, Kalpakkam, India (2013).
167. W. Gao, C. Glorieux, S.E. Kruger, K. Van de Rostyne, V. Gusev, W. Lauriks, J. Thoen, Investigation of the microstructure of cast iron by laser ultrasonic surface wave spectroscopy, *Materials Science and Engineering A* 313 (2001) 170–179.
168. J. D. Irwin, R. M. Nelms, *Basic Engineering Circuit Analysis*, Wiley, 8<sup>th</sup> edition, USA (2008).
169. H. A. Wheeler, Simple Inductance Formulas for Radio Coils, *IEEE Proceedings of the Institute of Radio Engineers* 16(10) (1928) 1398-1400.
170. H.L. Libby, *Introduction to Electromagnetic Non-destructive Test Methods*, Wiley-Interscience USA (1971).
171. D.J. Hagemaiier, *Fundamentals of Eddy Current Testing*, ASNT, Columbus, OH, USA (1990).
172. P. Rizzo, M. Cammarata, I. Bartoli, F. Lanza di Scalea, S. Salamone, S. Coccia, R. Phillips, Ultrasonic guided waves-based monitoring of rail head: Laboratory and field tests, *Advances in Civil Engineering* (2010) 1-13.
173. M.A. Meyers, *Dynamic Behaviour of Materials*, John Wiley & Sons, NY, USA (1994).

## Thesis Highlights

**Name of the Student:** M.M. Narayanan

**Name of CI:** Indira Gandhi Centre for Atomic Research Enrolment No.: PHYS 02 2012 04 012

**Thesis Title:** *Development of non-contact ultrasonic Guided Wave-based Methodology for Inspection of Steam Generator Tubes of PFBR*

**Discipline:** Physical Sciences

**Sub-Area of Discipline:** Elastic wave propagation and NDT

**Date of viva voce:** 20/04/2021

Steam generator tubes of fast nuclear reactors is very critical because SG tubes carry water for steam generation by extracting heat from hot liquid sodium flowing on the OD side. In the event of leakage of water/steam to sodium side will lead to sodium-water reaction, which is highly exothermic and it may lead to secondary damage. To test the integrity of SG tubes, ultrasonic guided wave methodology and an in-bore magnetostrictive transducer (ID side generation of guided waves) have been developed for examination.

Towards the development of a non-contact ultrasonic guided wave technique and methodology for inspection of steam generator (SG) tubes, ultrasonic longitudinal guided wave L(0,2) mode in the frequency range of 250 kHz-350 kHz is optimized in terms of long-range propagation of 46 m length of an SG tube, negligible dispersion, low attenuation and detection of multiple circumferential, axial, pinhole, tapered and sodium impingement defects in SG tubes. Fig. 1 shows Finite Element (FE) and experiment signals obtained in a 1.5 m long tube with multiple circumferential defects in the same line. The defect parameter that influences the reflection is found to be the cross-sectional area of a defect and all types of defects have been detected with the required sensitivity.

However, the developed methodology cannot be implemented as accessibility for inspection is only through IDs of the tubes. In order to extend the methodology developed, ferromagnetic property was exploited to generate L(0,2) mode through magnetostrictive means from the ID side. Towards this, systematic 2D- axisymmetric FE simulations for the design of an in-bore magnetostrictive transducer (MST) were performed to optimize the dimensions of the magnet and the transmitter and receiver coils. The optimized diameter and length of the magnet are 10 mm and 100 mm and the optimized length of the transmitter and receiver coils is half the wave length (=10 mm). The number of turns is optimized to be 80 turns using the Thevenin circuit model. By considering 75% fill-factor, the width of the coil has been optimized to two layers of 34 SWG copper wire.

With the optimized parameters, an in-bore magnetostrictive transducer (MST) has been fabricated, as shown in Fig. 2 and tested experimentally for long range propagation (51 m) and in the SG tubes welded to the tubesheet of the mock SG test facility. The detection sensitivity obtained was a 20%WT (0.46 mm) deep and 1 mm wide half circumferential groove. Fig. 3a shows the raw signal (SNR: 9.5 dB) obtained in an SG tube in the mockup system with five full circumferential grooves (20%WT deep) and Fig. 3b shows the corresponding DWT denoised signal (SNR: 15dB).

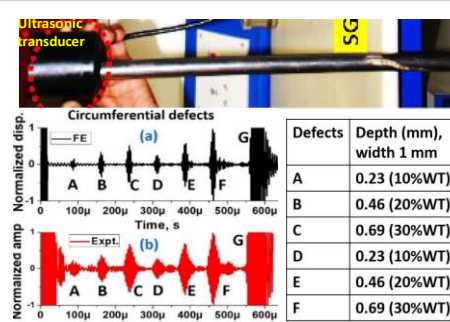


Fig. 1 Signals (FE & Expt.) obtained in a 1.5 m long tube with multiple circumferential defects (A-F) in the same line.

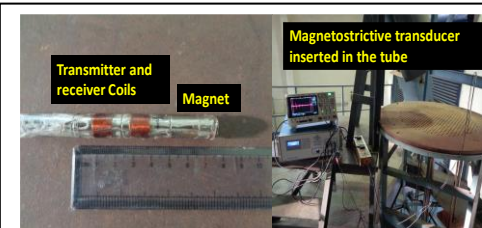


Fig. 2. Photographs showing developed in-bore magnetostrictive transducer used for data acquisition in the mock up SG system

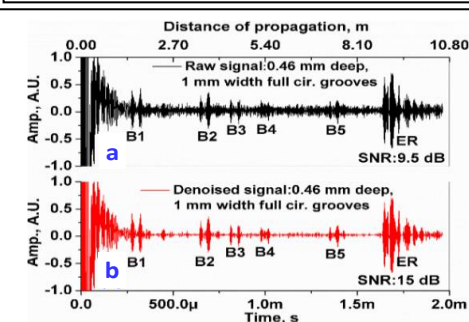


Fig. 3(a) shows the raw signal (SNR: 9.5 dB) obtained in an SG tube in the mockup system with five full circumferential grooves (B: 20%WT deep) obtained using the developed MST and (b) shows the corresponding DWT denoised signal (SNR: 15dB).